Alma Mater Studiorum - Università di Bologna

DOTTORATO DI RICERCA IN

AUTOMOTIVE PER UNA MOBILITÀ INTELLIGENTE

Ciclo 34

Settore Concorsuale: 09/B1 - TECNOLOGIE E SISTEMI DI LAVORAZIONE

Settore Scientifico Disciplinare: ING-IND/16 - TECNOLOGIE E SISTEMI DI LAVORAZIONE

STUDY AND EXPERIMENTAL CHARACTERIZATION OF THE LASER WELDING PROCESS FOR THE MANUFACTURING OF ELECTRIC POWERTRAIN COMPONENTS IN THE AUTOMOTIVE INDUSTRY

Presentata da: Vincenzo Dimatteo

Coordinatore Dottorato

Nicolò Cavina

Supervisore

Alessandro Fortunato

Esame finale anno 2022

INDEX

List of Figures

List of Tables

Abstract

The PhD project that will be presented in this thesis is focused on the study and optimization of the production process for the manufacturing of electrical powertrain components in the automotive field using the laser beam welding process (LBW). The objective is to define, through experimental activities, an optimized process condition for applications in the electrical field that can be generalized, that is, which guarantees its reproducibility as the types of connections vary and which represents the basis for extending the method to future applications in e-mobility sector. The work developed along two lines of research, the convergence of which made it possible to create prototypes of battery modules based on different types of lithium-ion cells and stator windings for electric motors with the aim of defining the best hardware solution and maximizing the mechanical and electrical properties in compliance with the process constraints imposed by each application. On the one hand, the different welding configurations involving the production of batteries based on pouch cells and therefore the welding of aluminum and copper in dissimilar configuration were studied, while for the prismatic cells only one configuration was analyzed. On the other hand, the welding of pure copper hairpins with rectangular shape in edge joint configuration was studied for the production of stator windings. Starting from these activities, the technological strategies for the design and production of components have been developed. The experimental tests carried out have demonstrated the feasibility of using the LBW process for the production of electric powertrain components entirely designed and developed internally as the types of materials and welding configurations vary; the methodologies required for the characterization methods, necessary for the end-of-line tests, for the evaluation of the properties of the different joint configurations and components (battery and electric motor) were also defined with the aim of obtaining the best performance. Finally, the activities carried out over the years have had as their final objective the design of an automated welding station following the results obtained during the research period. The entire doctorate program was conducted in collaboration with Ferrari Auto S.p.A. and the direct industrial application of the issues addressed has been faced. Experimental tests were conducted in the laboratories of the Industrial Engineering department of the University of Bologna while the validation of the prototypes and specific tests were carried out at the hybrid department of Ferrari Auto S.p.A.

Introduction

The progressive trend concerning limitation of CO_2 emissions by governments as well as the shortage of oil resources worldwide associated with the increase in the cost of fuel results in a global demand for alternative forms of energy in different field of applications**[1]**. In the transport and mobility sector, the request for these forms of alternative energy is contained within the mega trend of electric mobility (e-Mobility). A key enabler for the future of electric mobility is certainly represented by the design and manufacturing of durable efficient powertrain components with reduced industrial costs. As a results Electric vehicles (EVs), hybrid of plug-in hybrid (HEVs or PHEVs) vehicles will gain popularity due to market factors and technological developments in this regard**[2]**. Leaving aside the topic concerning power electronic, the heart of an EV or PHEV vehicles lies with battery pack and electric motor. Typically, a standard automotive battery pack consists of hundreds, even thousand, of single Lithium-Ion (Li-ion) cells that are connected in series or parallel in order to achieve the obtain the required power and energy**[3]**. For vehicle propulsion system there are three different types of cells, including cylindrical, prismatic and pouch cells; in applications relating to supercars or in any case vehicles that must deliver high power and energy, pouch or prismatic cells are mainly used, leaving the cylindrical cells to other applications. Li-ion pouch cells are widely used in high-performance vehicle thanks to their high energy density; the electric current collectors of the latter are produced by using thin pure aluminum(cathode) and copper (anode) sheets. During the assembly, various thickness and numbers of electrodes need to be joined for performance needing and manufacturing efficiency**[4]**. On the other hand, during prismatic cells assembly, in which anode and cathode are produced using pure aluminum, a busbar, which acts as a current collector, need to be joined to the electrode. Another key component is certainly the electric motor which consists of a stator and a rotor with permanent magnets that can be fitted on the surface or inserted into cavities**[5]**. The electric motor concept, in which the possibility of using laser welding was studied, refers to high-power electric machines with distributed winding characterized by a stator with cavities in which the wire-shaped copper windings or rectangular in shape are inserted and subsequently welded. In the manufacturing of electric drives a promising solution is to produce the winding stator with thick U-shaped insulated copper conductors with a rectangular cross section that must be connected **[6]**; this design allows to enhance both the torque and the power density by decreasing the packaging inefficiency. In addition, the chance of making the process highly automatable allows to reduce production costs, since each single vehicle, in relation to the configuration (EV or PHEV) contains within it from two to four engines. The considerations made above, combined with the fact that each single engine can have about two hundred welds, in relation to the size of the latter, show that from the point of view of manufacturing there is a need to have a flexible, repeatable, easily automatable

and possibly without contact between the parts since the parts to be welded are often very close to each other. It seems clear that the welding of copper and aluminum in similar and dissimilar configuration, with different thicknesses and geometries represents a key factor to reach the desired targets of the global market such as, for example: performance, reliability and cost reduction. Joining process of aluminum and copper in similar and dissimilar configuration by means of laser radiation has been gained an undoubtable industrial interest thanks to its particular advantages such as: high power density focused on a small spot, good welding quality, ease of automation and flexibility in comparison with conventional welding technology. All these features translate into a huge advantage in the welding of high-reflective materials for the production of components for electric propulsion system.

The work presented in this doctoral thesis fits into this context, which aims to verify the feasibility of an industrial process of laser welding of copper and aluminum in similar and dissimilar configuration for the production of battery module and winding stator through experimental activities and process optimization. The study, conducted together with the Hybrid Department of Ferrari Auto S.p.A., starts from the recent growth in the development of lithium-ion cells and the desire to create, from design to production, an entirely in-house electric propulsion system. The thesis is aimed at demonstrating that it is possible to obtain a connection with both good mechanical and electrical properties, obtaining the quality of the component produced while respecting the process constraints imposed by the application.

In support of all the experimental activity that has been carried out, the first chapters of this thesis concern, respectively, the generalities inherent to the laser welding processes (First Chapter) and the state of the art of the production process of battery packs and electric motors for automotive applications also focusing on problems related to the joining of aluminum and copper in similar and dissimilar configuration (Second Chapter). Following this theoretical section, the third chapter describes in detail the context within which the study was developed and describes its objectives.

The experimental section is presented starting from the study of the LBW process on pouch-type lithium-ion cells (Fourth Chapter) for which all the welding configurations that may occur during the production of a battery pack have been addressed by characterizing the joint obtained by a morphological, mechanical and electrical point of view.

After having demonstrated the feasibility of the process and having defined the optimal hardware solution, the welding process for prismatic cells was studied, following the characterization methodologies already presented for pouch cells, analyzing the busbar-tab configuration (Fifth Chapter).

Following these first results, relating to the production of battery modules, the project continued with the aim of using the same process also for the production of stator windings for electric motors (Sixth Chapter). In this regard, the welding of copper hairpins in edge configuration was studied with the aim of maximizing the properties of the connection.

1. Laser beam welding

1.1. Introduction

A LASER source (Light Amplification by Stimulated Emission of Radiation) is an instrument capable of generating a beam of light radiations belonging to the family of electromagnetic waves with unique characteristics, which combined with high versatility allows its application in many and different industrial sectors. Since the advent of this technology, which took place around the end of the 1950s, it was immediately observed a rapid spread of the same in the most disparate fields: from the telecommunications sector to that of entertainment, up to the medical sector or that of industrial processes**[7]**. In the field of materials processing, the laser is used to perform thermal operations: the beam transfers the heat from the source to the piece, which, once irradiated, undergoes rapid heating and, depending on the amount of heat released, can remain in the solid state, melt or even vaporize instantly. One of the main applications of laser technology, which in recent decades has met with great consensus and is constantly evolving, is welding. This term indicates the permanent joint, made at a microstructural level, between two or more components of similar or dissimilar material. The welding processes are classified according to the use or not of filler material, that is added from the outside, and are divided into: solid state welds, heterogeneous and autogenous welds**[8]**. The latter group includes those joining processes in which the base material reaches or exceeds its melting temperature, including laser welding. In particular, it is included in autogenous welding by fusion with a high energy concentration and is indicated with the abbreviation LBW (Laser Beam Welding). A substantial difference from the traditional ones is the energy source used to produce the thermal flux in the material, which can work with power densities of the order of kW/mm^2 concentrated on areas of minimum size. Table 1shows the power densities related to different technologies in order to better weld them between traditional and more innovative processes.

Joining Process	Power density [W/m^2]
Arc welding	$5 \cdot 10^6 \div 10^8$
Plasma welding	$5 \cdot 10^6 \div 10^{10}$
Laser welding	$10^{10} \div 10^{12}$

Table 1:Comparison of power density of different joining technologies.

Joining process by means of laser radiation, compared to conventional technologies, has had a rapid industrial diffusion without equal thanks to the possibility of having high powers concentrated on small areas, the high process speed, the absence of tools but above all to the unique characteristics of the beam**[9]**.

1.2. Laser beam characteristics

The laser beam can be described as an electromagnetic wave, i.e. a wave in which the energy is equally distributed over an electric field E (represents' the intensity of the electric field ') and a magnetic field B (represents' the density of the magnetic field '), always perpendicular to each other and varying in time and space with a sinusoidal law; the waves are characterized by a wavelength (λ), a phase (φ) and the respective amplitude (A) as shown in Figure 1.

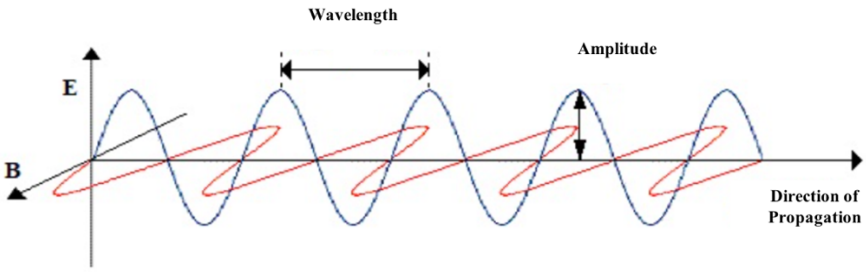

Figure 1: Electromagnetic wave scheme.

The vectorial product between the two vectors E and B allows to derive the propagation speed of the wave v:

$$ExB = v \quad (2.1)$$

otherwise expressed as the product of the wavelength (λ) and the frequency (f):

$$v = \lambda \cdot f \quad (2.2)$$

A first classification of electromagnetic waves can be made based on their wavelength; laser sources may have characteristic wavelengths that fall within the visible, infrared (longer waves) or ultraviolet (shorter) range. In industrial applications the waves have lengths of the order of $10^{-6} \div 10^{-3}$ [m], but the most commonly used ones fall within the infrared range. Figure 2 shows a diagram of the laser used in laser welding process with their respective characteristic wavelengths.

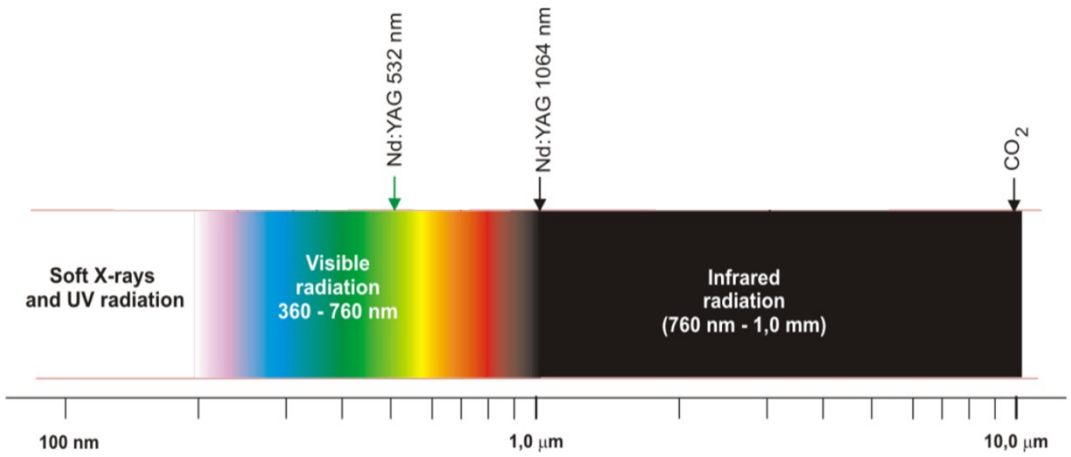

Figure 2: Most used lasers in welding process and location of wavelength inside electromagnetic spectrum.

A laser beam consists, as previously mentioned, of electromagnetic radiation similar to those emitted by light sources such as the sun or an incandescent light bulb. On the contrary, however, of the latter which are made up of components of different wavelengths and are oriented in space according to random directions, a beam produced by a laser source has the following properties, leaving out the specific talk relating to the generation of the beam:

- **Monochromaticity:**

The electromagnetic radiations of the laser beam all have the same wavelength, the value of which is determined by the nature of the active medium used. Wavelength λ and the frequency f of an electromagnetic wave are related to each other according to equation 2.3 where c is the light's speed**[8]**:

$$\lambda \cdot f = c \quad (2.3)$$

- **Spatial and temporal coherence:**

The waves that make up the beam all oscillate with the same phase, which remains unchanged over time(temporal coherence), just as the waves all have the same phase in all points of the beam section(spatial coherence)**[7]**.

- **Low divergence:**

When the laser radiation leaves the resonator (element in which the beam is generated) it has a very low divergence and thanks to particular optical devices it can be focused very easily; consequently, it is possible to concentrate large amounts of energy on small areas.

The above-described characteristics translate into a particular property of the beam, which is very important for industrial processing, namely:

- **High efficiency of the laser-material interaction:**

Without going into the specifics of the laser-material interaction mechanisms it can be said that the electromagnetic field of the beam exerts a force on the charged particles of the material. Its wave nature imposes an oscillatory trajectory on the particles with the result that the atoms of material exposed to the beam are set in vibration; this involves a considerable increase in temperature on the piece. The characteristics of uniqueness of the phase and monochromaticity make this interaction particularly efficient**[7]**.

1.3. Beam propagation and optics characteristics

At the exit of the resonant cavity, in most cases, the beam is not perfectly cylindrical, but has a divergent shape as shown in Figure 3.

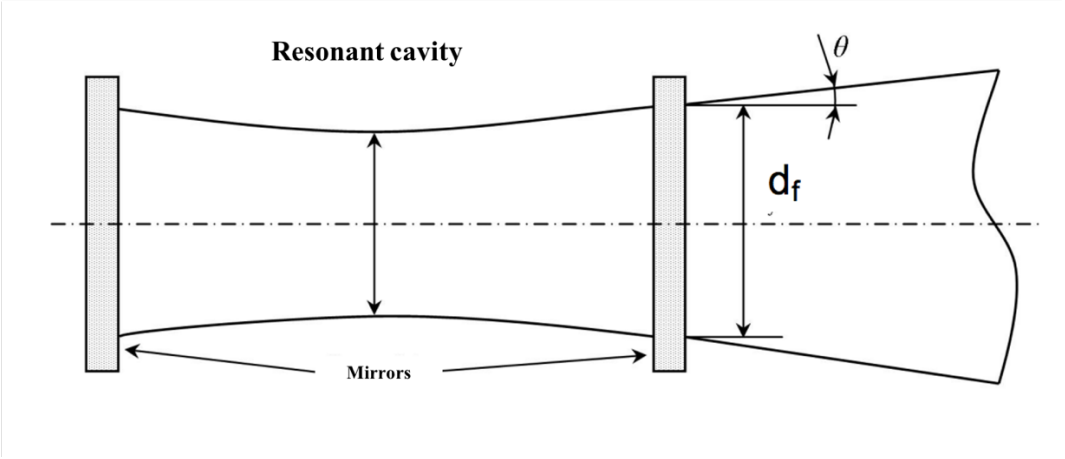

Figure 3: Divergence of laser beam[8].

Considering a Gaussian beam, i.e. with a peak at the axis and a decreasing trend towards the periphery, if a focusing lens with focal distance f is placed at a distance z of the semi-reflecting mirror (the one on the right in figure 3), as shown in Figure 4, the diameter of the beam radiating the lens is equal to $2w=d_f+2z\Theta$, assuming a small Θ. The beam diameter varies as the focal distance from the lens itself varies, as described by the equation 2.4.

$$d^2(z_f) = 4w_0^2 + (z_f - f)^2 \Theta_0^2 \quad (2.4)$$

At a distance from the lens equal to its focal length f, the beam radius has a minimum; with some geometric considerations, in which λ is the wavelength, relations 2.5 and 2.6 can be written:

$$w_0 \Theta_0 = w\Theta = \lambda/\pi = \text{constant} \quad (2.5)$$

$$\Theta_0 = w/f \quad (2.6)$$

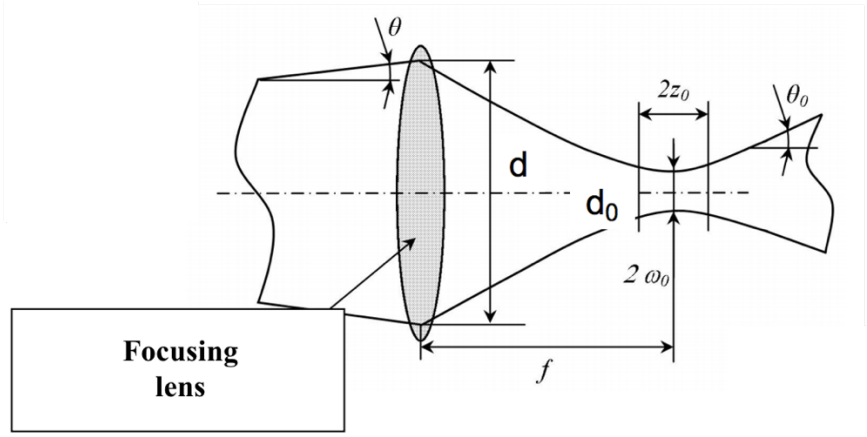

Figure 4: Focusing of a laser beam*[8]*.

By combining the relations 2.5 and 2.6 together, the radius of the Gaussian beam can be obtained, it is noted that the laser radiation is all the more focusable the shorter its wavelength and focal length of the lens and the greater the diameter of the incident beam**[8]**. The beam is rarely Gaussian as it has more transverse electromagnetic modes indicated by the TEM; in these cases, the focusability is worse. To take these phenomena into account, the M^2 factor is used.

$$M^2 = w_{0m}/w_0 \quad (2.7)$$

M^2 parameter is usually used to define the quality of a laser beam and its value is always greater than 1. Relation 2.8 can be used to define the minimum radius of a non-gaussian beam can be used.

$$w_{0m} = \frac{M\text{^}2f\lambda}{\pi w} \quad (2.8)$$

Another parameter of fundamental importance is the BPP which indicates the attitude of the beam to diverge, measured in mm * mrad. As defined, it is equal to the product of the laser beam at the focus point and the half-angle of divergence ($w_0\,\Theta_0$), but it can be also defined in relation of M^2 :

$$BPP = M^2\,\lambda/\pi \quad (2.9)$$

For a gaussian laser beam the BPP value is λ/π and therefore 0.34 mm*mrad when considering laser source with λ=1.06 μm. When no-gaussian beam are considered this parameter obviously increases to take into account the reduced quality of the beam. From the application point of view, a very important parameter is the depth of field, which provides information on the extension of the area at maximum energy density of the direction of propagation of the beam. Its measurement value is related to the length of the focal distance, the higher it is, the greater the depth of field. To measure this, a parameter called Rayleigh distance (R_d)is used to be defined; in particular for a gaussian beam:

$$R_d = \pi\, w_0^2/\,\pi \quad (2.10)$$

In laser welding, this is a very important parameter because if smaller focal lengths are used the process is very sensitive and may not guarantee the correct success of the processing when high reflectance materials, which require high power density, or high thicknesses must be worked.

1.3.1. Fiber delivery system

Among the most used transport systems there is certainly the optical fiber inside which the radiation is trapped. They can be considered as cables inside which transmission is transmitted by reflection; the core of the fiber is made of silica and has dimensions of the order of μm, in relation to the quality of the radiation that has to carry. The focusing of a radiation transported in the fiber occurs thanks to two elements:

- **Collimator:** has the objective of reducing the divergence of the radiation, as the divergence at the fiber exit increases.
- **Focusing lens:** which has already been discussed before.

The spot diameter(d_0) of a laser beam transported by fiber can be calculated as reported in relation 2.11, in which d_f is the fiber diameter, L_f is the focal length and L_c is the collimator length.

$$d_0 = (L_f/L_c)\, d_f \quad (2.11)$$

The success of laser welding systems in modern applications is above all due to the possibility of transporting the beam by means of optical fibers which allow to obtain both highly flexible systems and high-quality laser beam even in multi-kW configuration.

1.4. Welding mechanism

An important factor in laser beam welding is the interaction of the laser beam with the material. There are several parameters that influence the interaction mechanism, such as the laser power, the intensity distribution of this power on the surface, the welding speed, the properties of the material, the presence of the shielding gas and the length of wave of laser radiation. There are two modes of laser welding: conduction welding and keyhole or deep penetration welding; a first way of distinction is that relating to the power density used and the morphology of the weld beads that can be obtained as shown in Figure 5.

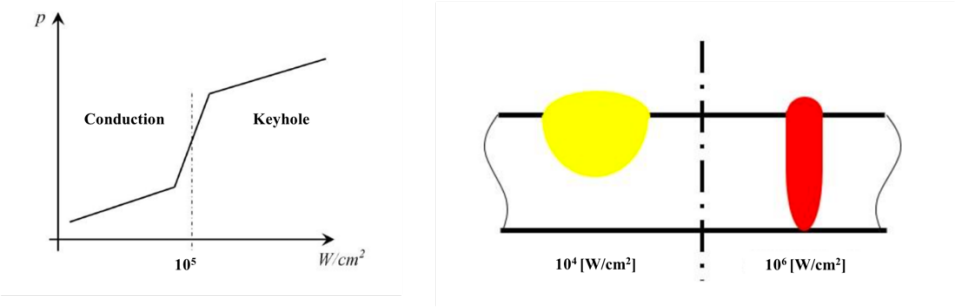

Figure 5: Trend of penetration depth as a function of power density (a), examples of beads obtained in conduction (left) and keyhole (right) (b).

1.4.1. Conduction mode welding

This type of welding at relatively low power density ($I < 10^5$ W/cm^2); it is comparable to a conventional process such as the arc welding. In conduction mode welding, laser energy irradiates the material, heating it and causing it to melt; consequently, the heat is transferred by conduction inside the workpiece. Analyzing a generic profile of the weld in a section orthogonal to the direction of advancement, it can be approximated to a semicircle with a width-depth aspect ratio of about 1:1, as shown in Figure 6. The shape assumed by the bead reflects the diffusive mechanisms of heat: the laser can be considered as a point source resting on the upper surface of the piece; the degree of isotropy and the heat conduction mechanisms give this particular shape to the joint**[7]**. In the process of welding highly reflective materials, the conduction mode is very difficult to obtain except six laser sources with wavelengths (blue or green) that are easily absorbed by the materials in question are used.

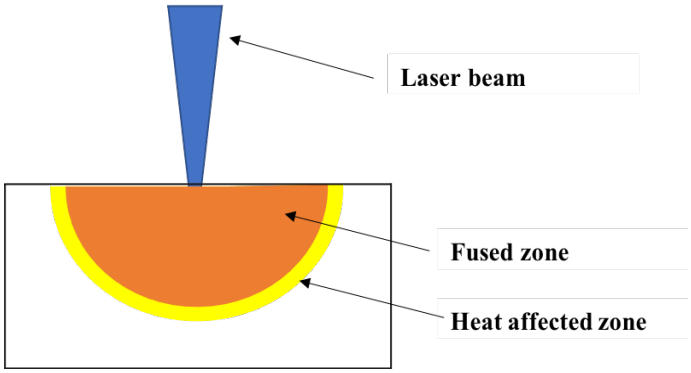

Figure 6: Conduction mode welding.

1.4.2. Keyhole mode welding

As the intensity of the laser beam increases, typically values of approximately 10^6 W/cm^2 the molten metal in the focus area of the laser beam starts to evaporate which, by vaporizing, rapidly moves away from the area; at this point the underlying layer is directly exposed to the ray, which again vaporizes a small layer. Under these conditions, a capillary channel (hole or "keyhole") of great depth is formed; the latter remains open due to the high pressures operated by metal vapors, and the material with which it comes into contact heats up, melts and vaporizes instantaneously along the entire depth. A small part of the formed plasma escapes from the surface giving rise to the phenomenon of "laser induced plume" which absorbs part of the incident power, constituting a source of inefficiency; a small part of the material splashes away from the bead in the form of spatters which in part also depend on the swirling motions that are established within the molten area. Due to the presence of the keyhole the energy is absorbed throughout the whole depth of the workpiece resulting in welds with a high depth to width ratio and a small heat affected zone (HAZ).

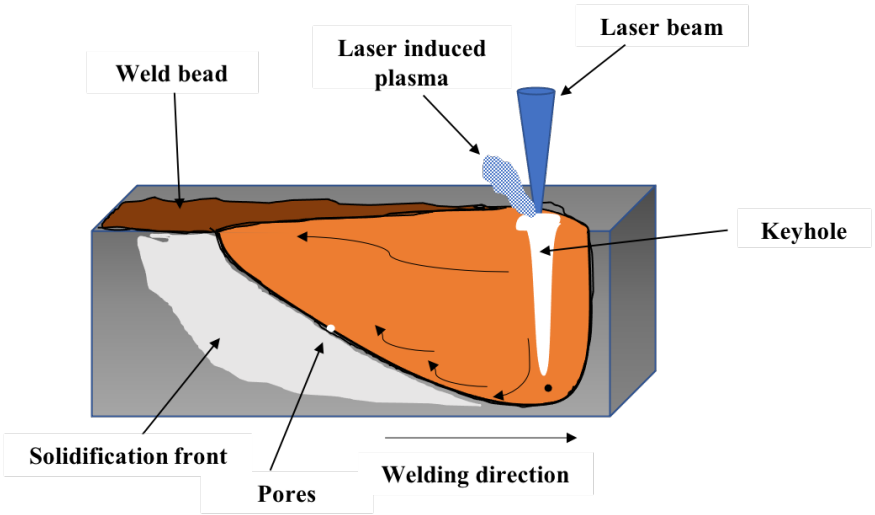

Figure 7: Keyhole mode welding.

1.5. Main components of an industrial laser system

The main components of a laser system, as shown in Figure 8, are:

- **The cooling unit (chiller):** acts as a cooling system ensuring the correct operation of the parts.
- **The beam transport system:** already discussed above.
- **The laser beam focusing system:** which focuses the beam on the workpiece. Fixed welding heads or galvanometric scan head can be found.
- **The laser head and workpiece handling systems:** industrial robots are usually used to move the laser head in correspondence with the work area; some solutions, on the other hand, provide for a fixed head and movement of the piece.
- **The laser source:** The laser source is the heart of the system; its purpose is to generate a beam with unique characteristics and effectively usable for mechanical processing. A source is constituted above all by a resonator, that is a resonant cavity, with a reflecting mirror and a semi-reflective one positioned at the ends of the same; an active medium is immersed in this cavity (it can be of a different nature) which is excited through an energy pumping system. The various types of existing sources, which generate beams with different characteristics, differ according to the physical state of the active medium, which can be solid, liquid or gaseous, and according to the geometry of the resonator. Without going into the specifics of the various types of existing laser sources, only the fiber sources which were used during the experimental phase will be analyzed.

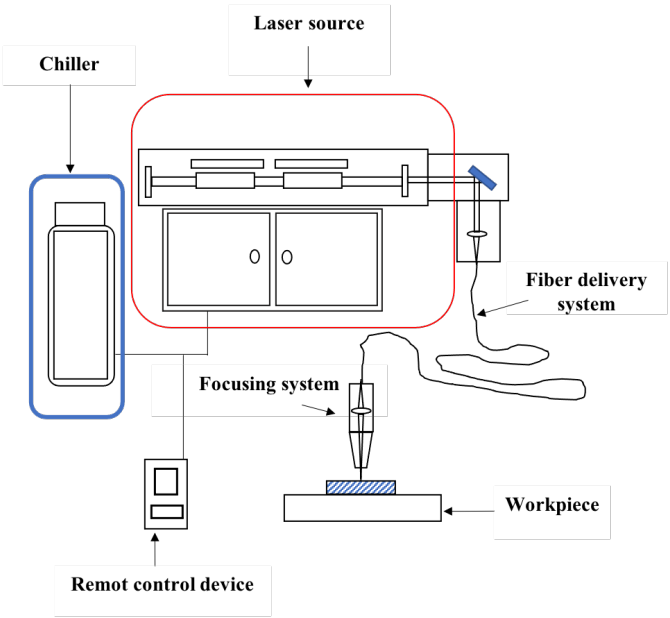

Figure 8: Main components of an industrial laser system.

1.5.1. Fiber laser source

The peculiarity of this type of laser source is the resonant cavity, which is made up of an optical fiber. Inside it there is an active medium in the solid state of glass crystals doped with ytterbium and at the ends there are two Bragg lattices, to perform the same function as the mirrors. The pumping is carried out by means of diodes, which are connected to the fiber with multimode couplers. The external sheath of the fiber, which is not doped, allows the passage of the radiations sent by the diodes; the latter enter the fiber and hit the active medium, exciting it. A schematic is shown in Figure 9. The generated laser beam passes through a collimator, which reduces its high divergence. Its wavelength is 1.080 μm and the focusability is very high, a factor that allows you to reduce the spots to a minimum size, useful for precision machining. Another peculiar feature of this type of source is the possibility of adding together several low-power beams in order to reach powers of the order of tens of kW while maintaining excellent beam quality.

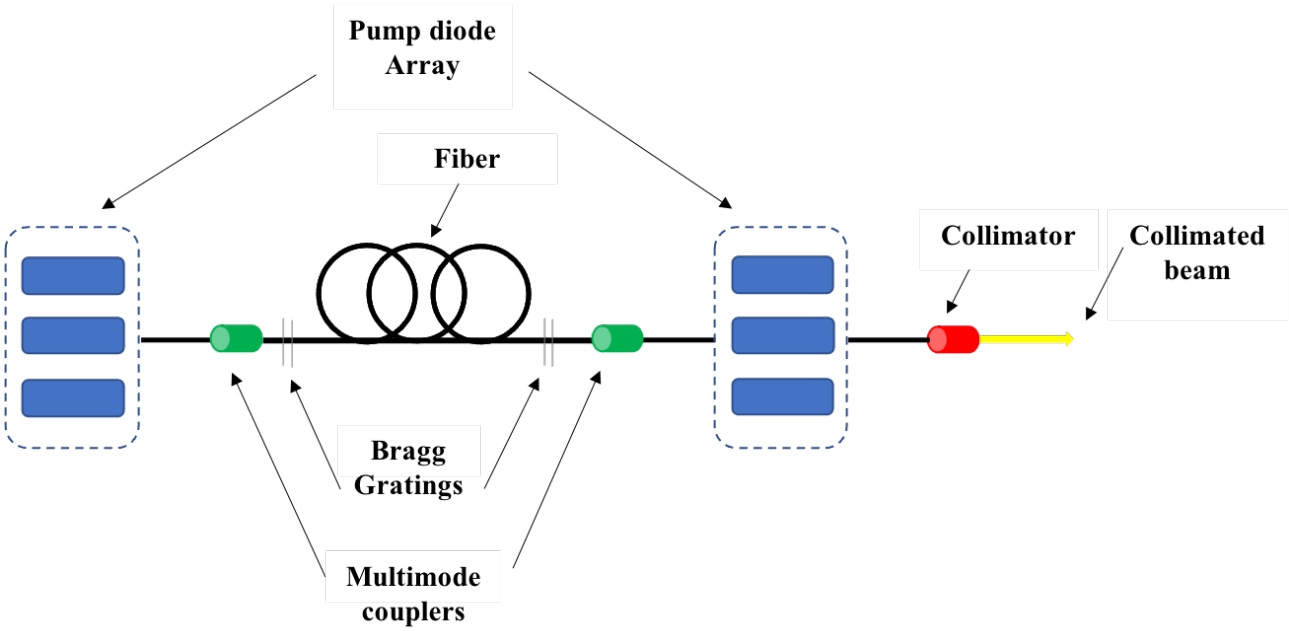

Figure 9: Fiber laser scheme.

1.6. Operating mode and energy parameters

The operating modes of a laser source can be of two types, in relation to the way in which it emits power over time: continuous wave mode (CW) and pulsed wave mode (PW).

1.6.1. Continuous wave mode

In the continuous mode, the power is emitted continuously from the source throughout the time span t during which the processing is carried out. The trend of the power P (t) as a function of time is shown in Figure 10.

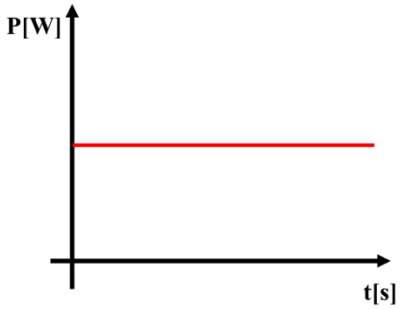

Figure 10: Power trend as a function of time in continuous wave mode.

The only parameter taken into consideration in this mode is the power emitted by the source; from this it is possible to derive other energy parameters, used in mechanical processing:

- Power density (I) = $\frac{Laser\ power}{Spot\ area}$ = [MW/cm^2] (2.12)
- Interaction time (t) = $\frac{Spot\ diameter}{Welding\ speed}$ = [s] (2.13)
- Energy density = Power density*Interaction time = [MJ/cm^2] (2.14)

The continuous operating mode is typical of CO_2 laser sources but in recent years it is particularly applied in solid state sources; it is applied in particular to processes such as cutting, deep penetration welding and heat treatments**[8]**.

1.6.2. Pulsed wave

In the pulsed mode, on the other hand, the power emitted by the resonator is not constant over time but periodically variable at intervals ranging from milliseconds to femtoseconds. The main purpose is to have high peak powers for each single impulse, maintaining low impulse energies and therefore low average powers. As can be seen in Figure 11, Each pulse has a duration d and is repeated with a pulsation frequency f = 1 / T over time, where T indicates the period that passes between two successive emissions.

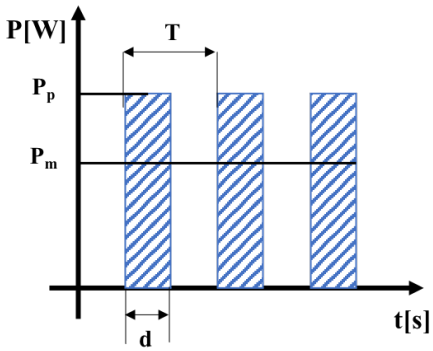

Figure 11: Power trend as a function of time in pulsed wave mode.

The area subtended by the curve representing a single pulse defines the energy (E) possessed by it, which can be expressed as:

$$E = \int_0^d P(t)dt = P_p * d \text{ [J]} \quad (2.15)$$

from which the peak power (Pp) of each single pulse is:

$$P_p = E/d \text{ [W]} \quad (2.16)$$

The average power emitted by the source is:

$$P_m = E * f = E/T \text{ [W]} \quad (2.17)$$

One last parameter can be defined, the duty cycle (∂) which represents the percentage of time in which the source emits radiation with respect to the period T:

$$\partial = f * d = d/T \text{ [\%]} \quad (2.18)$$

This operating mode is typical of sources with solid state resonators and is particularly used in marking and drilling operations where high peak powers are required to instantly vaporize the material**[8]**.

1.7. Shielding gas

Welding normally takes place in an uncontrolled atmosphere, i.e. in a free environment; in deep penetration welding, the high density of the laser beam tends to ionize the metal vapors, generating a plasma whose main effect is to absorb part of the energy emitted by the beam. Consequently, to counteract the negative effects of the plasma it is necessary to protect the melt pool with cover gas brought to the welding area by means of nozzles. The most commonly used shielding gases are:

- **Helium:** very suitable for covering the work area thanks to its high ionization potential, managing to keep plasma formation contained. Due to its high volatility, it tends to escape very quickly from the work area from which the need to use very high flow rates arises, increasing production costs**[8]**.

- **Argon:** due to the low ionization potential it tends to form plasma rapidly, especially for high power processes with long wavelengths (CO2); it is particularly suitable for welding with fiber sources. The high density and low cost compared to helium make it particularly suitable for reducing production costs**[8]**.

- **Nitrogen:** not being an inert gas, it tends to create undesirable chemical reactions especially with reactive metals. The only advantage is the cost which is lower than that of helium and argon

It can be concluded that the choice of the assist gas influences the formation of plasma and consequently the absorption of the energy of the laser beam, influencing the geometry of the weld bead, in particular the depth of penetration.

1.8. Metallurgical aspects of the weld bead

During a welding process, the material undergoes a complete thermal cycle of heating, permanence and cooling as shown in Figure 12. During heating, the temperature reaches values (T_{cr}) which may be higher than the melting temperature of the material itself (T_f). During permanence, the mechanisms of heat diffusion in the workpiece are triggered. The dwell time is a function of the speed with which the process takes place (τ) while the extent of heat diffusion depends on the power density chosen and ultimately on the strategy to be adopted. The last cooling phase is the most critical and is characterized by the cooling rate (v_f) on the basis of which different mechanical properties are obtained in the joint and propensities towards specific defects are developed. Cooling occurs by dissipation of heat through the material itself and therefore depends on the thermal conductivity and the amount of material available to cool the joint. The latter defines the drasticity of the thermal cycle, to which the mechanical characteristics of the bead are linked, which also depends on the heat input provided and the geometry of the piece.

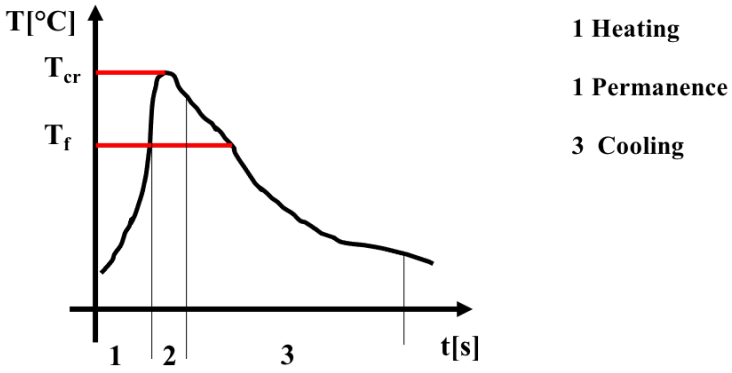

Figure 12: Welding thermal cycle.

Considering a heat source that moves along the piece, it can be seen that there is not a single thermal cycle for all the points of the weld bead, but it becomes less drastic as the distance from the joint axis increases. Consequently, the points closest to the joint axis begin to cool down later than the distant ones: this gives rise to expansion and shrinkage that compromise the properties of the joint.

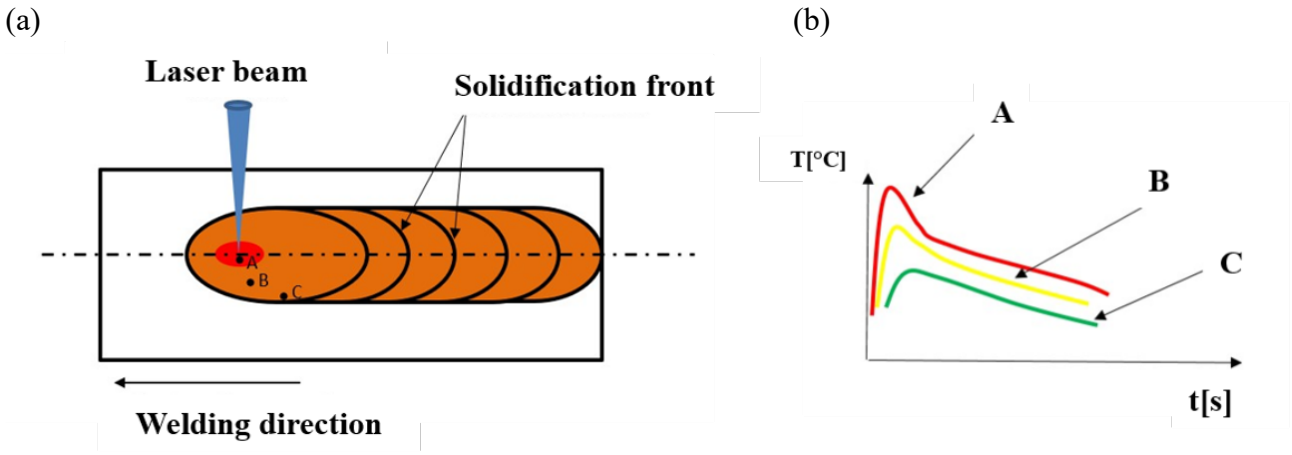

Figure 13: Weld bead(a) and qualitative thermal cycle(b) of selected points.

The drasticity of the thermal cycle, as highlighted, plays a fundamental role in the realization of a joint with good properties; the factors that influence it are:

- **Specific heat input:** namely the the energy per unit of welded length. As the specific heat input increases, the drasticity of the cycle decreases**[7]**.
- **Shape and thickness of pieces:** since the cooling takes place by conduction, stocky or very thick pieces cool before slender pieces**[7]**.
- **Workpiece temperature:** knowing that the cooling rate is proportional to the t between initial and final temperature, if the material is pre-heated at the start of processing the thermal cycle is less drastic.

By convention, considering a section perpendicular to that of welding direction, it is possible to identify three different zones, as shown in Figure 14:

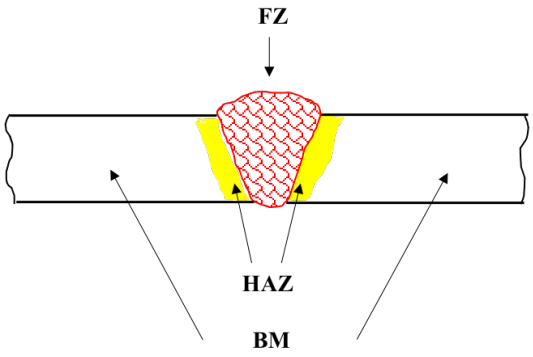

Figure 14: Weld bead zones.

- **Fused zone (FZ):** that is the portion of material that has reached the melting temperature and subsequent re-solidification. A characterizing factor is the dilution ratio (R_d), defined as **[7]**:

$$R_d\% = \frac{Volume\ of\ fused\ metal}{Volume\ base\ material} 100 \quad (2.19)$$

In autogenous welding processes such as laser it is worth 100%. From metallurgical point of view, the microstructure mainly consists of larger equiaxed grains due to the permanence at high temperature; on the sides of the FZ the grains are dendritic since solidification occurs in a directional way from the outside towards the inside.

- **Heat affected zone (HAZ):** it is the zone near to the molten one in which the transition of solid-liquid state has not occurred, but the temperature is still high to trigger microstructural changes. The type and extent of changes produced by the thermal cycle that is imposed on the material. It represents the most critical area of its joint due to this transition property condition: it is not easy to delineate the transition between one microstructure and another, but it is possible that intermetallic phases or precipitates may form which affect the final mechanics of the joint or they can trigger corrosive phenomena. In laser welding thanks to the higher welding speed heat affected zone is reduced **[7]**.
- **Base material (BM):** part of the material that is not affected during the joining process; part of the material that is not affected during the joining process where there are no changes in the microstructure.

1.9. Weld defects

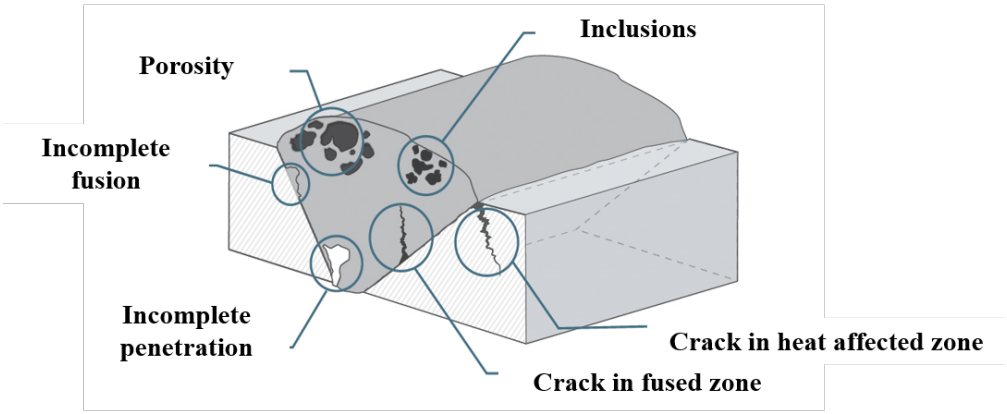

Figure 15: Weld defects.

The thermal cycle imposed on the material during welding can lead to defects and irregularities at the micro and / or macroscopic level, which can compromise the mechanical and electrical properties. In Figure 15 some of most common defects have been reported. Each zone, whether melted or thermally altered, has specific problems, but in both cases the cooling part due to the thermal cycle is the most critical: at the end of the process, in the transition from liquid to solid there are phenomena of thermal

concentration responsible for problems related to geometry but also to any residual stress rates**[7]**. The defects characterizing a component subject to have accumulated during the solidification phase and are due to the thermal contraction of the material, which occurs in its transition from liquid to solid state. They are: component distortions and induced residual stresses, to which brittle failure is correlated, and hot and cold cracks. To these defects are added those due to fusion, such as the porosities, inclusions intermetallic phases, the oxidation of the molten bath or the presence of marginal incisions and splashes of material outside the bead, which all conditions from the type of welded materials and operating conditions.

- **Residual stress and components deformation:** in the welding of thin sheets, usually, thanks to the possibility of concentrating high quantities of power on small areas, the deformations are quite contained and consequently the distortions of the piece are small so they will not be discussed in depth.
- **Micro-crack:** they differ in hot or cold cracks in relation to the temperature in which they occur. Hot cracks are generated in the molten zone before the molten zone reaches room temperature and is totally solidified; solidification occurs in two different stages: germination and grain growth. During germination the first solid nuclei are formed within the liquid phase and consequently enlarge their dimensions; the grains begin to stress the material from which internal tensions arise. Furthermore, between the grains in the growth phase, there may be films of still not solidified liquid material, this series of factors can give rise to rupture called hot cracks**[8]**. The presence of low melting elements, which could be placed at the edges of the grain, and impurities promote their appearance. Cold cracks, on the other hand, occur at lower temperatures, during the cooling part of the thermal cycle imposed by welding, one of the causes is in fact attributed to the excessive cooling speed of the joint or to the high content of hydrogen, which can cause this type of cracks appear even days after the welding**[7]**. Possible solutions for these defects are: the use of materials with a low level of impurities, the coverage of the melt bath with assist gas, the reduction of the percentage of humidity in the work area and the cooling rates, or the application of post welding stress relieving treatments.

- **Porosities:** they manifest as inclusions of gas bubbles or impurities, resulting in the appearance of lesions and reduced resistant section of the seam. In deep penetration welds, the presence of porosity is also caused by the instability of the keyhole which, during collapse, causes the expulsion of material from the molten area in the form of sprays and increases the porosity in depth and irregularities on the upper surface of the weld bead. Other possible causes of porosity formation can be excessive covering gas flows or with turbulent motions,

excessive humidity of the base material or the presence of dirt, paints and oxides. From metallurgical point of view, hydrogen has a high solubility at high temperature but is drastically reduced at room temperature; due to the high cooling rates characteristic of welding, the bubbles are unable to escape through the melt pool and remain trapped in it, thus creating micro porosity.

- **Incomplete penetration and fusion:** an insufficient energy and therefore thermal input generates a bead that does not affect the entire thickness with a decrease in the resistant section of the joint.

2. Manufacturing of electric powertrain components in the automotive industry

In this short prefatory chapter, the challenges and opportunities associated with welding copper and aluminum in similar and dissimilar configurations for the production of electric powertrain components will be faced. To address these, both the problems and the possible solutions during the welding of this type of materials will be discussed and subsequently the problems from the production point of view of battery modules and stator windings of electric motors will be analyzed.

2.1. Aluminum and copper alloys

Over the years, aluminum alloys are assuming an increasingly central role within many sectors of the industry. From the field of structural engineering to the automotive and aerospace field they represent, thanks to their properties and wide versatility, a valid and, sometimes, convenient alternative to materials that have adequate properties but with obvious drawbacks. Aluminum is the third most available element after that oxygen and silicon. It is prepared by the electrolysis of alumina from dissolving in fused cryolite; alumina is also extracted from bauxite through the Hall-Héroult process **[10]**. It finds various applications thanks to its properties, which will be discussed later, but above all its high strength-to-weight ratio and excellent machinability **[11-12].** Aluminum alloys can be of two types: wrought and cast aluminum alloys. With reference to wrought alloys, they are classified, according to the EURONORM (UNI EN 1780), into different grades depending on the alloying elements as reported in Table 2. Cast aluminum alloys are left out since they are not the subject of this work since in the electrical application pure aluminum alloys are widely used.

Type of alloys	Series	Major alloying elements	Heat treatable
Wrought alloys EN-AW	1xxx	None (min. 90%Al)	Non-heat treatable alloys
	3xxx	Manganese (Mn)	
	4xxx	Silicon (Si)	
	5xxx	Magnesium (Mg)	
	2xxx	Copper	Heat treatable alloys
	6xxx	Magnesium + Silicon	
	7xxx	Zinc (Zn)	
	8xxx	Other	

Table 2: EURONORM designation of wrought aluminium alloys.

Copper is a metal that takes the twenty-ninth place of the periodic table (chemical symbol Cu), belongs to the metal class of silver in the same column as gold and with which it presents many similarities on a physical and chemical level; it shows a red color and in the solid state it is characterized by a face-centered cubic structure (CFC) crystal lattice. From a metallurgical point of view, the copper ores used for the extraction of the metal are mainly copper sulphides and iron (cupriferous pyrites). The main industrial applications of pure copper, thanks to its characteristics that will be discussed later, are electrical, automotive, naval components industry. Rarely, in industrial applications, it is used in pure form but very often it is found in the form of a metal alloy; the most used are brass (zinc as alloy element), bronze (tin), cupronickel and aluminum-copper alloys. However, pure copper preserves the best electrical and thermal conductivity capabilities compared to other commonly used metals. Among the different types of pure copper, the largest quantities are produced for realize two different solutions:

- **Cu-ETP** (Electrolytic Tough Pitch) characterized by the presence of oxygen and the total absence of phosphorus.
- **Cu-DHP** (Deoxidized High residual Phosphorous) copper totally free of oxygen but with phosphorus content ranging between 0.015 ÷ 0.04%.

To obtain a copper with very high conductivity, even higher than that of Cu-ETP, it must be reduced to the minimum the presence of oxygen in it: for these reasons copper is processed at high conductivity free of oxygen **(Cu-OF).** Typically, the content of oxygen ranges from 0.001 to 0.003%, with a maximum of other impurities which must never exceed 0.03% in total. The material properties of copper and aluminum which are widely used for electrical application are reported in Table 3. Lightness, good machinability with machine tools, excellent properties in terms of electrical and thermal conductivity and good resistance to corrosion are some of the properties that have contributed to making aluminum and copper alloys a valid alternative to other materials in many industrial sectors**[13–17]**. But of all the sectors, it is certainly the automotive sector that has seen an almost exponential increase in the use of copper and aluminum, especially in the e-mobility**[18–20]**.

	Aluminum 1050 (99.5 Al)	**Copper (Cu-ETP)**
Density [g/cm^3]	2.7	8.93
Melting point [°C]	650	1083
Heat conductivity [W/m K] at 20°C	210	394
Heat capacity [kJ/kg K]	0.89	0.385
Thermal expansion coefficient [°C^{-1}]	$2.4 \cdot 10^{-5}$	$1.7 \cdot 10^{-5}$
Electrical resistivity [Ωmm^2/m]	0.0265	0.0173
Electrical conductivity [S/m]	$37.7 \cdot 10^6$	$59.6 \cdot 10^6$

Table 3: Aluminium and copper properties.

While the aforementioned exceptional physical and chemical properties have made the use of aluminum and copper alloys extended to various sectors, the latter make the joining process, required in many applications, difficult to carry out. The marked difference in the melting temperatures, the coefficients of thermal expansion, the high thermal conductivity of the two metals and the different densities make the joining process, especially in the dissimilar configuration, hard to obtain if no precautions are applied**[21–23]**. However, the main issue is represented by the reduced solubility in the solid state between the two metals, resulting in the formation of hard and brittle intermetallic compounds that compromise the properties of the connections **[24–26]**; the topic just mentioned will be discussed in depth in the next paragraph.

2.2. Challenges and opportunities in joining process of aluminum and copper in similar and dissimilar configuration

2.2.1. Laser welding of aluminum

Pure aluminum 1050 alloy is recognized for its high ductility, outstanding corrosion resistance at warm temperatures, and highly reflective finish **[27-29]**. Thin sheets of Aluminum 1050 alloy are widely used in different industries including construction, automotive, food and chemical process plants. Its product applications range from food containers, current collector, lighting fixtures, decoration panels, house appliances and solar reflective films**[30]**. Nowadays, aluminum alloys, in particular 1xxx series, tend to be the preferred material for busbar components, during battery manufacturing, due to their good properties and reduction in costs compared to copper**[31]**. For instance, by using aluminum busbars the weight reduction is about 50% and cost saving by up to 20% compared to copper busbars **[32]**. From the point of view of technology, laser welding is generally difficult to apply to aluminum alloys due to its higher thermal conductivity and lower viscosity**[33]**; the high thermal conductivity promotes a rapid heat transfer avoid concentration of the energy in the melt pool and the low viscosity reduce the extension of the melt pool before the solidification **[34]**. Joining process of aluminum alloys by means of near-infrared (IR) standard laser radiation is particularly challenging due to high reflectivity to the radiation's wavelength and consequent low energy absorption rate; it has been reported that, at room temperature, approximately 95% of IR laser gets reflected from the aluminum surface **[35]**, while it increases as the temperature increases as well. To overcome this challenges, a laser system characterized by a laser source with an high beam quality and a focusing length which allows obtain a small focusing spot is usually used **[36]**. High-intensity

small spot is ideally used in cutting or marking operations but it also suitable for welding process by using particular scanning strategy such as the beam oscillation (wobbling). For example, Das. El al. **[36]** studied the feasibility of laser welding process of pure aluminum 1050 series, for electrical applications, by means of a beam oscillation in fillet edge configuration; they demonstrated that the key geometric features of the weld bead can be controlled by laser power and wobbling amplitude obtaining from mechanical point of view good results in terms of mechanical strength while a reduction in hardness values near within the fused zone of about 5-10 $HV_{0.05}$ have been measured due to new grain formation. Another important issue to be faced during the welding of aluminum alloys is the presence of porosities. Two different types of porosities may occur during laser welding: i) key-hole induced porosity and ii) metallurgical porosity which mainly depends on the chemical reaction related to the low solubility of H_2 but also to the presence of CO and N_2 which are common gases detected in metallurgical porosity**[37]**. In laser deep penetration welding of aluminum alloys, a keyhole is formed and maintained by the evaporation recoil pressure which counterbalances the effects of the surface tension and the gravity. One of the key points, on which the success of the process depends, is represented by the stability of the keyhole determined in turn by different forces such as, recoil pressure, surface tension, hydrodynamic and hydrostatic pressure. As the heat input increases the recoil pressure increases as well which lead to the unbalance of the forces resulting in the instability and collapse of the keyhole; therefore, the gas inside gets isolated and bubbles are formed. To overcome the presence of pores inside the weld bead it has been demonstrated that high welding speed and a circular oscillation of the beam have a positive effect on the joint's properties**[38] [39]**.

2.2.2. Laser welding of copper

Due to the growing global demand for electric power in the energy applications the consumption of copper is rapidly increasing particularly in the aerospace, automobile, nuclear, electrical and communication industries because of its high electrical and thermal conductivity, coupled with favorable combination of strength and ductility and high formability **[40][41]**. Therefore, with growing demand of copper materials, the easy of automation, high efficiency, and quality of the copper joining process become inevitable in modern industrial production**[42]**. As for aluminum, joining process of copper alloys by means of laser radiations poses several challenges. Copper has both low infrared laser absorptivity and high thermal conductivity, which reduce energy concentration during the joining process**[43]**. Biro et al. reported that the absorptivity of pure copper for a near-infrared laser (wavelength of about 1000 nm) is 4.89% at room temperature **[44]**; increasing to 40 % at 450 nm. Based on this, several researchers suggest exploiting "green" and "blue" laser sources; however, applications are still limited by the lack of high power industrially applicable solutions **[45]**. On the other hand, particular attention has been paid to high-brilliance infrared laser sources that can concentrate high power densities in small focal spots**[46][47][48]**. The analysis of the literature shows that laser welding of copper has two important issues. The first is related to the high power required for laser deep penetration welding of copper, mainly due to the high reflectivity and high thermal conductivity of copper; thanks to advances in laser technology in which high-powered lasers are available with focusing lenses that allows to obtain small points of focus the problem would seem solved. Due to the fact that only a keyhole mode can be achieved with this material, the process is much more prone to instability, pore formation and spatter. In deep-penetration laser welding, a keyhole is formed and maintained by the evaporation recoil pressure, which counterbalances the effects of surface tension and gravity. Due to multiple reflections at the bottom of keyhole, the effective power intensity is at times inhomogeneous, resulting in over-expansion of the lower part of the keyhole and instability of the keyhole and molten pool. Therefore, the most frequent defects observed during laser welding of copper, such as pores and spattering, are due to the formation of a metal vapor bubble at the bottom of the keyhole, which ejects molten material if the pressure of the bubble exceeds the load of the melt pool**[49]**. Several authors observed also that welding with high laser power and high welding speed can effectively reduce spatters and consequently pores formation**[49]**.

2.2.3. Laser welding of copper and aluminum in dissimilar configuration

Dissimilar laser joining process of aluminum (Al) and copper (Cu) is widely used for light and high power electrical applications, such as electric mobility or battery applications **[19]**. By combining these two materials, numerous advantages are obtained in terms of flexibility and design of structures with good properties in terms of corrosion, thermal and electrical properties, especially considering the characteristics of the parent metals**[25]**. For years, both materials have been considered not weldable; however, growing demand for aluminum and copper components poses new challenges. Fusion welding of Al and Cu has a lot of drawbacks due to their significantly different chemical composition and physical properties. Welding of Al and Cu is challenging due to the fact that while mutual solubility between the two metals occurs in the liquid state, brittle intermetallic compounds (IMC) form after solidification resulting in degradation of the weld properties **[50]**. From the Al–Cu equilibrium phase diagram reported in Figure 16, it can be noted that the maximum solubility of Cu to Al for a solid solution is only 5.65 wt.% of Cu; consequently, several intermediate intermetallic compounds (IMC) can be found.

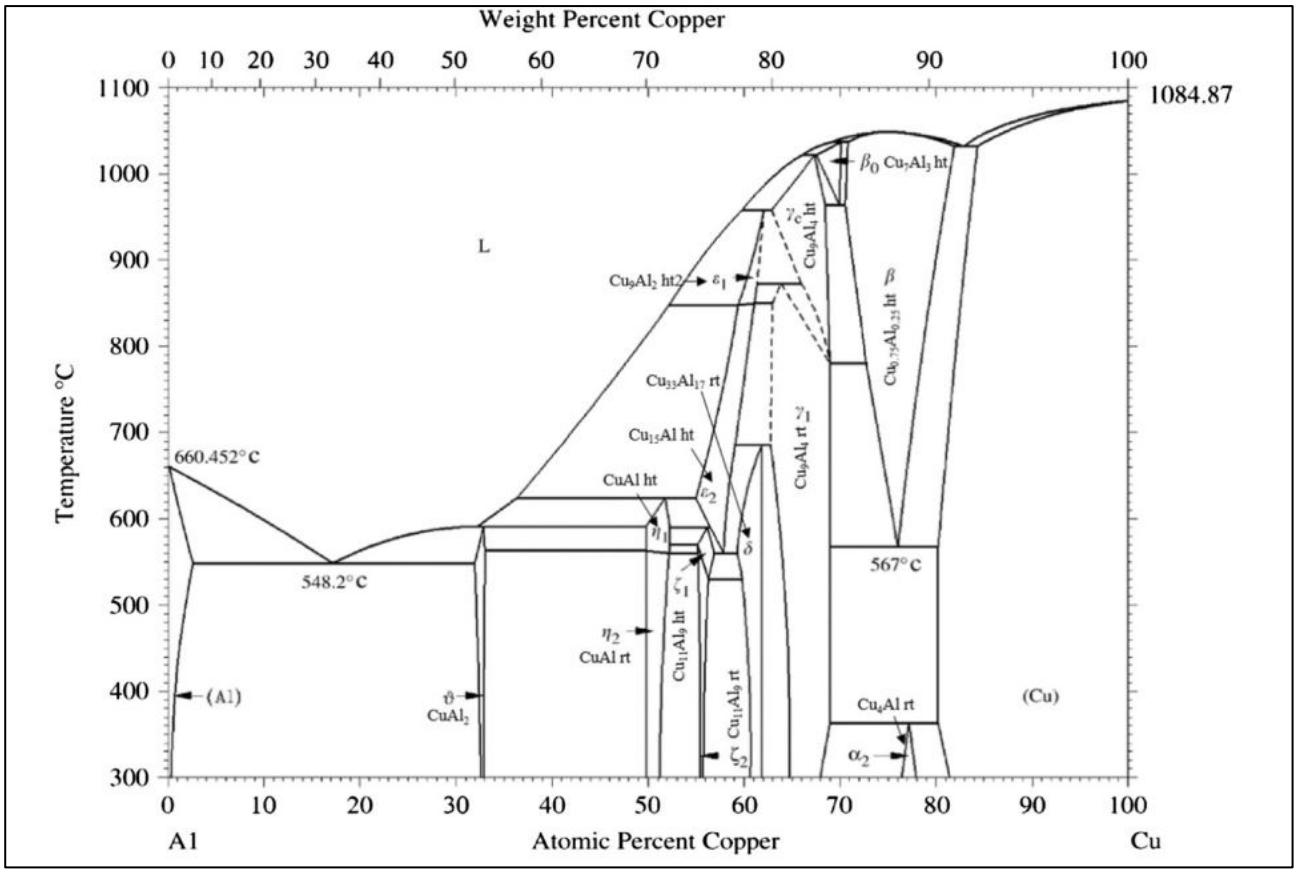

Figure 16: Al–Cu equilibrium phase diagram [21].

Table 4 shows the main properties and characteristics the intermetallic compounds formed after solidification, which are taken from **[25][51][52]**. It can be noted that intermetallic compounds exhibit very different properties compared to pure aluminum and copper. The difference in hardness with values higher than the base materials can be explained by the increasing ionic, covalent and the reduced amount of metallic bonding phenomena; reduced metallic bonds also leads to higher electrical resistivity compared to the base materials. Furthermore, the complex crystal structure restrains the reduction of stress which leads to high brittleness**[51]**. It can be noticed thus that the intermetallic compounds, that are inevitably formed, reduce both the electrical and mechanical properties of the junction; in addition, they can act as crack initiation points due to the difference in melting temperature, thermal conductivity and expansion between the base metals. It is clear that in order to obtain a reliable joint, the formation of intermetallic compounds must be avoided or at least minimized. Several studies have found that there is a relationship between the properties of the weld bead, in particular the mechanical properties and its fracture behavior, and the amount of intermetallic compounds, i.e. the thickness of their layer. For example, Braunovic et al. found that the contact resistance of Al-Cu joints increases linearly with the thickness of the intermetallics with consequent brittle behavior of the weld interface**[53]**. The main goal is therefore to reduce the heat input and the processing time as well as to have temperature gradients far away from equilibrium in order to limit the formation of intermetallics. Laser beam welding is well suited to these requirements; its high energy density makes it possible to melt dissimilar metals with different thermal conductivities, while the low heat input results in rapid heating and cooling, which translates into a unique advantage in terms of welding dissimilar metals**[54]**.

Phase	**Nominal composition**	**Chemical composition [% at. Cu]**	**Spec. Electrical resistance [μΩ cm]**	**Hardness [HV]**
(Al)		0-2.2	2.4	36
Θ	Al_2Cu	31.9-33	8.0	630
η	AlCu	51.9-54.8	11.4	905
ζ	Al_3Cu_4	56-57.5	12.2	930
γ	Al_4Cu_9	64-69	14.2	770
(Cu)		80.3-100	2.0	75

Table 4:Characteristics of intermetallic compounds.

In recent years, several efforts have been made in the field of laser dissimilar welding of aluminum and copper thin sheets. Particular attention has been paid towards high-brilliance laser sources that

represent a key tool for industrial manufacturing in terms of wavelength and available power in continuous wave (CW). Welding of dissimilar metals with a CW laser involves significant mixing of the two materials, with large cracks along the weld seam being a significant problem. Many authors suggest the use of spatial beam oscillation to weld dissimilar metals and to improve joint quality**[55][56]**. Uniform mixing of the two materials in the weld seam has been demonstrated using a single-mode fiber laser and spatial beam oscillation **[57]**. Fetzer et al. explored the possibility of exploiting laser beam oscillation to control the depth and width of the weld bead during lap-welding of 1 mm thick aluminum onto 1 mm thick copper sheets**[58]**. The authors found that both element mixing in the fused zone and crack formation were reduced for larger oscillation amplitudes; however, despite the results on how the oscillation parameters affect the mixing of the metal are satisfactory there are no data on how the latter can affect the electrical and mechanical properties of the joint. An alternative to obtain the power required to melt highly-reflective materials but at the same time reducing overall heat input is represented by the pulsed laser source **[59][60][61]**. Although the correct modulation of the various parameters that characterize the pulse processing allows to obtain good results, the process suffers from particular disadvantages such as low welding speeds compared to a continuous source that make it unsuitable for mass production and thus it will not be considered in the present work.

2.3. Manufacturing of batteries for propulsion system

Modern electrified vehicles (EVs), both complete and hybrid models, are gaining popularity due to the market push and the technological demanding for electric mobility. The main efforts in the development of electric transmission technology have focused on the development of batteries with a higher energy density**[62]**. Special efforts have been made in the field of battery packs with lithium-ion cells since they provide the highest energy density of all available systems and are one critical technology that may decide the auto industry's future in the next several decades**[63]**. A typical automotive battery pack consists of a large number of cells connected to each other, as shown in the Figure 17 , to deliver the required power and driving range.

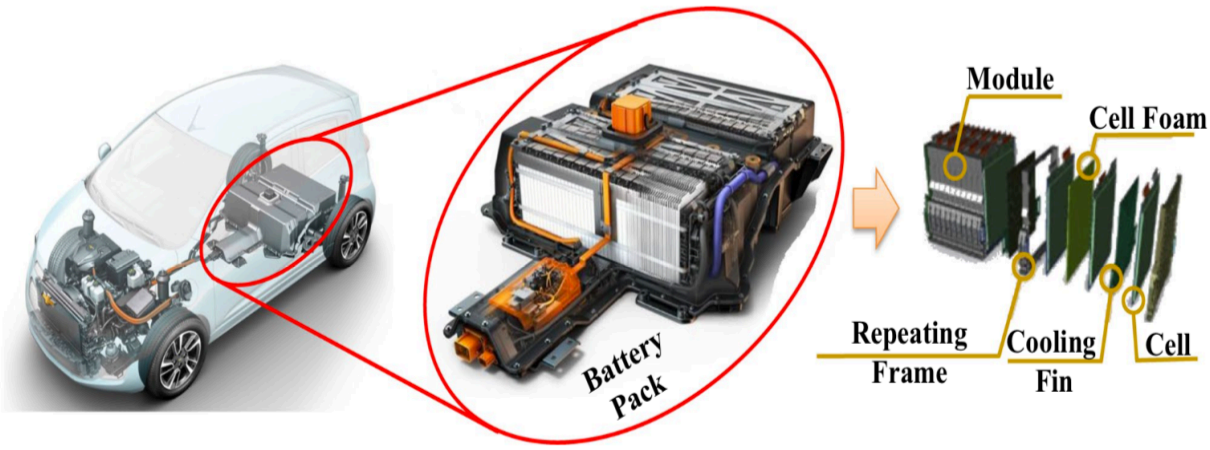

Figure 17: A schematic view of a battery pack for electric propulsion (from Chevrolet Spark EV battery pack)[64].

From a manufacturing point of view, automotive battery assembly can be divided into three levels, i.e., cell level, module level and pack level. An individual cell is composed of negative and positive electrodes, separators, an electrolyte and the protective case; all the joining and manufacturing process involved in this phase is owned by the manufacturers of the single cell and the cars manufacturers, which produce their own battery pack, are not directly involved as they only deal with the subsequent assembly. A battery module, on the other hand, is designed by connecting the single cells in series or parallel connection in order to obtain the required performance of the propulsion system; during the assembly of a battery module different welding configuration occur for example the tab-to-tab or tab-to-busbar configurations. The busbar acts as a current collector between the cells on which voltage sensor or temperature sensor is applied. For car manufacturers who want to produce in-house battery packs, this is an important step that includes both design and manufacturing parts; in fact, they can freely decide the types (series, parallel or both) and the number of connections to be

made to obtain the desired performance. Consequently, at pack level, the battery pack will be produced, joining together various modules previously obtained.

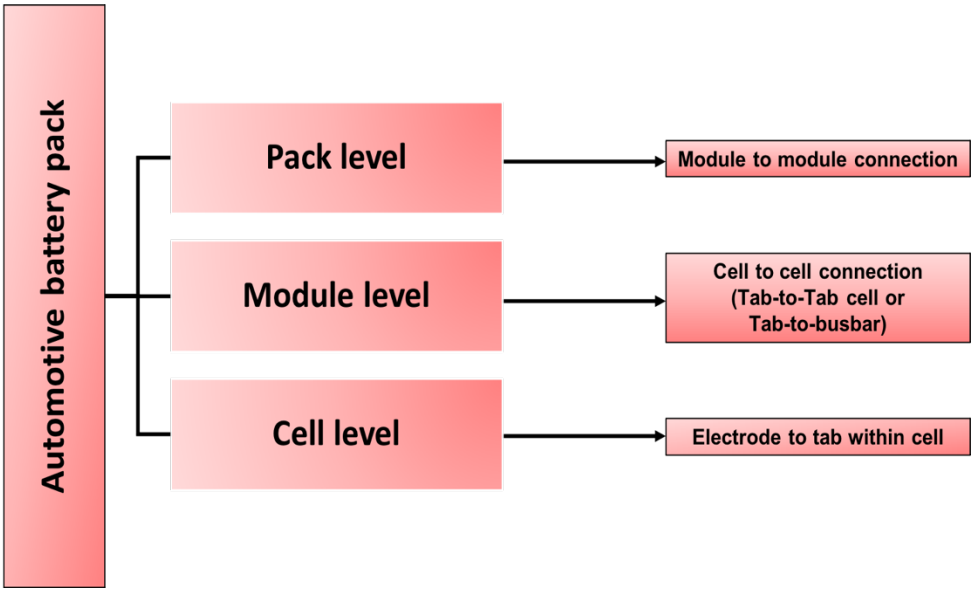

Figure 18: Assembly levels of a battery pack.

To date, commercially available lithium-ion battery cells can be divided according to their structure and characteristics **[65]**; in particular cylindrical, pouch and prismatic cells. Cylindrical cells (Figure 19 (a)) are extremely popular on the market and are used both as primary and secondary accumulators. These cells are very popular because they are easy to make and to assemble together, their cylindrical structure can withstand internal pressures without deforming and guarantee high safety during their operation; usually, the negative tab, placed in the lower part of the cell which also acts as a case, is made of stainless steel, while the positive tab, placed in the upper part is always in stainless steel; no other reasoning will be made in this regard since they have not been studied in this work. The pouch cell (Figure 19 (b)) typically has a rectangular shape not having a rigid container, with a reduced weight; cooling is greatly facilitated thanks to the high exchange surfaces. As a weak point, it is necessary to highlight the low mechanical resistance, which requires an adequate packaging system. Inside, the anode made is made with a laminated copper sheet, while the cathode is made of aluminum. The terminal part that comes out of the cell is called tab. The nickel-plated copper tab is the negative terminal, while the aluminum tab is the positive terminal; usually, the tabs are of thin sheet materials with a thickness lower than 0.5 mm, they come out of the cell on the same side, but there are also pouch cell models where the two tabs come out on the two opposite sides. During the assembly of pouch cells based module, the positive or negative tabs need to be connected each other

or joined to a busbar with a consequent request of joining different thickness and materials **[66]**. This prismatic cell (Figure 19 (c)) has a prismatic container of aluminum or thin steel which allows for excellent packaging and use of space. Among the main disadvantages, in addition to the weight, the prismatic cell is expensive to make and is difficult to cool due to the large size of the exchange surfaces; as in the previous cases, there is a structure consisting of several superimposed layers of anode and cathode, interspersed with each other by electrically insulating separator sheets. The case has a protective function while both the positive and negative terminals are usually made of aluminum with thicknesses of about 3-4 mm**[67]**. When assembling the prismatic cell module, the welding configuration involves joining of a busbar to both the negative and positive terminals**[65]**.

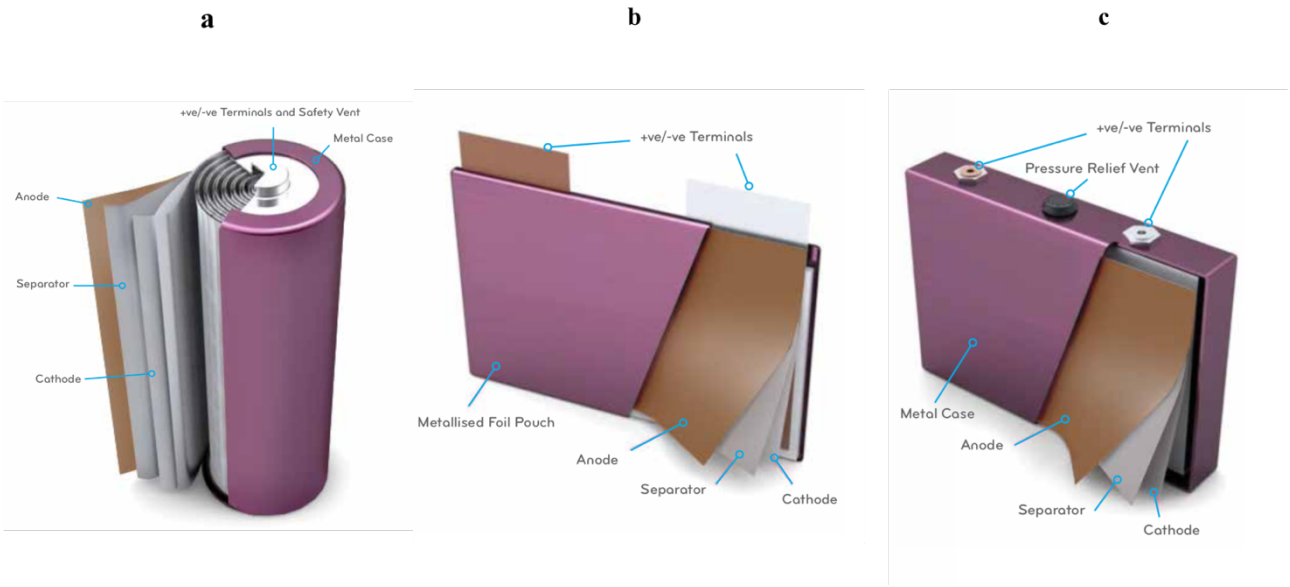

Figure 19: Li-Ion cell types: cylindrical cell (a), pouch cell (b) and prismatic cell (c).

From what has been observed so far, it can be deduced that the assembly of a battery pack for electric traction must face several challenges, which can be summarized as follow:

- **Mechanical challenges:** first of all, try to avoid vibrations or sudden movements during the assembly, as they may cause internal shorts or fire**[68]** ; obtain a joint with good mechanical properties, avoid its fragile behaviour and good durability during the battery life.
- **Electrical and thermal challenges:** since the connections between cells and module are not only having a structural purpose but also conduct current from or to the cells it is crucial to consider electrical aspects, too. For this purpose, a weld bead with lower electrical contact resistance is needed with several positive effects on the battery performance. In fact, the higher the electrical contact resistance, the higher the energy loss and the generation of heat that will dissipate, resulting in the need for greater cooling, reducing the performance of the battery. The heating of a battery module can cause faster cell degradation (ageing) or thermal

runway which consequently results in battery damage or even the explosion of the latter**[69][70]**. Furthermore, low heat input and reduced process times are preferable, especially when joining with fusion-type welding, as exposure of the cell to high heat can melt compromise the seals or cause internal shorting. Lastly, the properties of the joint due to thermal fatigue caused by the current transmission must also be verified and validated.

- **Metallurgical challenges:** making these joints involves several challenges, including joining multiple, thin and dissimilar materials of various thicknesses; highly conductive and reflective surfaces coated with different coatings. Formation of intermetallic compounds when the union of dissimilar materials is required with consequent decay of the properties of the connection, hence the need to control their formation and understand how the process parameters can reduce their presence.

Hence, it seems to be clear that there is a need for suitable joining techniques to support different joining requirements during battery pack manufacture. Without going into the specifics of the different technologies that can be used during the assembly of a battery pack, laser technology, thanks to its numerous advantages, is the most suitable to meet the demands and overcome the challenges that characterize the manufacturing of battery pack for automotive traction **[71]**.

2.4. Manufacturing of electric motors

Driven by the need to reduce the consequences of climate change, the use of electric powertrain in various fields of application will gradually increase. To this end, electric motors represent one of the most important components that must be improved in terms of efficiency, weight reduction, reliability and cost. The application of electric motors has become of primary importance in many strategic fields, with increasing demand for electrification pushing production and development of these components to higher levels. The demand for efficient and high-performance electric motors provides new challenges in terms of design and manufacturing**[72]**. An electric motor consists of a stator and a rotor equipped with permanent magnets that can be fitted on the surface or inserted into cavities**[73]**. The design and production of winding stators has received much attention in recent years as a correct design of the latter allows to obtain high performance in terms of efficiency of the electric machine during operation by reducing also the weight of the parts. To improve efficiency and power density, one of the key aspects is to reduce the phase resistance of the winding. For this purpose, it is recommended to increase the copper filling ratio in the active part of the stator obtaining a lower electrical contact resistance. In addition, the length of the winding can be greatly reduced by reducing the height of the winding head, which also reduces the resistance of the winding with positive effects on the power density which can be increased as the length of the motor can be reduced by shortening the length of the winding**[74]**. In order to meet this outcome, a promising solution is to produce the windings with thick U-shaped insulated copper conductors characterized by a rectangular cross section which allow to simplify also the manufacturing of the stator. Manufacturing this kind of winding involves several steps, including shaping, assembly and twisting of the copper terminals. Once the winding is assembled, the terminal parts of the copper conductors protrude laterally from the face of the stator in the form of numerous pin couples placed side-by side, which must be welded together in the so-called “hairpin” configuration**[75]**. In Figure 20 the major steps in the assembly of winding stator are shown, At the beginning, the wire is plastically deformed to form a U shape and give the hairpin head the desired geometry. Then the pre-formed forks are assembled in the grooves of the stator and then twisted. Finally, the twisted ends of the conductors are joined to form a mechanical and electrical connection to close the winding. The number of connections that must be produced are related to the size of the motor but in most of application there are up to two hundred connections in a single winding.

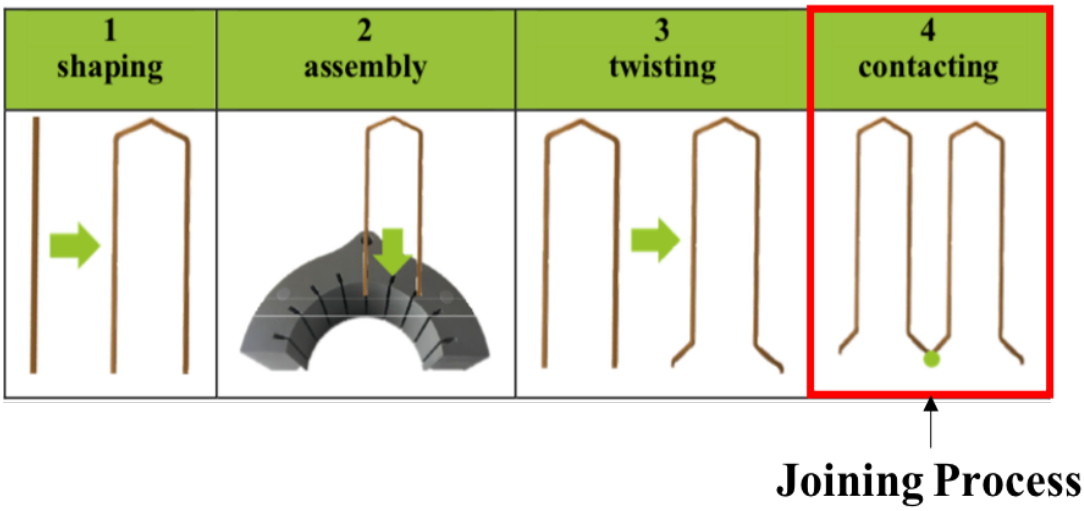

Figure 20:Assembly steps of winding stator[6].

During the joining process several challenges must be faced due to the particular characteristics of the pins which are placed in the stator already assembled. First of all, the working zone is characterized by very limited accessibility and the presence of spatter during welding could easily lead to damage of the insulating layer and the birth of short circuit. It is necessary to obtain a weld bead with good mechanical and electrical properties to ensure both good mechanical resistance during the life of the motor which is subjected to stress and vibrations and good performance in terms of electrical power delivered. In addition, the high number of contacts require short process cycle, high process stability and easy of automation. These technological requests make conventional joining technologies such as ultrasonic, arc, brazing or resistance welding very difficult to apply due to their drawbacks, without neglecting the fact that the conductors are made of copper with all the welding problems illustrated above. In this scenario, laser beam welding represents a suitable solution for hairpin welding, thanks to its intrinsic positioning accuracy, high energy density, high degree of automation and good weld quality **[74][76].**

3. Aim and reason of the research project

This chapter aims to clarify the idea on which the work carried out for this thesis developed and what was the main purpose of the work. To achieve the targets that will be described shortly for this work, two main issues were addressed: the optimization of the laser welding process for both the fabrication of battery module, mainly based on pouch and prismatic cells, and the manufacturing of winding stator of an electric motor. As regards the first topic, all the different welding configurations have been studied, which include the welding of aluminum and copper in similar and dissimilar configurations, which can occur during the assembly of a battery pack with each type of cell analyzed. With regard to the tab-tab-busbar configuration of pouch cells, the effect of aging due to the passage of current on the properties of the connection at the end of battery life will also be studied. Regarding the welding of stators for electric motors, the joining process of copper hairpins with a rectangular shape will be investigated.

3.1. Industrial context

The context within which the research project was born concerns the possibility of producing customized electric powertrain components, in particular electric motors and batteries for electric propulsion, both for prototype models and for high-performance series cars. Driven by increasingly stringent regulations on the reduction of polluting emissions around the world and by laws that prohibit, especially in city centers, both the sale and circulation of vehicles powered by internal combustion engines, we are attending an epochal turning point in terms of mobility. In Figure 21 a comparison of CO_2 emission targets of different country has been reported. As it can be seen from 2030 the target of emission value for passenger car will be set to 59 g CO_2/km; anyway, a similar target will be fixed for several countries all over the world. This epochal change affects all major car manufacturers, especially those that design and manufacture high-performance vehicles. In fact, if on the one hand the development of traditional combustion engines has reached its maximum in terms of both performance and emissions targets, this does not translate into compliance with the rigorous targets set by the legislations. In order to innovate the architecture of the propulsion systems both towards a reduction in production costs but above all towards the request to produce vehicles that meet the desired performance objectives, in line with the new world regulations for the automotive sector, the industrial division of Ferrari Auto S.p.A. has decided to invest heavily in research and development and to introduce the laser welding process within the company for the production of internally designed and manufactured electrical powertrain components.

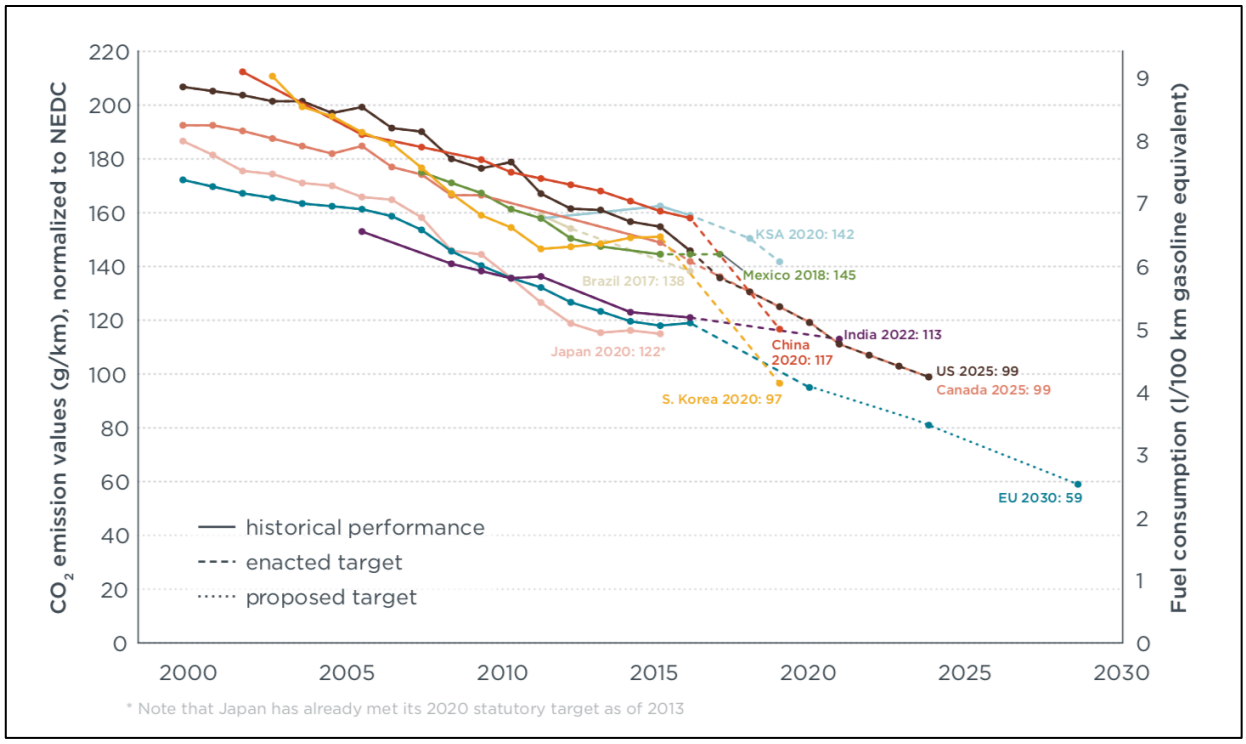

Figure 21: Comparison of global CO_2 regulations for new passenger cars[77].

The knowledge acquired by the company made it possible to study the different technical specifications regarding both the individual Li-Ion cells and the different types of stator windings made available on the market; this has led to studies relating to the feasibility of producing the aforementioned components without the help of suppliers which could cause various problems during the assembly of a vehicle. The need to undertake this activity, that is to produce internally a certain type of components characterized by a high technological content, is first of all part of a company culture, that is of developing know-how but above all trying to develop components that integrate with the rest of the car.

The welding process, within the production chain, is the most important one since both the quality of the product but above all the performance depend on the latter and requires transversal skills in several areas such as for example in the field of materials, in the field of advanced technologies without neglecting the process constraints imposed by the various applications. Facing a new issue for the company such as laser welding of materials that were considered not weldable until recently in this type of application also required close collaboration with manufacturers of laser sources and welding heads but also with suppliers of materials and treatments in order to create ad hoc solutions to ensure maximum performance, not just by "simply joining objects". Another fundamental aspect was to deal with the welding control process, especially for end of line test, by creating a kind of internal regulation that defines the acceptability criteria for each application of company interest.

3.2. Research project

Getting inside the research project conducted, it must be remembered that two different issues have been addressed: the one concerning the batteries and the one concerning the winding stators of electric motors from a manufacturing point of view. As for the batteries, prismatic and pouch cells were taken into consideration for the strategic choices of the company; regarding the cells the characteristics in terms of performance, weight etc. etc. will not be discussed, for privacy reason, but what will be discussed and studied are the tabs or the electrodes of the cells that must be welded together.
Regarding pouch cells, all the configurations, i.e. tab-to-tab or tab-to-tab-busbar, involved during the manufacturing of battery module have been investigated. First of all, for the tab-to-tab connection, a continuous laser source with scanner head both welding configurations (Al-Cu and Cu-Al) have been investigated with the aim of understanding which was the best configuration in terms of the position of the tabs on the characteristics of the joint; oonce the welding configuration was determined, the effect of the focus spot diameter on the properties of the connection has been studied. Subsequently the possibility of welding multi-layer thin thicknesses of copper and aluminum in dissimilar configuration was evaluated with the aim of making series and parallel connections with a single weld bead and thus design e manufacture efficient and compact battery modules. Finally, with the optimized set-up, the tab-to-tab welding configuration has also been characterized and the effect of thermal aging due to current transmission on the properties of the connection were investigated. Concerning prismatic cells, busbar-to-tab configuration has been studied and the whole process have been characterized. With the set-up previously identified, the welding of pure copper hairpins for the manufacturing of the stators was evaluated; particular attention was paid to the study of the effect of the process parameters in order to reduce the presence of pores inside the connection thus obtaining the maximum performance taking into account the process constraints imposed by the application.
To achieve the set objectives, a purely experimental approach was chosen, considering the real geometries and materials of the elements characterizing each application. To do this, it was decided to proceed as follows:

- Welding with different set-up and configurations.
- Identification of process feasibility window.
- Metallographic analysis of the welded samples to evaluate the effect of the parameters on the morphology and characteristics of the beads.
- Mechanical characterization tests.
- Electrical resistance measurements.

- Analysis by means of scanning electron microscope to obtain qualitative information on the characteristics of the intermetallic compounds that have formed.
- Welding tests of both battery modules prototypes and stator winding to verify the robustness and repeatability of the process and in order to characterize the mechanical and electrical behavior of the powertrain components.

It is important to underline that confidentiality agreements made between the parties involved in this work will not allow the results obtained to be presented in full. During the discussion, some parts necessary to ensure compliance with these agreements will be omitted, highlighting them where necessary.

4. Welding of pouch cells

The first experimental chapter describes in detail the properties and the results of the joints obtained for the different welding configurations regarding pouch cells, therefore aluminum and copper thin sheets. The optimization of this type of welding represents the heart of the activity carried out during the research period and aims to demonstrate the feasibility of the process to produce increasingly compact and performing battery modules. For this reason, tab-tab welding was first faced in order to understand the actual feasibility and which configuration, in terms of positioning of the materials and hardware components, would have been convenient. Subsequently, the study of a multilayer welding configuration first for the tab-tab case and then tab-tab-busbar was conducted. For this reason, many aspects related to the characterization of the welding process have been addressed, from understanding how the process parameters interact with the different materials and thicknesses, to the morphological characterization, microstructure up to the mechanical and electrical properties in such a way as to be able to build a standard internal validation of the welds for each different configuration.

4.1. Continuous laser welding with spatial beam oscillation of tab-tab-configuration

In this paragraph the welding of aluminum and copper thin sheet in dissimilar configurations (Al to Cu and Cu to Al) has been investigated. It represents a preliminary activity carried out to understand how the process parameters and welding configurations affect the properties of the weld bead. A single mode fibre laser with maximum output power of 1 kW in combination with galvanometric scanner head have been used with the purpose to find a feasibility window and characterize the process with the optimized parameters. The trials were conducted by varying power laser, welding speed and amplitude of wobbling. In the first phase, the effect of process parameters on the morphology of the weld seam and thus, surface width, width at the interface and penetration depth. Afterwards, some of the welds, which have partial penetration, have been mechanically characterized by means of shear tensile tests. Finally, taking into account the best conditions, double weld seam was performed and tested to improve the joint properties. In this first phase the maximum temperatures obtained during the process were also monitored, to get an idea if the chosen setup is the correct one and to avoid cell degradation during assembly.

4.1.1. Materials and methods

A single-mode IPG YLR 1000-SM fiber laser with a near-infrared wavelength of 1064 nm and a maximum power of P=1000 W was utilized in combination with a galvanometric scan head with an F-Theta scanning lens for the welding tests. During the trials, the laser beam was orthogonal to the surface and the focal point was on the top plate material's surface. During the welding experiments,

no shielding gas was employed, and no back-reflection effect was detected. Figure 22 shows a representation of welding setup used.

(a) (b)

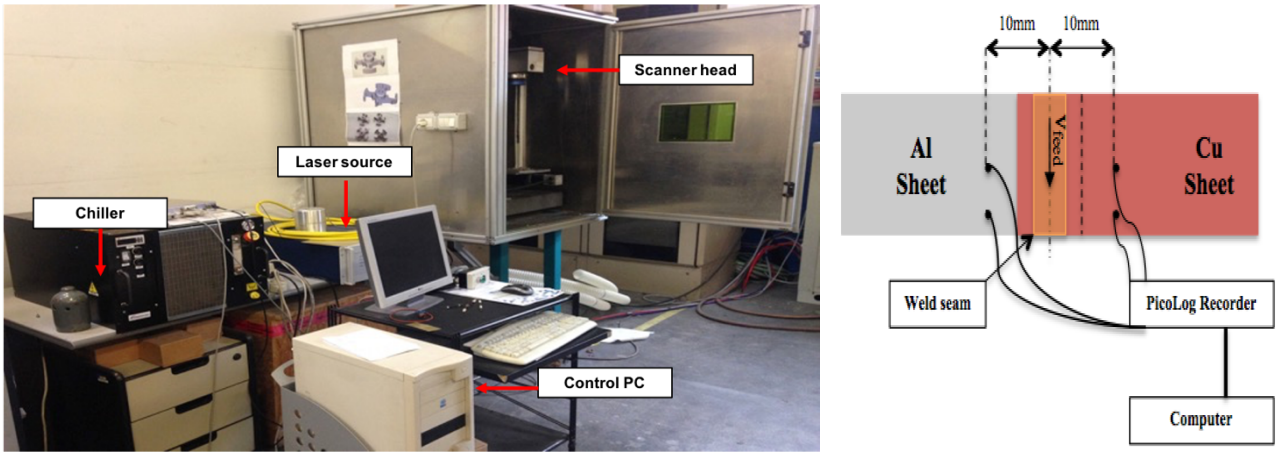

Figure 22: Setup used during the preliminary activity(a), welding configuration(b).

In Table 5 the characteristics of the laser source and optical chain have been reported.

Laser source		**Optical chain**	
Specification	**Value**	**Specification**	**Value**
Emission Wavelength	1064 nm	Collimation length	100 mm
Operating mode	CW	Focal length	420 mm
Emission power	1000 W	Fiber core diameter	14 µm
BPP	0.4 mm*mrad	Focal spot diameter	60 µm

Table 5:Laser and optics specifications for welding process with wobbling strategy.

Aluminum alloy EN-AW 1050 (99.5 percent Al) in 0.45 mm thick sheet and pure copper C1020-HO (99.9% Cu) in 0.3 mm thick sheet with a thin coating of nickel (2.5 m) electroplated to enhance both beam absorption when the copper sheet was on the topside and corrosion resistance were the materials investigated. The samples were 45 mm broad and 70 mm long, and they were welded in an overlap configuration with a 15 mm overlap. A clamping system was created in order to guarantee a proper adhesion between the part before the welding. Four K-type thermocouples, with a thickness of 1 mm, have been positioned, on the top part of the sheets at a distance of 10 mm from the welding area to monitor the maximum temperature reached during the process, as shown in Figure 22(b). The study's goal was to analyze the welding process with circular spatial beam oscillation. The wobbling strategy

was implemented by programming the galvo head in such a way that the real laser beam path was the consequence of superimposing a circular and a linear motion, as shown in Figure 23(top).

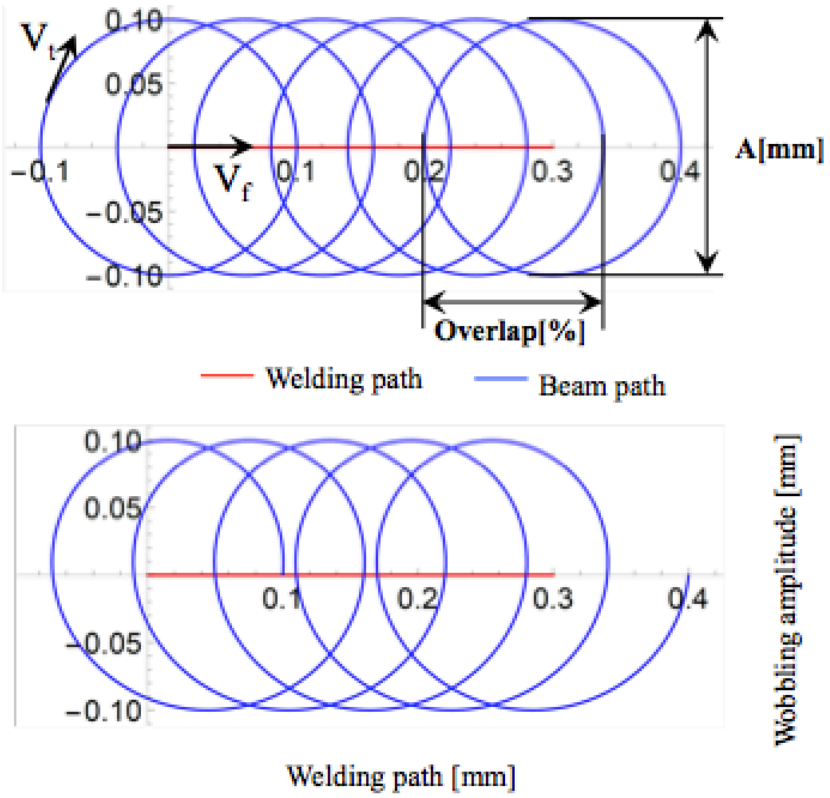

Figure 23: Description of spatial beam oscillation[54].

At a tangential speed Vt, which is also the laser beam velocity, the beam rotates around a circle with a diameter equal to the wobbling thickness A. The circular path's center is shifted along the welding direction at a constant speed Vf, causing two consecutive revolutions to overlap by a given amount Overlap percent. In equation 5.1 are reported the governing formula of the motion.

$$\begin{cases} x(t) = \frac{A}{2}\cos\left(\frac{2V_t}{A}t\right) + V_f t \\ y(t) = \frac{A}{2}\sin\left(\frac{2V_t}{A}t\right) \end{cases} \quad (5.1)$$

The obtained beam path, based on these factors, is a cycloid, similar to the one depicted in Figure 23 (bottom). The equipment utilized in this experiment was configured in terms of wobbling amplitude (A), overlapping (Overlap), and tangential speed (Vt): these parameters can simply be converted into a wobbling frequency (f) and a welding speed (w) using equations 5.2 and 5.3.

$$f = \frac{V_t}{\pi A} \quad (5.2)$$

$$V_f = f\left(A - \left(\frac{A \cdot Overlap}{100}\right)\right) \quad (5.3)$$

Table 6 shows the parameter used. For every set of parameter welds of 45 mm length were generated and the experiments were repeated three times under the same conditions. The process parameters were obtained through a preliminary activity not discussed in the present paragraph.

Configuration	Laser Power [W]	Welding speed [mm/s]	Wobbling amplitude [mm]	Scanning frequency [Hz]
Al to Cu	600 – 700 - 800	133 – 156 - 178	0.2 – 0.5 – 0.7	272÷ 1273
Cu to Al	800 – 900 - 1000	89 – 111 - 134	0.2 – 0.5 – 0.7	182÷ 955

Table 6: Welding parameters used during the wobbling trials in tab-tab-configuration.

Hot mounting of the samples was used to prepare the cross sections, which were previously polished with sandpapers of various grits and then polished with 1 and 0.5 μm alumina suspension. Polished cross sections were made for evaluation in the optical microscope to analyze the weld seam. The microscope was a ZEISS Axio Vert.A1M, and there was no etchant utilized because the goal was to detect the weld seam geometry. The welds were tested by means shear strength tests at room temperature in an INSTRON model 8033 tensile testing equipment with a crosshead speed of 0.025 mm/s. The sample dimensions used during the mechanical characterization were the same indicated in Figure 22(b). It's worth noting that the tensile test samples were not standardized because the goal was to assess the tightness of the joint qualitatively. The tests were carried out to determine the

ultimate tensile load and the location of the fracture. Two specimens were welded for each parameter combination, and then average shear-tensile load values were measured.

4.1.2. Optical microscope results

Figure 24 shows microscopy images of typical results obtained when aluminum is used as the topside material. Under-welded, good-welded, and over-welded conditions have been obtained by considering the penetration depth in the lower material. The under-welded condition (Figure 24 (a)) was observed at the highest trace width, in this case 0.7 mm, as well as the highest welding velocity and power of 600 W and 700 W; clearly, the heat transferred from the laser beam to the material was insufficient to achieve fusion of the top side material and subsequent mixing in this condition. The most common configuration, i.e. good-weld, (Figure 24 (b)) was reached with all trace widths examined; it is worth noting that each trace width has its own set of optimized parameters. There was no excessive mixing or pore formation when the topside material did not permeate entirely into the bottom side material. Excessive mixing of materials and the creation of pores happened when the power density was too high. This last condition should be avoided due to the increased presence of defects and material dropping, which could compromise the joint's properties.

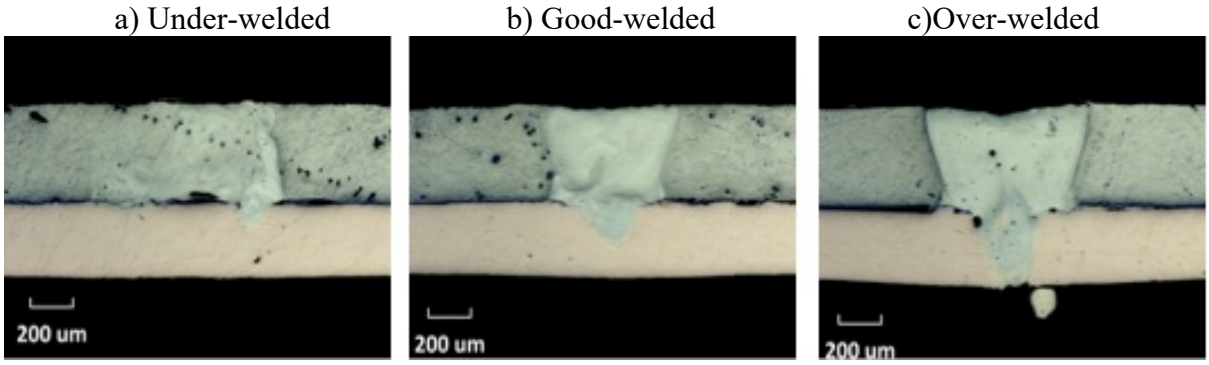

Figure 24: Cross section of Al-Cu configuration obtained with wobbling strategy[54].

It was possible to measure the geometric characteristics once the weld seam cross-section was obtained. The depth in the lower sheet measured from the interface is the penetration depth; the weld width was measured at the interface between the two sheets. Figure 25 shows the relationship between weld width, penetration depth, and wobbling amplitude at 700 W laser power and various welding speeds; this power was chosen as an exemplary representation of the results obtained. Weld width increases linearly when wobbling amplitude increases from 0.2 to 0.5 mm; however, at higher speeds, an increase in wobbling amplitude has little effect on weld width. As can be seen, the weld width is roughly 0.7 mm at 156 and 178 mm/s for both the 0.5 and 0.7 mm wobbling amplitudes. The weld width is determined by the wobbling amplitude in particular at lower speeds. It is important to note that the process in terms of weld width is highly influenced by the wobbling amplitude; greater values, such as 0.5 and 0.7 mm in this case, allow the process to be stabilized for different welding rates. In contrast, as the wobbling amplitude increased from 0.2 to 0.5 mm, the penetration depth is reduced.

Over-welded condition was reported with a wobbling amplitude of 0.2 and a welding speed of 133 mm/s; analyzing the same amplitude, the penetration depth reached a value of 0.18 mm. At 0.7 mm was recorded the lowest value of 0.05 mm for a welding speed of 178 mm/s. The same results have been obtained with the others power levels considered in the experiment. It is clear that to reach a good-welded condition and so a partial penetration in the lower sheet, higher wobbling amplitude should be used, since it strongly influences the weld seam geometry.

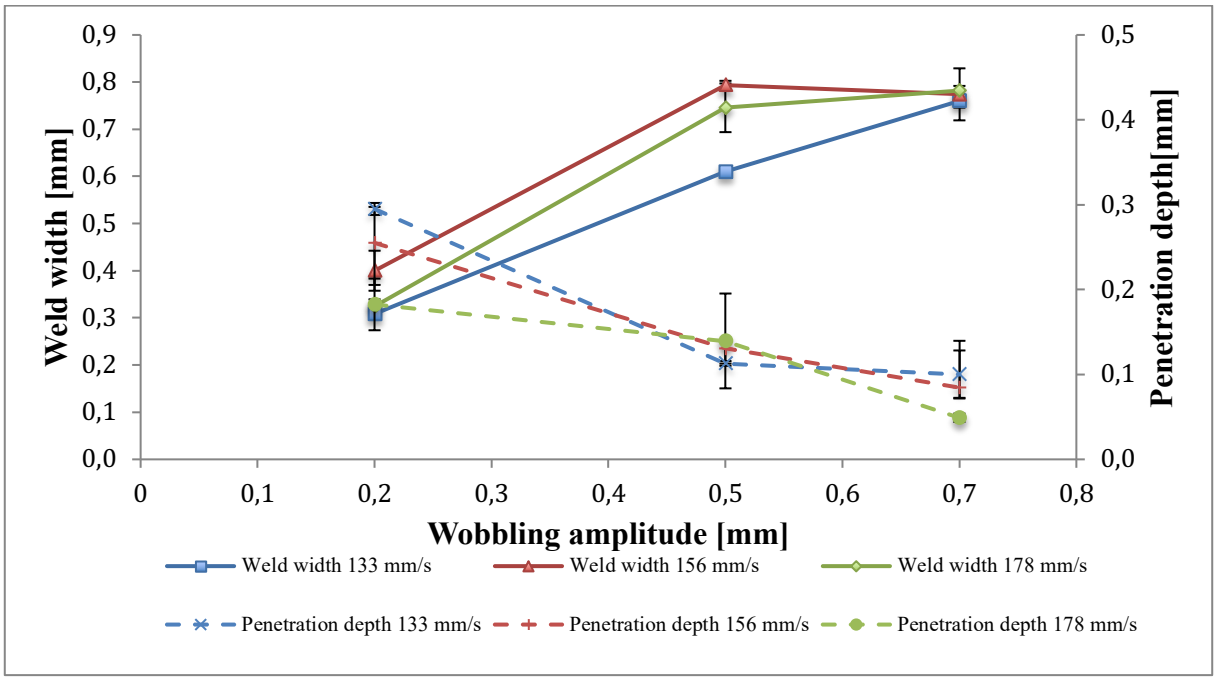

Figure 25: Weld bead characteristics of Al-Cu configuration with wobbling strategy at laser power of 700 W.

Same considerations can be made for the configuration in which the copper is placed above the aluminium. In this case, two different conditions have been achieved, as reported in Figure 26. When the copper was the topside material the welding process was more unstable and difficult to obtain a good joint free from defects such as pores. From the optical microscopic analysis can see how the copper fused due to a high density compared to aluminium sinked in the bottom side material thus obtaining complete penetration in most of experiments. No-welding condition has never been obtained due to the reason explained above. Partial penetration (Figure 26 (a)) has been achieved with wobbling amplitude included between 0.5 and 0.7 mm and lower power such as 800 and 900 W. By increasing the laser power with the same amplitude, complete penetration and cutting is obtained. Full penetration, as it can see in (Figure 26(b)), shows a high amount of defects that compromise the

mechanical properties of the joint. Wobbling amplitude of 0.2 mm, from a first optical analysis, was not the best option to achieve a reliable joint.

a) Good-welded b) Over-welded

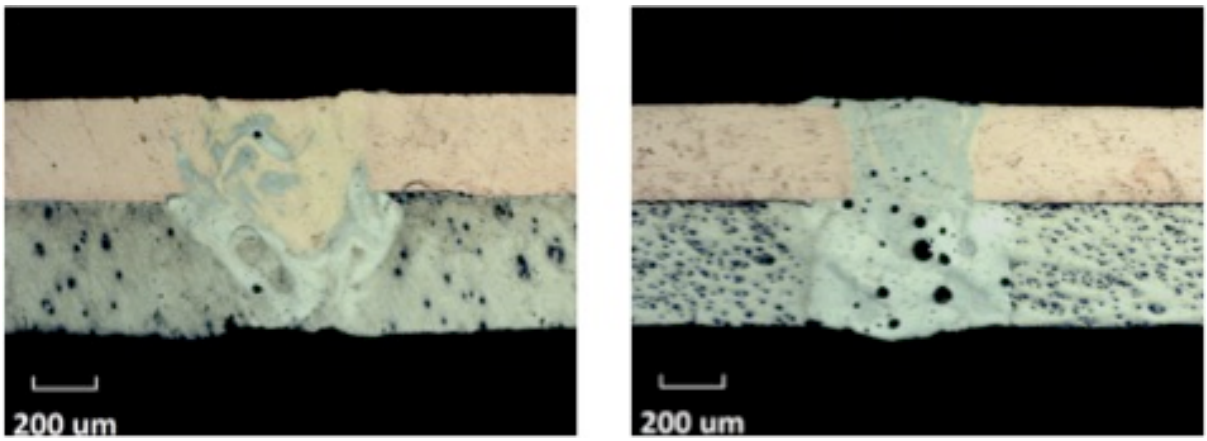

Figure 26: Cross-section of Cu-Al configuration obtained with wobbling strategy[54].

Figure 27 shows the relationship between weld width, penetration depth, and wobbling amplitude at 800 W laser power and various welding speeds. When the welding speeds were 111 and 134 mm/s, increasing the wobbling amplitude resulted in a constant weld width because the trend of the graphs did not reveal a significant variation. Weld width increased linearly with a welding speed of 89 mm/s, with the wobbling amplitude reaching 0.7 mm. The lowest values of weld width were achieved with the maximum welding speed, as expected, for the same wobbling amplitude. The penetration depth, on the other hand, is affected by the value of wobbling amplitude, as the penetration depth decreased with increasing wobbling amplitude, as it can be noted for the other configurations. With all welding speeds, complete penetration was achieved for the wobbling amplitude of 0.2 mm. The welding speed of 89 mm/s was not the greatest option because it produces weld bead with a full penetration condition. At 0.5 and 0.7 mm of wobbling amplitude, the lowest values of penetration depth were obtained with the maximum welding speed. We can conclude that increasing the oscillation amplitude to the higher value of 0.5mm has little effect in terms of geometric properties because the width of the weld and the depth of penetration are essentially the same at higher speeds[54].

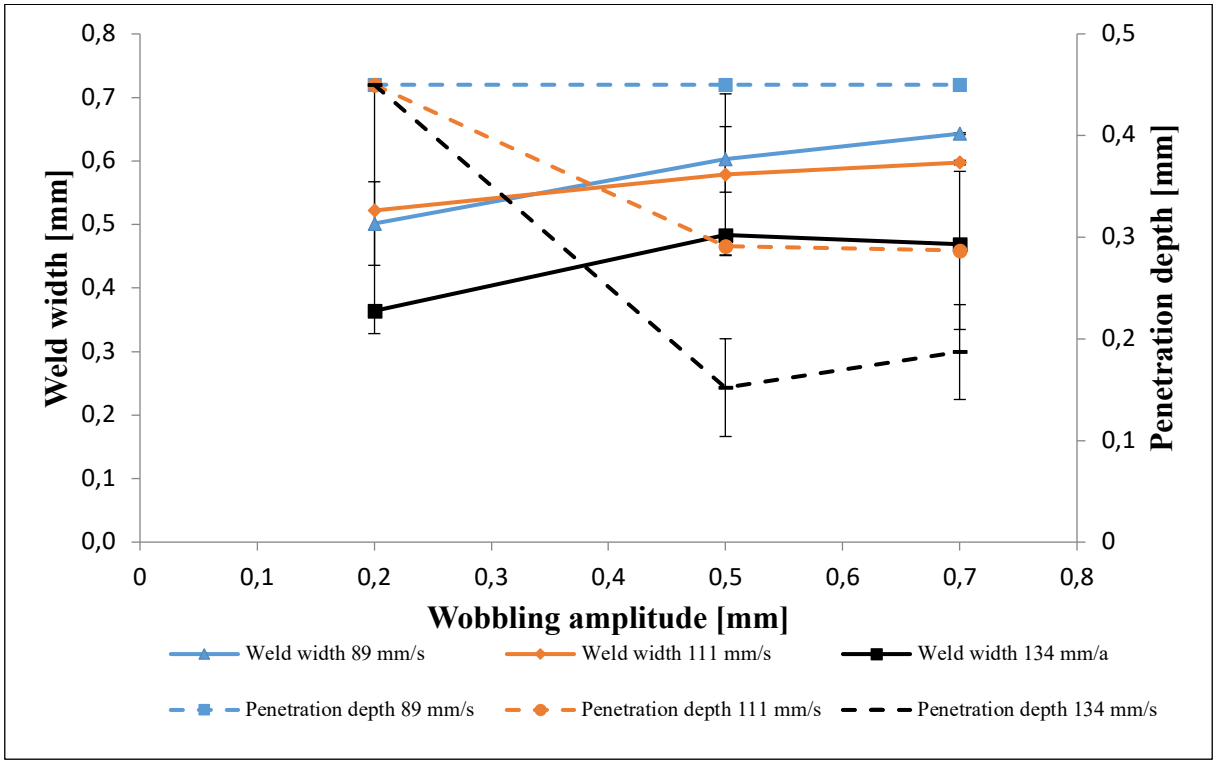

Figure 27: Weld bead characteristics of Al-Cu configuration with wobbling strategy at laser power of 800 W.

4.1.3. Shear tensile test results

Shear tensile test was performed after metallographic preparation and optical microscopic analysis which allowed to collect information about the weld bead characteristics. As previously stated, tensile tests have been considered for the conditions that allow partial penetration. The goal was to conduct a qualitative examination of the joint and determine the maximum breaking load. Table 7 summarizes the parameters used for the tensile test. A few conditions were chosen to limit the number of trials, including one sample for each amplitude of wobbling. Two tests were carried out, and the average was then calculated.

Configuration	Sample	Power [W]	Welding speed [mm/s]	Wobbling amplitude [mm]	Weld width [mm]	Penetration depth [mm]
Al to Cu	A	600	156	0,2	0,30	0,19
	B	600	156	0,5	0,60	0,10
	C	800	134	0,7	0,82	0,17
Cu to Al	D	800	89	0,2	0,50	0,45
	E	900	134	0,5	0,60	0,40
	F	800	134	0,7	0,47	0,19

Table 7: Welding configurations used for tensile tests with wobbling strategy.

In Figure 28 were reported the maximum breaking loads as a function of weld width for both the configurations. When the aluminium is the topside material, the maximum breaking load of 1206 N was obtained with a weld width of 0.6 mm; with a weld width of 0.3 mm the maximum breaking load was 1010 N and with a value of 0.82 mm the load was 1098 N. Considering the copper-aluminium configuration is shown that the higher maximum breaking load was recorded with a weld width of 0.47 mm; increasing the weld width the load decrease. It can be noted that an increase of weld width as a positive effect on the properties of the weld bead when aluminum was placed as upper materials; on the other hand, it seems to have a detrimental effect when the welding configuration involves copper to aluminum.

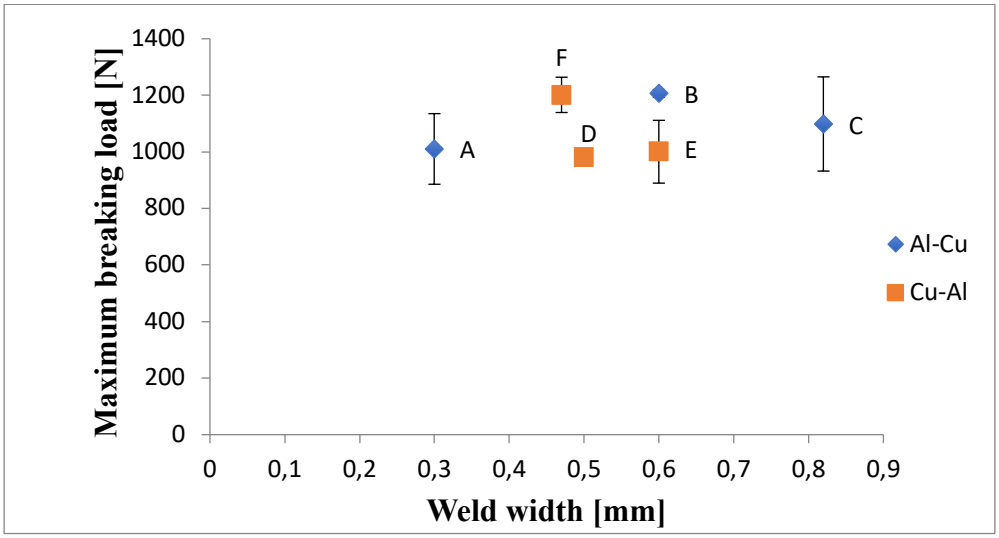

Figure 28: Maximum breaking load as a function of weld width.

In Figure 29 maximum breaking loads as a function of penetration depth are shown. It is clear that as the penetration depth increases, the maximum breaking load decreases for both the configuration. Maximum values have been reached with penetration depth of 0.1 mm (Al-Cu) and 0.187 mm (Cu-Al). It seems clear that a partial penetration in the lower sheets allows to maximize the properties of the joint; the reason could be due to the fact that greater penetration is obtained with greater energy inputs which lead to the formation of harder and more fragile intermetallic compounds.

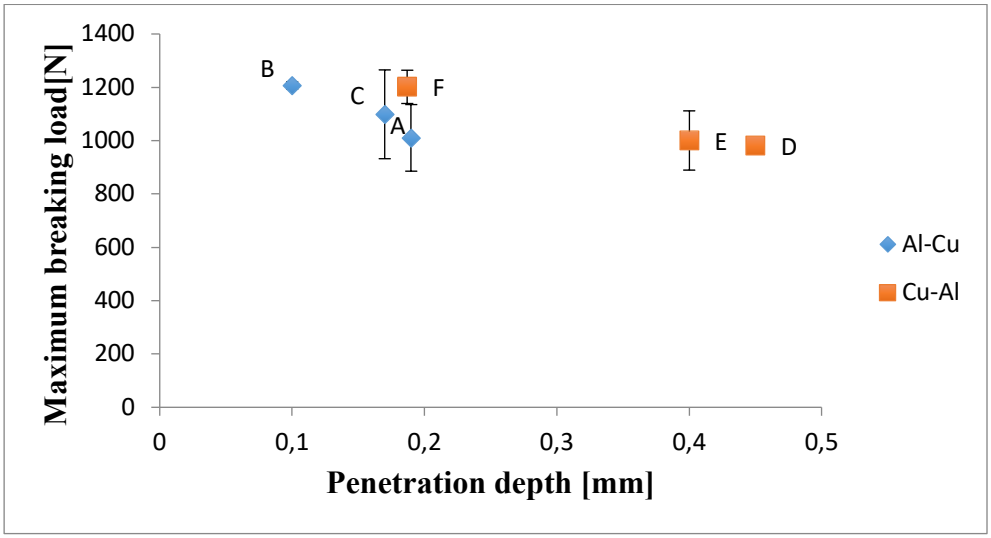

Figure 29: Maximum breaking load as a function of penetration depth.

After the properties of a single weld bead were assessed, was analyzed the possibility of performing the double weld seam with the aim of improving the mechanical properties. The results obtained with the double weld seam are shown in Figure 30. It was shown how the double seam increases the mechanical properties by about 20 % for each chosen sample except for samples C and F to which they correspond wobbling amplitude of 0.7 mm. It can be concluded that the double weld seam it is not convenient with higher amplitude wobbling since there is a greater probability of having a larger

molten zone and heat-affected zone and therefore greater chance of finding defects that can compromise the mechanical properties. Finally, the breaking methods were analyzed. It has been found that when the aluminium is the topside material the break was recorded at the base material indicating that the weld seam was much more resistant than the materials in both single and double cord. When the copper was the topside material and full penetration occurred the break was recorded at the welding seam; the break location so close to weld seam could be due to the formation of Cu-richer intermetallic compounds **[25].**

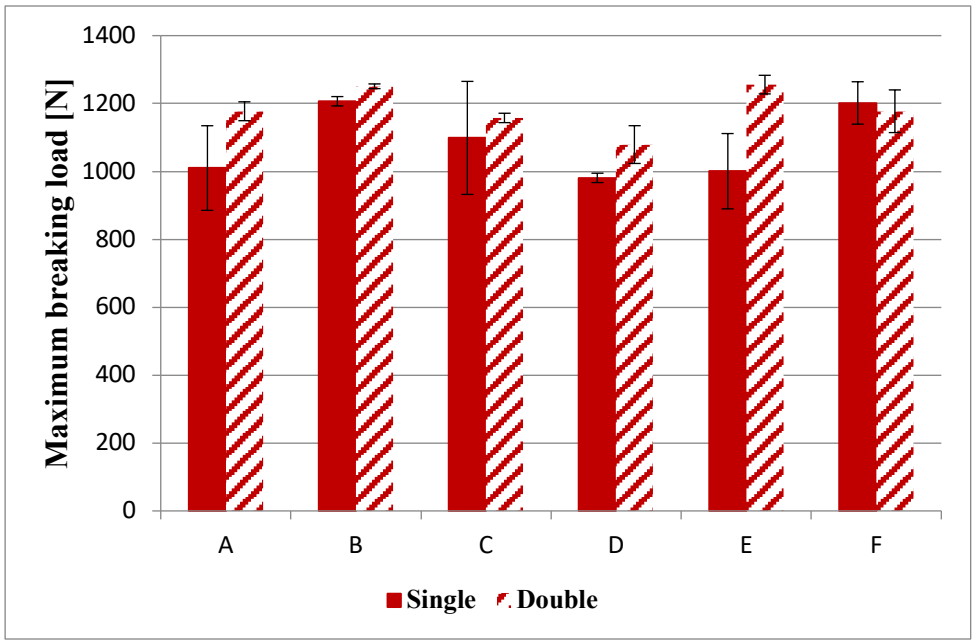

Figure 30: Maximum breaking load of the single weld bead compared to the double weld seam.

4.1.4. Micro Hardness results

The micro-hardness testing was carried out on the cross sections with 100 gf load force and 20 s dwell time. The indentations, on both sheets, were performed in the longitudinal direction in fused zone (FZ) at a distance of 300 µm each other. Starting from the central axis of the weld seam, five indentations have been carried out: one at the axis and two on the right and left side. The hardness profiles obtained for both configurations are shown in Figure 31. In Figure 31 (a) was reported the hardness profile corresponding to specimen B with a wobbling amplitude of 0.5 mm. Interesting to observe how the peak of hardness was reached near the molten zone in two different zones matching to the extremes of the trace where the laser energy per unit length achieve a maximum value. It seems

that with one only trace two weld seams were generated. The base materials had a hardness of 26 HV (Al) and 60 HV (Cu) while the peak in the fused zone was 190 HV. The phenomenon observed previously is not repeated for Cu-Al configuration, Figure 31(b). The peak of 490 HV was reached in the molten zone close to the copper sheet. By comparing the mechanical results and the hardness, it was found that hardness up to 300 HV has a negative influence on mechanical properties. Particularly, analyzing the tensile tests curves we noted how the break is more fragile in Cu-Al than the Al-Cu configuration. The SEM-EDS analysis can provide more accurate information on the chemical composition of the intermetallic phases that have formed but have not been carried out as it was considered appropriate not to proceed with these activities at the beginning of the research.

(a)

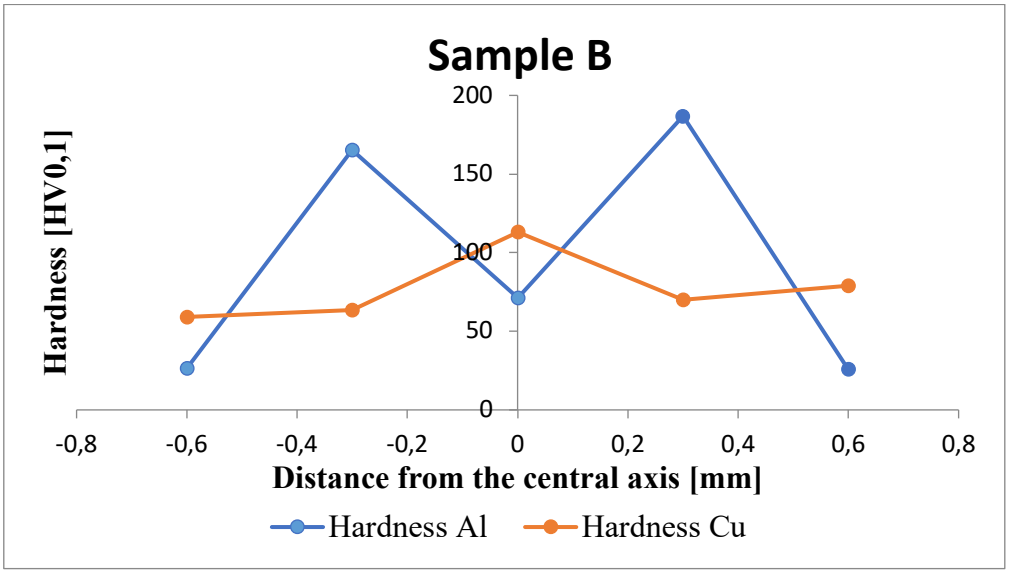

(b)

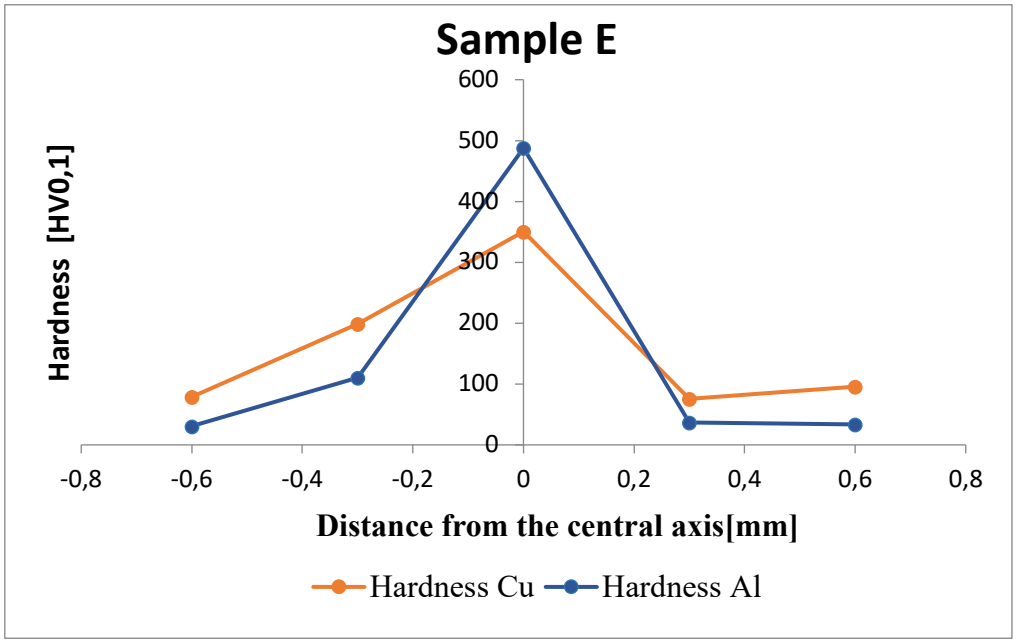

Figure 31: Example of hardness profiles obtained for both Al-Cu and Cu-Al configuration.

4.1.5. Temperature results

During the manufacturing of battery module, it is important not to exceed high temperatures in order to avoid melting of the polymeric casing that surrounds the individual cells. The maximum temperature constraints within which it is necessary to work are defined both by the type of cell and by the supplier who produced it; when using pouch cell, it is necessary to avoid exceeding 60 ° C in order to not have thermal runaway The maximum temperatures recorded, during tab-tab configuration, are shown in Figure 32(a). For Al-Cu configuration, namely specimens A, B and C, the maximum temperatures were about 28°C in case of single weld seam. There is not a substantial difference among the dates recorded since the welding speeds and power used do not change significantly and the wobbling amplitude does not seem to influence as well. With double weld seam the temperatures reach a value of about 33°C. For Cu-Al configuration, specimens D, E and F, the temperatures were about of 32 °C in case of single weld-seam and reached a value of about 40 °C with double cordon. The power densities and welding speeds used in this work allow to realize a reliable joint reducing thermal stress. The most stressed point, in red in Figure 32(b), was in correspondence with the central welding area on the sheet irradiated by the laser beam. The temperatures that are reached are however low compared to conventional welding technologies.

(a) (b)

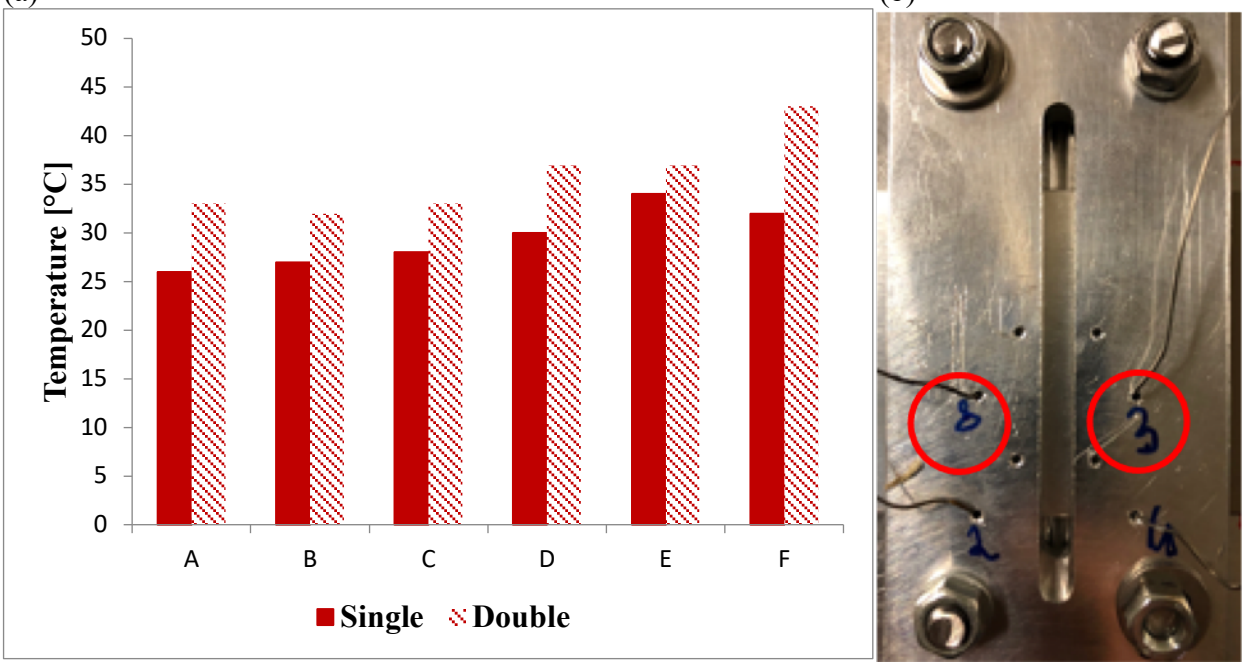

Figure 32: Maximum temperature recorded with wobbling strategy(a), thermocouples' layout(b).

4.1.6. Conclusions

Dissimilar laser joining process with spatial beam oscillation of thin copper and aluminum sheet in lap-joint configuration was investigated in order to collect information about the influence of process parameters on properties of the connections and which weld configuration could be useful to enhance the joint's performance. The process has been studied by varying the laser power, the welding speed, wobbling amplitude and the placement of the sheets. To determine the properties of welded joints, microscope analysis, mechanical, micro-hardness and temperature measurements were carried out. In conclusion the study can be summarized as follow:

- A feasibility process window in terms of laser power, welding speed and wobbling amplitude has been defined for both the configurations (Al to Cu, Cu to Al). Wobbling amplitude greatly influences the aspect ratio of the weld seam in Al-Cu configuration; less obvious in Cu-Al configuration. As the amplitude of the oscillation increases, the energy input necessary to melt the materials increases, with consequent dilution between the materials and the chance of formation of hard and brittle compounds. It is desirable to increase the wobbling amplitude to have greater resistant section but not beyond a certain limit. Good welding seams was obtained, when the aluminium is the top side material, with laser power of 600 W and welding speed of 156 mm/s and a wobbling amplitude of 0.5 mm. For Cu-Al configuration the optimized parameters are laser power of 800 W, welding speed of 134 mm/s and wobbling amplitude of 0.7 mm.
- If on the one hand the mechanical properties, in terms of maximum breaking load, are little influenced by the width value at the seam interface, the same cannot be said for the penetration depth. In fact, it has been found that the maximum breaking load decreases as the penetration depth increases. The double weld bead leads to an increase in mechanical properties of about 10-20%.
- Micro-hardness results showed an increase of hardness in fused zone as a result of mixing between base materials and consequent formation of intermetallic compounds. The values of hardness measured are strictly related to the process parameters used and welding configuration investigated.
- The temperatures, measured with thermocouples placed 10 mm from the weld, were below 45 ° C; The most stressed point was close to the central area of the weld.

4.2. Effect of focusing spot diameter

After having assessed that continuous welding with scanner head allows both to respect the process constraints and to obtain good mechanical properties in the copper-on-aluminum configuration, an experimental study on the effect of the focusing spot on the properties of the joint, always in the overlapping configuration has been conducted. From now a setup change has been evaluated; in fact, a configuration very close to a possible laser cell present in the production line was used. For this purpose, a 6gdl industrial robot was used, on which the head was mounted, to refer the welding head to the workpiece. The robot is used only for the correct positioning of the head, while the movement of the laser beam is performed by the galvos. The aim of the activity was therefore to analyze the influence of focal spot diameter on weld quality for joining of copper and aluminum in a lap joint configuration. In order to make the investigation more effective, two different focal lengths were exploited: 163 mm for standard high-power density applications and 420 mm for remote welding. After defining a feasibility window, the effects of power and welding speed on the weld bead geometry were assessed. SEM-EDX analysis allowed considerations to be made in relation to the composition of IMC formed after welding. Subsequently, samples were mechanically analyzed with tensile and electrical contact resistance tests.

4.2.1. Materials and methods

The materials tested are pure copper (Cu > 99.5 %, 0.3 mm thick) coated with a thin (2.5 µm) electroplated nickel layer and commercially pure aluminum (EN-EW 1050, 0.45 mm thick) sheets were used for experiments. Test specimens comprised a 60x45 mm Cu sheet welded onto a 60x45 mm Al sheet in a lap-joint configuration with the copper sheet on top (see Figure 33(a)). The overlap between the two sheets was 10 mm, while the length of the weld bead was kept shorter than the width of the specimen to avoid extending the fusion zone to the edges of the sheets and forming fusion notches.

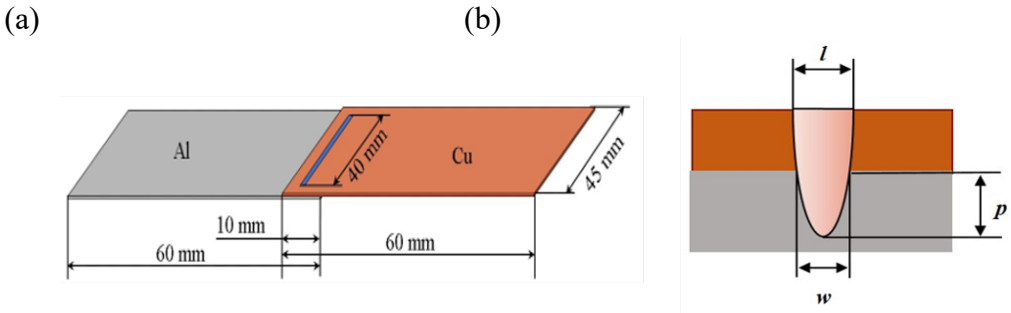

Figure 33: Sample dimensions(a), weld bead characteristics(b).

An nLight Alta 3.0 kW continuous-wave Yb:Fiber laser (BPP < 2.8 mm*mrad) with a wavelength of 1070 nm was used for all trials. The feeding fiber core diameter was 50 µm while the focusing optics comprised a Scanlab HurryScan 30 galvo scanner combined with two Wavelength fused silica high power F-Theta lenses with focal lengths of 163 mm and 420 mm, respectively. The focusing optics were mounted on a 6-axis anthropomorphic robot (Yaskawa-Motoman HP-20) that allowed movement of the optics within the welding area. During the welding process, the head was kept stationary while movement of the beam was performed by the galvos. No shielding gas was used; however, a high-pressure lateral air jet was used to protect the scanning optics. Figure 34 shows an image of the setup used.

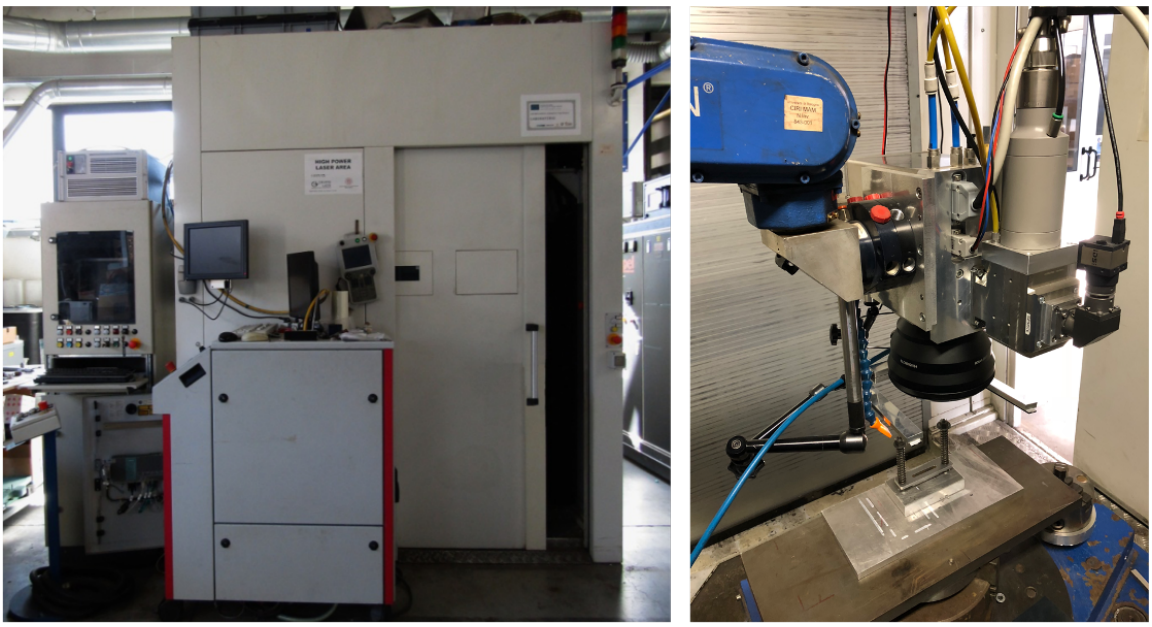

Figure 34: Laser welding area(a), setup for welding of tab-to-tab configuration(b).

As stated before, since the aim of the experimental activity was to collect information on the effect of focusing spot diameter on the joints' properties, the galvo scan head was equipped with two different F-Theta lenses that allowed generation of two different spot dimensions. The laser beam was focused on the surface of the top sheet without tilting the head. Optics specifications are shown in Table 8.

	Lens 1	**Lens 2**
Collimation length [mm]	120	120
Focal length [mm]	163	420
Magnification rate	1.36	3.5
Spot diameter [µm]	68	175
Rayleigh length [mm]	0.6	3.8

Table 8: Optics specifications of the F-theta lens used during the trials.

Welding was performed with both lenses, in linear mode, by varying the laser power and welding speed in order to define a process window and evaluate how the process parameters affected weld bead formation. Laser power was between 600 W and 1000 W for the smaller spot size and between 1000 W and 1500 W for the larger one. The welding feed rate was varied from 150 mm/s to 250 mm/s for both configurations. With the aim of comparing the two spot diameters, parameters were chosen to obtain roughly the same range of energy density (power density·interaction time) for both focal lengths (see Table 9-10).

Sample	Power [W]	Welding speed [mm/s]	Power Density [MW/cm^2]	Energy Density [MJ/cm^2]
A1	600	150	18.08	0.7835
A2	600	200	18.08	0.5576
A3	600	250	18.08	0.4701
B1	800	150	24.11	1.0447
B2	800	200	24.11	0.7835
B3	800	250	24.11	0.6268
C1	1000	150	30.14	1.3059
C2	1000	200	30.14	0.9794
C3	1000	250	30.14	0.7835

Table 9: Process parameters for 160 mm lens (spot diameter 68 µm).

Sample	Power [W]	Welding speed [mm/s]	Power Density [MW/cm^2]	Energy Density [MJ/cm^2]
D1	1000	150	4.16	0.4850
D2	1000	200	4.16	0.3638
D3	1000	250	4.16	0.2910
E1	1250	150	5.20	0.6063
E2	1250	200	5.20	0.4547
E3	1250	250	5.20	0.3638
F1	1500	150	6.24	0.7276
F2	1500	200	6.24	0.5457
F3	1500	250	6.24	0.4365

Table 10: Process parameters for 420 mm lens (spot diameter 175 µm).

Preliminary observations of the weld seam were performed with a stereomicroscope to obtain information regarding spatters and the possible presence of other defects such as micro-cracks. In order to characterize the weld beads in terms of dimensions and morphology, cross sections were prepared by cold mounting the samples in resin and polishing them with SiC paper followed by

alumina in suspension. No etchant was used to identify the weld seam geometry. The specimens were also mechanically characterized via shear tensile tests performed at a crosshead speed of 0.025 mm/s with an Instron 8033 testing machine equipped with a 10 kN load cell. It must be noted that the samples used for tensile tests did not comply with any specific standard in relation to their shape and dimensions, as the aim was to qualitatively evaluate the overall strength of the joint. For each combination of parameters, three specimens were welded, and the average value of maximum failure load calculated. Electrical resistance was measured at room temperature via the four-point method with a test length of 20 mm; the set-up used has been reported in Figure 35. Measurements were performed with a Chauvin Arnaux CA 6255 micro-ohmmeter characterized by an accuracy of 0.1 μΩ and a measurement current of 10 A for 20 s. A scanning electron microscope (SEM) equipped with an energy dispersive X-ray spectrometer (EDS) was used to analyze the weld specimens with the aim of obtaining information about the chemical composition of the formed IMC.

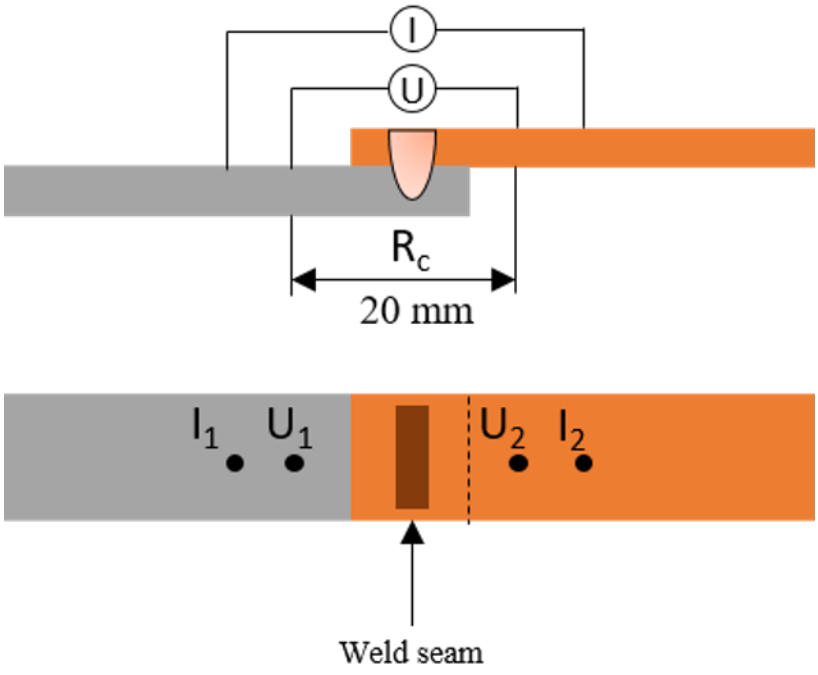

Figure 35: Electrical contact resistance setup for tab welding configuration.

4.2.2. Optical microscope results

Microscope and stereomicroscope images of specimens welded with the smaller spot size are shown in Figure 36 . The set of parameters that were chosen allowed weld seams without defects (micro-cracks) to be obtained, as can be seen from the cross sections. The weld beads were fairly regular along the entire surface, with negligible presence of spatters. With this configuration, good welding (without a cut or full penetration in the lower sheet) in terms of weld seam morphology was obtained with a wide range of process parameters (see Figure 36). The interface width was not clearly influenced by the energy density, with values varying between 150 and 250 µm. As energy density increased, penetration depth into the lower aluminum sheet increased, reaching full penetration with the highest values of this parameter. Full penetration involved evident mixing of the two materials within the interface area.

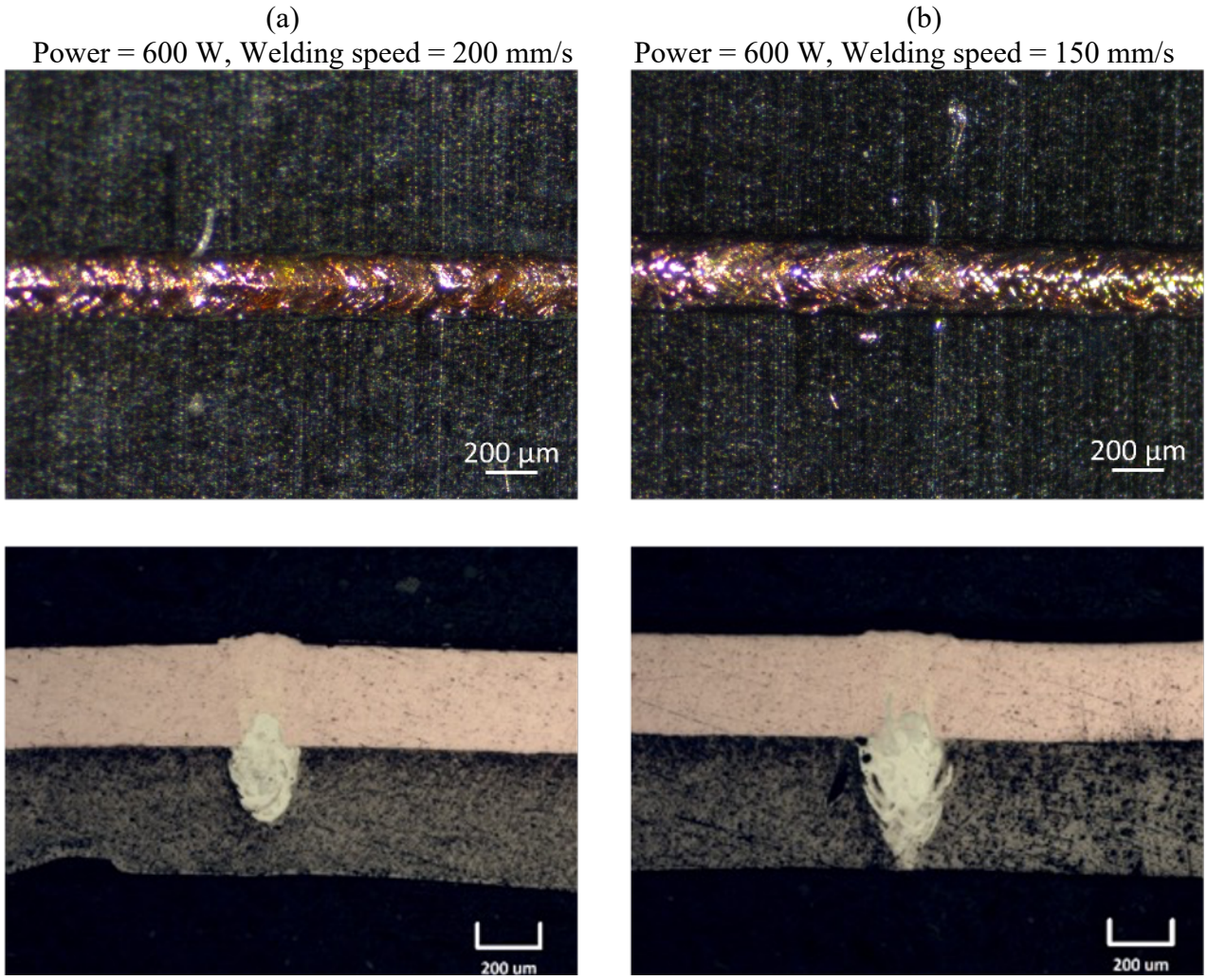

Figure 36: Top and cross sections of welded sample with 163 mm lens[78].

The larger the spot size the higher power required to overcome the high reflectivity of the upper copper layer. Microscope and stereomicroscope images of weld seams representative of the ones obtained in this configuration are shown in Figure 37. In this case, transversal and longitudinal cracks were found in some of the weld seams. This effect was due to the higher specific heat input in this configuration, which caused the formation of a larger amount of intermetallics (IMC) and promoted a thermal cycle that made the bead prone to cracking. Crack formation may be caused by residual stresses or differences in the thermal expansion coefficient and hardness of Al-Cu IMC. When the heat input is too high, temperature increases are larger, thus producing higher residual stresses with the appearance of cracks along the weld seam of particular importance, especially during an end-of-line test, to evaluate the color of a weld. In this case it has been seen that a weld with a color tending to gray will certainly have complete penetration and presence of defects; instead, a weld tends to yellow / orange is a sign of partial and reduced penetration or absence of defects[78].

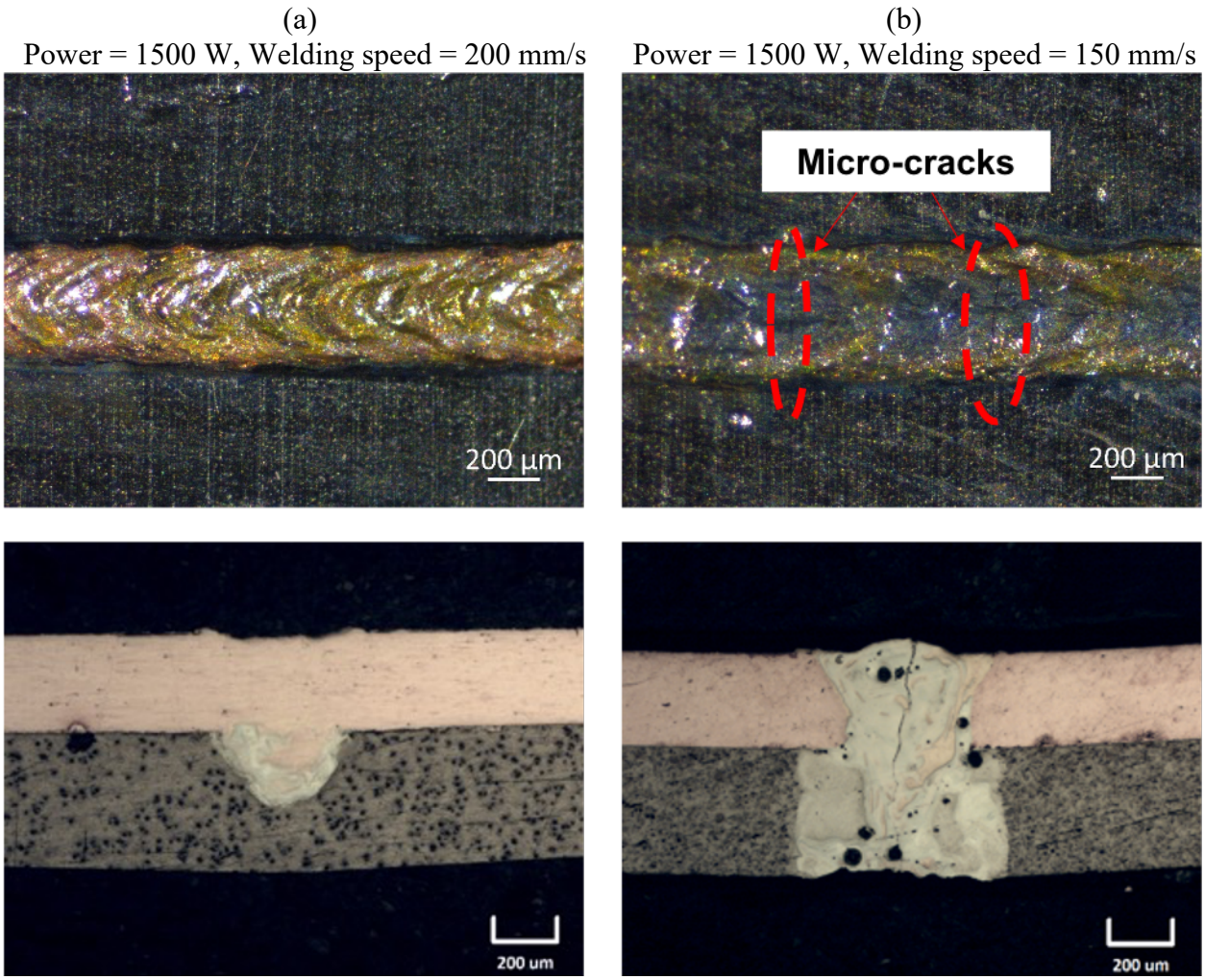

Figure 37: Top and cross sections of the welded sample with 420 mm lens[78].

Once weld seam cross-sections were obtained, it was possible to measure their geometry. Weld width was measured at the interface between the two sheets, while the penetration depth into the lower sheet

was measured from the interface between the two materials. The correlation between laser power, welding speed and interface width is reported in Figure 38(a) for a spot diameter of 68 µm. At 150 mm/s, weld width increased from 127 µm at 600 W to 220 µm at 800 W, after which no further differences in weld width were recorded with increasing laser power. In Figure 39(b) penetration depth is reported as a function of laser power. At 150 mm/s, full penetration was obtained at all power levels employed during the activity. At 250 mm/s, the penetration depth increased with laser power from 150 µm at 600 W to 390 µm at 1000 W**[78]** .

(a) (b)

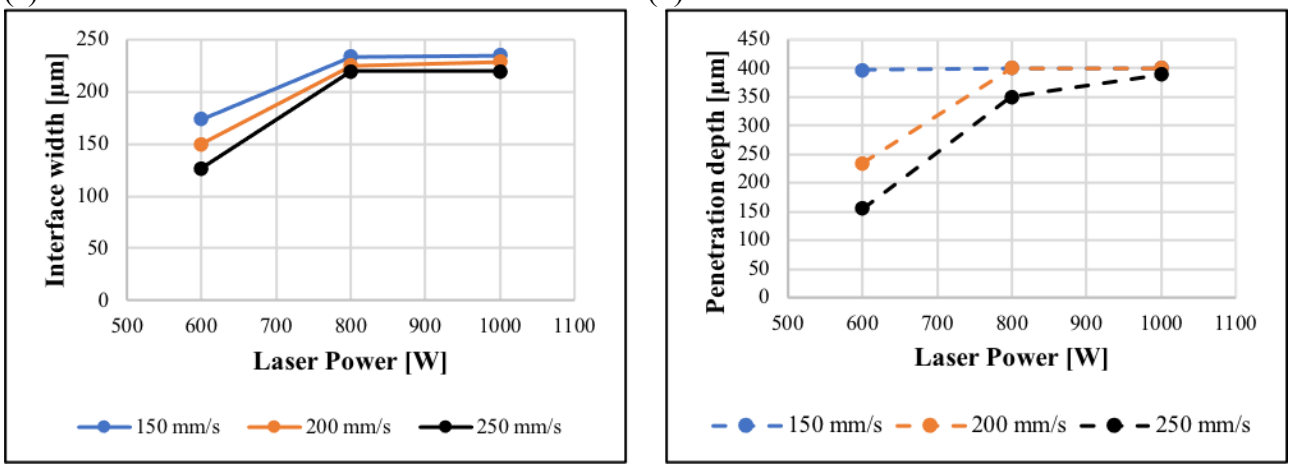

Figure 38: Weld width(a) and penetration depth (b) as a function of laser power and welding speed measured with 163 mm lens[78].

Using the 420 mm focal length (see figure 39), no welding was achieved at 250 mm/s regardless of the laser power. The interface width at 150 and 200 mm/s instead increased with laser power. By observing figure 6(b), it can be noted that partial penetration could only be obtained with a limited range of parameters. Values of 60 µm and 150 µm were obtained with a laser power of 1250 W and 1500 W at 200 mm/s**[78]**.

(a) (b)

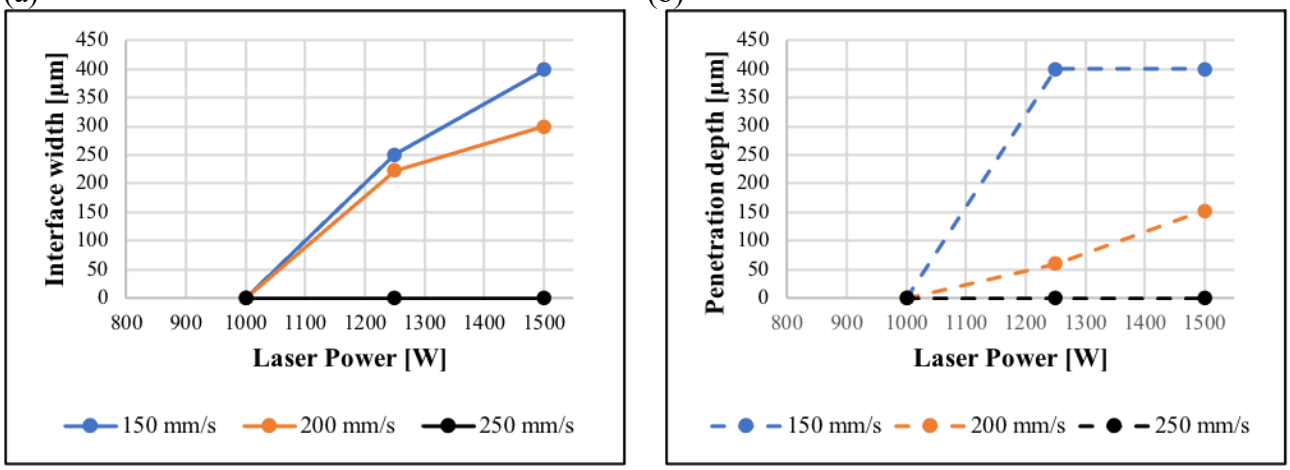

Figure 39: Weld width(a) and penetration depth (b) as a function of laser power and welding speed measured with 420 mm lens.

Cross-section images obtained with the optical microscope allowed a process feasibility window to be defined in terms of power and welding speed, as reported in Figure 40. With high energy input, a weld seam with full penetration was obtained, leading to high levels of mixing and a greater probability of brittle and hard intermetallic compounds being present (Figure 40d)). This joint shape also potentially creates problems as it may damage nearby components during the assembly of a battery pack. On the other hand, a weld seam with partial penetration reduced such problems as mixing of the materials involved only a small portion of the bead without breaking through the lower sheet (Figure 40 (c)). Due to physical and optical properties of copper, the larger spot size required higher power to melt the material. In this case, adjustment of the power and speed was difficult because the weld seam shifted from a no-welding condition to full penetration with cracks and pores very quickly. Good results in terms of weld seam morphology were nonetheless obtained with a welding speed of 200 mm/s and power of 1250 and 1500 W. A spot diameter of 68 µm favored a wider process window with better control of the penetration depth and dilution of the base metals. Due to high power density, a no-welding condition was never obtained with the parameters used during these tests. With a welding speed of 250 mm/s and a power of 600 and 800 W, weld seams with partial penetration and reduced presence of defects were obtained. It can be concluded that a smaller spot allows welding with reduced overall power, thus reducing the total heat input during the process. Furthermore, higher welding speeds can be employed, enabling greater productivity from manufacturing point of view and less liquid interaction of welded metals**[78]**.

(a)

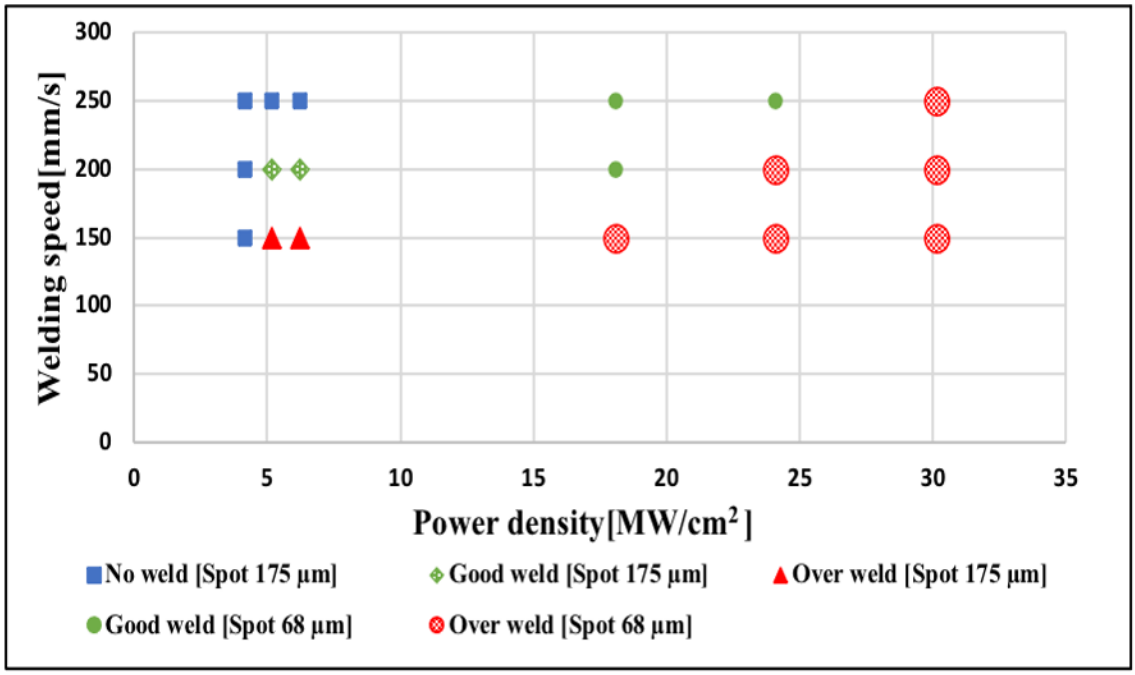

(b) (c) (b)

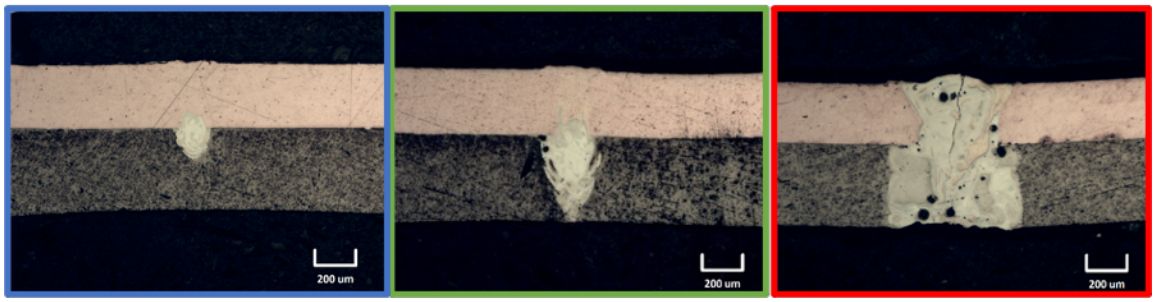

Figure 40:Feasibility process window(a), example of no-weld (b), good-weld (c) and over weld condition(d).

4.2.3. Shear tensile test results

Tensile shear tests were performed with the aim of obtaining information about the maximum load, fracture mode and failure position. In order to get a comparison, three different energy densities were chosen for each focal length. Figure 41 reports the maximum load of the joints as a function of energy density. Tensile strength values between 750 N and 900 N were obtained with the larger spot, while values between 650 and 750 N were obtained with the smaller one. The relationship between energy density and maximum load was linear and decreasing in both analyzed configurations. For a given value of energy density, highest loads were obtained with the large spot due to the larger interface area characteristic of this configuration (see Figure 38(a) and Figure 39(a)). As noted above during the welding with spatial beam oscillation, also in this case for both the spot diameter investigated higher energy density and therefore larger penetration depth in the lower sheet results in reduced mechanical properties of the connections due to the greater severity of the thermal cycle and consequent probability of having harder and more fragile intermetallic phases.

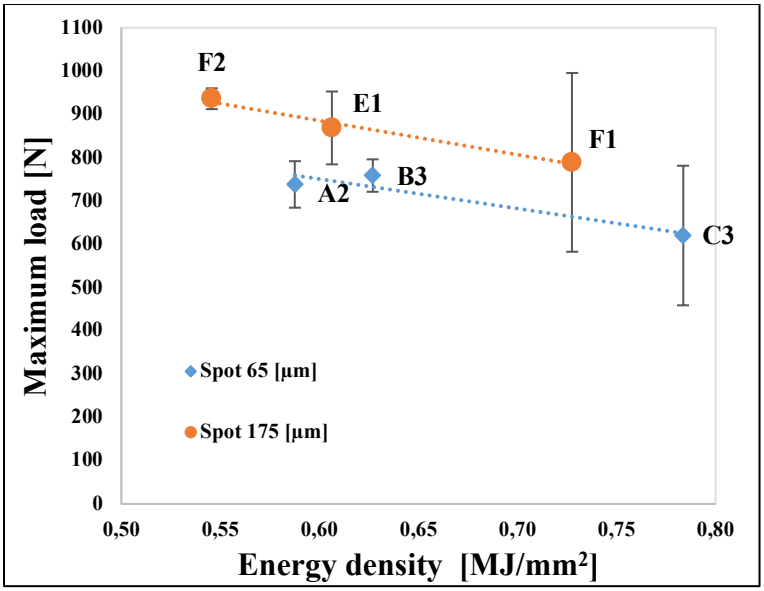

Figure 41:Shear tensile test results for both the focal length analyzed[78].

It is interesting to observe the role of spot size on the tensile test curves reported in Figure 42. With reference to the red curve, plastic deformation was more limited and brittle fracture took place with the larger laser spot size. On the other hand, the plasticity of the joint was greater and ductile fracture took place with the smaller laser spot size.

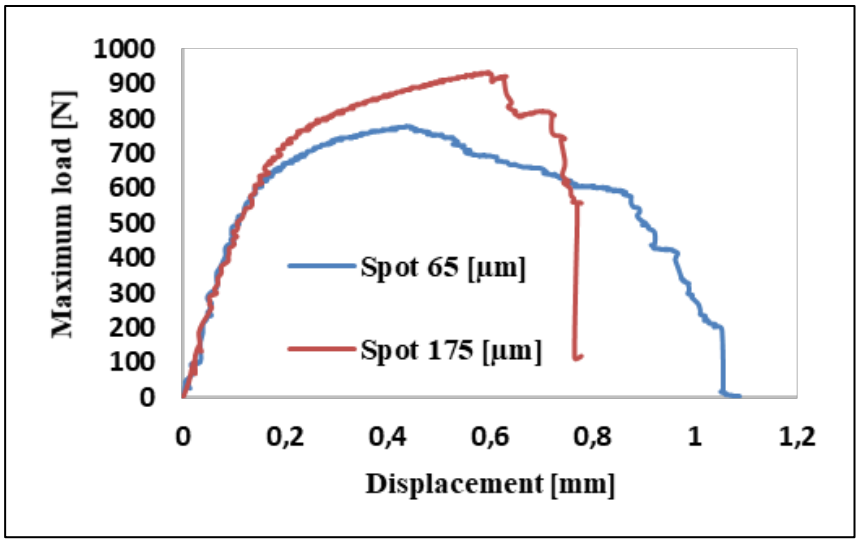

Figure 42: Example of maximum load-displacement curves.

Finally, the fracture mechanisms were investigated using the stereomicroscope images presented in Figure 43. When welding with a larger spot, it was discovered that fracture occurred in the fused zone on the copper side. Higher powers were required to achieve fusion and welding of the sheets due to the larger spot area, resulting in the production of brittle and hard intermetallic compounds along the whole weld seam. When welding was done with a smaller laser point, failure occurred at the interface between the two sheets. Microscope images show that in this case mixing between the two materials, and thus the formation of intermetallic compounds, was reduced and limited to the interface. Higher mechanical strength and brittle fracture behavior with the larger spot size was therefore due to the formation of copper rich phases with higher hardness. When welding was done with a smaller laser point, failure occurred at the interface between the two sheets. Microscope images reveal that in this case mixing between the two materials, and therefore the creation of intermetallic compounds, was decreased and limited to the interface. The formation of copper rich phases with higher hardness resulted in higher mechanical strength and brittle fracture behavior with larger spot sizes.

(a) (b)

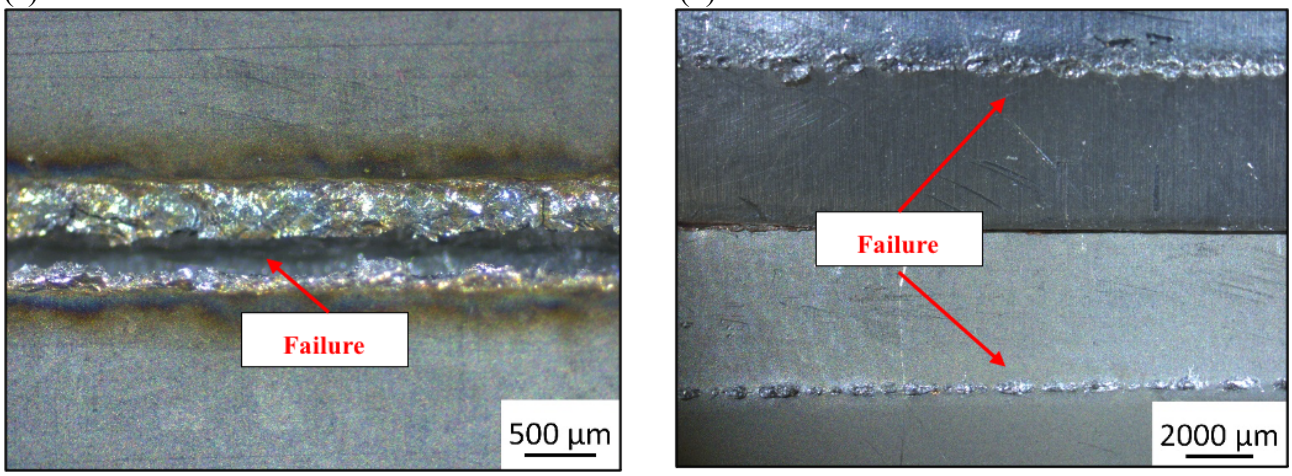

Figure 43: Example of breaking mode, failure near the weld seam (a) and failure at the interface between the sheets(b).

4.2.4. Electrical contact resistance results

The findings of electrical contact resistance measurements are shown in Figure 44. The reduced spot diameter resulted in results ranging from 45 to 42 μΩ. The greatest values were seen in samples C3 and A2, which was most likely attributed to the shape of the weld bead. Higher energy density (sample C3) resulted in the development of hard and brittle intermetallic compounds with higher electrical resistivity, as well as more mixing of the base material and full penetration of the upper sheet into the lower one. Instead, sample A2 was distinguished by a thin resistant part that also had a high contact resistance. The electrical contact resistance and mechanical qualities were both maximized using a partial penetration situation (sample B3). Values between 47 and 40 μΩ were measured with the larger spot diameter. As previously stated, full penetration, more mixing, and defect formation (pores and cracks) resulted in higher contact resistance (samples F1 and E1). Partial penetration, achieved thanks to the optimal choice of energy density, improved the overall performance of the connections. It's worth noting that electrical and mechanical qualities are inextricably linked due to a linear relationship. What was obtained, is an important result, since the measurement of the electrical resistance in this type of application is difficult to do due to its very low values and the errors that could arise during the acquisition. Consequently, first a visual evaluation of the seam, for example based on the color of the weld, and subsequently a destructive test such as the tensile test can provide satisfactory results to ensure the success and good properties of the joint.

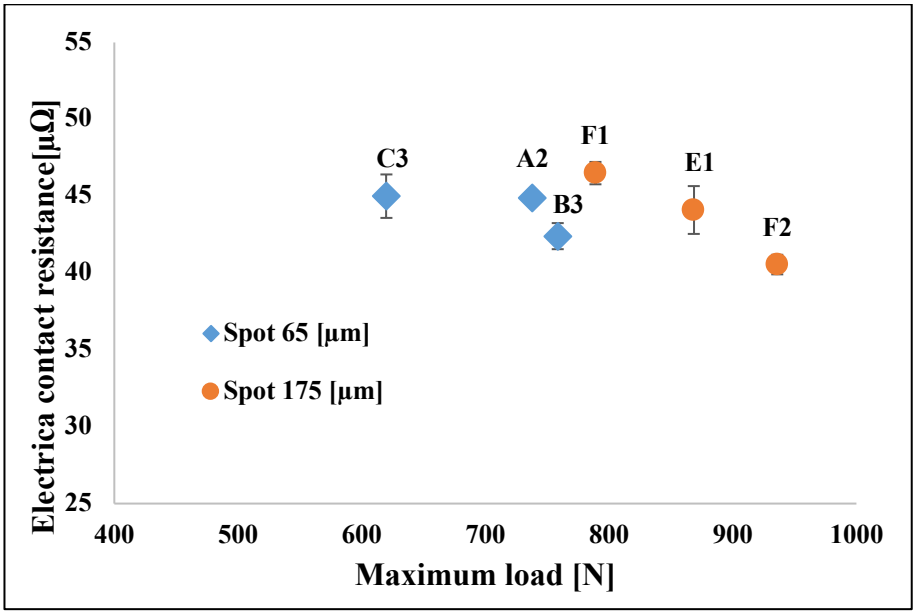

Figure 44:Electrical contact resistance results[78].

Table 9 summarizes the characteristics in terms of weld bead morphology of the samples used for mechanical and electrical tests. From the analysis of the data, it can be seen that there is no linear correlation between the width at the interface and the electrical properties of the joints. The best performances were obtained for weld bead with a particular morphology, in particular when full penetration of the copper in aluminum sheet was avoided; the reason could be that for weld beads with high interface widths and high penetration depths, greater thermal inputs are required with consequent formation of both hard and brittle intermetallic phases which are characterized by greater electrical resistivity.

Sample	Power [W]	Welding speed [mm/s]	Spot diameter [µm]	Interface width [µm]	Penetration depth [µm]	Maximum load [N]	Electrical contact resistance [µΩ]
C3	1000	250	68	220	390	620	45
A2	600	200		150	230	738	44.9
B3	800	250		220	350	758.5	42.4
F1	1500	150	175	399	400	789	46.5
E1	1250	150		223	60	868	44.1
F2	1500	200		300	150	936	40.5

Table 11: Summary of the samples tested by mechanical and electrical tests.

4.2.5. SEM-EDS analysis

SEM-EDS analysis was performed with the aim of obtaining information about the chemical composition of intermetallic compounds formed during welding and how the spot diameter affected their formation. For this purpose, two samples obtained with different levels of energy input were analyzed for each spot size, considering different zones of the weld seam. Cross-section images of sample A2 are shown in Figure 36 (a). When partial penetration took place, mixing between the two metals was limited to the aluminum sheet and a small part of the copper sheet. The chemical composition of the marked points in Figure 45 are listed in Table 12. In the upper part of the weld seam (Figure 45 (A)), presence of the Θ(Al_2Cu) phase was detected in the form of serrated dendrites. At the interface zone and in the lower part of the weld seam, the copper content never exceeded 25 at%, resulting in the detection of Al-Cu eutectic alloy with a vermicular shape. The EDS spectra of the marked point in Figure 45 are reported in Figure 46 . Due to the low heat input and reduced cooling time, the melt pool and thus the base metals were not subjected to violent fluctuations in copper content, resulting in a homogenous phase composition**[78]**.

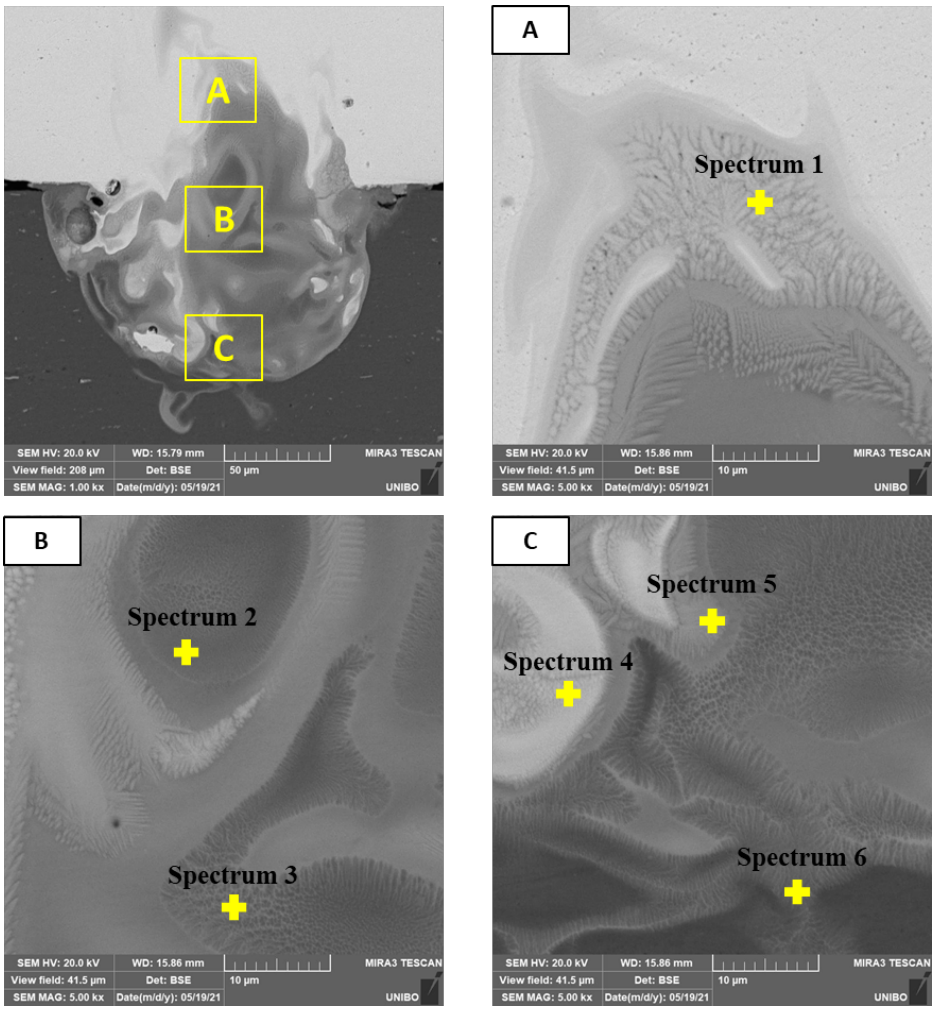

Figure 45:SEM images of sample A2.

Spectrum	Al (at%)	Cu (at%)	O (at%)	Possible Phase
1	55.78	43.92	0.3	$\Theta(Al_2Cu)$
2	82.05	15.02	2.85	Al-Cu eutectic
3	81.73	16.69	1.58	Al-Cu eutectic
4	44.43	54.98	0.59	η (AlCu)
5	71.17	27.75	1.08	Al+ $\Theta(Al_2Cu)$
6	88.57	8.56	2.86	Al-Cu eutectic

Table 12:Chemical composition of denoted zone in figure 45.

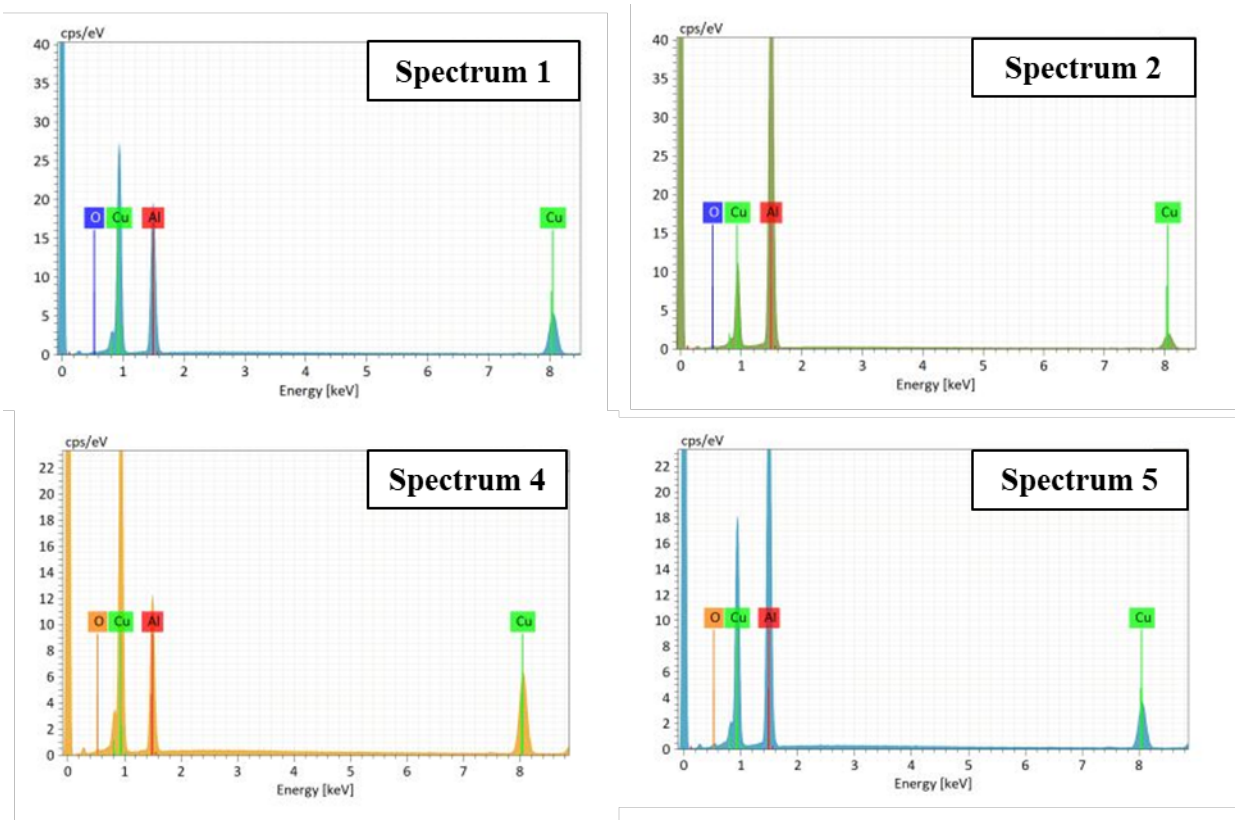

Figure 46:Spectra of the marked points in figure 45.

Figure 47depicts cross-section images of sample C3. The chemical compositions of marked points are listed in table 13. By increasing the energy density from 0.5576 to 0.7835 MJ/mm^2, mixing was more pronounced, and a greater quantity of copper was found in the upper part of the weld bead while molten aluminum flowed upward. As a result, the η (AlCu) and $\gamma(Al_4Cu_9)$ phases were detected in the form of columnar grains. At the interface, in the transition zone (Figure 47(B)), the η (AlCu) phase was detected, while in the lower part of the weld seam, the $\Theta(Al_2Cu)$ phase and Al-Cu eutectic alloy formed, as seen in the previous case (Figure 45 (C)). Since heating was concentrated in a small area and the interaction time was very low with the smaller spot diameter, the $\Theta(Al_2Cu)$ and $\gamma(Al_4Cu_9)$ phases formed in the weld seam due to their low formation energies**[79]**. The intermetallic compound layers formed as a result of chemical reactions via inter-diffusion of Al and Cu atoms between the copper and aluminum sheets at the interface.

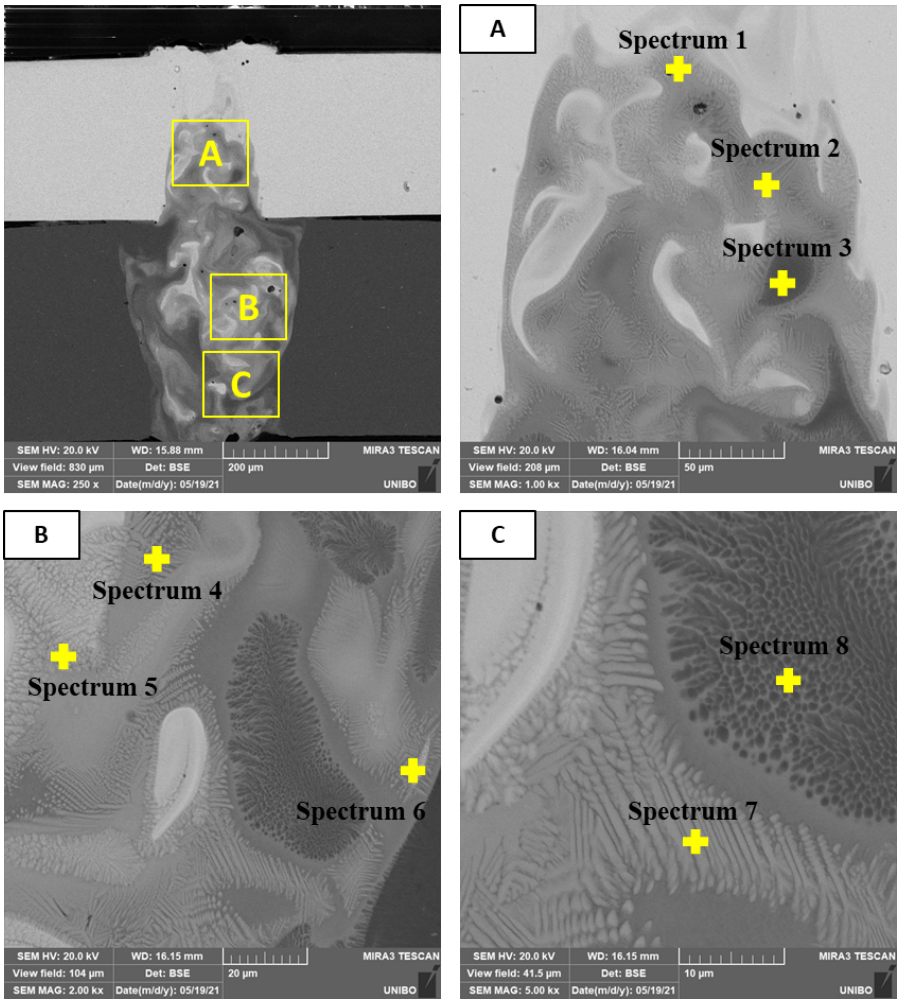

Figure 47:SEM images of sample C3.

Spectrum	Al (at%)	Cu (at%)	O(at%)	Possible Phase
1	48.56	50.93	0.51	η (AlCu)
2	70.04	28.62	1.34	Al+ Θ(Al_2Cu)
3	93.26	2.58	4.15	Al-Cu eutectic
4	76.21	22.97	0.82	Al+ Θ(Al_2Cu)
5	64.66	34.75	0.59	Θ(Al_2Cu)
6	57.16	42.45	0.39	η (AlCu)
7	68.28	31.33	0.39	Θ(Al_2Cu)
8	90.97	6.31	2.72	Al-Cu eutectic

Table 13:Chemical composition of denoted zones in figure 47.

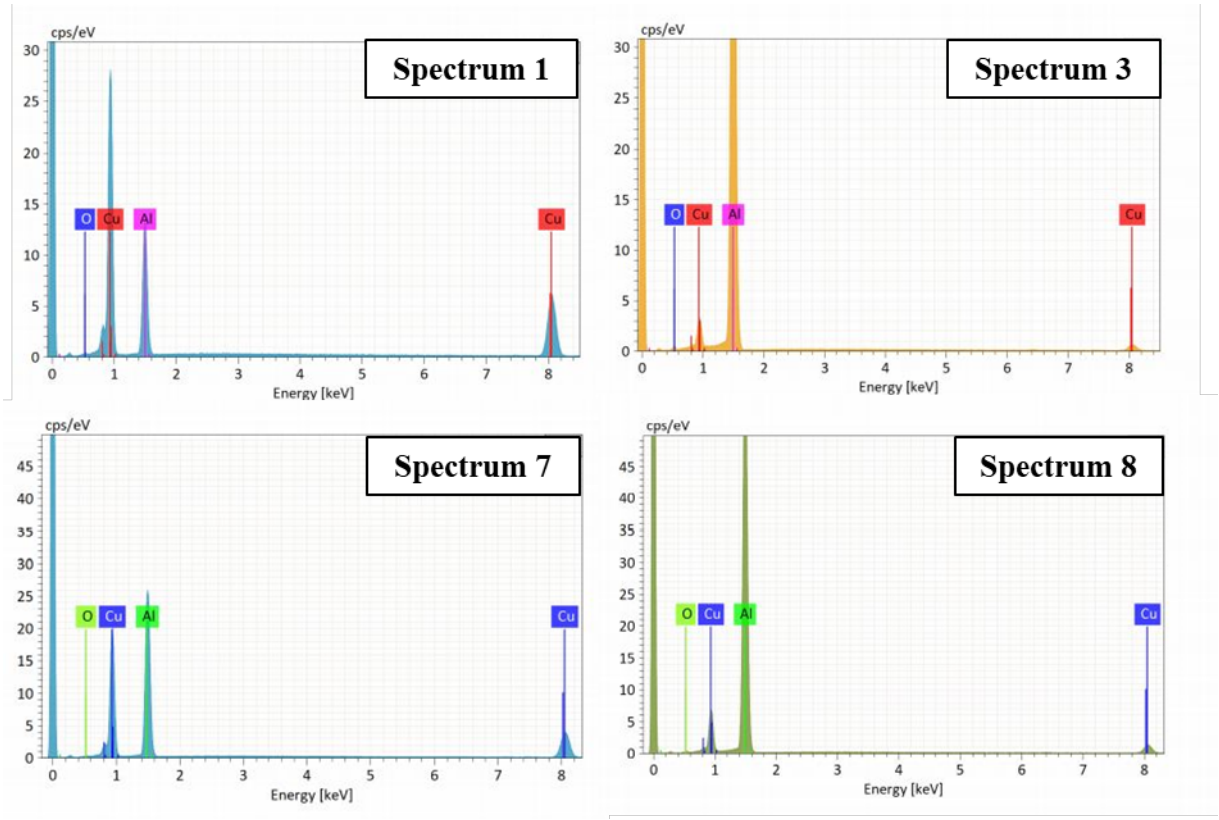

Figure 48:EDS spectra of marked points in figure 47.

Cross-section SEM images of sample F3 obtained with the larger spot diameter, a laser power of 1500 W and a welding speed of 250 mm/s are shown in Figure 49. By analyzing the image, it is possible to state that welding occurred via a conduction mode since mixing was limited in the lower part of the weld seam. The upper part of the joint consisted of copper in solid solution, while at the interface zone Θ(Al_2Cu) and η (AlCu) phases formed, characterized by columnar morphology. A composition change was also observed in zone C. Approaching the copper sheet, the Al-Cu eutectic was firstly detected followed by the Θ(Al_2Cu) phase as the amount of copper increased.

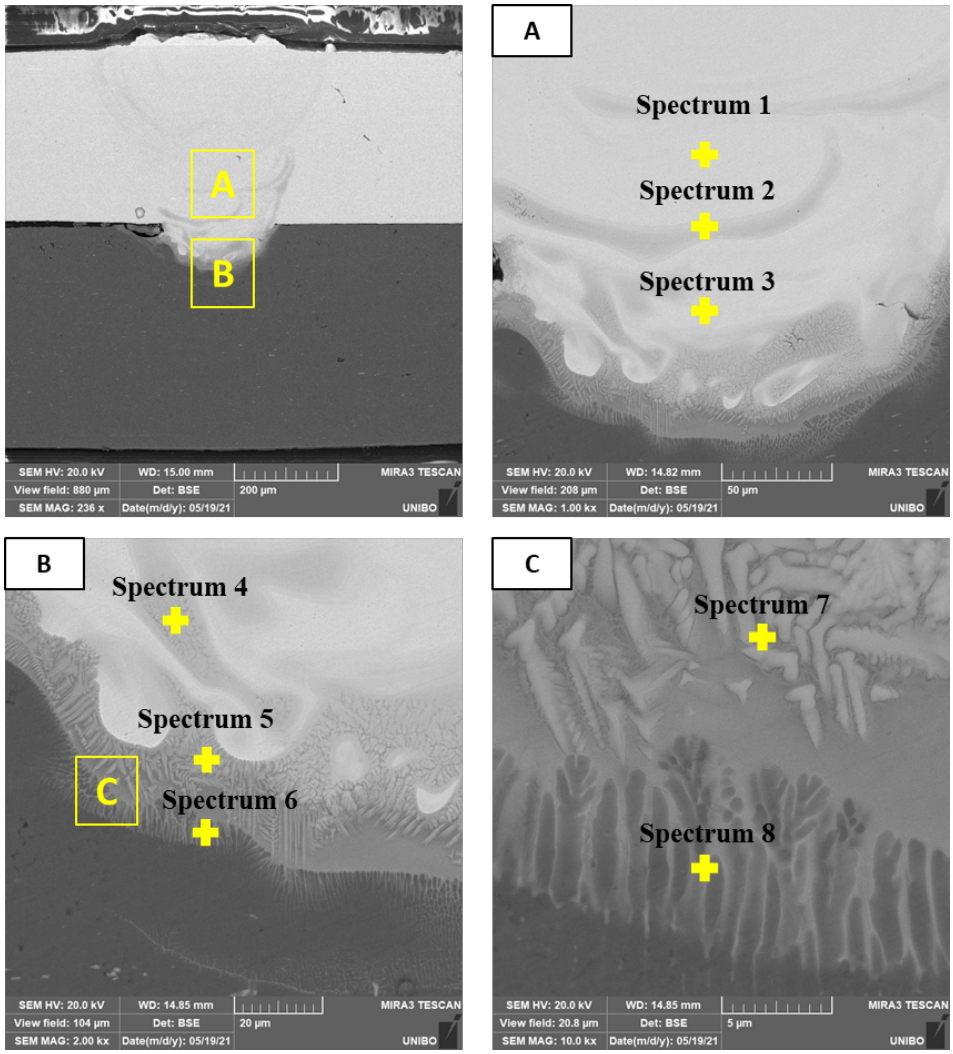

Figure 49: SEM images of sample F3.

Spectrum	Al (at%)	Cu (at%)	O(at%)	Possible Phase
1	1.43	98.48	0.09	Cu
2	28.32	70.22	1.47	$\gamma(Al_4Cu_9)$
3	7.71	91.99	0.3	Cu
4	44.83	53.81	1.36	η (AlCu)
5	76.51	20.07	3.41	Al+ $\Theta(Al_2Cu)$
6	88.07	9.37	2.56	Al-Cu eutectic
7	68.28	31.33	0.39	$\Theta(Al_2Cu)$
8	90.97	6.31	2.72	Al-Cu eutectic

Table 14: Chemical composition of denoted zones in figure 49.

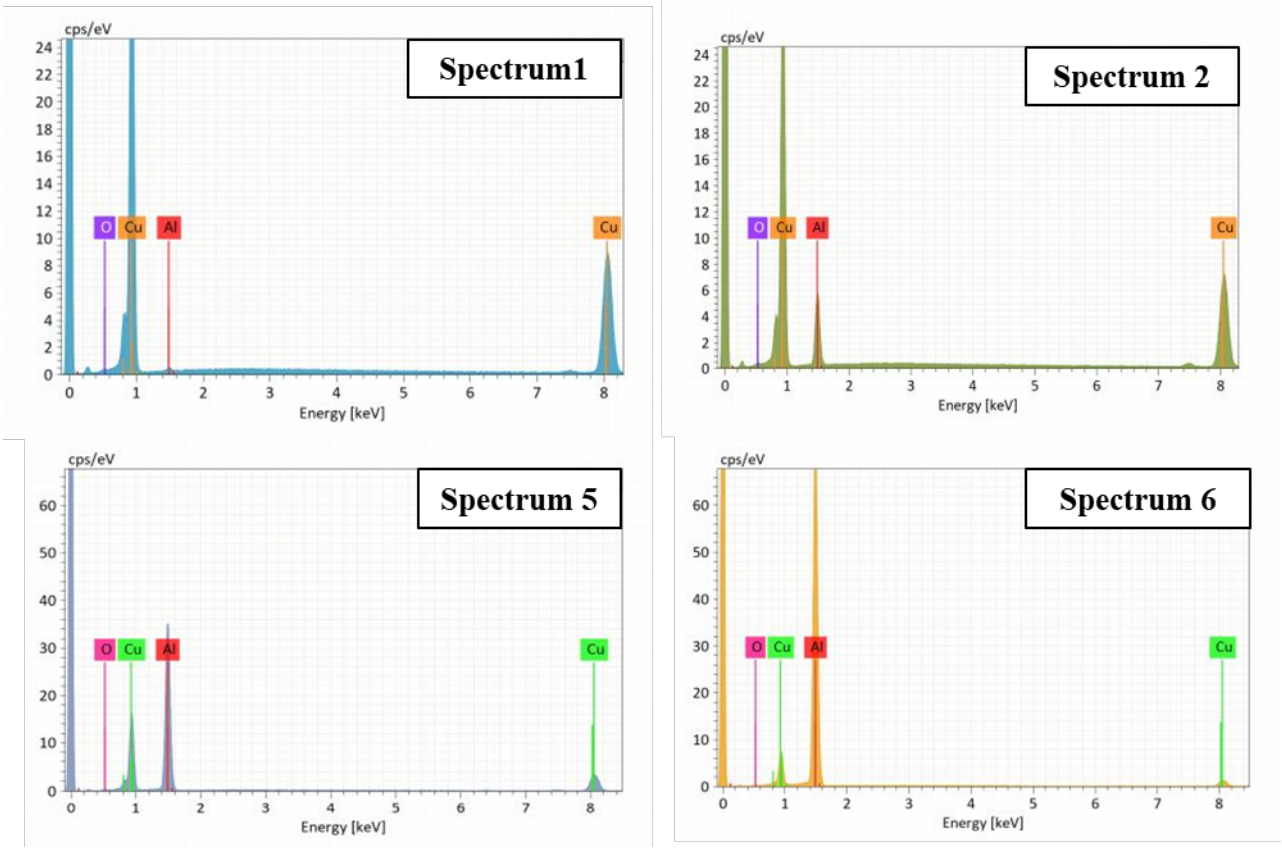

Figure 50: EDS spectra of marked points in figure 49.

With the larger spot diameter, a variation in welding speed at constant power led to elevated mixing of the base metals. When full penetration occurred, as shown in Figure 51, large amounts of copper (more than 50 at%) were found throughout the weld bead. As a result, considering the Al-Cu binary system, the $\zeta(Al_3Cu_4)$ and $\gamma(Al_4Cu_9)$ phases formed, which are the hardest and most brittle intermetallic compounds. Unlike the other phases, which are easily recognizable from their morphology, copper rich IMC are difficult to detect as they appear as a cluster of copper without a specific form. It is interesting to observe that most of the cracks propagated along the copper rich intermetallic compounds.

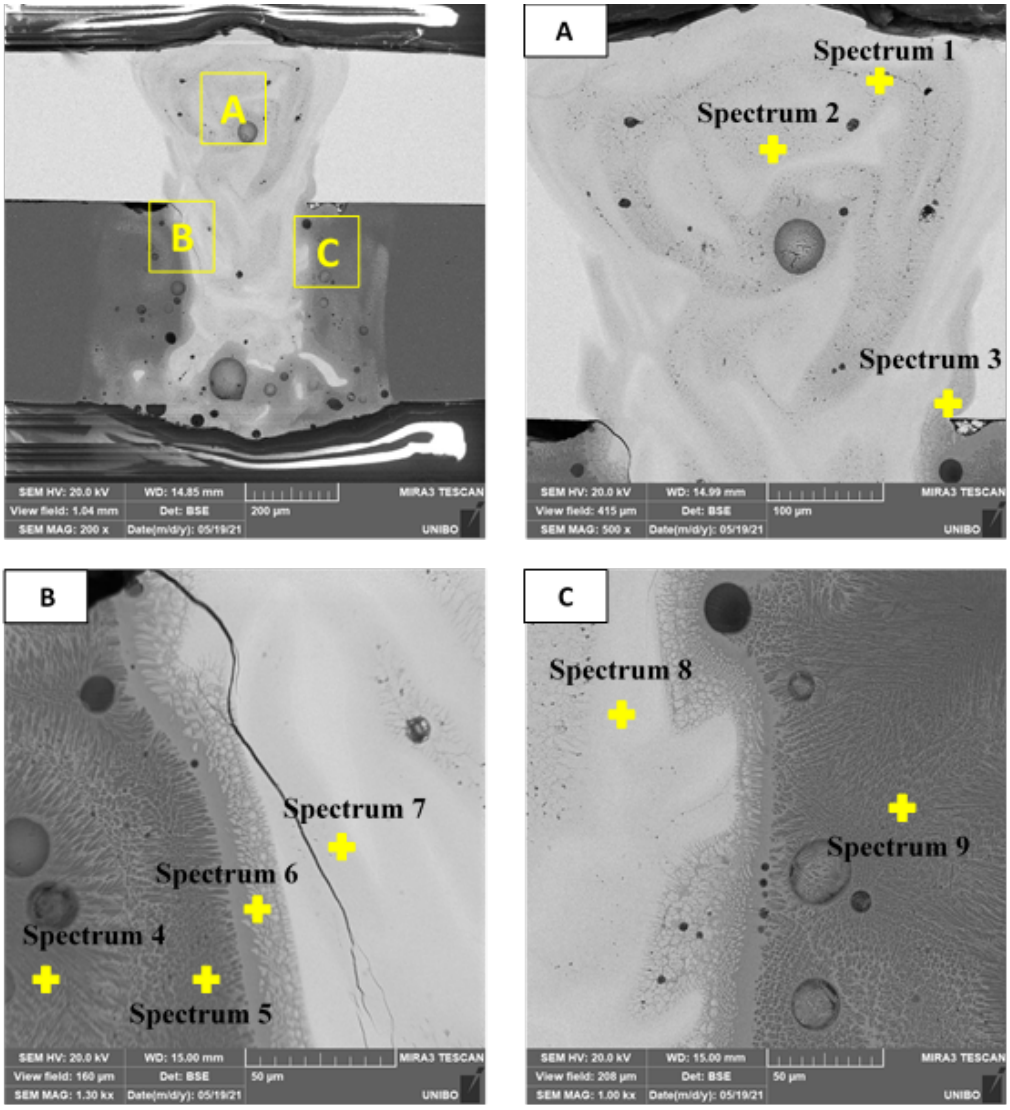

Figure 51:SEM images of sample F1.

Spectrum	Al (at%)	Cu (at%)	O(at%)	Possible Phase
1	52.05	47.25	0.71	η (AlCu)
2	47.63	51.08	1.30	η (AlCu)
3	56.74	41.47	1.8	Θ(Al_2Cu)
4	91.46	4.29	4.25	Al-Cu eutectic
5	91.52	3.68	4.8	Al-Cu eutectic
6	68.06	31.47	0.48	Θ(Al_2Cu)
7	37.03	62.8	0.18	ζ(Al_3Cu_4)
8	46.04	53.79	0.17	η (AlCu)
9	93.28	4.03	2.69	Al-Cu eutectic

Table 15:Chemical composition of denoted zones in figure 51.

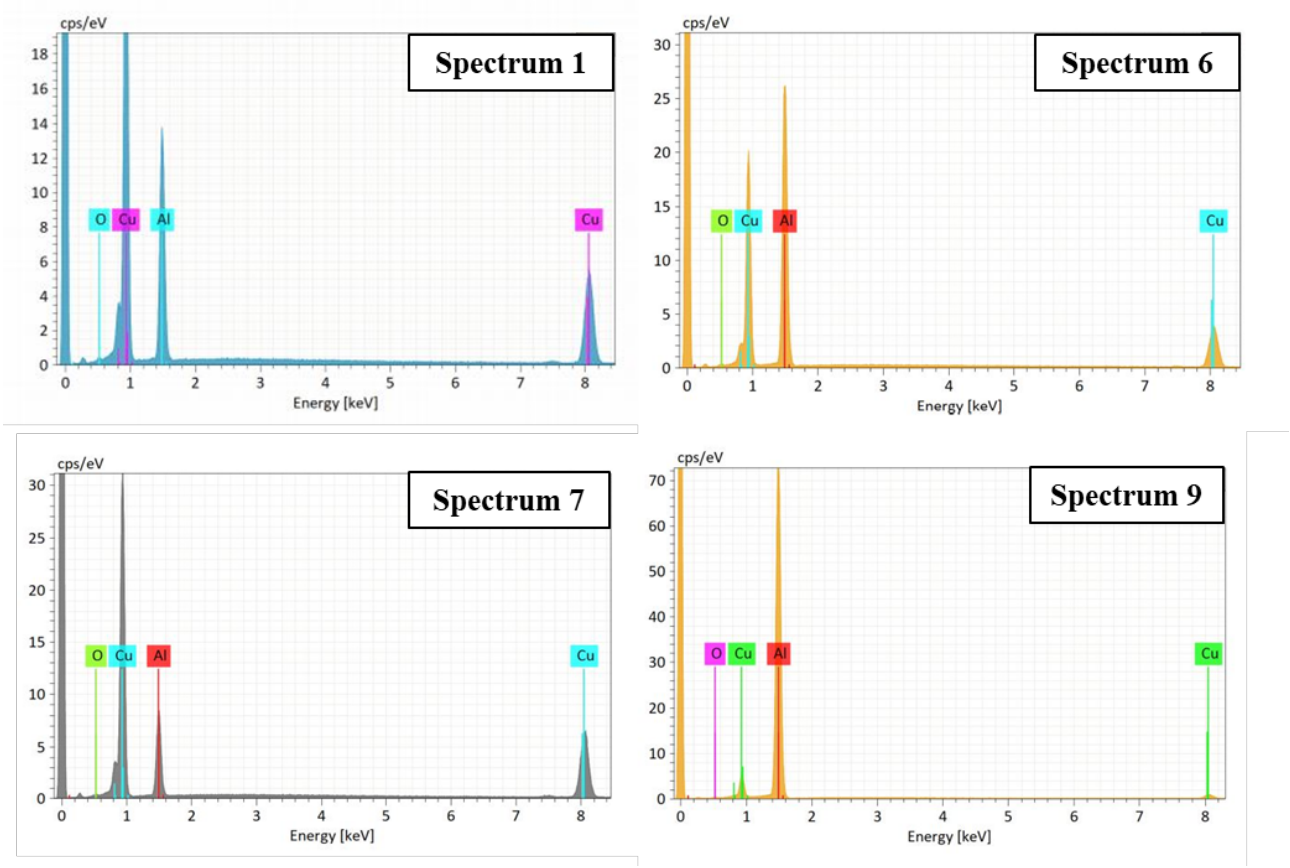

Figure 52:EDS spectra of marked points in figure 51.

4.2.6. Conclusions

The effect of different focal lengths which allows to obtain different spot diameter during continuous laser welding of copper and aluminum thin sheets has been studied. For each focal length, laser power and welding speed have been varied and the results were characterized by mean of metallographic analysis, mechanical and electrical tests and SEM-EDS analysis was conducted in order to obtain qualitative information on chemical composition of intermetallic compounds formed after the solidification. The main conclusions are:

- The high reflectivity to the near-infrared wavelength and the high melting temperature of the copper base material mean high laser power using a larger spot diameter. With this hardware configuration, a proper choice of welding parameters was difficult to obtain due to the fact that the weld bead quickly shifts from a no-welding condition to full penetration with the presence of cracks and pores.
- A smaller laser spot allows joining with lower overall power, thus reducing the total heat input during the process. It also favored a wider process window with better control of penetration depth and mixing of the base materials.
- Mechanical properties in terms of maximum breaking load are strictly related to the energy density supplied and the weld bead dimension (interface width and penetration depth). The optimum energy density was around 0,5-0,6 MJ/mm^2, achieving tensile loads of roughly 800 N with the larger spot and 700 N with the smaller one. Brittle fracture behavior was recorded with the large spot size, while ductile behavior was recorded with the smaller one. Despite the lower maximum breaking load obtained with the smaller spot diameter, a double weld seam could be a valid solution to enhance the mechanical properties by optimizing also the dilution between the materials of the single weld bead.
- Electrical properties, in terms of contact resistance, are strong influenced by the weld bead morphology; the best performances are achieved when full penetration was avoided. The measured values, obtained with optimized parameters, were about 42 μΩ with smaller spot and 40.5 μΩ with larger one. Highest mechanical strength and lowest contact resistance were achieved with the same process parameters probably due to the fact that the higher the energy input, the higher the penetration depth with consequent formation of hard and brittle intermetallic compounds.
- SEM-EDS analysis revealed how a small spot diameter minimized the formation of copper-rich intermetallic compounds, with 50-60 at. % of copper, which are detrimental to weld bead properties.

4.3. Characterization of dissimilar laser welding process in multilayer configuration

In this paragraph the joining process of thin copper and aluminum sheet in multilayer configuration was investigated. The need to combine multiple layers arises from the request to obtain more compact battery modules that guarantee excellent performance, especially as regards electric vehicles in which hundreds or even thousands of cells are connected to each other; in fact, the connection between two cells can be of different types, in particular in series or in parallel. With the first there is an increase in voltage while with the second there is an increase in capacity, by considering the single cell which has its own voltage and capacity. Starting from these, it is possible to calculate the characteristics in terms of voltage or total capacity and therefore from the performance of the complete battery pack. According to this, the possibility of joining four layers of copper and aluminum to create, with a single weld bead, a parallel connection (between the two similar layers) and subsequently a series between the four laminations has been studied. The setup used is the same in the previous paragraph, but in this case a circular oscillation of the beam has been investigated in order to increase the size of the section area where the current passes. The results were characterized by means of metallographic analysis, mechanical and electrical test and finally SEM-EDS analysis was conducted to obtain information of dilution between the base materials and the chemical composition of intermetallic compounds formed.

4.3.1. Materials and methods

The welding experiments were carried out in a lap-joint configuration utilizing pure copper (0.35 mm thick, 45 mm wide and 60 mm length) with a thin-layer of electroplated nickel (2.5 μm) and pure aluminum EN-AW 1050 (0.45 mm thick, 45 mm wide and 60 mm length). As anticipated before, the configuration was composed of two copper sheets and two aluminum sheets welded with an overlap of 10 mm, as depicted in Figure 53. Weld seams with a length of 40 mm were performed.

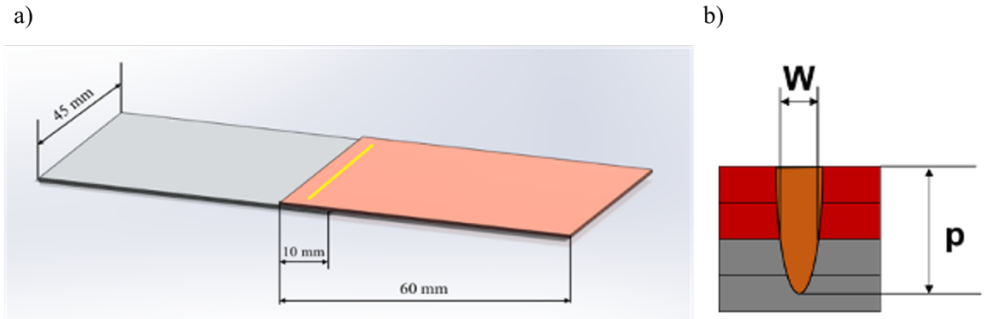

Figure 53: Weld specimen dimensions(a), weld bead characteristics(b)[80].

The welding setup was the same, shown in figure 34, used in the previous paragraph except that in this case only the small focal length was used on the basis of the results obtained previously.

Experimental activity was carried out in order to characterize the welding process with a spatial oscillation of the beam, implemented by programming the galvanometric scanning head achieving a laser path which is characterized by a super positioning of a circular path and a linear motion as shown in Figure 23. Preliminary studies were conducted with the aim to identify a feasibility process window; an experimental campaign was designed in which laser power, welding speed and wobbling amplitude were investigated. Starting from laser power and welding speed, other process parameters can be calculated as follow:

- Power density = $\frac{Laser\ Power}{Spot\ area}$ [MW/cm^2]
- Interaction time = $\frac{Spot\ diameter}{Welding\ speed}$ [s]
- Energy density = Power density * Interaction time [MJ/cm^2]

For each set of parameters, welds of 40 mm of length were generated and replicated three times.

Laser Power [W]	800 - 1000 - 1200
Welding Speed [mm/s]	60 - 80 - 100
Power density [MW/cm^2]	22.03-24.78-27.54
Energy density [MJ/cm^2]	0.015÷0.0312
Wobbling amplitude [mm]	0.2 - 0.4
Scanning frequency [Hz]	500

Table 16: Welding parameter for the multilayer configuration.

The analysis methods are the same as previously indicated, therefore they will not be resumed. A small note on the tensile tests; also in this case, non-standardized tests were carried out to qualitatively evaluate the mechanical properties of the joint on specimens with real dimensions. In particular, the test was performed by taking hold of the first and last layer in the grips as it is mandatory that all layers are welded together, as shown in Figure 54. The electrical resistance measurements, as for the tensile tests, were carried out between the first and last sheet on the same samples with the four-point method.

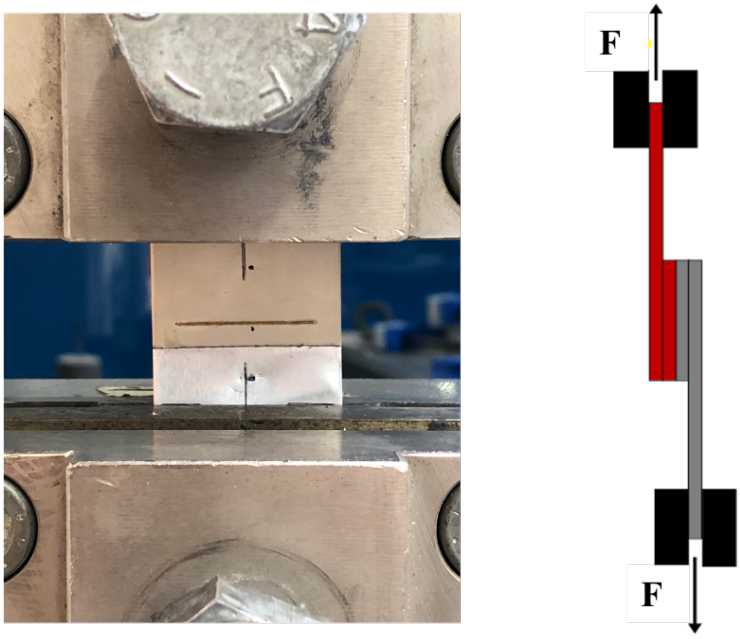

Figure 54: Tensile test specimen and setup.

4.3.2. Optical microscope results

Cross-section images of the typical results obtained are shown in Figure 55. Three conditions have been obtained, in particular: no welding condition which is not depicted, partial penetration condition (Figure 55 (column a)) and full penetration condition (Figure 55 (column b)). The no - welding configuration occurs when not all the layers are welded together; this is to be avoided since all the layers must be connected together to form an electrical connection. Partial penetration instead occurs when the weld bead includes all the layers but there is no breakthrough in the lower part of the last sheet or when there is a slight trace of welding in the latter. Otherwise, full penetration happens when all the layers are joined together but there is but there is excessive dripping in the lower part of the last sheet.

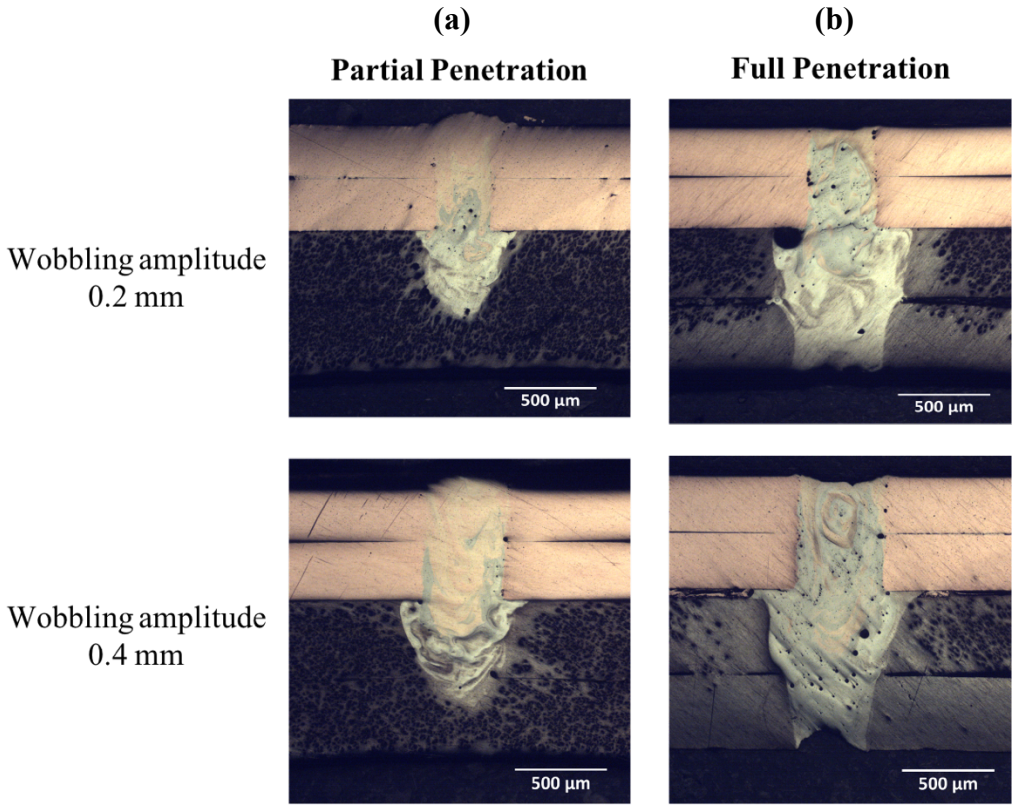

Figure 55: Cross-section of welded samples in multilayer configuration.

In Figure 56 the interface width measure of the samples welded with a wobbling amplitude of 0.2 mm is reported. As it can be seen, the value increases as the laser power increases as well for all the welding speed analyzed. With a fixed laser power, the higher interface with was measured with the lower welding speed since the heat input supplied during the process is higher. Values between 0.28 and 0.45 mm have been measured with all the laser parameters investigated.

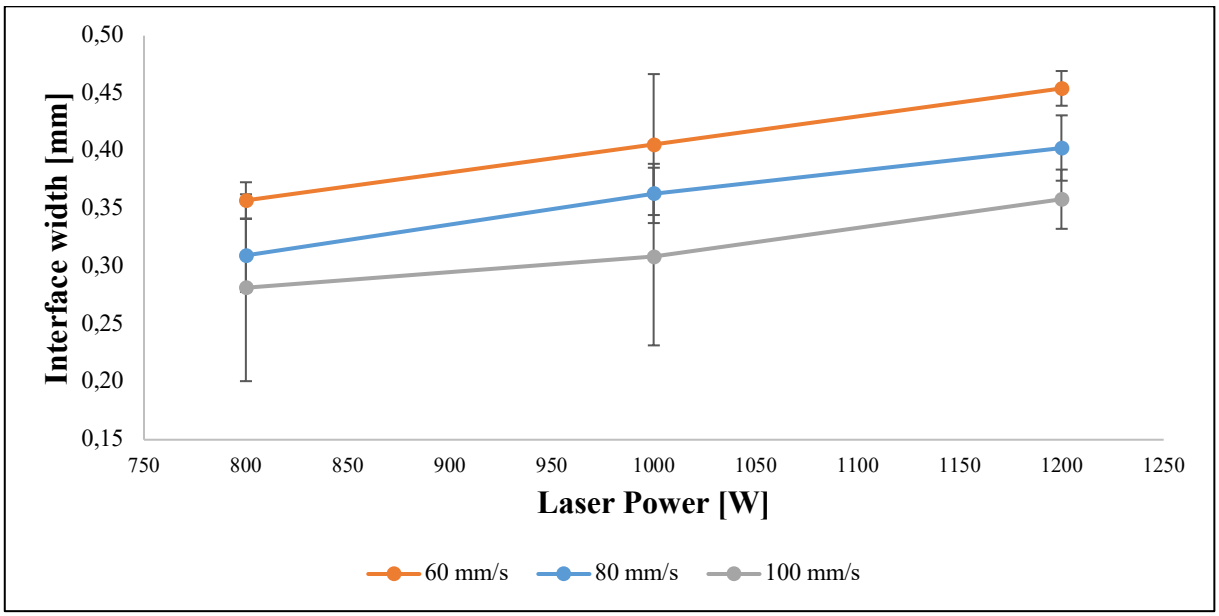

Figure 56: Interface width as a function of laser power and welding speed with wobbling amplitude of 0.2 mm.

Figure 57 shows the influence of laser power, welding speed and wobbling amplitude of 0.2 mm on the penetration depth. The welding depth increases as laser power increases as well, except at 60 mm/s in which full penetration was measured when laser power was 1000 and 1200 W. At a fixed laser power, higher welding speeds result in lower penetration depth, since the interaction time of the beam during the process is reduced the heat input namely the energy density is not sufficient to permeate into the last sheet. It is noted that a partial penetration, with values between 1.3÷1.4 mm, that includes all the layers has been obtained with few parameters

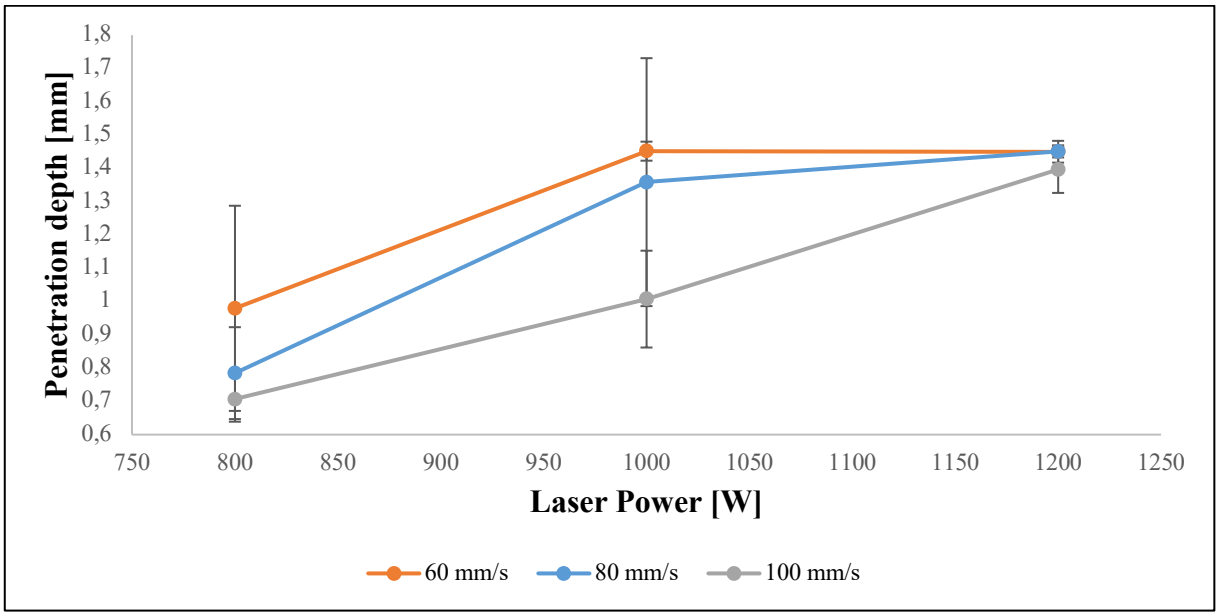

Figure 57: Penetration depth as a function of laser power and welding speed with wobbling amplitude of 0.2 mm.

The same conclusions can be made with a wobbling width of 0.4 mm for both geometric characteristics of the weld bead, reported in Figure 58 and Figure **59**gure 59; a greater wobbling amplitude, allows to obtain a connection with a width at the interface greater than in the previous case since the laser beam scans a greater area, in fact values of about 0.35÷0.5 mm were measured. Concerning the penetration depth, with the same laser parameters, the penetration depth decreases as the wobbling amplitude increases; due to the larger scanning path that laser beam has to perform the heat cannot concentrate deeply.

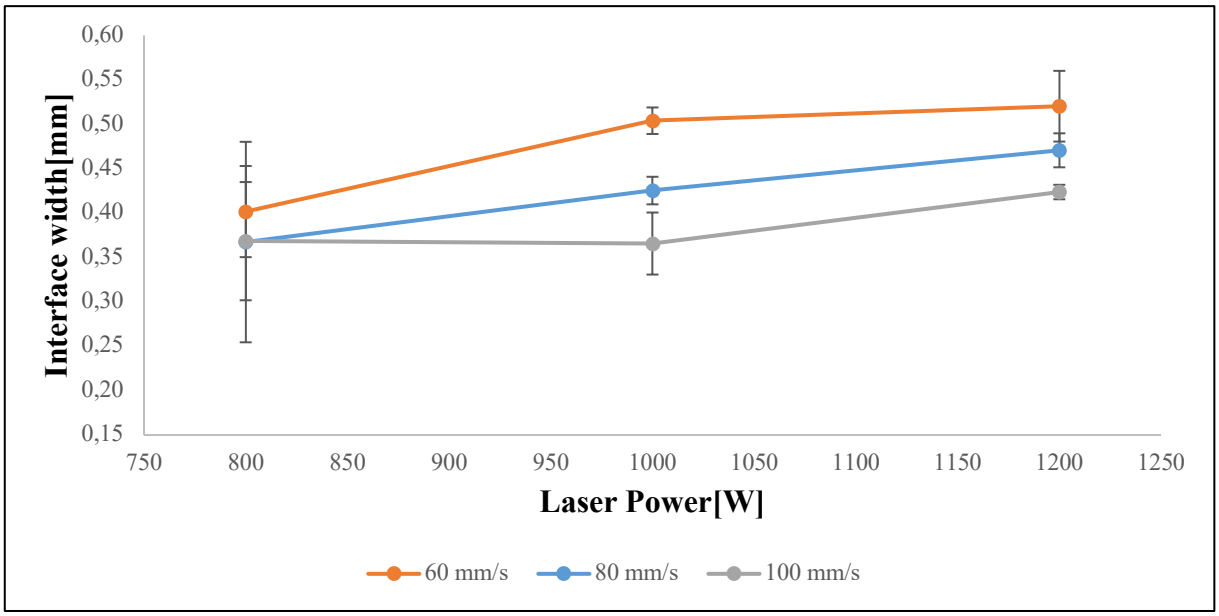

Figure 58: Interface width as a function of laser power and welding speed with wobbling amplitude of 0.4 mm.

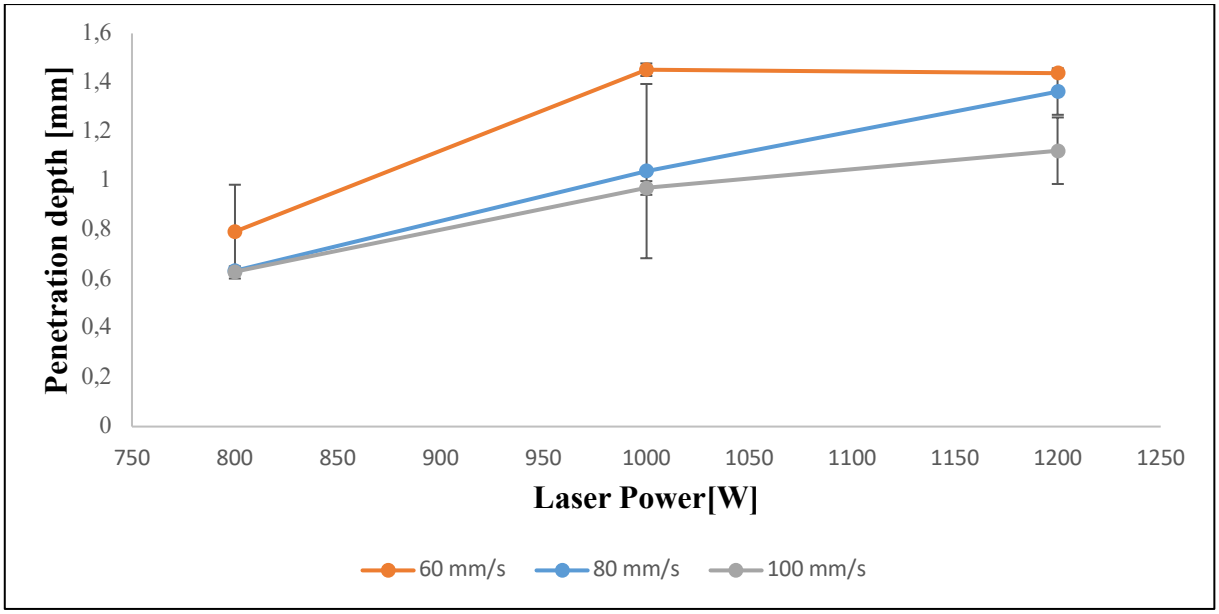

Figure 59: Penetration depth as a function of laser power and welding speed with wobbling amplitude of 0.4 mm.

Considering these results, it was possible to create a process feasibility window for both investigated amplitudes. At oscillation amplitude of 0.2 mm, no welding condition was obtained with a laser power of 800 W and for all investigated welding speeds; the heat input supplied during the process and transferred from the laser beam to the material was not sufficient to melt all the layers. Given the high reflectivity of the copper and high melting point a minimum in term of energy density (Power Density*Interaction time) is required in order to melt the material and achieve a penetration in the lower sheets. On the other hand, at 60 mm/s with 1000 and 1200 W the heat input was to excessive and consequently full penetration occurs; to this, a high mixing of materials is added and, due to the instability of the keyhole, there is also formation of porosity inside the joint. A correct setting of parameters allowed to obtain weld seam with partial penetration, limited mixing and reduced presence of porosity; with laser power of 1000 W and welding speed of 80 and 1000 mm/s weld seams with good morphology have been obtained. When oscillation amplitude increases to 0.4 mm, the same considerations made previously remain almost valid. As the laser path is increased, more energy is needed to join the sheets, and therefore with laser power of 1000 W and welding speed of 100 mm/s no weld occurred, while laser power of 1200 W and welding speed of 80 mm/s do not cause excessive material's dripping.

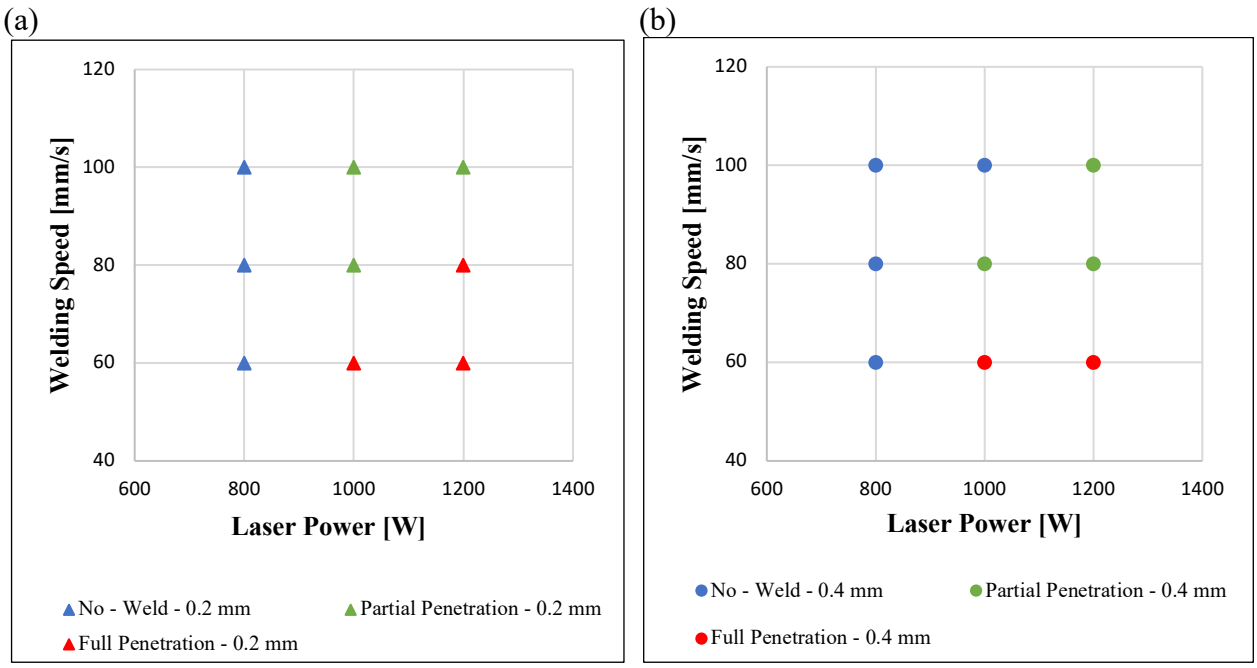

Figure 60: Feasibility process window in terms of laser power and welding speed for both the wobbling amplitudes; 0.2 mm(a) and 0.4 mm(b).

4.3.3. Shear tensile test results

In Table 17 test parameters used for the mechanical strength evaluation are summarized. Not all conditions have been investigated, both because with the metallographic analysis it was possible to choose the weld seam that present better morphology and to reduce the number of experiments. Each condition was repeated three times and the mean value was calculated.

Sample	Laser Power [W]	Welding speed [mm/s]	Energy density [MJ/cm^2]	Wobbling Amplitude [mm]	Number of repetitions
1	1000	80	0.0234	0.2	3
2	1000	60	0.0312	0.2	3
3	1200	100	0.0225	0.2	3
4	1200	80	0.0281	0.4	3
5	1200	100	0.0225	0.4	3

Table 17: Welding configurations used for tensile tests in multilayer configuration.

In Figure 61 (a) maximum breaking load as a function of energy density are shown. For both wobbling amplitudes, as the energy density increases the maximum breaking load decreases with a rather linear trend. The highest mechanical strengths were obtained with scanning amplitude of 0.2 mm; in particular, with an energy density of 0.0225 MJ/cm^2 value of 1010 N was measured. With these process parameters, the ductile break was recorded at the base aluminum in an area far from the seam, as shown in Figure 61 (b). By increasing the energy density up to 0.0312 MJ/cm^2 the mechanical properties are reduced, obtaining values of about 900 N with poor repeatability between the tests (high Std. dev.). A similar trend was recorded when scanning amplitude was set at 0.4 mm; it can be noted that, despite the samples had higher width at interface the mechanical strength was lower, with breaking loads of about 100 N less than in the previous case. This could be due to the fact that the greater the area the beam has to scan, the greater the powers required to melt the material with consequent formation of thermal cycles that favor the appearance of hard and brittle intermetallic phases; this is confirmed by the fact that the break, of a fragile type in this case, occurred at the weld seam.

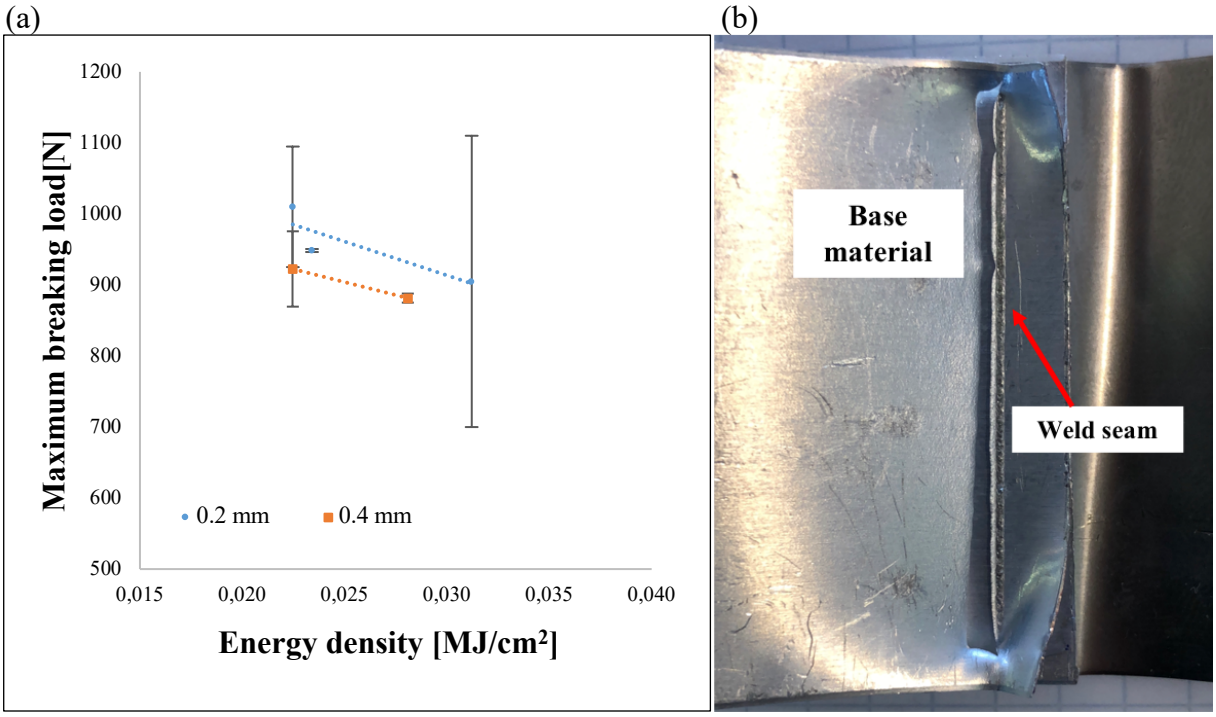

Figure 61: Tensile test results (a), failure with the optimized parameters(b)[80].

4.3.4. Electrical contact resistance results

Concerning the electrical contact resistance results, the measurements are summarized in Figure 62. As it can be noted, different trends were obtained for the two wobbling amplitudes. Values of about 43 μΩ have been measured at higher energy density investigated when the scanning amplitude was set to 0.2 mm; a reduction of heat input allows to a reduced penetration depth and consequently a smaller section useful for the current flow. On the other hand, values of about 45 μΩ were measured with wobbling amplitude of 0.4; the greater the path that the laser has to make the greater the power needed to obtain a joint that includes all the layers. The laser powers involved, and the thermal cycles promote the formation of hard and brittle intermetallic compounds. The results confirm that a higher mixing of the base metals leads to joints with lower mechanical and electrical properties due to the formation of hard and brittle IMC**[81]**. Increasing the wobbling amplitude does not seem to reduce the contact resistance, on the contrary, slightly higher values are obtained. It is important to note that thermal power dissipated in an electrical circuit is proportional to resistance and to the square of the current; since there are hundreds of contacts in an automotive battery pack, even a small reduction in resistance results in less heat losses due to Joule effect.

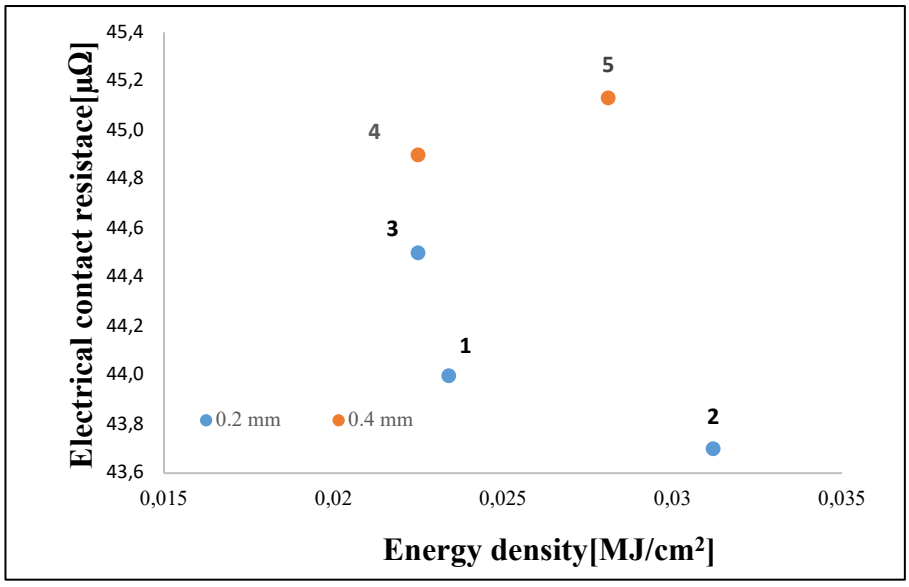

Figure 62: Electrical contact resistance results in multilayer configuration.

4.3.5. SEM-EDS analysis

To investigate the metal mixing and intermetallic compounds formed after the welding SEM-EDS analysis were conducted. Starting from the EDS spectra, information was obtained on the quantities of copper and aluminum within the layers from which the possible phases that were formed were obtained. The pictures concerning the sample welded with laser power of 1000 W, welding speed of 60 mm/s and wobbling amplitude of 0.2 mm are shown in Figure 63. The scanning images shows two distinctive regions. The EDS shows that on the upper part, spectrum 3, of the weld seam is mainly composed of copper in solid solution (see Table 18). Near the center of the weld bead the energy supplied during the process melt the copper which diffuses into the aluminum sheet. The EDS analysis shows a mixing at the interface zone between the copper and aluminum sheet; an occurrence of Θ(Al_2Cu) phase with the shape of serrated dendrites can be detected; due to the lower formation energy the Θ phase are difficult to avoid during the solidification. In the lower part of weld seam, Figure 63(b), the copper content never exceeds the 10 at% resulting in the detection of aluminum in solid solution with vermicular shape. All these phases are not detrimental intermetallic phases, also analyzing the failure mode of the sample. This region is mainly Al rich, which indicates metallurgical bonding based on the eutectic reaction. The diffusion in this region is mainly due to the heat conducted from highly intermixed zone. In the limited diffusion zone, formation of detrimental intermetallic phases is minimum or avoided.

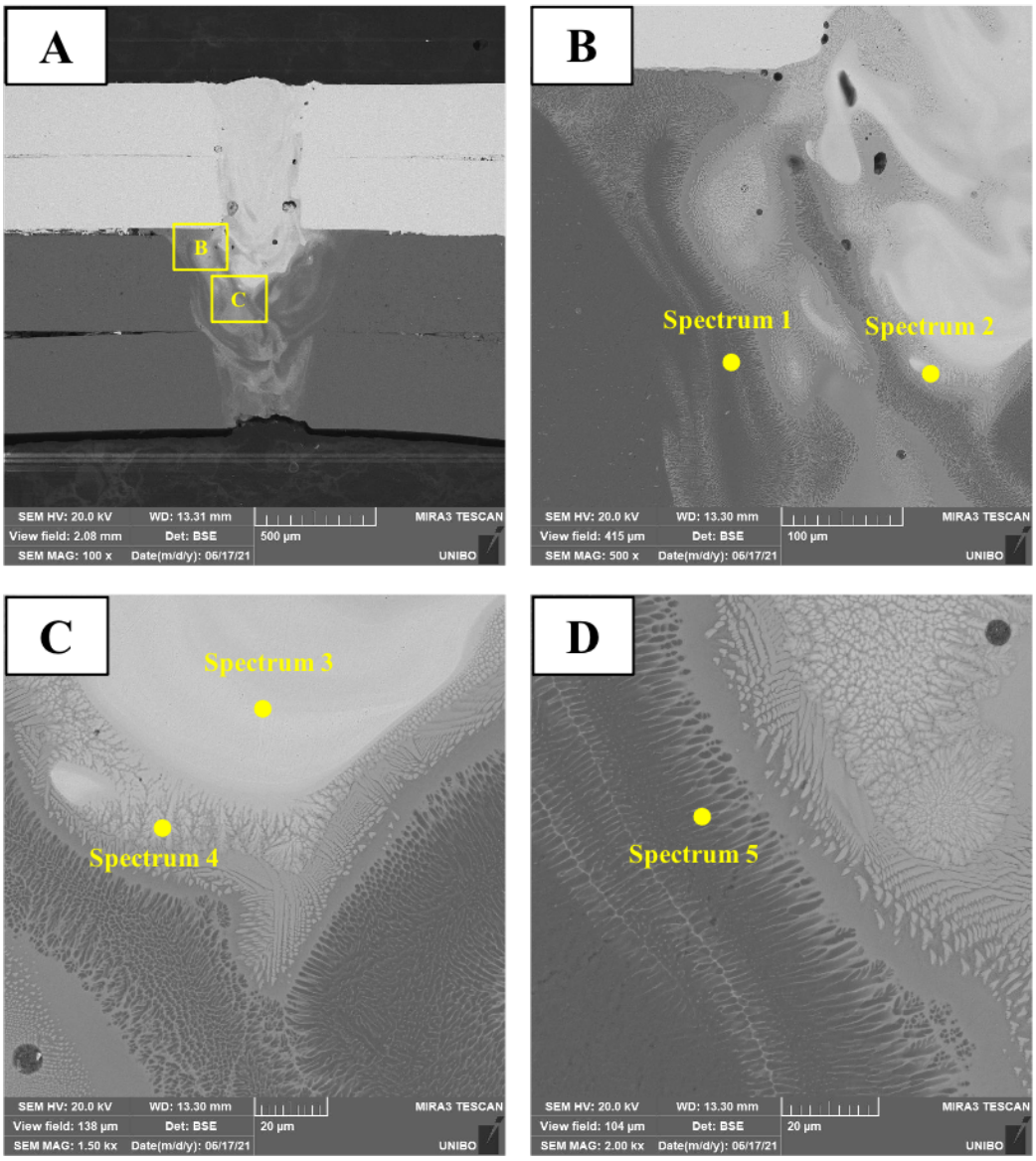

Figure 63: Scanning electron microscope image of the sample welded with power 1000 W, welding speed of 60 mm/s and wobbling amplitude of 0.2 mm.

Zone	O (at. %)	Al (at. %)	Cu (at. %)	Possible Phase
Spectrum 1	4.30	94.80	0.89	Al solid solution
Spectrum 2	0.55	58.45	41	$\Theta(Al_2Cu)$
Spectrum 3	0.01	17.43	82.56	Cu solid solution
Spectrum 4	1.18	59.21	39.60	$\Theta(Al_2Cu)$
Spectrum 5	1.85	89.92	8.23	Al solid solution

Table 18:Chemical composition of denoted zones in figure 63.

In order to understand how the mixing of Al and Cu occurs along the weld bead, EDS scan line is performed alongside the sheets as shown in Figure 64(b). The result of the line scan is plotted in Figure 64(b) with the distance in x-axis and the normalized intensity count element in y-axis. The results show that the upper part of the weld seam is mainly composed of copper in solid solution,

while at the interface zone between the second copper and first aluminum sheet dilution occurs between materials with consequent formation of intermetallic compounds.

(a) (b)

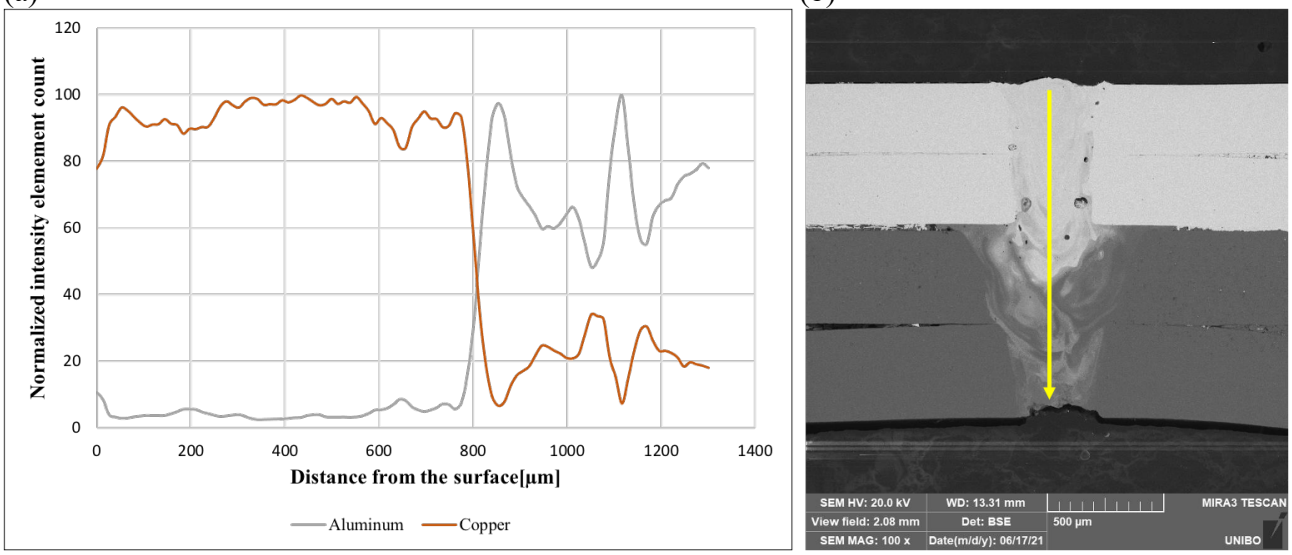

Figure 64: EDS scan line of the sample welded with wobbling amplitude of 0.2mm.

When wobbling amplitude was set to 0.4 mm, higher laser powers are requested in order to have a reliable weld seam which allows to join the four layers. As a result, the mixing is more pronounced, and more aluminum can be found in the upper part of the weld bead; according to this η (AlCu) phase in the form of columnar grain can be detected. The presence of the η phase was also recorded in areas far from the center of the weld bead, see spectrum 2, probably due to the fact that when the circular oscillation of the beam is applied, where there is an inversion of the motion (i.e. at the ends of the trace), the speed is low and of consequently the energy supplied (according to the relation E = P / v) is greater in those points. Even in this welding configuration, a higher dilution between base materials occurred at the transition area between copper and aluminum. Analyzing the chemical composition of the spectra in Figure 65(d) Θ(Al_2Cu) phases occurred; it can be noted that the thickness of the intermetallic compounds layer is larger than the one observed in the previous case. It can be concluded that both mechanical and electrical properties are influenced primary by the chemical composition of the intermetallic compounds but also by the thickness of the latter which is difficult to measure.

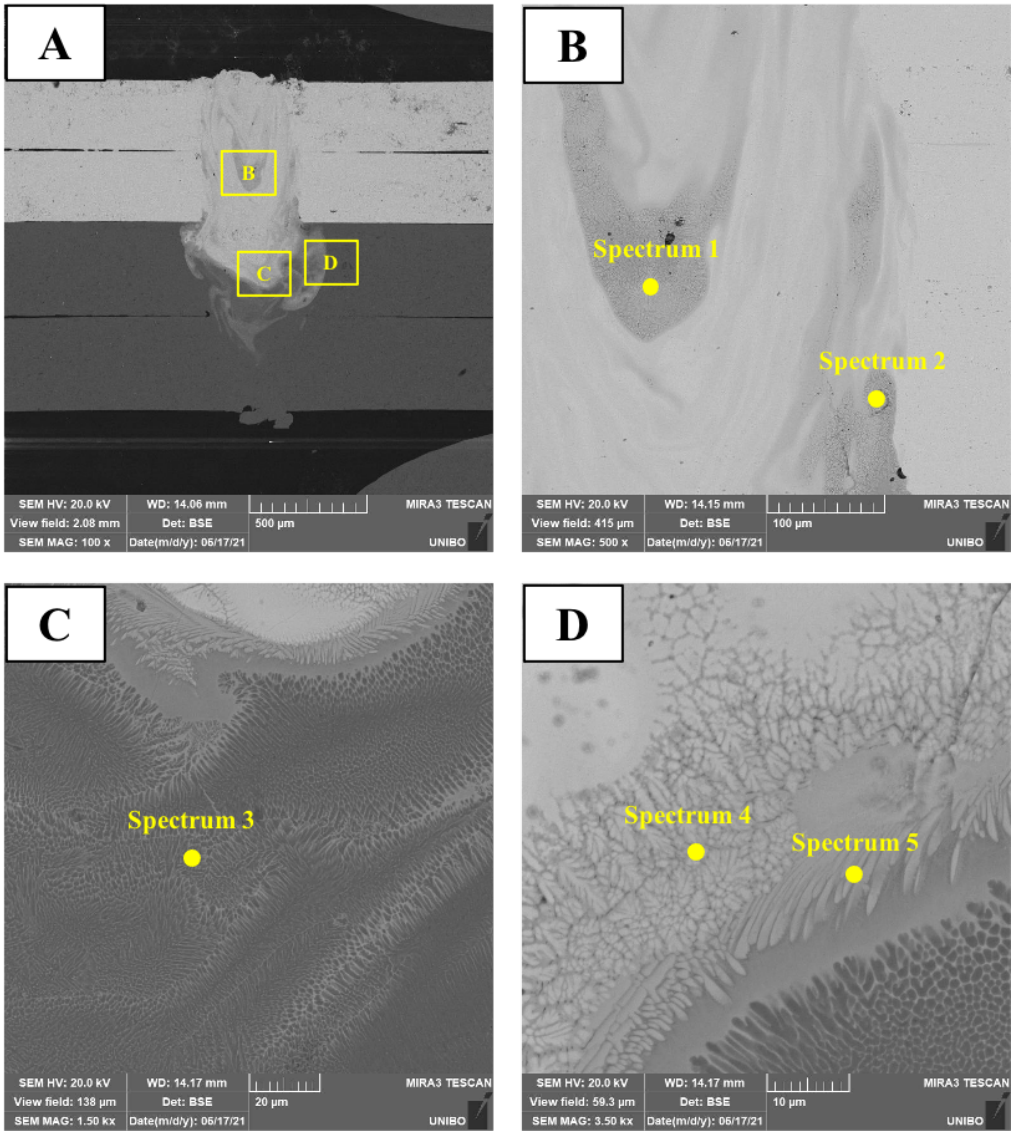

Figure 65:Scanning electron microscope images of the sample welded with power of 1200W, welding speed of 100 mm/s and wobbling amplitude of 0.4 mm.

Zone	O (at. %)	Al (at. %)	Cu (at. %)	Possible Phase
Spectrum 1	0.01	53.9	46.09	η (AlCu)
Spectrum 2	2.56	44.23	53.21	η (AlCu)
Spectrum 3	2.89	93.40	3.71	Al
Spectrum 4	0.46	60	39.54	$\Theta(Al_2Cu)$
Spectrum 5	0.2	78.6	21.2	Al+ $\Theta(Al_2Cu)$

Table 19: Chemical composition of denoted zones in figure 64.

EDS scan line of the sample welded with wobbling amplitude of 0.4 mm is shown in Figure 66. In particular, as can be seen by analysing the curve, the mixing takes place already after 400 µm (i.e. after the first copper sheet) with a strong dilution between the materials which results in formation of intermetallic compounds detrimental for the mechanical and electrical properties of the connections.

(a)

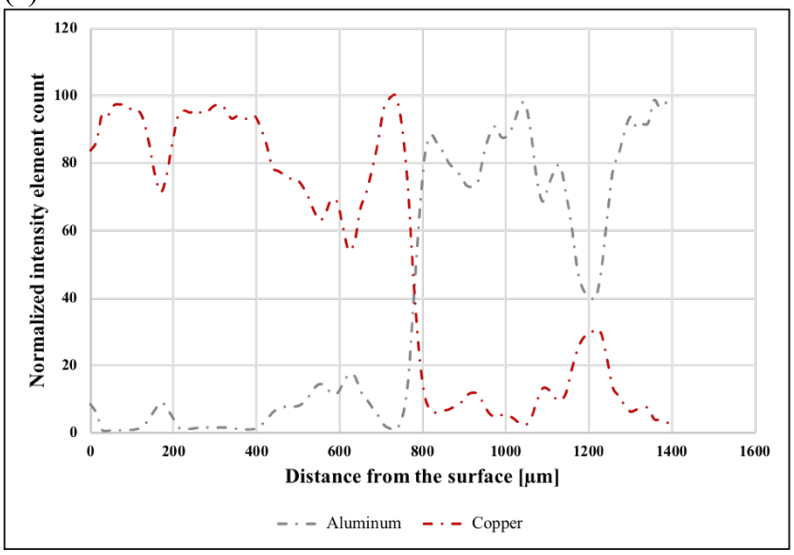

(b)

Figure 66: EDS scan line of the sample welded with wobbling amplitude of 0.4 mm.

4.3.6. Conclusions

The possibility of joining several layers of thin copper and aluminum sheet in dissimilar configuration by means of circular beam oscillation has been investigated in this paragraph. The conclusions of this study can be summarized as follow:

- The process is feasible, very important is the placement of the materials; in fact, the copper, thanks to its higher density and the reduced thermal expansion coefficient, sinks into the aluminum layers obtaining a joint with a regular shape that includes all the layers without the presence of defects (such as transversal cracks).
- A process windows, for each wobbling amplitude investigated, has been developed in terms of laser power and welding speed. Although a larger wobbling amplitude allows to obtain beads with a slightly greater width at the interface, this does not guarantee better properties of the connections. The best performance has been achieved with an oscillation amplitude of 0.2 mm, a power of 1000 W and a speed of 60 which allow to obtain a weld bead with full penetration without excessive dripping of material at the bottom; contrary to what has been seen in the other cases, for the analyzed configuration it is necessary that there is full penetration otherwise there is separation of the last sheet.
- Mechanical properties in terms of maximum breaking loads decreased as the energy density increases for both the wobbling amplitudes investigated. A maximum breaking load of 1000 N has been recorded with a failure of ductile type at the base material with optimized parameters.
- Electrical contact resistance depends both on the morphology of the weld bead but also on the mixing of materials with values of about 43 and 45 μΩ. Despite a larger size of the weld seams, obtained with 0.4 mm, the electrical resistance is greater probably due to the presence of hard and brittle intermetallic compounds which are also characterized by lower electrical conductivity.
- SEM-EDS analysis confirmed what was previously found, namely that the joint with greater wobbling amplitude have hard and brittle intermetallic compounds, with a copper content of 50 at. %, along the weld bead while with 0.2 mm the mixing is concentrated at the copper and aluminum sheets interface only.

4.4. Dissimilar laser welding process of tab-tab-busbar configuration

After having analyzed and investigated the welding between the electrodes of the cells (tabs), the last welding configuration required during the production of a battery module was studied, i.e. the one concerning the cell tabs and a busbar. During the manufacturing of battery pack terminals of each cell are connected with busbar, which act as current collector, to create an electrical circuit of series and parallel connections leading to desired voltage level of the module; moreover, from this busbar it is possible to obtain various data such as temperature and voltage, through connections to control boards, which allow the correct operation of the entire battery. The results were characterized with the methodologies already seen previously as well as the same setup developed for the previous welding configurations was used. With this configuration, which is the most used in a real case, the effect of thermal aging due to the current transmission was studied. After monitoring a series of parameters, destructive tests and SEM-EDS analyzes were carried out to obtain information on the properties after the aging.

4.4.1. Materials and methods

The materials tested were pure copper (0.4 mm thick, 30 mm wide and 20 mm length) with a thin layer of electroplated nickel (2.5 μm), pure aluminum EN-AW 1050 (0.4 mm thick, 30 mm wide and 20 mm length) while as a busbar pure aluminum EN-AW 1050 with a thickness of 1 mm (30 mm wide and 7 mm length) coated with a thin layer of nickel (5-15μm) welded in lap-joint configuration with an overlap of 5 mm. Weld seams with a length of 28 mm were performed (figure 67(c)). Both the configurations were investigated, the one with the aluminum as upper material and that with the copper as upper material as reported in Figure 67.

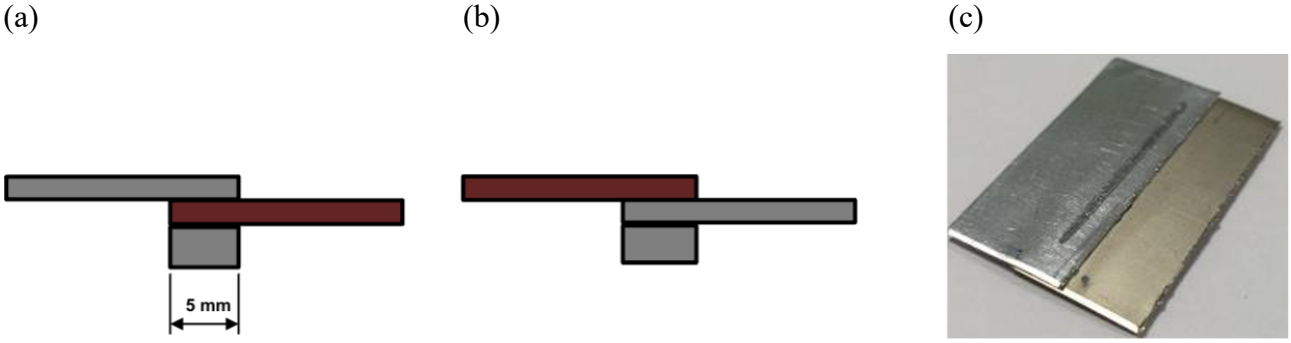

Figure 67: Welding configuration for tab-tab-busbar(a,b), example of welded sample(c).

The welding setup was the same, shown in Figure 34, used in the previous paragraph Experimental activity was carried out in order to characterize the welding process with a spatial oscillation of the beam, implemented by programming the galvanometric scanning head achieving a laser path which

is characterized by a super positioning of a circular path and a linear motion as shown in Figure 23. For each configuration, the effect of laser power, welding speed and wobbling amplitude has been investigated; the experimental plan was reported in Table 20.

Configuration	Laser Power [W]	Welding speed [mm/s]	Wobbling amplitude [mm]	Frequency [Hz]	Power density [MW/cm^2]	Energy density [MJ/cm^2]
Al-Cu Busbar	600-700-800	40-50-60	0.2-0.5	250	16.5-19.2-22	0.018÷0.037
Cu-Al Busbar	650-750-850	40-50-60	0.3-0.5	250	17.9-20.6-23.4	0.020÷0.04

Table 20: Welding parameters for tab-tab-configuration.

The analysis methods are the same as previously indicated, therefore they will not be resumed. A small note on the tensile tests; In particular, the test was performed by taking hold of the first and last layer in the grips as it is mandatory that all layers are welded together. The electrical resistance measurements, as for the tensile tests, were carried out between the first and last sheet on the same samples with the four-point method; for each weld seam three measures were conducted and the average value was calculated, as shown in Figure 68.

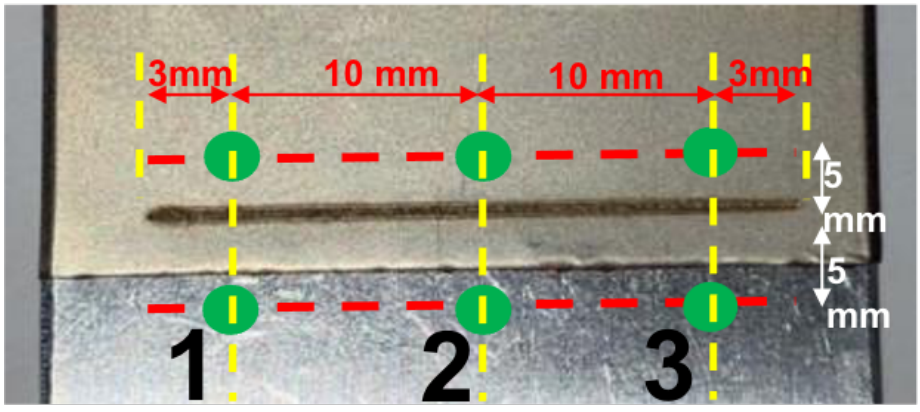

Figure 68: Electrical contact resistance measurement scheme.

4.4.2. Optical microscope results

Optical microscope cross-sections of samples welded at 60 mm/s with different laser power and wobbling amplitude are shown in Figure 69. Not all the sectional images obtained have been reported in order not to make the part relating to the results of the metallography very lengthy. From the analysis with the optical microscope it can be seen that, with a fixed oscillation amplitude, a slight increase in the laser power from 600 W to 800 W leads to an increase in particular in the depth of penetration passing from a light welding of the third layer to a complete breakthrough of the latter especially with 0.2 mm. Due to the fact that the smaller the wobbling amplitude, the greater the energy that is concentrated near the centre of the trace with a consequent increase in the depth of penetration. Indeed, when the width is 0.5mm, there is an increase in the width at the interface and a reduced penetration compared to the previous case due to the fact that, with the same process parameters, the laser beam must scan a larger area not thus managing to penetrate the third layer.

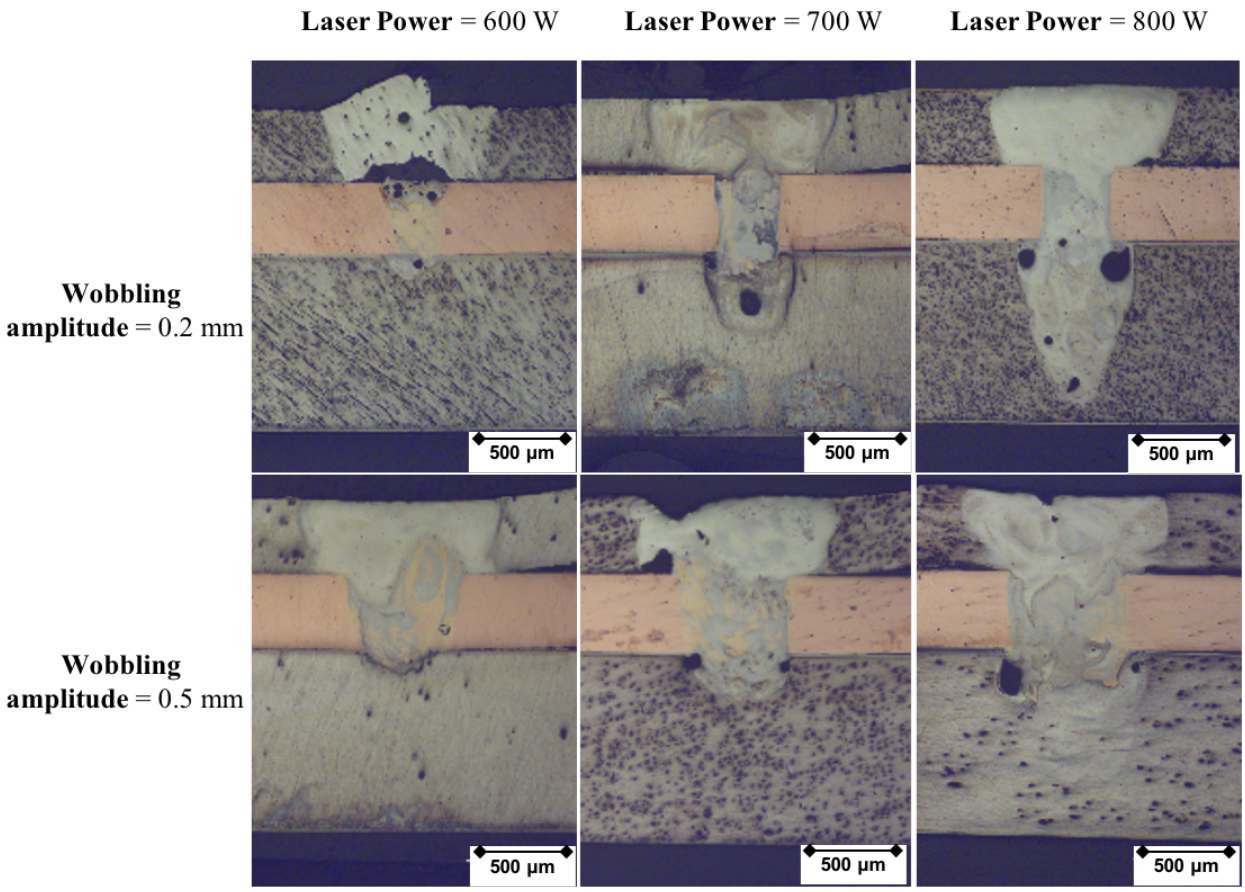

Figure 69: Cross-section images of welded samples at 60 mm/s in Al-Cu-Busbar configuration.

The optical microscope analysis made it possible to obtain information above all on the morphology of the bead, the characteristics of which are shown in Figure 70, obtained with the various parameters.

The attention was paid in particular to the parameters L_1, i.e. the width at the interface between the aluminum and copper laminations, as it guarantees the passage of current and the penetration depth P considered from the surface of the bead to its end which allows a correct connection between the tabs and the busbar.

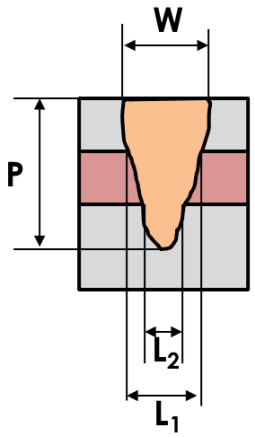

Weld seam morphology:

- Surface width **(W)**
- Interface width between first and second layer **(L_1)**
- Interface width between second and third layer **(L_2)**
- Penetration depth **(P)**

Figure 70: Weld seam characteristics of tab-tab-configuration.

Figure 71 shows the influence of welding parameters on interface width L_1 and penetration depth P. Considering the width at the interface, see Figure 71(a), it can be seen that it is little influenced both by the laser power used and by the welding speed; in fact, it remains almost constant as these last parameters vary. Unlike what happens with power and speed, an increase in the wobbling width results in an increase in the width of the bead for the reasons explained above, thus obtaining beads with a width of approximately 0.6 mm compared to 0.4 mm obtained with a smaller wobbling amplitude. As for the depth of penetration, on the other hand, the latter increases almost linearly as the laser power used increases as well for almost all conditions investigated. With a fixed laser power, a lower welding speed results in a higher penetration depth due to the higher energy density supplied during the process. Unlike what was noted before, an increase in the wobbling trace, with the same parameters, reduces the penetration depth as the laser beam, scanning a larger area, the energy supplied in not enough to penetrate the last layer.

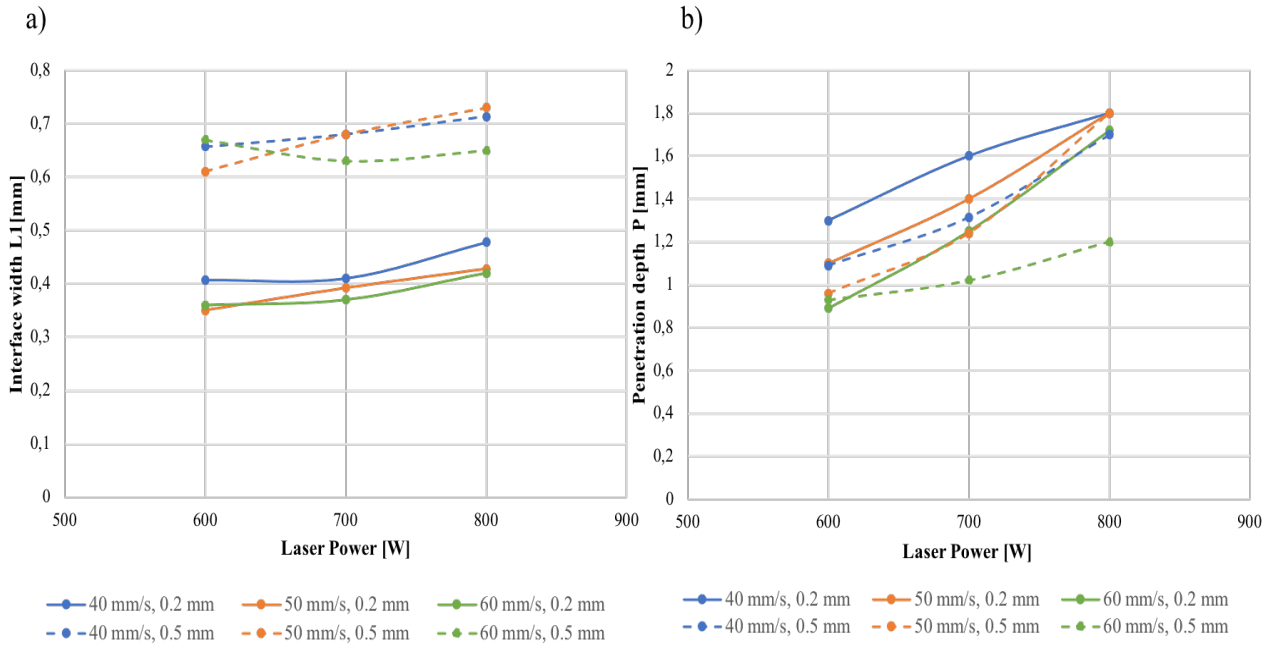

Figure 71: Interface width(a) and penetration depth (b) as a function of laser power, welding speed and wobbling amplitude for Al-Cu-Busbar welding configuration.

Considering these results, it was possible to create a process feasibility window, in Figure 72, for both investigated amplitudes, by considering the morphology of the weld seam; in fact, the condition required for the application is the one with a partial penetration in the third layer. For both oscillation amplitude, laser power of 800 W and for all welding speeds results in a full penetration weld bead and consequent formation of defects such as pores; the heat input supplied during the process and transferred from the laser beam to the material was too high to melt all the layers. An increase of wobbling amplitude results in an increase of laser power required to melt the layer which translates in high mixing between the materials in particular near the second layer and presence of defects. A correct setting of parameters allowed to obtain weld seam with partial penetration, limited mixing and reduced presence of porosity; with 0.2 mm, good results were obtained with a wide range of parameters, while with 0.4 mm the weld seam shifts from a no-weld to full penetration by slightly varying the parameters. A final observation regarding the results obtained with this configuration is the presence of transverse micro-cracks along the seam due and mainly due to the different physic and chemical properties of the materials. Aluminum has a high thermal expansion coefficient which leads to the formation of residual stresses during cooling and therefore cracks. Another reason is due to the severity of the thermal cycle that derives from the need to work with high energies as it is also necessary to melt the third layer.

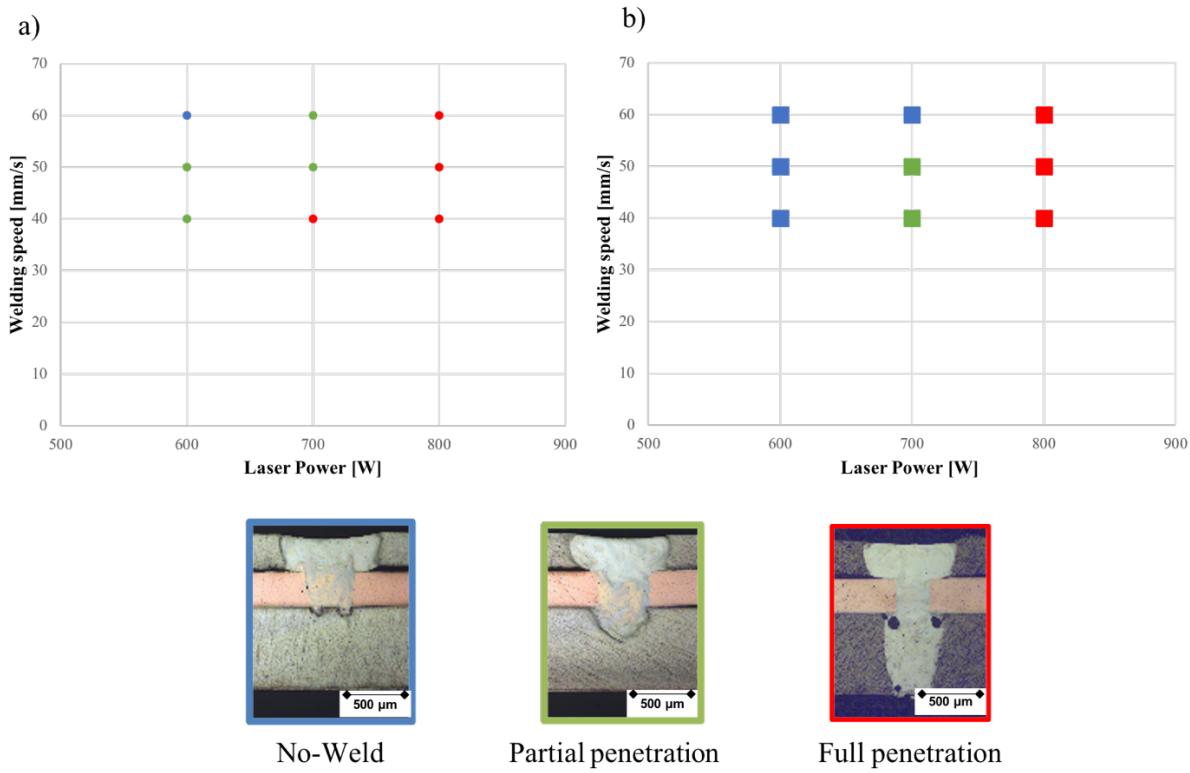

Figure 72: Feasibility process window for Al-Cu-Busbar with wobbling amplitude of 0.2 mm(a) and 0.5 mm(b).

Optical microscope cross-sections of samples welded at 60 mm/s with different laser power and wobbling amplitude for Cu-Al-Busbar configuration are shown in Figure 73. From the images it can be seen that, with a fixed oscillation amplitude, a slight increase in the laser power from 650 W to 850 W leads to an increase in particular in the depth of penetration passing from no welding of the third layer to a complete penetration of the latter especially with 0.3 mm. The same considerations made previously apply, as regards the penetrations and the morphology of the seam. When laser power of 850 W is applied, regardless the welding speed or wobbling amplitude, in the upper part of the weld seam there is a lot of aluminum made to flow upwards by turbulent motions and several presences of pores probably due to the instability of keyhole.

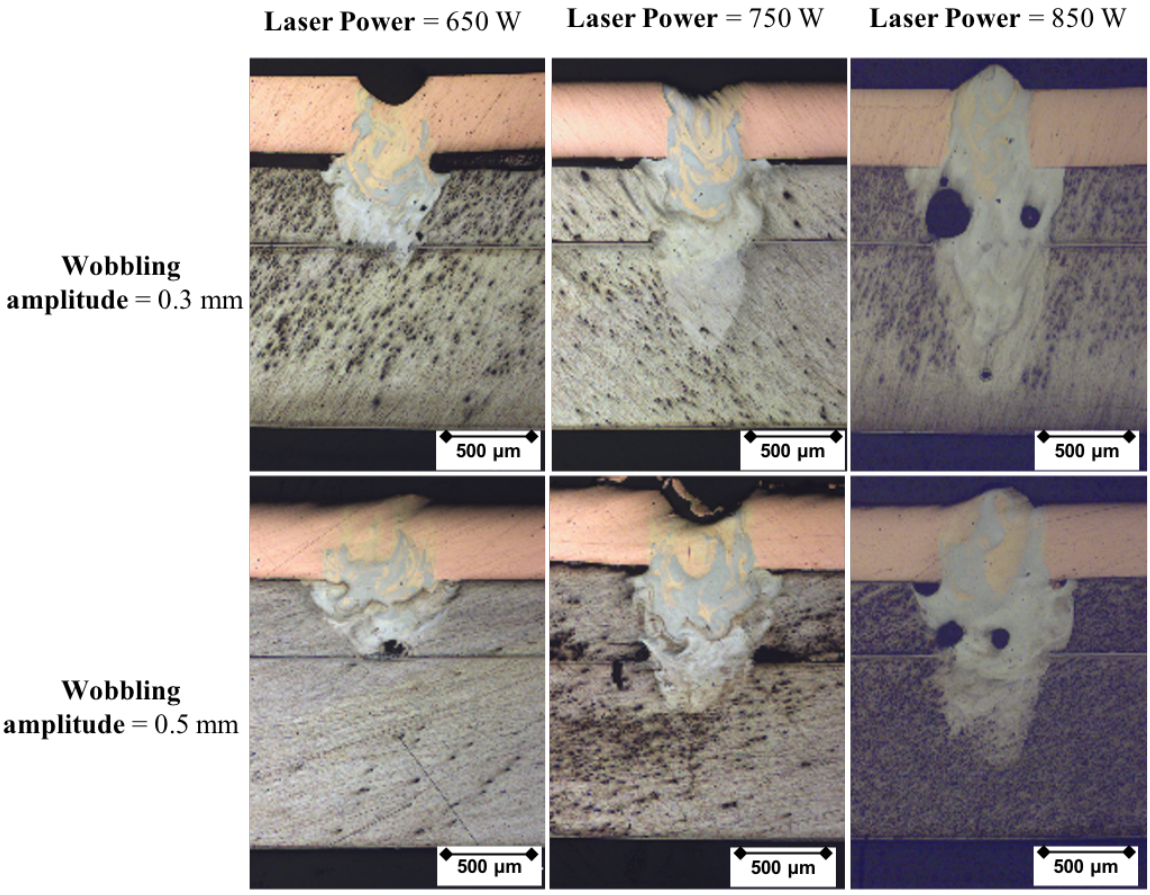

Figure 73:Cross-section images for welded sample at 60 mm/s in Cu-Al-Busbar configuration.

Figure 74 shows the influence of welding parameters on interface width L_1 and penetration depth P. Considering the width at the interface, see Figure 74(a), it can be seen that it is little influenced both by the laser power used and by the welding speed; in fact, it remains almost constant as these last parameters vary. Unlike what happens with power and speed, an increase in the wobbling width results in an increase in the width of the bead for the reasons explained above, thus obtaining beads with a width of approximately 0.6-0.7 mm compared to 0.4-0.5 mm obtained with a smaller wobbling amplitude. As for the depth of penetration, on the other hand, the latter increases almost linearly as the laser power used increases as well for almost all conditions investigated in particular with a wobbling amplitude of 0.3 mm. With a fixed laser power, a lower welding speed results in a higher penetration depth due to the higher energy density supplied during the process. An increase in the wobbling trace, with the same parameters, reduces the penetration depth as the laser beam, scanning a larger area, the energy supplied in not enough to penetrate the last layer.

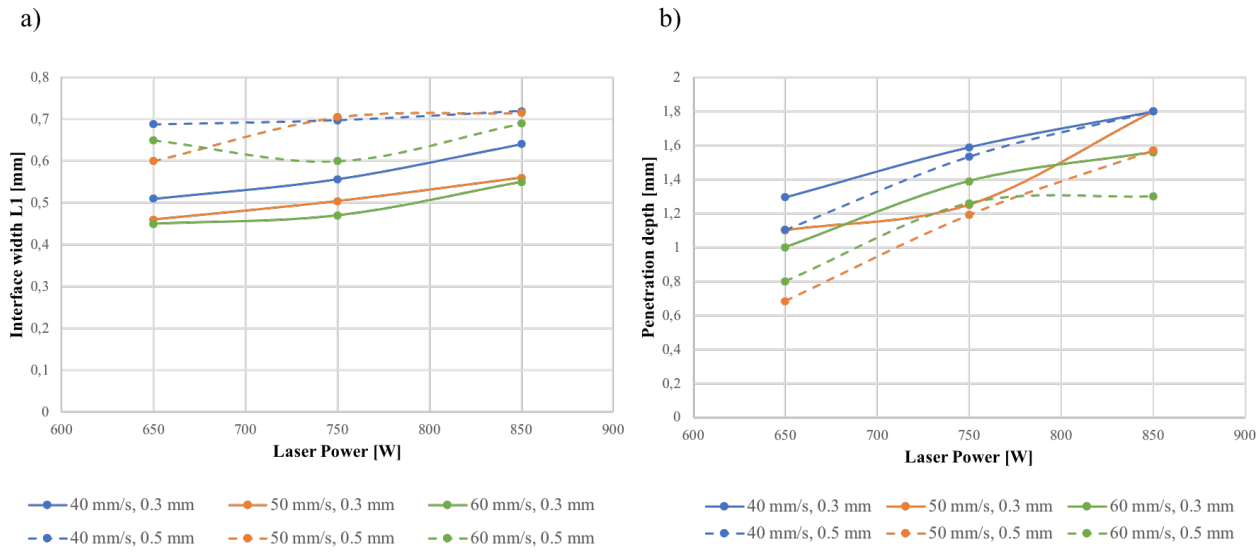

Figure 74: Interface width(a) and penetration depth (b) as a function of laser power, welding speed and wobbling amplitude for Al-Cu-Busbar welding configuration.

The feasibility process window for both investigated amplitudes for Cu-Al-Configuration. At oscillation amplitude of 0.2 mm, see Figure 75(a), no welding condition was obtained with a laser power of 650 W and welding speed of 50 and 60 mm/s; the heat input supplied during the process and transferred from the laser beam to the material was not sufficient to melt all the layers. Given the high reflectivity of the copper and high melting point a minimum in term of energy density (is required in order to melt the material and achieve a penetration in the lower sheets. On the other hand, at 850 W and welding speed of 40 and 50 mm/s the heat input was to excessive and consequently full penetration occurs; to this, a high mixing of materials is added and, due to the instability of the keyhole, there is also formation of porosity inside the joint. A correct setting of parameters allowed to obtain weld seam with partial penetration, limited mixing and reduced presence of porosity; with laser power of 750 W and for all welding speed investigated weld seams with good morphology have been obtained. When oscillation amplitude increases to 0.5 mm, the same considerations made previously remain almost valid. As the laser path is increased, more energy is needed to join the sheets, and therefore with laser power of 750 W and welding speed of 60 mm/s no weld occurred, while partial penetration condition was obtained with a wide range of parameters.

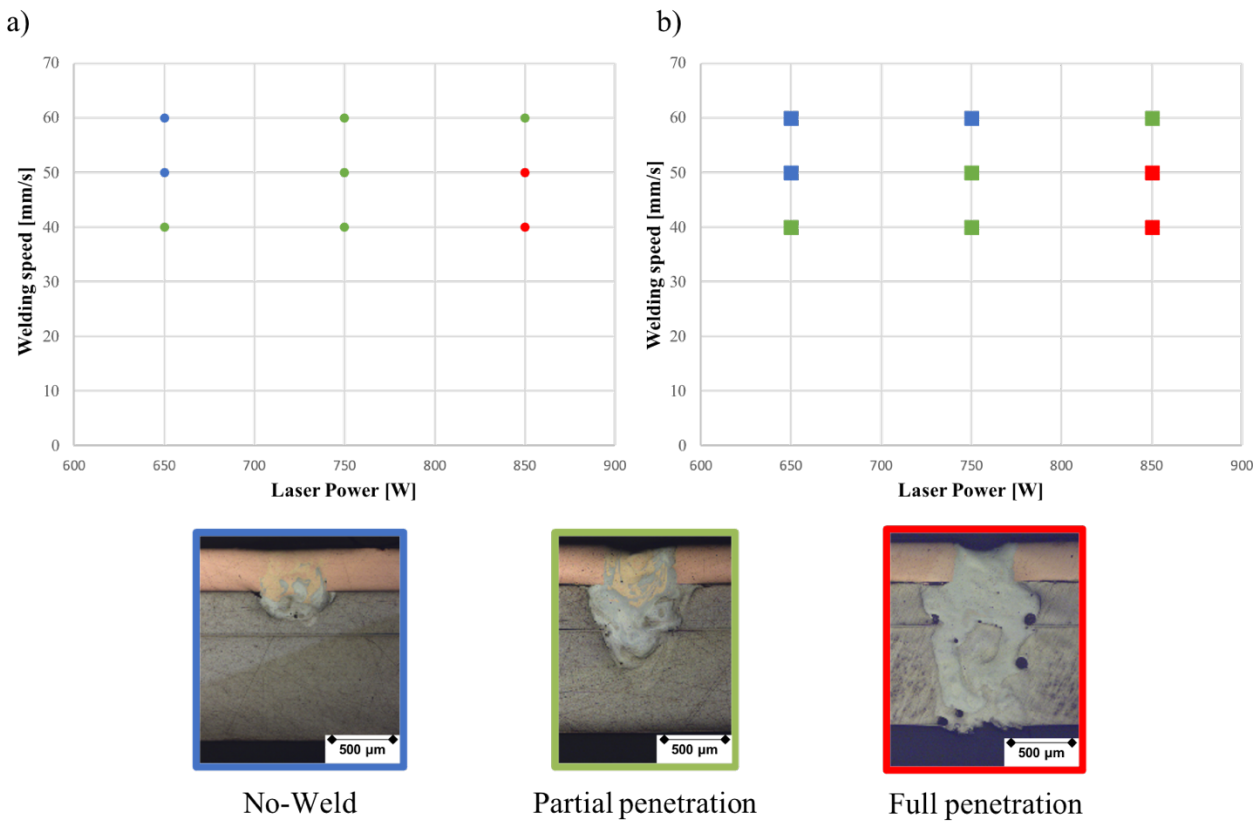

Figure 75: Feasibility process window for Cu-Al- Busbar with wobbling amplitude of 0.3 mm(a) and 0.5 mm(b).

4.4.3. Shear tensile test results

After having defined by metallographic analysis, which were the parameters capable of meeting the minimum requirements in terms of the morphology of the bead, shear tensile tests were performed on a limited number of conditions. Table 21summarizes the parameters used for the tensile test. As can be seen, for each configuration (Al-Cu-Busbar and Cu-Al-Busbar) a minimum of one sample for each amplitude of wobbling was investigated; particular attention was paid to those with copper as upper material, especially because they had the best morphology and the absence of defects

(transverse micro-cracks). The sample were cut with dimensions of 40mmx50mm and welded with an overlap of 5mm. Three tests were carried out, and the average was then calculated.

Configuration	Sample	Laser Power [W]	Welding speed [mm/s]	Wobbling amplitude [mm]	Energy density [MJ/cm^2]	Interface width L_1 [mm]	Penetration depth P [mm]
Cu-Al-Busbar	A	750	50	0.5	0.0281	0.70	1.19
	B	750	40	0.5	0.0351	0.705	1.54
	C	850	60	0.5	0.0265	0.69	1.3
	D	750	50	0.3	0.0281	0.5	1.25
	E	750	60	0.3	0.0234	0.47	1.3
Al-Cu-Busbar	F	700	50	0.5	0.0262	0.68	1.24
	G	700	40	0.5	0.0328	0.68	1.31
	H	600	50	0.2	0.0225	0.35	1.1

Table 21: Welding parameters used for tensile test in tab-tab-busbar configuration.

Figure 76 reports the average maximum breaking load for the samples tested. For Cu-Al-Busbar welding configuration the highest value of 900 N was obtained with sample C which has a weld width of about 0.69 mm and a penetration depth of 1.3 mm; similar strength, although lower, was obtained with sample A. By increasing the energy input (sample C), and therefore the penetration depth, it is noted that the breaking load decreases until it reaches values of about 550 N with poor repeatability of the results (high standard deviation). Although with a smaller wobbling amplitude, beads with a slightly smaller resistant section are obtained, breaking loads of about 800 N have been obtained for the sample E; from the data obtained, it is possible to understand very well that the mechanical properties of the joint do not depend only on the morphology of the bead but above all on the chemical composition of the phases that are formed and on their size. When aluminum was placed as upper material, breaking loads of about 700 N were obtained with sample F-G while a smaller resistant section results in a reduction of mechanical properties of the weld bead.

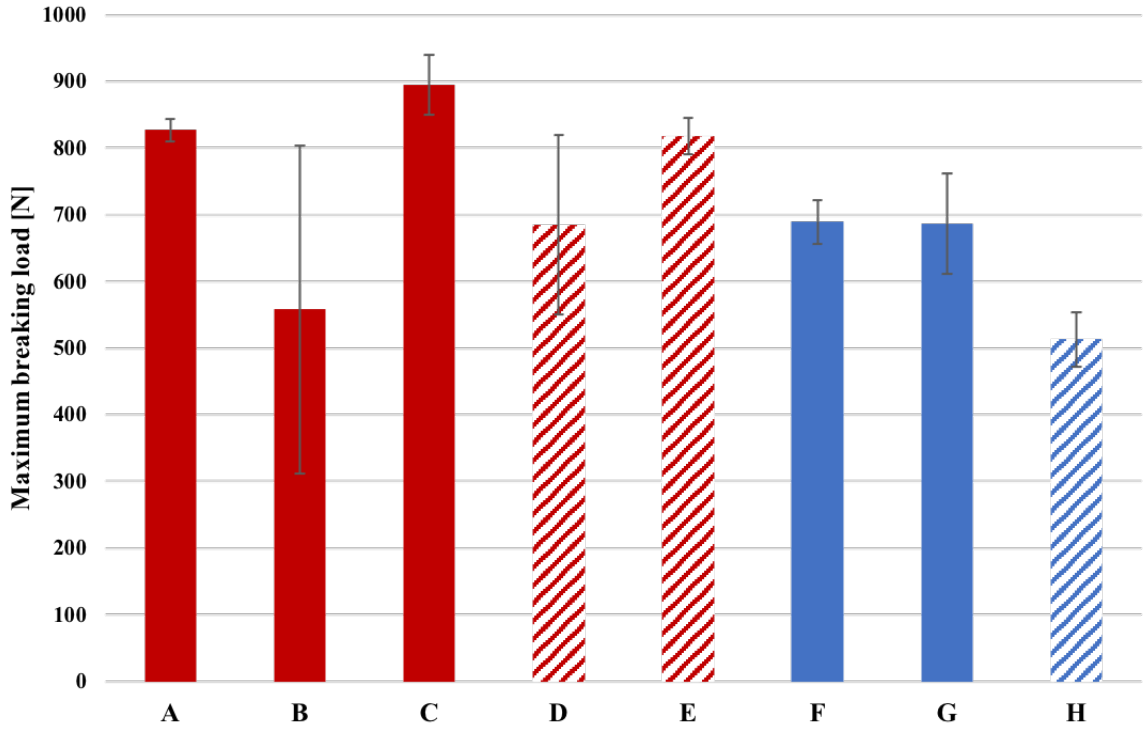

Figure 76: Tensile test results for tab-tab-busbar configuration.

It is interesting to observe the role of welding parameters on the tensile test curves reported in Figure 77. With reference to the black and blue curves (sample B-D), plastic deformation was more limited and brittle fracture took place when high energy input was applied at each wobbling amplitude. On the other hand, the plasticity of the joint was greater and ductile fracture took place with a correct setup of the process parameters.

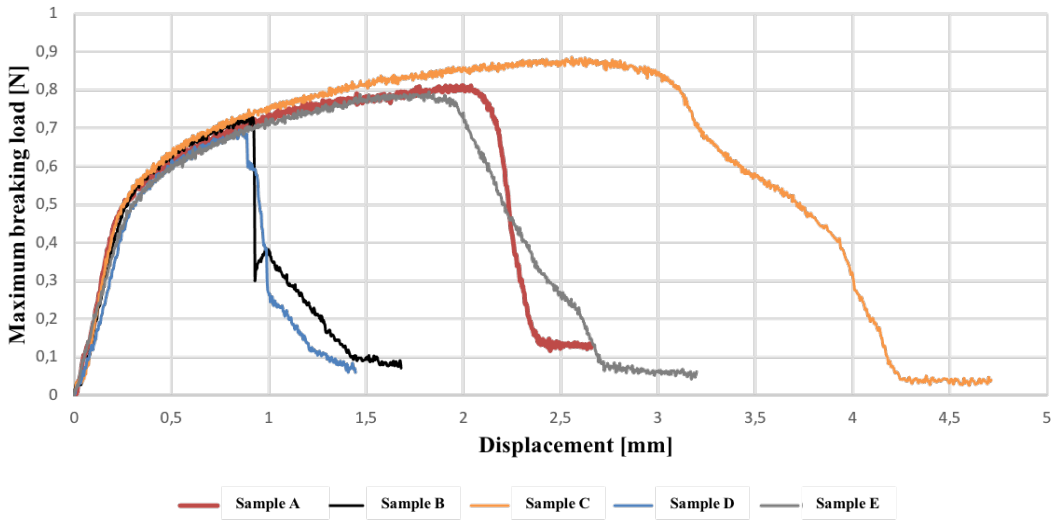

Figure 77: Maximum load-grip displacement curves for samples welded with copper as upper material.

Finally, the fracture mechanisms were investigated using the stereomicroscope images presented in Figure 78 . When welding with high energy input, it was discovered that fracture occurred at the weld seam on the copper side, see Figure 78(a) due to formation of brittle and hard intermetallic compounds along the whole weld seam. When welding was done with a correct energy input, failure occurred at the base material far from the weld seam (Figure 78 (b)).

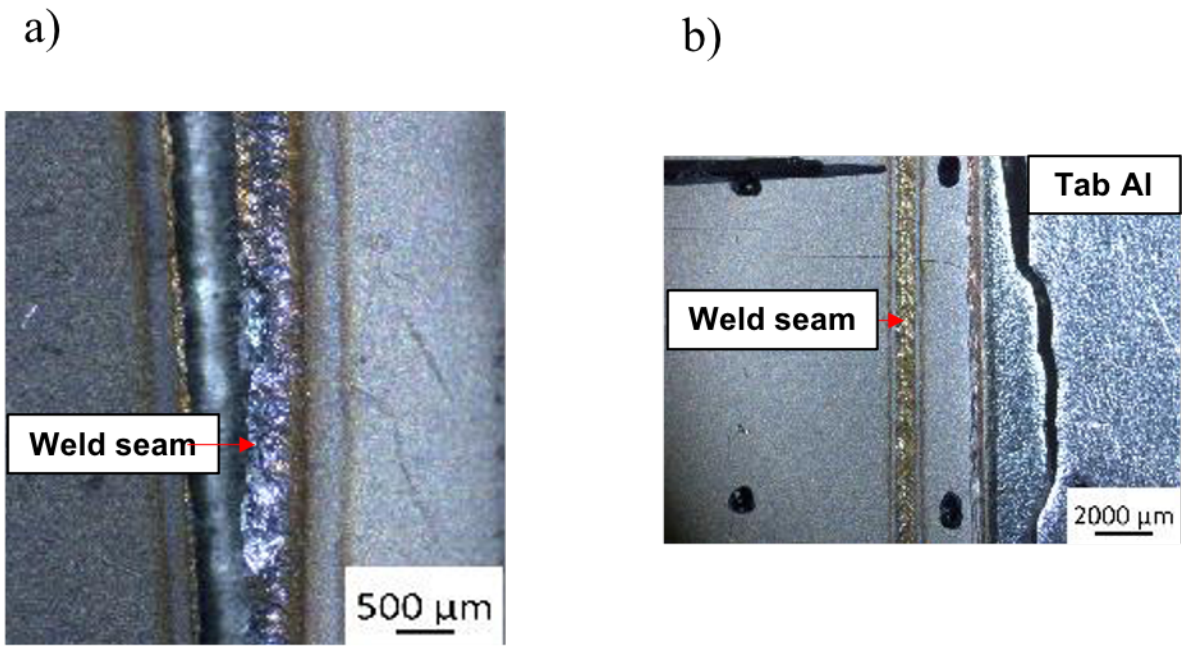

Figure 78:Example of failure mode for Cu-Al-Busbar: failure at the weld seam(a), failure at the base material (b)

Also for the configuration with aluminum as upper material, different load-displacement curves were obtained, as shown in the Figure 79. In particular, a more ductile behaviour was recorded for samples F-G welded with wobbling amplitude of 0.5 mm in which the failure occurred at the base material (aluminum tab) far from the weld seam (Figure 80 (b)). On the other hand, for sample H, welded with a wobbling amplitude of 0.2 mm, failure occurred at the weld seam at the copper layer with a more fragile behaviour. The reduced trace of wobbling, the placement of the materials and the energy input energy needed to reach the third layer led to an excessive mixing and formation of hard and brittle phases in correspondence with the second layer where the sample broke.

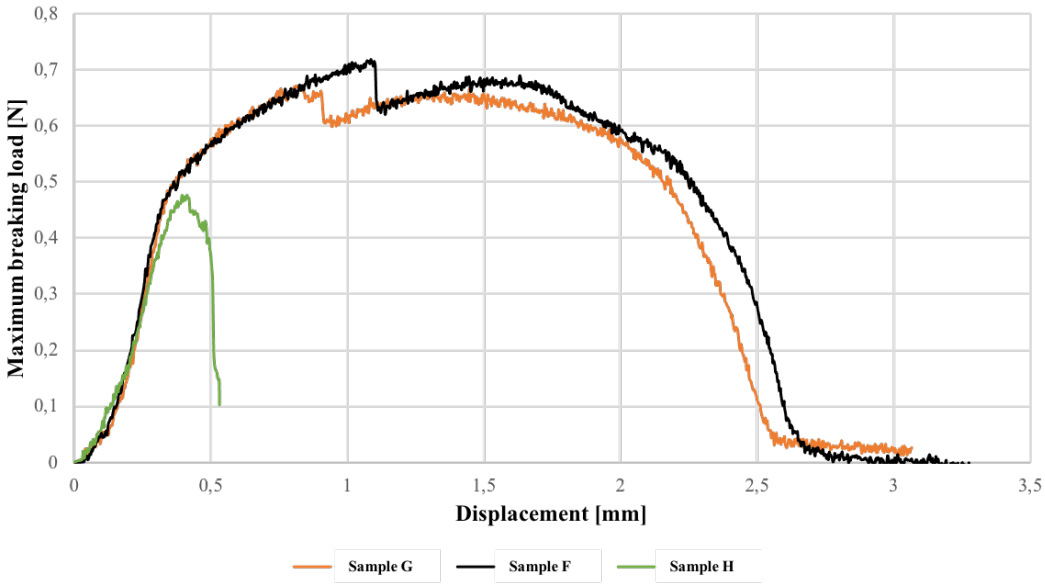

Figure 79: Maximum load-grip displacement curves for samples welded with aluminum as upper material.

a) b)

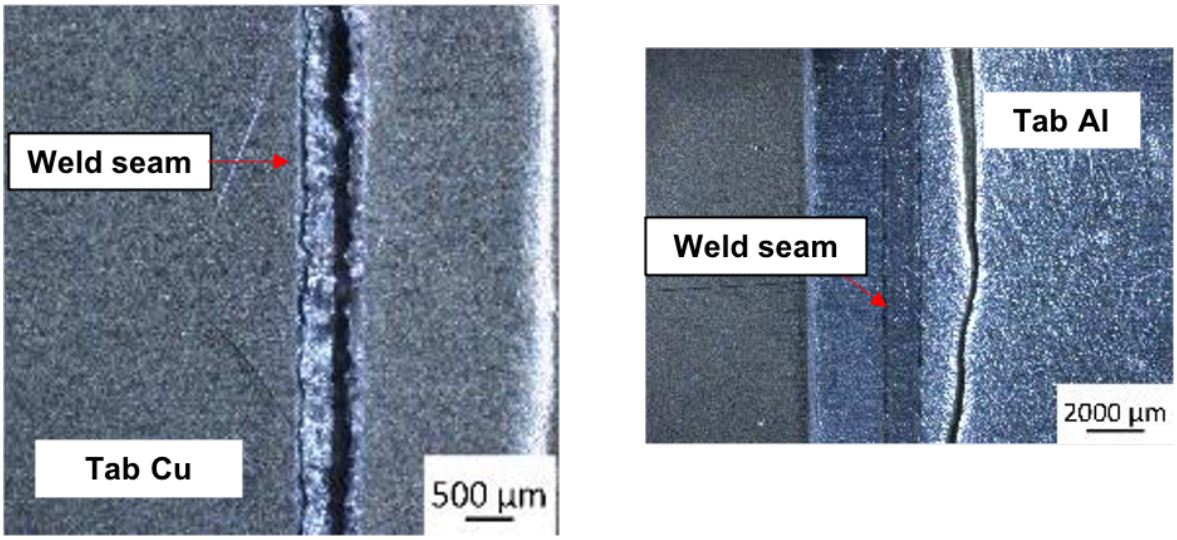

Figure 80: Example of failure mode for Al-Cu-Busbar: failure at the weld seam(a), failure at the base material (b).

4.4.4. Micro Hardness results

The micro-hardness testing was carried out on the cross sections with 100 gf load force and 20 s dwell time. The indentations, on both sheets, were performed in the longitudinal direction in fused zone (FZ) at a distance of 100 µm each other. Starting from the central axis of the weld seam, five indentations have been carried out: one at the axis and two on the right and left side. The hardness profiles obtained for Cu-Al-Busbar configurations are shown in Figure 81. In Figure 81(a)was reported the hardness profile corresponding to specimen C with the parameters which allows to obtain a maximum breaking load. Interesting to observe how the peak of hardness was reached near the center of the weld seam on the aluminum layer reaching values of about 700 $HV_{0.1}$; the other peak of hardness on the first and third layers were reached near the molten zone in two different zones matching to the extremes of the trace where the laser energy per unit length achieve a maximum value. By increasing the energy value (sample B) the peak of hardness of 800 $HV_{0.1}$ was reached at the copper layer along the entire weld bead; also in this case, a second peak of hardness of about 800-900 $HV_{0.1}$ was obtained at the second layer near the extremes of the traces scanned by the laser beam. The results obtained with the micro-hardness profiles seem to confirm the findings of the tensile tests, in particular the break occurred where a peak of hardness was recorded.

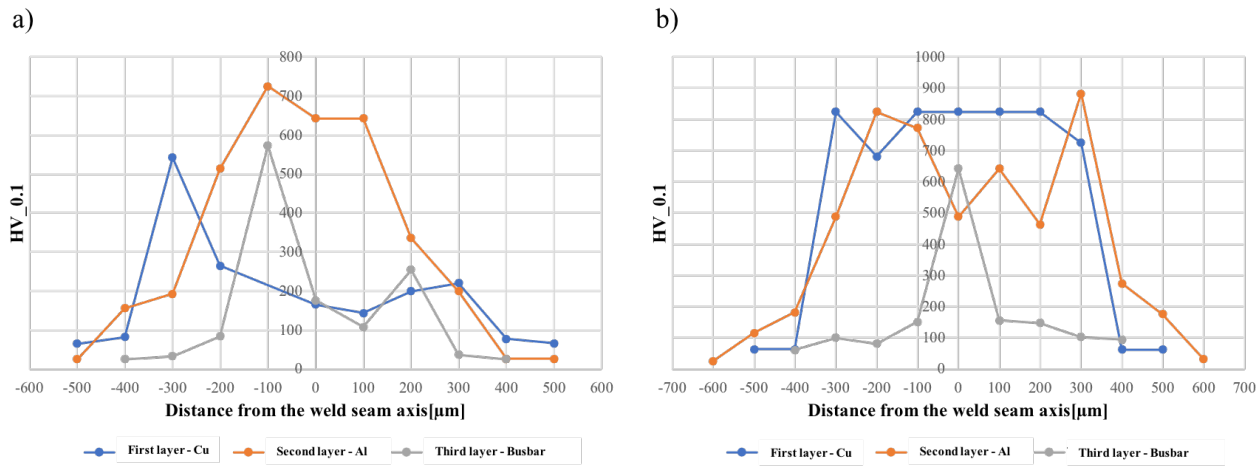

Figure 81: Example of hardness profiles obtained for Cu-Al-Configuration, sample C (a) and sample B (b).

Different results but which seem to confirm what was found with the tensile tests also for the configuration with aluminum as upper material. When welding occurred with wobbling amplitude of 0.5 mm, sample F (Figure 82 (a)), the peak of hardness of about 700-800 $HV_{0.1}$ was measured at the second layer (Cu sheets) not at the center of the weld seam but at the extremities of the trace; the

compounds that have formed, which present this hardness, do not seem to compromise the properties of the joint, as seen in sample C. The first aluminum layer has a hardness of about 400 $HV_{0.1}$ along the entire weld bead which confirms that a limited mixing occurred. On the other hand, when welding was performed with wobbling amplitude of 0.2 mm, a peak of hardness of about 1000 $HV_{0.1}$ was recorded near the second layer; as can be seen, also for the other layers the hardness reached its maximum at the center of the weld seam thus obtaining poor mechanical properties as seen previously and a failure of a brittle type in correspondence with the second layer.

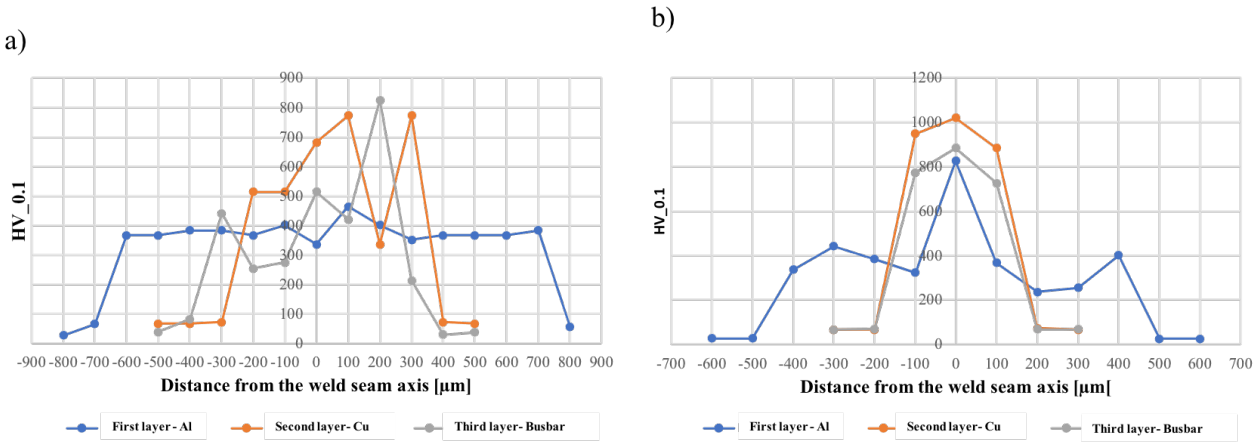

Figure 82: Example of hardness profiles obtained for Al-Cu- Configuration, sample F (a) and sample H (b).

4.4.5. Electrical contact resistance

The electrical contact resistance results are shown in Figure 83. Concerning the Cu-Al-Busbar configuration the lower value of about 26 μΩ was obtained with the sample C which presented the maximum breaking load as seen previously. By increasing the energy input, sample B, not only the mechanical resistance decreases, but also the electrical resistance value undergoes an increase probably due to the formation of hard, fragile but also low thermal conductivity intermetallic phases. When wobbling amplitude of 0.3 mm was applied, contact resistances of about 28 μΩ were measured, in particular for sample E despite a smaller section useful for the passage of current. These findings once again underline that the electrical and mechanical properties of this type of connections are strongly linked to a series of factors such as the morphology of the bead, therefore the energy supplied during the process, the type and size of the intermetallic phases that are obtained following cooling. Concerning the Al-Cu-Busbar configuration the lowest value of 26 μΩ was obtained with sample F welded with amplitude of wobbling 0.5 mm; no particular difference was noted by welding with 0.3 mm (sample H) since the contact resistance value is about 26 μΩ probably due to the different formation of intermetallic compounds, mainly Al-rich phases which have lowest electrical resistance.

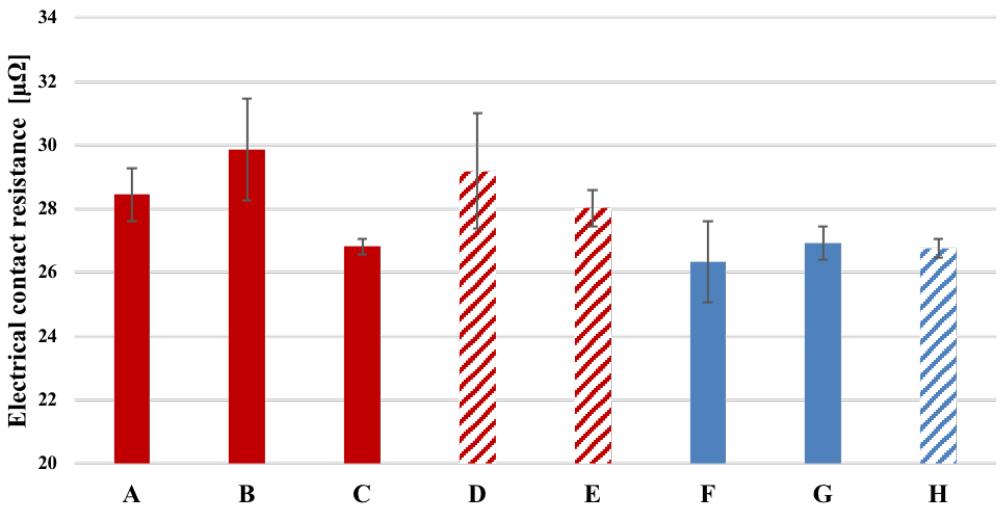

Figure 83:Electrical contact resistance results for tab-tab-configuration.

In Figure 84 the relationship between mechanical and electrical properties is shown. In particular a linear correlation has been found for the Cu-Al-Busbar configuration, since as the mechanical properties in terms of maximum breaking load increase the electrical contact resistance of the connection decreases; on the other hand, no particular correlation has been found when the aluminium was placed as upper material. Especially for the Cu-Al-Busbar configuration, the results obtained are

very important because if on the one hand the measurement of electrical resistance involves the use of very precise instruments and the possibility of making measurement errors, the mechanical resistance test, more reliable, giving us information on the maximum breaking load, the modality and the point in which the breaking occurs, it can also provide us with useful data on what could be the electrical performance of the joint. On the other hand, during an end-of-line test, the measurement of the electrical contact resistance of the weld bead, which is a non-destructive test, can give us useful information about the mechanical properties of the connection.

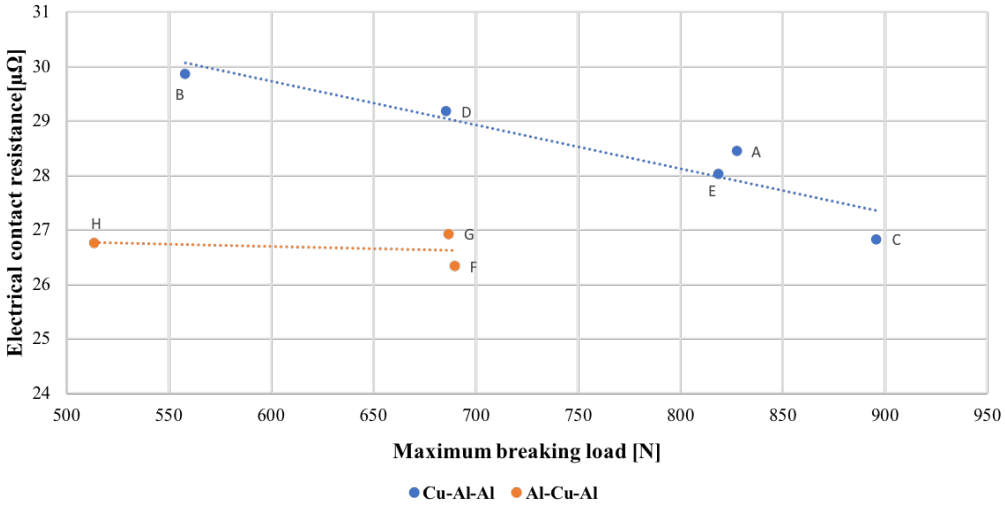

Figure 84: Relationship between mechanical and electrical properties for tab-tab-configuration.

4.4.6. Aging test

With this welding configuration, once the best parameters were obtained, the aging due the current transmission and the effect on the connection properties have been studied. During the activity various parameters were monitored and for reasons of industrial confidentiality not all of them will be shown and discussed. The aim was not only to study the aging of the weld and verify the mechanical and electrical characteristics at the end of its life but also to understand which defects that can occur during the assembly of a battery pack that will most affect the performance of the entire battery pack.

4.4.6.1. Setup

For each welding condition, 5 welds have been performed in a single mini module and then placed in the climatic chamber where current was passed as shown in Figure 85 (b). The test conditions cannot be disclosed, but during aging a current of about 200 A was passed between the welds in series for a specified time followed by both natural and forced cooling; during the tests, temperature of the chamber was kept stationary, while the temperature near the centre weld seam was monitored by means of K-thermocouple. The current cycles, the duration and the number of repetitions is based on a series of factors that derive from the number of missions that the car has to do during its life

a)

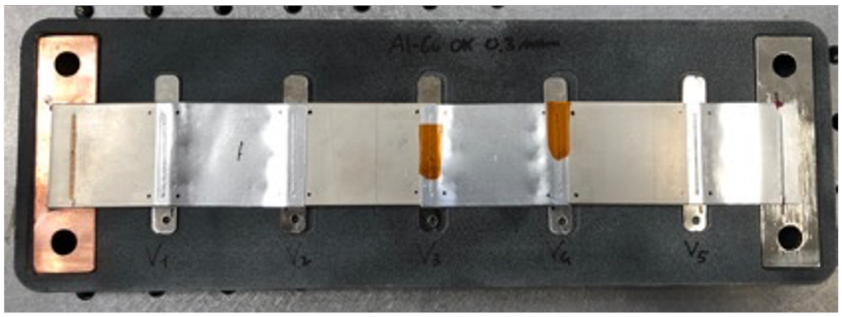

b)

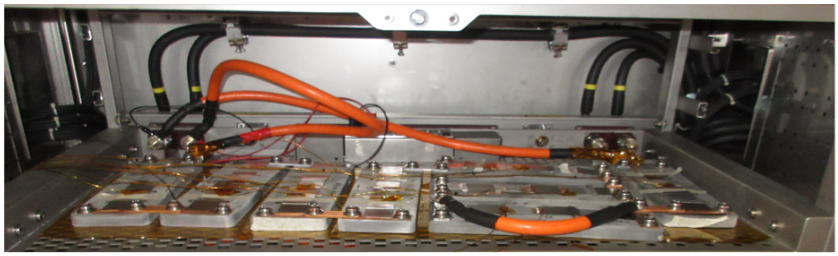

Figure 85: Example of mini module for aging test(a) and placement in climatic chamber.

The welding parameters of the mini module used for aging test are reported in Table 22. As can be seen, for both the configurations two conditions (OK Welding), one for each amplitude of wobbling, were chosen. Concerning the Cu-Al- Busbar configuration, the effect of an incorrect work distance was studied since a slight variation of the focal distance, for the optical chain present, involves a considerable reduction of the power density on the plane; consequently, the possibility of performing a linear rework of the weld was also evaluated. The incorrect push was not evaluated since produce the same result (no welding) of an incorrect work distance. Regarding Al-Cu-Busbar configuration as the previous case, the effect of both an incorrect work distance and incorrect push were studied when larger wobbling amplitude is applied; no rework was evaluated since if incorrect work distance occurs, when aluminum is the upper materials, the welding takes place without particular problems thanks to the lower melting temperature and reduced reflectivity at the wavelengths of the near infrared compared to the copper.

Quantity	Configuration	OK Welding 0.5 mm	OK Welding 0.2 mm - 0.3 mm	Incorrect Push	Incorrect work distance	Incorrect work distance + Linear rework
4	Cu - Al Busbar Al	P=750 W v=50 mm/s A=0.5 mm	P= 750 W v=60 mm/s A=0.3 mm		P=750 W v=50 mm/s A=0.5 mm	P=750 W v=50 mm/s A=0.5 mm Linear P= 1000 W v=150 mm/s
4	Al - Cu Busbar Al	P=700 W v=50 mm/s A=0.5 mm	P= 600 W v=50 mm/s A=0.2 mm	P=700 W v=50 mm/s A=0.5 mm	P=700 W v=50 mm/s A=0.5 mm	

Table 22: Test plan for aging test.

The purpose of the post processing phase, which will be discussed later in the results and discussion paragraph, was first to understand how the presence of defects or not-correct setup affect the weld seam properties at the end of battery life in a working condition similar to the real one. Furthermore, for the OK samples, the properties in terms of mechanical load and electrical resistance have been evaluated with respect to the phase preceding the aging. To do this, at the end of the tests, measurements of electrical resistance, tensile tests and cross-sections of the samples, on which SEM-EDS analyzes were carried out, were performed as reported in the previous paragraph and therefore they will not be discussed.

4.4.6.2. Results and discussions

After carrying out the aging cycles, to simulate an accelerated aging of the tabs, the individual mini modules were cut, and the samples were first analyzed under the stereo microscope and then the cross section was observed under an optical microscope. Top and cross sections of the samples welded for the Al-Cu-Busbar configuration are shown in Figure 86. From the top view, the weld bead is quite regular for the first three configurations, while it can be seen that where the thrust has not been corrected the bead is not continuous; also in this case, after the aging test, transverse micro cracks were found along the weld seam. Optical microscope analysis has shown that the morphology of the bead is quite regular, with reduced presence of defects such as porosity inside the weld seam; small pores can be found at the interface zone between the second layer and the busbar probably due to the fact that the gases are unable to move away from the melt pool due to the high process speeds. When the working distance was not correct, by acting on the positioning of the welding head at an incorrect focal distance, the seam is thinner with a slightly lower penetration than in the previous case while an incorrect push of welding jig results in a no-complete welding due the non-correct adhesion between the layers.

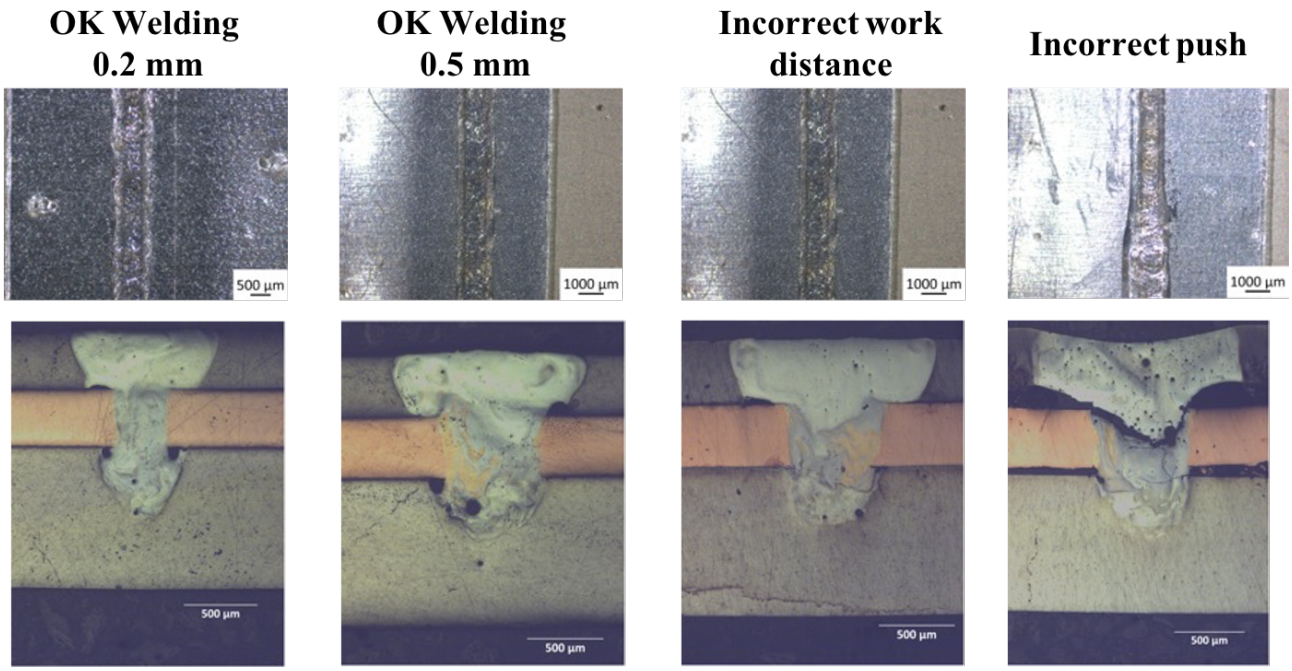

Figure 86: Top and cross section images of welded sample of Al-Cu-Busbar configuration after aging test.

In Figure 87 top and cross section images of the samples welded with Cu-Al-Busbar configuration are shown. No particular defects such as spatters o cracks can be found by analysing the top view

images; when the welding was performed with an oscillation of 0.5 mm, it is noted that the bead has a more greyish colour, a sign that greater dilution has occurred between the materials and more aluminum has risen towards the copper layer. When the working distance is not correct, with copper as the upper material, there is no welding but only a slight trace of the beam's passage from which the need to carry out a linear rework, due to the reduced spaces of the welding area; consequently a very small bead is obtained, with the presence of defects such as surface humpis and gas porosity due to the instability of the keyhole.

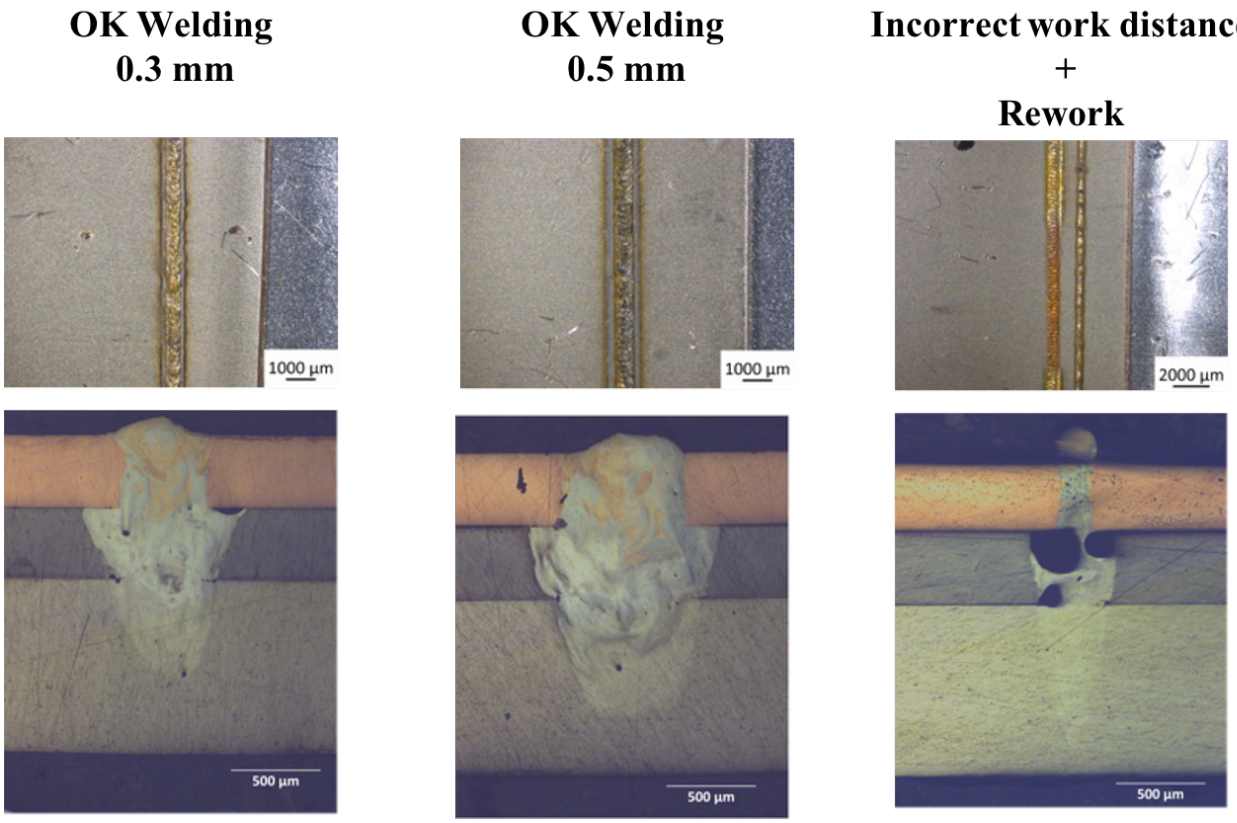

Figure 87: Top and cross section images of welded sample of Cu-Al-Busbar configuration after aging test.

Shear tensile tests were carried out on samples taken from the mini modules and therefore smaller than those used during the pre-aging phase. For each welding configuration three samples were tested, and the average value was measured. The results concerning the Al-Cu-Configuration after aging test are reported in Figure 88(a). With the optimized parameters, a maximum breaking load of about 600 N is obtained with a greater oscillation amplitude, while a reduction in mechanical strength was obtained with an oscillation amplitude of 0.2 mm due to the fact that the weld has a smaller resistant section; an incorrect thrust also results in a reduced mechanical resistance due to the reasons indicated above with reduced repeatability among the results. Otherwise, an incorrect focal length seems to have a positive effect on the mechanical properties; in fact, the induced error implies a reduction in

the heat input provided, which on the one hand slightly modifies the morphology of the bead, on the other hand translates into a reduced mixing between the materials and probably less hard and brittle intermetallic phases. Comparing instead the maximum load at break between pre- and post-aging, only on OK samples, a different behaviour is noted between the two investigated amplitudes (Figure 88(b)); on the one hand, amplitude of wobbling of 0.5 mm, the properties decrease even if slightly, while in the other case the mechanical resistance seems to increase.

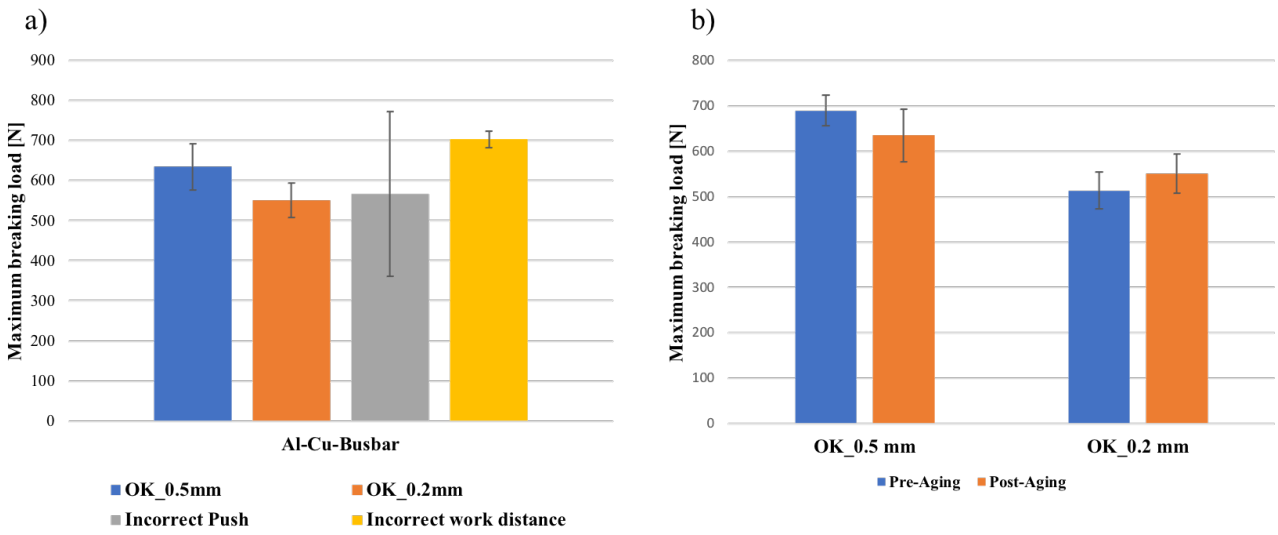

Figure 88: Shear tensile test results after aging test (a) and a comparison between breaking loads between before and after (b) for Al-Cu-Configuration.

The examples of the failure modes obtained following the post aging tensile tests when aluminum is the upper material are shown in Figure 89. The failure modes are in line with what has been achieved both in terms of maximum breaking load and with the pre-aging phase. In fact, with a small amplitude, the failure, of a fragile type, always occurs in correspondence with the bead near the copper tab (Figure 89(a)); on the other hand, when larger amplitude was applied the failure occurs at the weld seam, see Figure 89(b), on the aluminum tab due to the high presence of hard and brittle intermetallic compounds. When welding is carried out with an incorrect working distance, which presents the higher mechanical properties after the aging test the failure occurs at the base material(Figure 89(c)), while an incorrect push results a failure at the interface (Figure 89(d))between the sheets due to a non-correct adhesion.

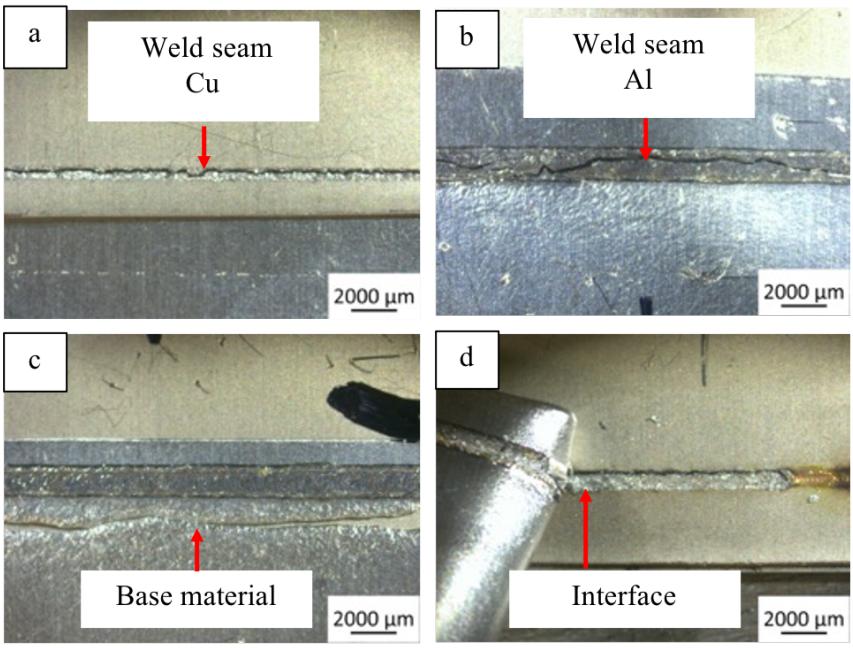

Figure 89: Example of failure mode for Al-Cu-Busbar: failure at the weld seam near the Cu tab(a), failure at the weld seam(b), failure at the base material (c) and failure at the interface (d).

The results of the tensile tests relating to the other configuration, the one with copper above, are shown in Figure 90(a). The best properties, in terms of maximum breaking load, were obtained when wobbling amplitude of 0.3 mm was applied with value of about 900 N, while a slight decrease was observed with the greater amplitude with value of about 800 N. An incorrect working distance results in a KO in terms of mechanical properties as it is more of a bonding than a welding, while in the case of rework maximum breaking load of 700 N was obtained. As in the previous case, after the aging test the weld with a smaller amplitude has the best mechanical properties although the increase is weak.

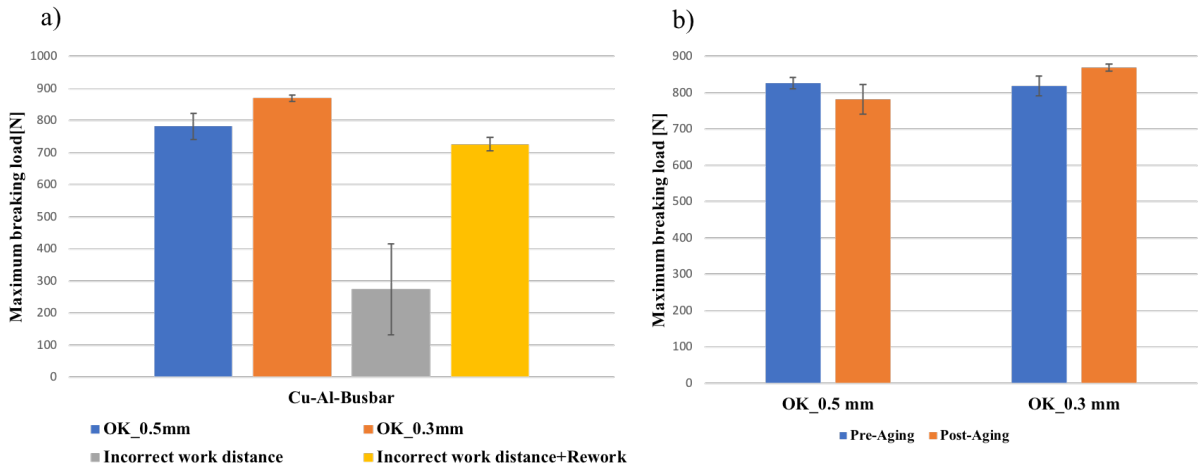

Figure 90: Shear tensile test results after aging test (a) and a comparison between breaking loads between before and after (b) for Cu-Al-Configuration.

The examples of the failure modes obtained following the post aging tensile tests when copper is the upper material are shown in Figure 91. The failure modes are in line with what has been achieved both in terms of maximum breaking load and with the pre-aging phase. In fact, with optimized parameters failure, of ductile type, occurs at the base material neat the aluminum tab for both the wobbling amplitude investigated (Figure 91(a,b)) while the failure at the interface(Figure 91(c,d)) occurs when linear rework was applied due to reduced resistant section of the weld bead.

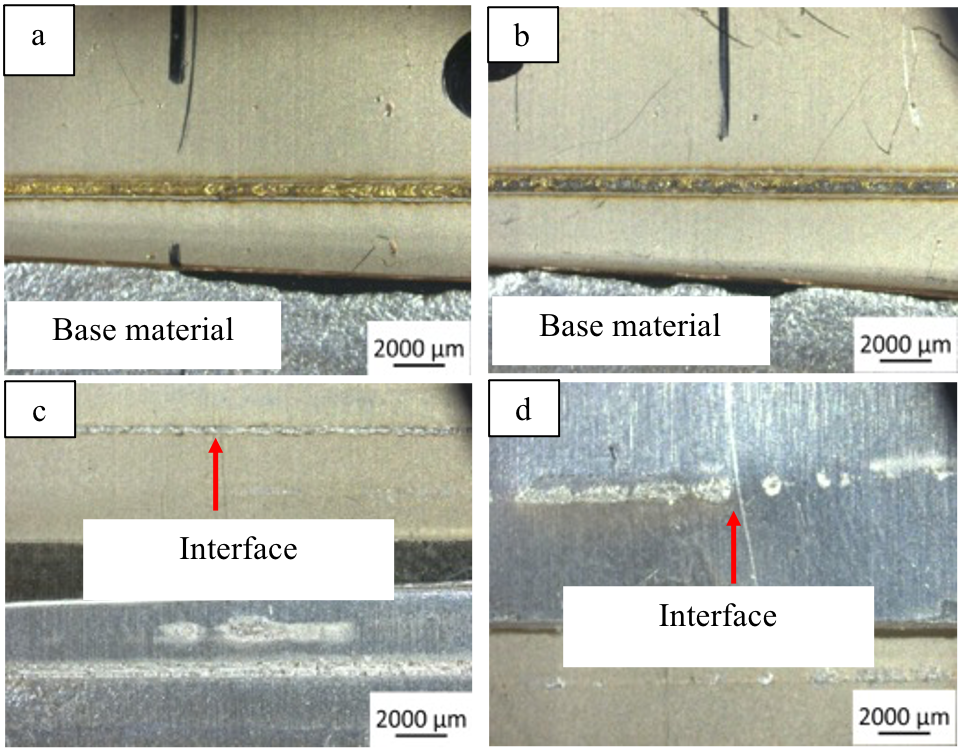

Figure 91: Example of failure mode for Cu-Al- Busbar: failure at the base material (Tab Al) (a,b) and failure at the interface (c,d).

The results relating to the electrical measurements for both configurations are shown in Figure 92. The measurements were carried out before and after the aging tests and the results reported are an average of the measurements taken on all the samples. The electrical resistances measured post aging are in all cases greater than the pre-aging values (the distance between the measurement leads and any measurement error must also be considered). The samples with electrical resistance, at the end of the cycles, are for the Al-Cu-Busbar configuration the one with the wrong focal distance, while for the Cu-Al-Busbar configuration it is the 0.3 mm sample. Even in this case, the results in terms of electrical resistance are in line with the results of the tensile tests. Although the reworked sample has a poor mechanical resistance, it does not have poor values in terms of electrical conductivity, a sign that the junction, which guarantees the passage of current, has occurred.

a) b)

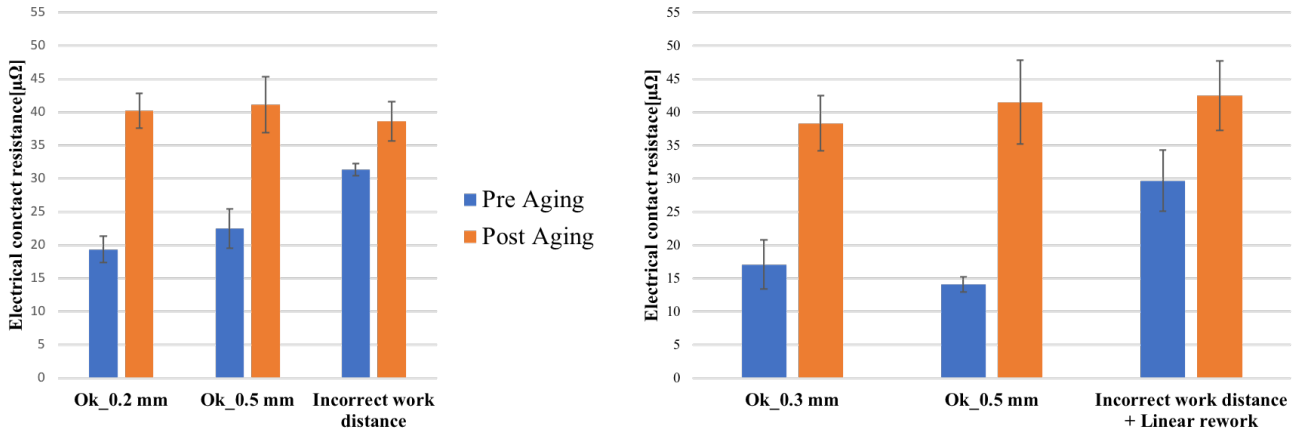

Figure 92: Electrical contact resistance results after aging test, Al-Cu-Busbar (a) and Cu-Al-busbar (b).

Figure 93 shows the SEM images of the sample welded with lower wobbling amplitude for Al-Cu-Busbar configuration. For each weld, EDS analysis were performed in different parts of the weld seam in order to obtain information about the chemical composition formed, listed in Table 23. At the interface zone, Figure 93(B), the average copper content is reduced, and it never exceeds the 10 at. % resulting thus in Al-Cu resulting in the detection of Al-Cu eutectic alloy with a vermicular shape; light mixing, with copper clusters, is also found near the center of the bead on the first layer. Instead, at the second layer (Figure 93(B)) the copper presence is higher with an average content of about 50 at. % and thus, the detection of a larger layer of η (AlCu) phase inside which a crack develops along the entire section of the bead. The mixing between the base materials was also detected in the lower part of the weld seam, in which there are copper cluster, which has sunk into the lower aluminum foil, with Θ(Al_2Cu) phase formations. The EDS analysis confirmed what was found with the previous analysis, namely that the reduced mechanical and electrical properties, the breakage at the center of the bead are mainly due to the presence of intermetallic phases with an average copper content of 50 at. %.

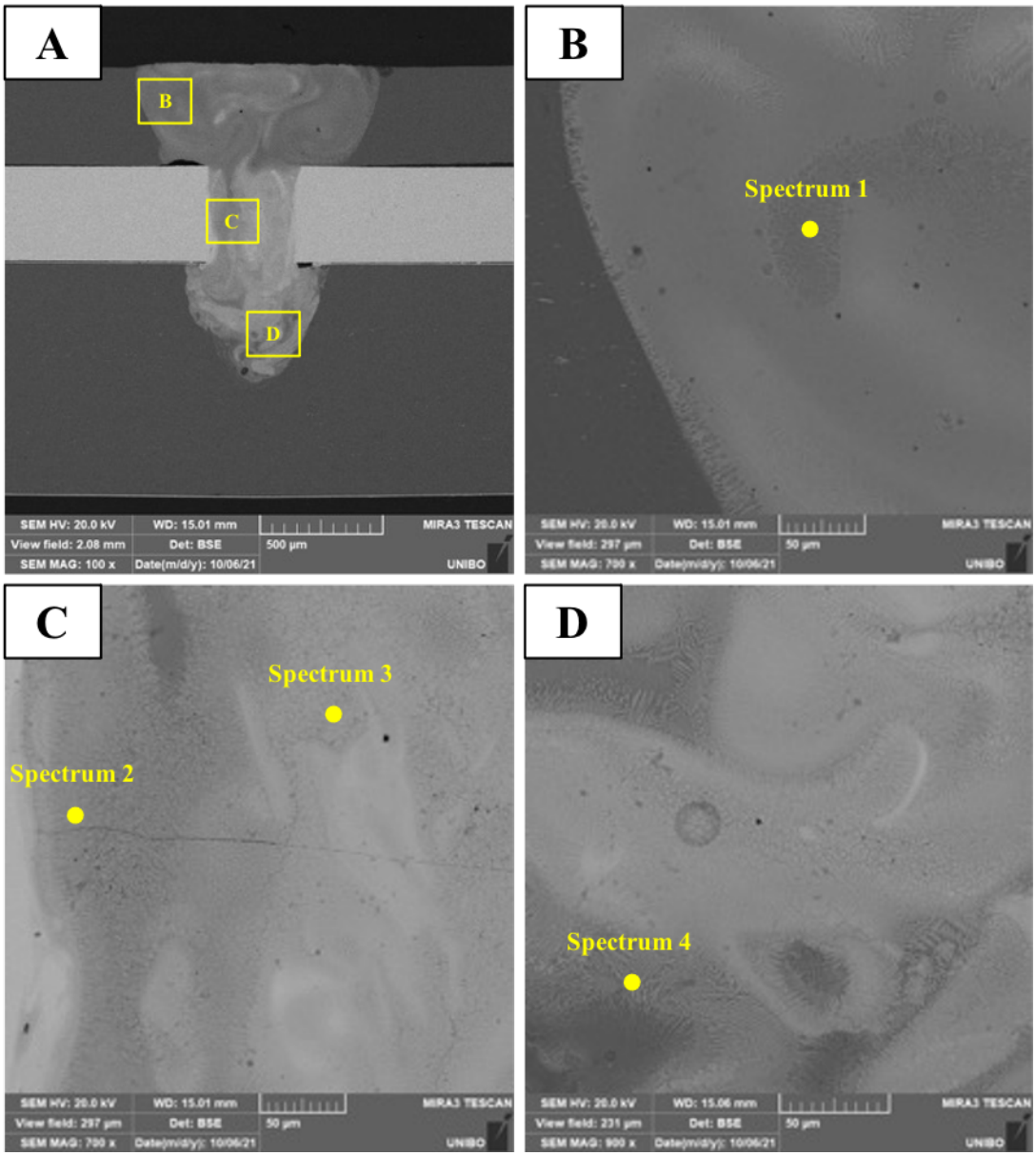

Figure 93: Scanning electron microscope images of the sample welded with power of 600W, welding speed of 50 mm/s and wobbling amplitude of 0.2 mm.

Zone	O (at. %)	Al (at. %)	Cu (at. %)	Possible phase
Spectrum 1	1.35	89.54	9.11	Al-Cu eutectic
Spectrum 2	0.49	48.12	51.39	η (AlCu)
Spectrum 3	0.95	48.53	50.52	η (AlCu)
Spectrum 4	0.51	72.98	26.51	Al+ Θ(Al_2Cu)

Table 23: Chemical composition of denoted zones in Figure 93.

The SEM-EDS results related to the welded sample with larger wobbling amplitude investigated for Al-Cu-Busbar configuration are reported in Figure 94, and the chemical composition of denoted zones are listed in Table 24. It can be seen that the greater the energy input provided, the greater the mixing between the materials, especially in the upper part of the bead where cluster of copper can be

detected more frequently with consequent formation of richer copper-type phases such as η (AlCu) and Θ(Al_2Cu) phases. Equally, the content of copper also at the interface between the two layers and the lower part of the bead always remains around the 30 – 40 at. % . The findings can be confirmed by also analyzing the EDS element mappings which show that copper is concentrated mainly near the bead axis but also in the upper part of the bead when energy input increases.

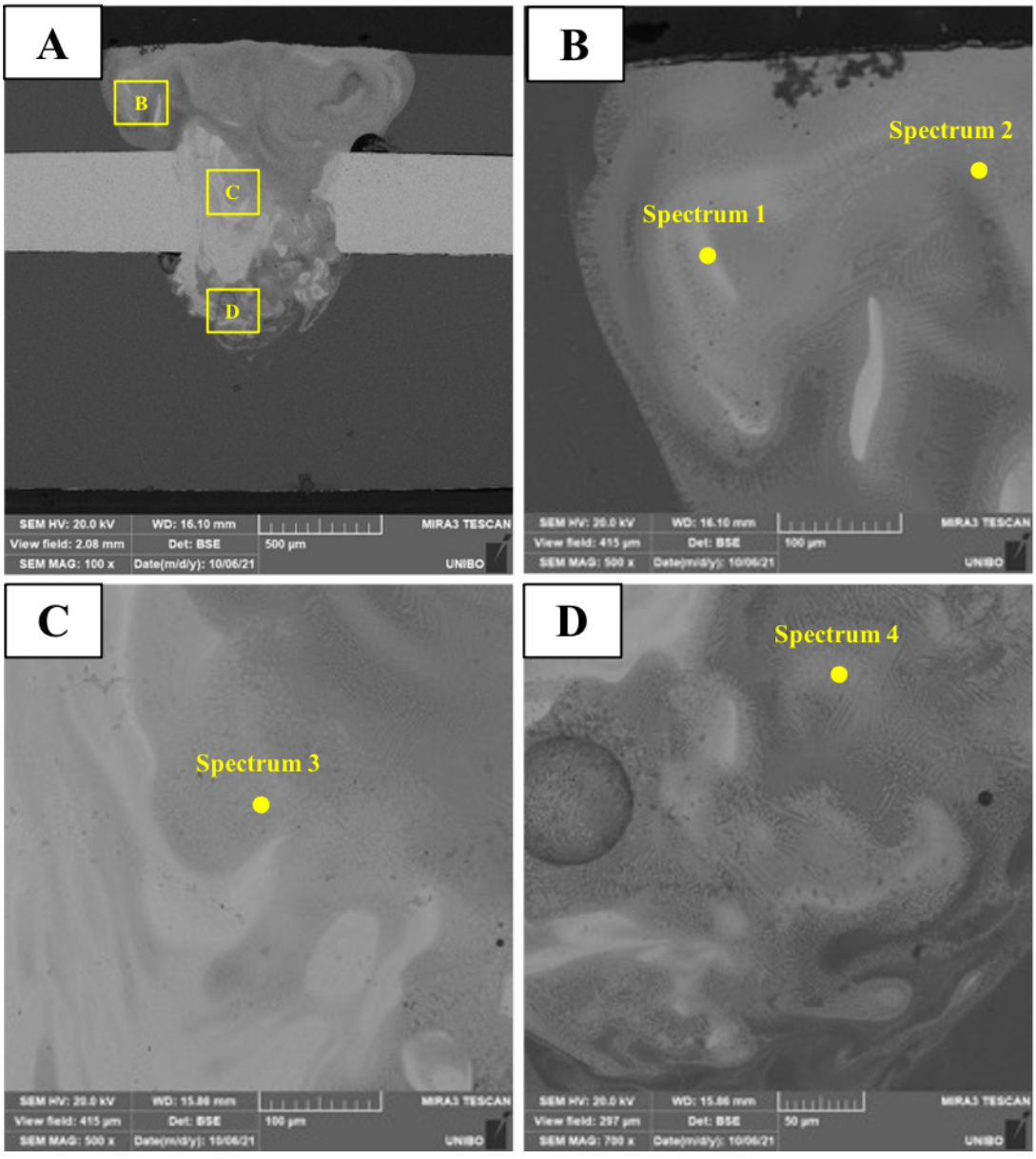

Figure 94: Scanning electron microscope images of the sample welded with power of 700W, welding speed of 50 mm/s and wobbling amplitude of 0.5 mm.

Zone	O (at. %)	Al (at. %)	Cu (at. %)	Possible Phase
Spectrum 1	0.99	53.65	45.36	η (AlCu)
Spectrum 2	0.27	67.77	31.96	Θ(Al_2Cu)
Spectrum 3	0.69	53.43	45.88	η (AlCu)
Spectrum 4	0.84	58.34	40.82	η (AlCu)

Table 24: Chemical composition of denoted zones in Figure 94

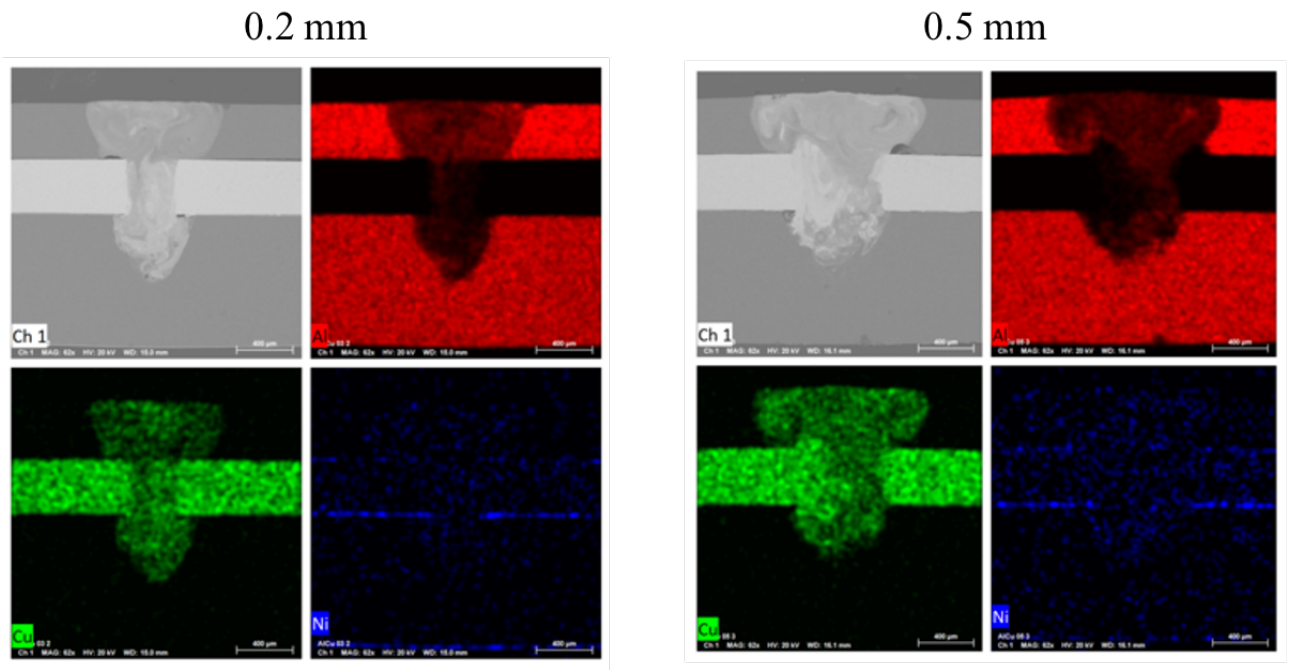

Figure 95:EDS element mapping of welded sample with aluminum as upper material.

Figure 96 shows the results concerning the sample welded with wobbling amplitude of 0.3 mm whit copper as upper material. The upper part of the weld bead is mainly composed of copper in solid solution while the mixing occurs at the interface zone between the first and second layer in which η (AlCu) phase with a copper content of about 30 at. % was detected. The formation of intermetallic compounds at the end of the scan trace was also detected, i.e., where there is the maximum of the absorbed energy since in those points the beam speed is minimal due to the change of direction; however, the copper content never exceeds the average of 30 at. % both in that zone but also in the lower part of the weld bead where clusters of Al-Cu eutectic were detected.

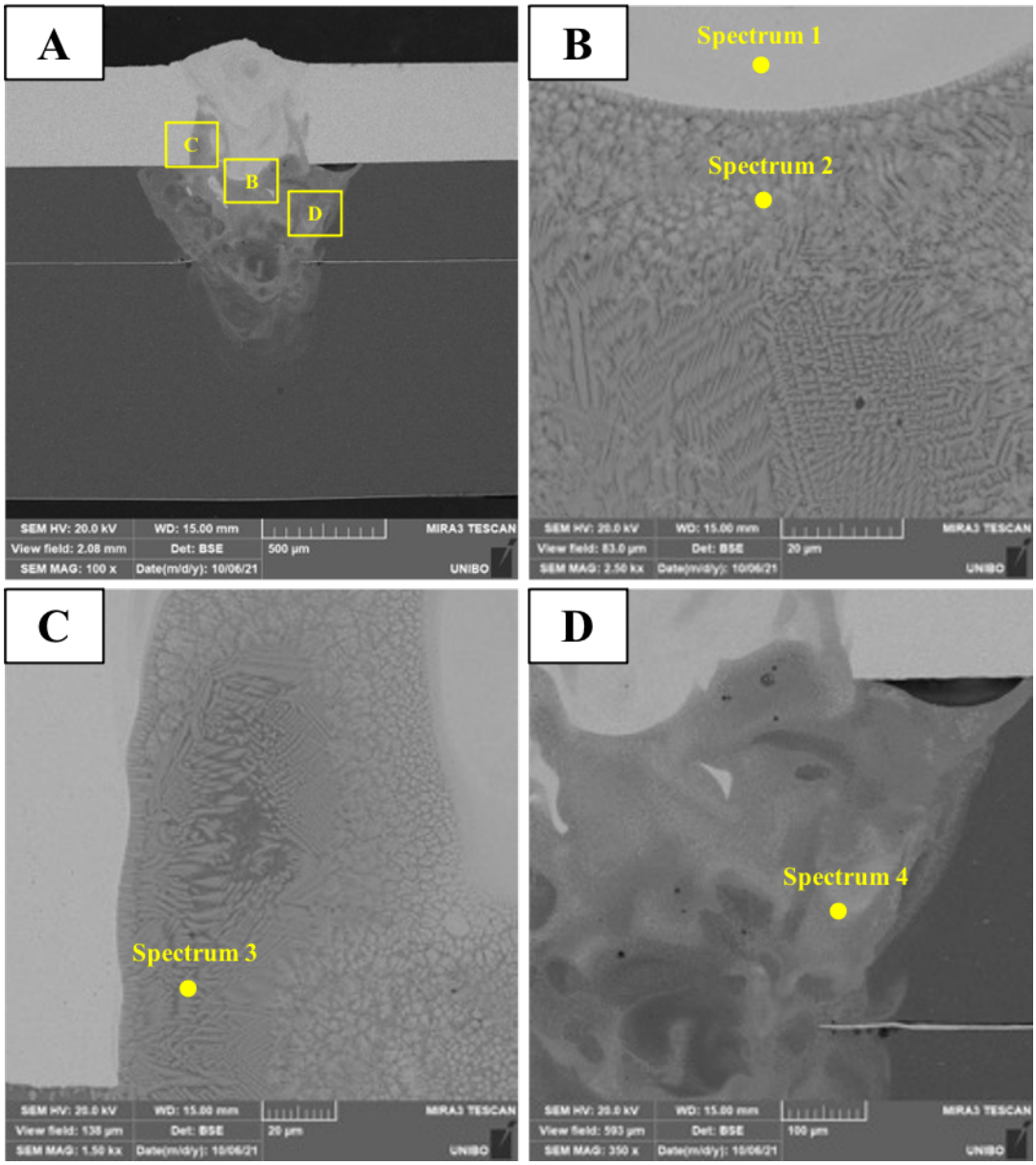

Figure 96: Scanning electron microscope images of the sample welded with power of 750W, welding speed of 60 mm/s and wobbling amplitude of 0.3 mm.

Zone	O (at. %)	Al (at. %)	Cu (at. %)	Possible Phase
Spectrum 1	1.34	20.71	77.95	Cu
Spectrum 2	1.44	68.21	30.35	η (AlCu)
Spectrum 3	1.78	72.46	25.77	Al+ Θ(Al_2Cu)
Spectrum 4	0.72	81.77	17.51	Al-Cu eutectic

Table 25: Chemical composition of denoted zones in Figure 96.

As for the welded configuration with aluminum as upper material and larger wobbling amplitude, also in the Cu-Al-Configuration and wobbling amplitude of 0.5 mm the mixing is more pronounced along the entire weld bead as reported in Figure 97. The EDS analysis show a higher copper content in the upper part of the weld seam, in which the average of copper is about 50 at. % and therefore,

the occurrence of η (AlCu) or ζ(Al_3Cu_4) copper-richer phases due to the high presence of aluminum which has risen upwards from the bottom; hard and brittle intermetallic compounds can be also detected in the lower part of the weld seam. The mappings of the EDS elements confirm what has been found, namely that when the welding has been performed with a lower oscillation amplitude, mixing occurs limited to the interface between the layers, while as the amplitude and therefore the energy supplied increases the mixing is more accentuated along the entire weld seam but also more aluminum can be detected in the copper layer.

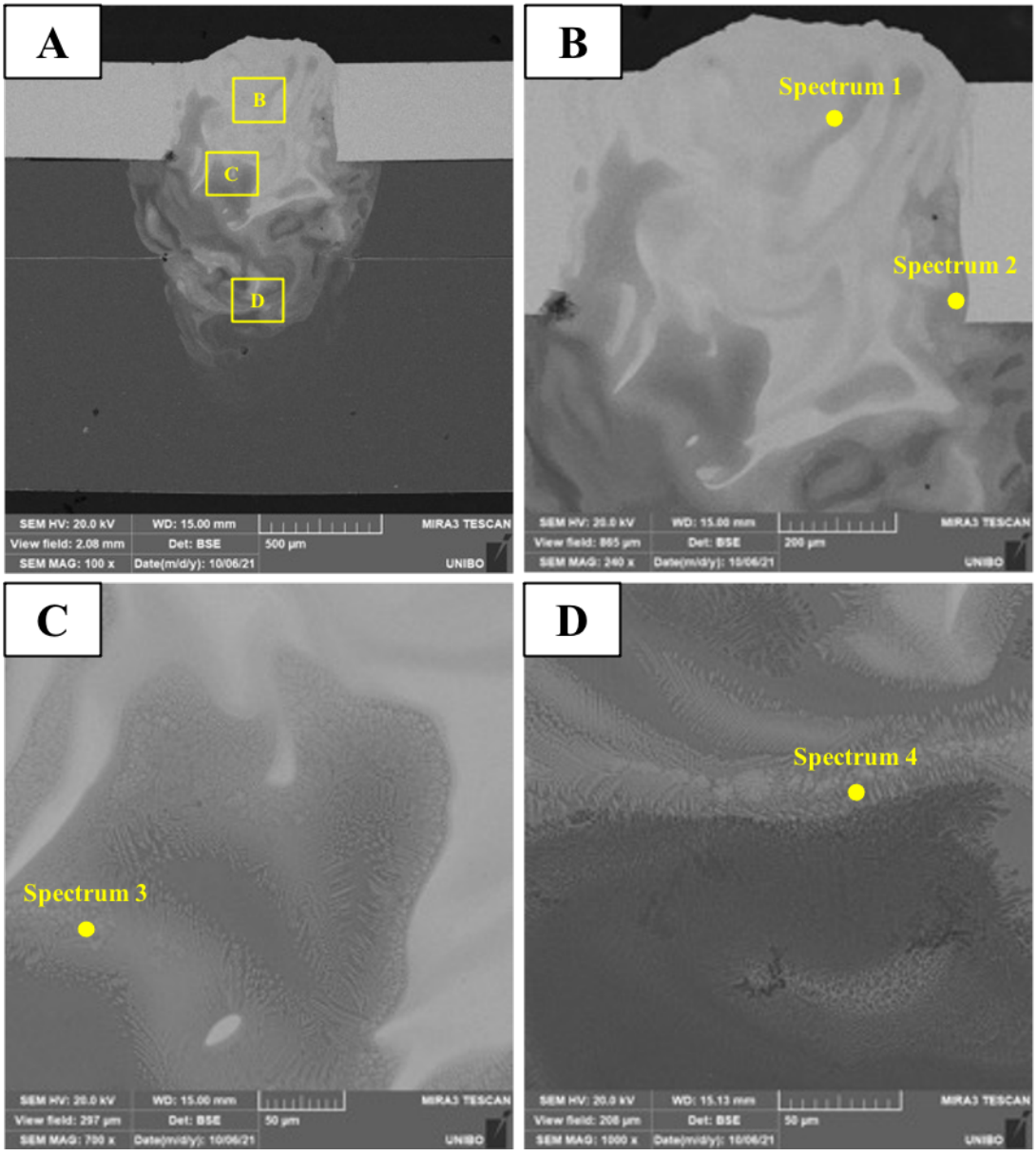

Figure 97: Scanning electron microscope images of the sample welded with power of 750W, welding speed of 50 mm/s and wobbling amplitude of 0.5 mm.

Zone	O (at. %)	Al (at. %)	Cu (at. %)	Possible Phase
Spectrum 1	0.34	53.31	46.35	η (AlCu)
Spectrum 2	1.13	40.34	58.53	$\zeta(Al_3Cu_4)$
Spectrum 3	0.8	74.22	24.98	Al+ $\Theta(Al_2Cu)$
Spectrum 4	1.11	46.14	52.75	η (AlCu)

Table 26: Chemical composition of denoted zones in Figure 97.

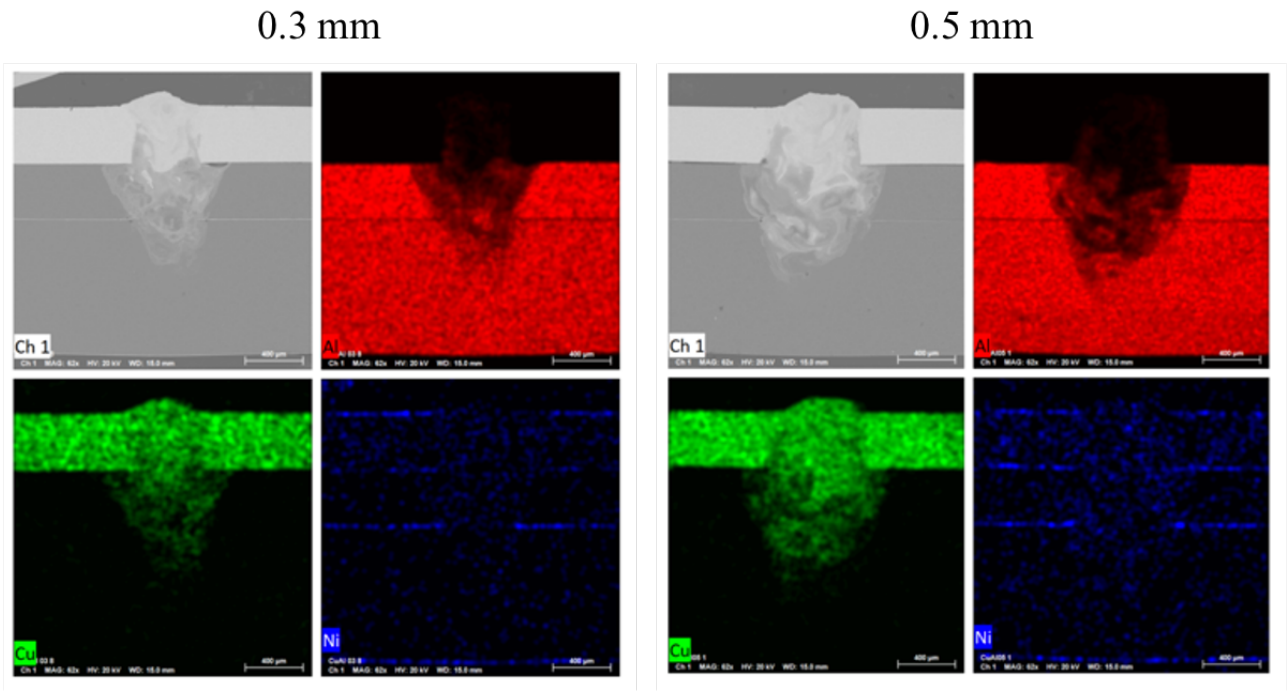

Figure 98: EDS element mapping of the welded sample with copper as upper material.

4.4.7. Conclusions

The effect of process parameters on the weld seam properties during the welding of tab-tab-busbar configuration have been investigated. Both possible welding configurations have been studied, in relation to the different positions of the layers during the assembly of the battery module from which important choices in terms of design arise. For each configuration, laser power and welding speed and wobbling amplitude have been varied and the results firstly were characterized by means of optical and stereo microscopes, mechanical and electrical tests in order to characterize the joining process. After a feasibility process window was defined, aging tests due to current transmission have been carried out with the aim to obtain firstly both information about the properties of the connection at the end of battery life in terms of current cycles and defining the possible defects / errors that can most affect the success of the process during the assembly of a real module and finally understand which configuration is more convenient taking into account all these variables. To do this, after having monitored several properties of the connections, the results were characterized by means of optical microscope, shear tensile test, electrical contact measurements and SEM-EDS analysis. The main conclusion can be summarized as follow:

- Both the welding configurations in terms of materials placement have been investigated with good results for both; when aluminum is the upper materials micro transversal cracks, which seem to not affect the joint's performance, can be found due to physical properties of the base materials.
- A larger wobbling amplitude allow to enhance the interface width of the connection, by reducing the penetration depth of the latter if the same laser parameters are applied. However, the greater the area to be scanned, the greater the energy to be provided with greater dilution of the materials and formation of hard and brittle phases.
- For the Cu-Al-Busbar configuration, the maximum measured breaking load was about 900 N with a wobbling amplitude of 0.5 mm; the ductile break was recorded at the aluminum tab in an area far from the weld bead. As the energy density increases, the mechanical properties are reduced and the breakage, of a brittle type, occurs at the weld bead. The same considerations apply to the Al-Cu-Busbar configuration; the maximum measured breaking load was about 700 N with failure located in the center of the weld seam near the copper tab.
- The micro-hardness profiles have confirmed that, at the center of the bead, there is an increase in the hardness values due to the mixing between the materials; higher values have been

obtained when the energy supplied is high and especially for the configuration with aluminum as upper material with values of about 900 $HV_{0.1}$.

- The measured electrical resistance values, with the optimized parameters, were approximately 26 μΩ for both welding configurations. Especially for the Cu-Al-Busbar configuration a linear correlation was obtained between the electrical and mechanical properties of the joint.
- After the aging cycles, it can be said that if on the one hand, the configuration with aluminum as a material in 'contact' with the laser allows greater freedom (during battery assembly) in terms of focal distance and possible errors, this is not the best solution in terms of joint performance, especially at the end of its life. The configuration with copper as upper material allows to obtain the best properties obviously at the expense of greater accuracy, especially in respect of the focal distance; a possible rework, although not ideal, has been shown to be a valid alternative in case of errors.
- From the point of view of the process parameters, the best solution is the one that provides for a reduced wobbling width as the lower the energy input provided with better mixing between the materials. The results were confirmed by the SEM-EDS analysis.

5. Welding of prismatic cells

The second experimental chapter describes the results concerning the welding of prismatic cells. During the assembly of a battery module based on this type of cells only one welding configuration occurs, i.e. the one that involves the joining of a busbar and the electrodes of the cell both made of pure aluminum. For this reason, only the welding of the busbar with the tab of the cell was investigated and the entire process was characterized in compliance with the process constraints that the application provides.

5.1. Materials and methods

The tested material is EN- AW1050 aluminium alloy having a nominal elemental composition of 0.40 wt% Fe, 0.25 wt% Si, 0.07 wt% Zn, 0.05 wt% of each Mg, Ti, Mn, Cu, 0.03 wt% other and the balance Al (i.e. ~99.5 wt%). In this study, 1.5 mm Al sheet was used as the upper material and welded to 4 mm thick Al sheet in lap joint configuration as shown in Figure 99.

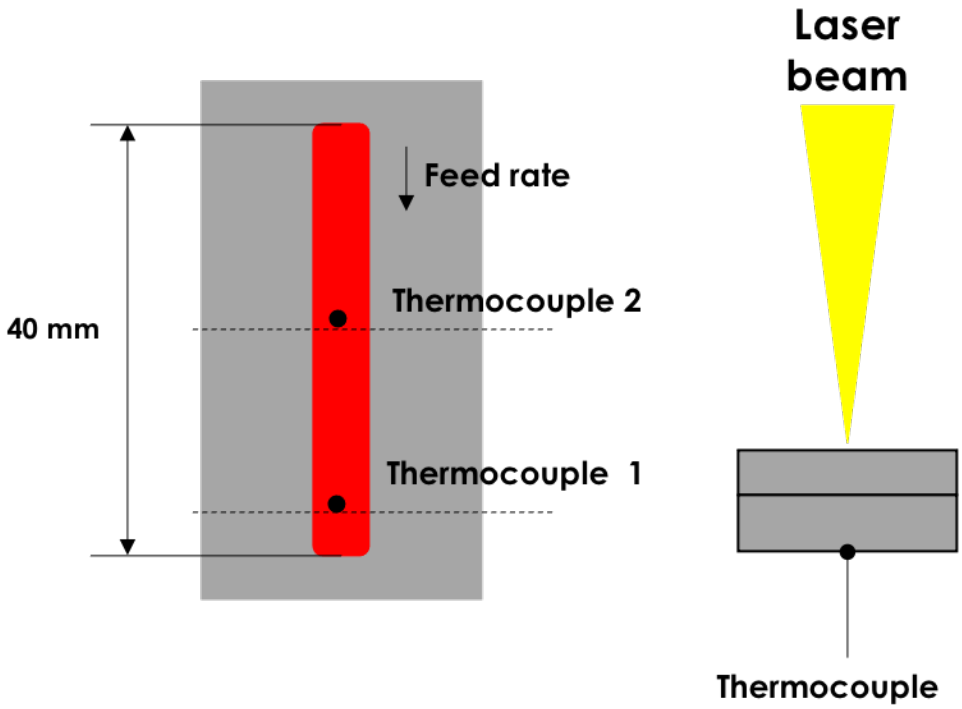

Figure 99: Welding setup for prismatic cell welding.

The laser welding was conducted using a nLight Alta 3.0 kW Yb:Fiber laser with a near-infrared wavelength of 1070 nm and delivery fiber core diameter of 50 µm was used for experiments; the

employed welding optics included a Scanlab HurryScan galvanometric scanning head combined with a fused silica f-theta lens characterized by a 163 mm focal length, achieving a theoretical spot size of 68 μm. The hardware specifications are reported in Table 27.

Laser source		**Optical chain**	
Specification	Value	Specification	Value
Wavelength	1070 nm	Collimation length	120 mm
Operating mode	CW	Focal length	163 mm
Emission power	3000 W	Fiber core diameter	50 μm
BPP	≤ 2.8 mm·mrad	Focal spot diameter	68 μm

Table 27:Hardware specifications used during the prismatic cell trials.

A series of preliminary tests were conducted to establish the parameter range to be used in the study. Based on this study, the laser power was varied from 1500 W to 2000 W and welding speed from 20 mm/s to 60 mm/s while the wobbling amplitude was fixed at 0.2 mm and wobbling frequency was 250 Hz. During the preliminary tests also the effect of different shielding gas on the weld bead's morphology was investigated; in any case, the beads obtained had superficial defects and high porosity, above all due to the turbulent phenomena that arise due to the particular shape of the tool used to ensure correct adhesion between the layers. For this reason, no shielding gas was used during the trials. The welding parameters used during this study are reported in Table 28.

Laser power [W]	**Welding speed [mm/s]**	**Wobbling amplitude [mm]**	**Wobbling frequency [Hz]**
1500	20	0.2	250
1500	40		
1500	60		
1750	20		
1750	40		
1750	60		
2000	20		
2000	40		
2000	60		

Table 28: Welding parameters for busbar-tab welding configuration of prismatic cells.

The study involved two different phases, the first in which 40 mm long linear seams were made as shown in Figure 99; the samples were cut and then mounted in g resin. They were ground and polished and then etched in order to reveal the microstructure of the fusion zone by using Keller reagent for 15s. Penetration depth and interface width were determined by means of optical microscope ZEISS Axio Vert.A1M. Microhardness profiles were measured using 100 gf load and a 20s dwell time to observe the hardness values of the weld region and base materials. After understanding how the laser parameters interact with the material, shear tensile tests were carried out tests were performed at room temperature with an INSTRON 8033 tensile testing machine at a crosshead speed of 0.025 mm/s. For this purpose, with the aim of testing a possible final welding configuration during assembly, circle-shaped welds, with a radius of 5 mm, were carried out on specimen using the scanning head, as shown in Figure 100(a). The samples were 70 mm long and 30 mm wide welded with a 25 mm overlap; the tests were repeated three times under the same conditions and average values was obtained. On the same specimens, electrical contact measurements were conducted by means of probe point measurements technique using a Chauvin Arnaux CA 6255 micro-ohmmeter characterized by an accuracy of 0.1 μΩ by applying a current of 10 A for 20 s with a measurement length between the points of 30 mm as shown in Figure 100 (b). During the trials, two K-type thermocouples were positioned in the lower part of the last sheet to monitor the maximum temperature attained during the process since a critical aspect during the assembly of this kind of cells is the temperature reached near the last sheet, which simulates the cell's in contact with the electrolyte; an increase in temperature, beyond a threshold value, leads to a thermal runaway of the cells with consequent damage to the entire battery pack.

a) b)

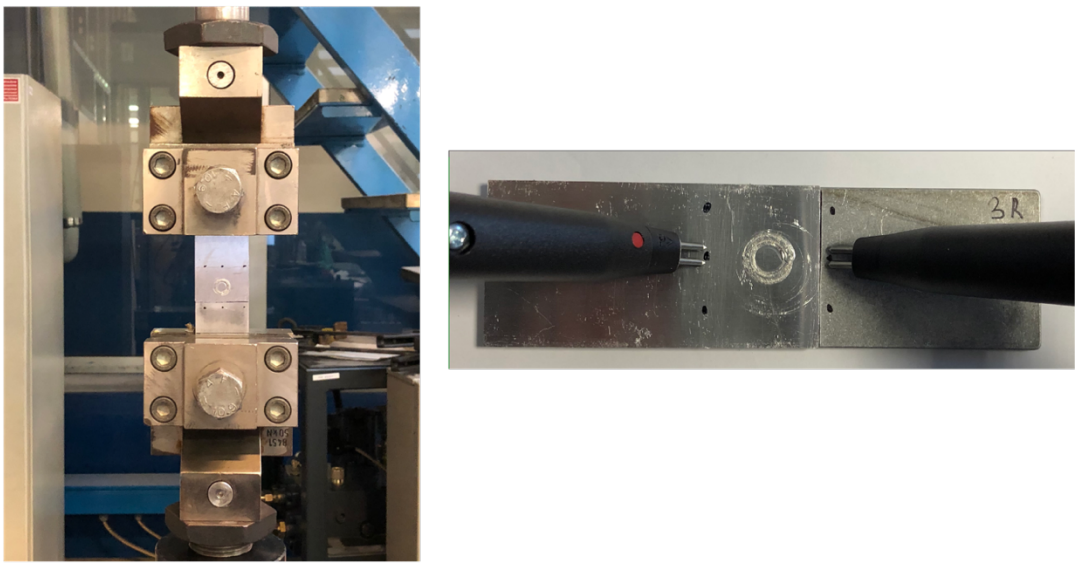

Figure 100: Shear tensile test setup (a) and electrical contact resistance measurements (b).

5.2. Metallographic analysis

The cross sections of the weld seam obtained with different welding parameters are shown in Figure 101; once cross-sections were obtained, it was possible to measure the geometric characteristics of the weld seam, in particular the weld width at the interface and the penetration depth taken into account from the interface of the sheets as shown in Figure 102. It is evident that the weld bead dimension increases as the welding speed decreases due to the rises of the heat input, in terms of linear energy density; this is in accordance with what found and discussed by Sanchez-Amaya et al. **[82]**. Using the same images of Figure 101, it was possible to determine the presence of porosity, the most common defect in aluminum welding due both to the low solubility of hydrogen in solid aluminum and to the stability of the keyhole, determined in turn by different forces such as, recoil pressure, surface tension, hydrodynamic and hydrostatic pressure **[83][84]**. As the heat input increases the recoil pressure increases as well which lead to the unbalance of the forces resulting in the instability and collapse of the keyhole; therefore, the gas inside gets isolated and bubbles are formed. Regarding the welding parameters, there seems to be a beneficial effect in increasing the welding speed, since it is true that the size of the weld seam is reduced from 20 mm / s to 60 mm /s, but also the presence of pores and their size decreases. These results agree with previously studied and analysed by other authors; for example, Norris et al. **[85]** found that more pores can be generated at lower welding speed and the average size of porosity increases when heat input increases as well. The effect of process parameters on interface width and penetration depth are reported in Figure 102. It was observed, for all the laser power investigated, that the interface width decreases as the welding speed increases as less energy was available to melt the materials. With laser power of 2000 W the interface width was about 1.9 mm at 20 mm/s up to values of 0.8 mm with 60 mm/s, while with the lower laser power of 1500 W values between 1.2 mm and 0.8 mm were measured. An increase in heat input produces weld seams with a wider interface width and deeper penetration depth as shown Figure 102(b). As seen previously, also in this case an increase in speed translates into a reduction of the penetration depth due to due to decreased time to melt and fuse materials. The penetration depth measured was 1.3 mm at 20 mm/s and was gradually decreases to 0.9 mm with laser power of 2000 W; by reducing the laser power to 1750 W the values were about 1.3-0.8 mm. At lower laser power of 1500 W, the penetration depth measured were about 0.9-0.6 mm.

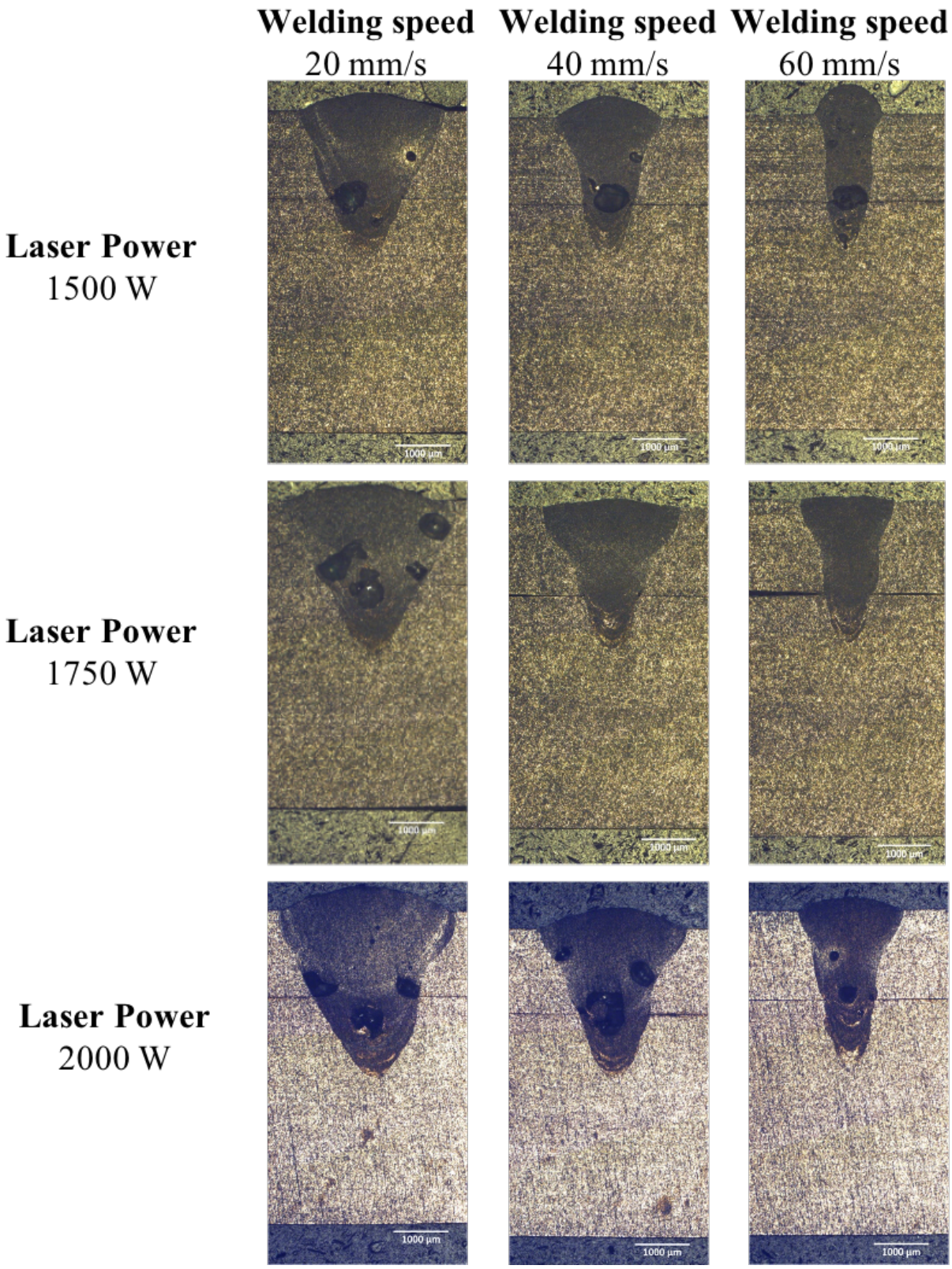

Figure 101: Cross section images of the busbar-tab weld configuration for prismatic cells.

a)

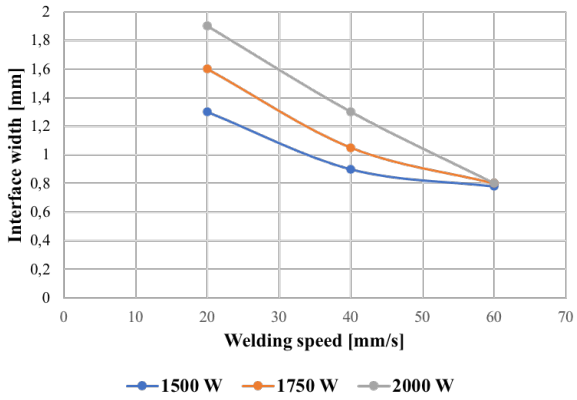

b)

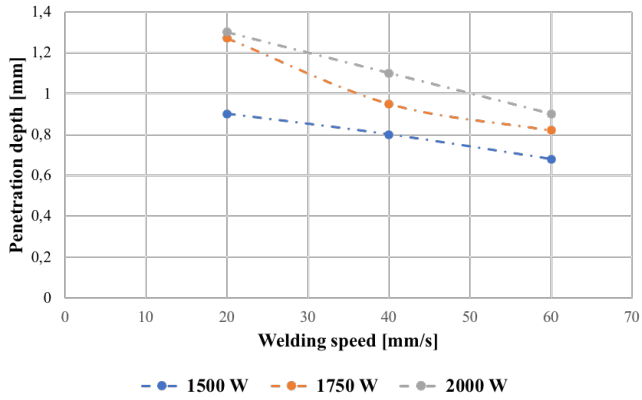

Figure 102: Effect of process parameters on interface width (a) and penetration depth(b) in busbar-tab configuration.

5.3. Shear tensile test results

Table 29 summarized the process parameters used for tensile tests; as it can be noted, the samples obtained at 20 mm/s were not tested as the metallographic analysis revealed a high presence of defects and due to the excessive heating of the parts. Three repetitions were conducted for each welding configuration and average values were obtained.

Sample	Power [W]	Welding speed [mm/s]	Weld width [mm]	Penetration depth [mm]
A	1500	40	0.9	0.8
B	1750		1.05	0.95
C	2000		1.3	1.1
D	1500	60	0.78	0.68
E	1750		0.8	0.8
F	2000		0.8	0.9

Table 29: Process parameters used for tensile test in busbar-tab configuration

The average maximum breaking loads as a function of laser power and welding speed are plotted in Figure 103. At 40 mm / s a small variation in the maximum breaking load was recorded between 1500 and 1750 W with values of about 2.1 kN; at 40 mm / s a small variation in the maximum breaking load was recorded between 1500 and 1750 W with values of about 2.1 kN; increasing the laser power again to 2000 W there is a net increase in resistance with loads of about 2.9 kN which may be due to the increasing larger interface width or deeper penetration depth. A reduction in the resistant section is the reason for having lower resistances at 60 mm/s in which the maximum breaking load reached acceptable values of about 2 kN at laser power of 2000 W; the lower mechanical properties, to which corresponds values of 1.4 kN, were obtained with power of 1500 W. In general, the failure occurred near the transition zone between the first and second lamination, where there is the greatest concentration of porosity and therefore a reduced resistant section.

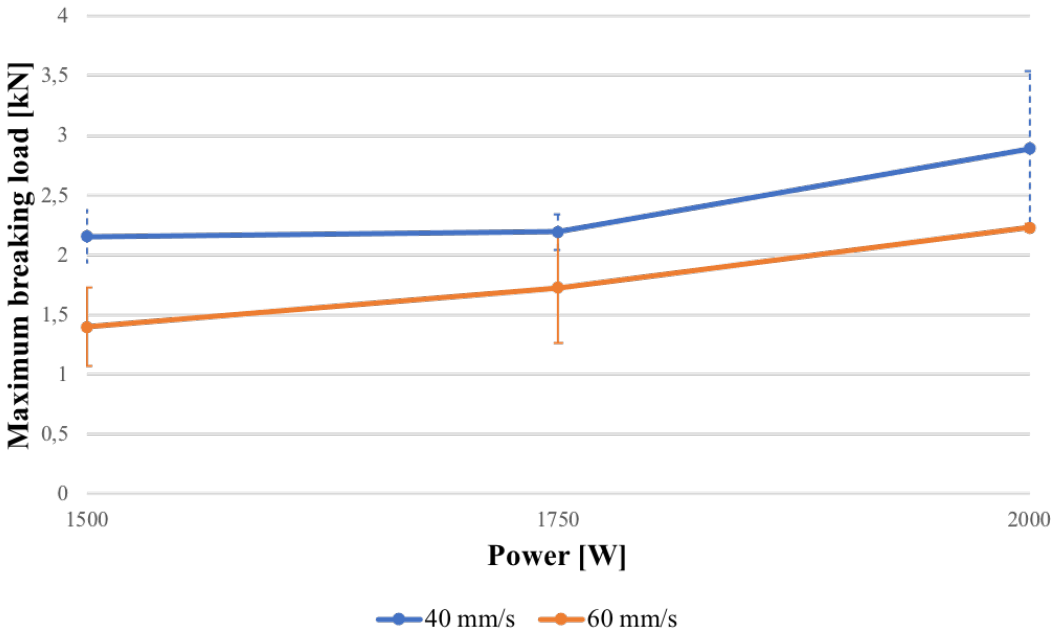

Figure 103: Shear tensile test results for busbar-tab configuration.

5.4. Micro Hardness results

For micro hardness measurement, a sample was selected from a good quality joint. The hardness distribution of weld produced with the laser power of 1750 W and 40 mm/s welding speed is shown in Figure 104. It can be observed that the hardness of the as-received 4 mm thick lower base material was approximately 38 $HV_{0.1}$ whereas the average of the upper 1. 5 mm sheet was around 36 $HV_{0.1}$. A total of 7 measurement points were made between the bead and the base materials for both sheets at a distance of 100 µm from the interface between the latter. Starting from the base material, the micro hardness value undergoes a reduction in correspondence with the heat affected zone and in the central zone of the weld seam up to values of 27 $HV_{0.1}$ and then returns to the values of the base material. Same trend for the lower sheet, in fact there is a decrease in the hardness value near the center of the bead. The uneven formation and distribution of the grains can be responsible for the fluctuations of the hardness drop inside the fused zone. The heat input and softening during laser welding resulted in the release of internal tensions between the grains and the formation of new grains inside the melting zone, with a consequent reduction in hardness in the fused zone and in HZA.

a) b)

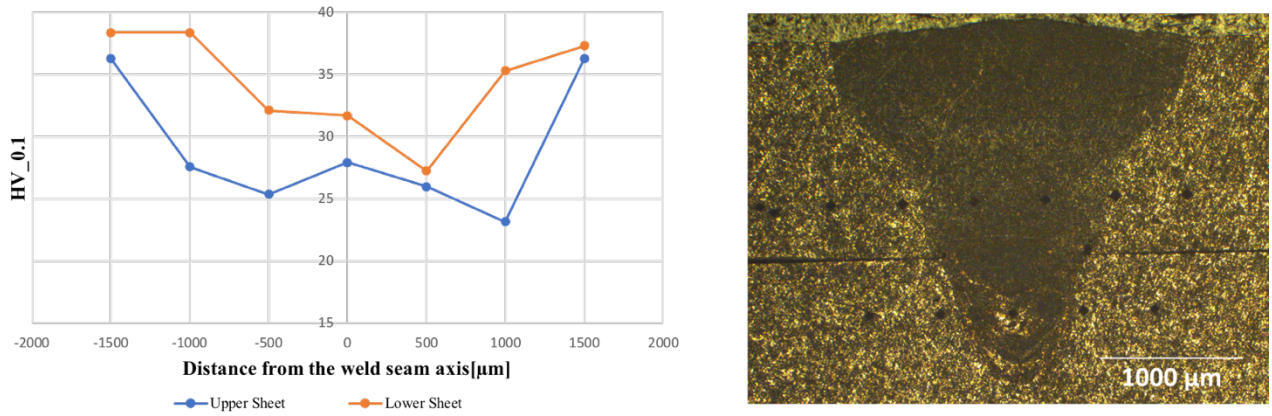

Figure 104:Hardness profile of the samples welded with laser power of 1750 W and welding speed of 40 mm/s(a), Vickers indentations position(b).

5.5. Electrical contact resistance results

Figure 105 reports the electrical contact resistance results for the tested sample with different process parameters. The values obtained are approximately constant and included between 13 and 15 μΩ for all the tested conditions. Unlike the joining between dissimilar materials, where the intermetallics that are formed have low electrical conductivity, in the welding of the tabs of the prismatic cells these problems do not arise as the welding is between similar materials and therefore there are no intermetallics compounds after the solidification. Although the values differ from each other by a few micro-ohms, it must be remembered that an electric vehicle is made up of thousands of cells connected to each other; even the reduction of a few micro-ohms, on a high number of connections, involves a reduction of the thermal power dissipated by the Joule effect with increases in terms of vehicle performance and efficiency. Considering the data in terms of electrical contact resistance, the electrical performance of the prismatic cells is the highest ever and therefore to be preferred in the assembly of a battery pack for an electric vehicle.

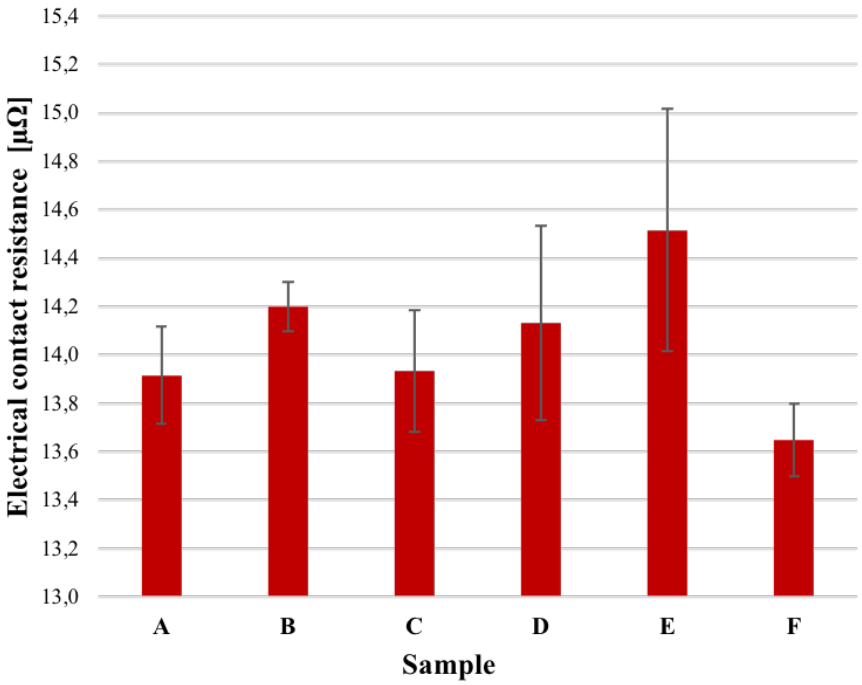

Figure 105: Electrical contact resistance results for busbar-tab configuration.

5.6. Temperature measurements

One of the challenges to be faced during the assembly of the battery module based on a prismatic cell is that due to the temperature that can be reached near the electrode (both positive and negative). In fact, an increase in temperature beyond a critical threshold, identified by the cell supplier, generates a thermal stroke of the cell which results in thermal propagation of the internal module with consequent dangers deriving from the triggering of uncontrolled combustion. The results of the temperatures measured at the lower part of the second sheet, which simulates the cell's tab, during the execution of a single circular soldering point are shown in Figure 106. As can be seen, the highest temperatures were measured at 40 mm / s for all the powers investigated with values of about 70 °C; a small increase in temperature was observed by increasing the welding power from 1500 to 2000 W. A net reduction in the temperatures measured was obtained with a speed of 60 mm /s; in fact, higher welding speed, with the same power, allow to reduce cycle times and consequently the temperatures reached. At lowest welding power of 1500 W, the temperature measured was about 55°C, which reached 65 ° C with laser power of 2000 W. From the results obtained, it can be seen that the high process speeds and the possibility of concentrating high quantities of energy on small areas guarantee compliance with the main constraint imposed by the application.

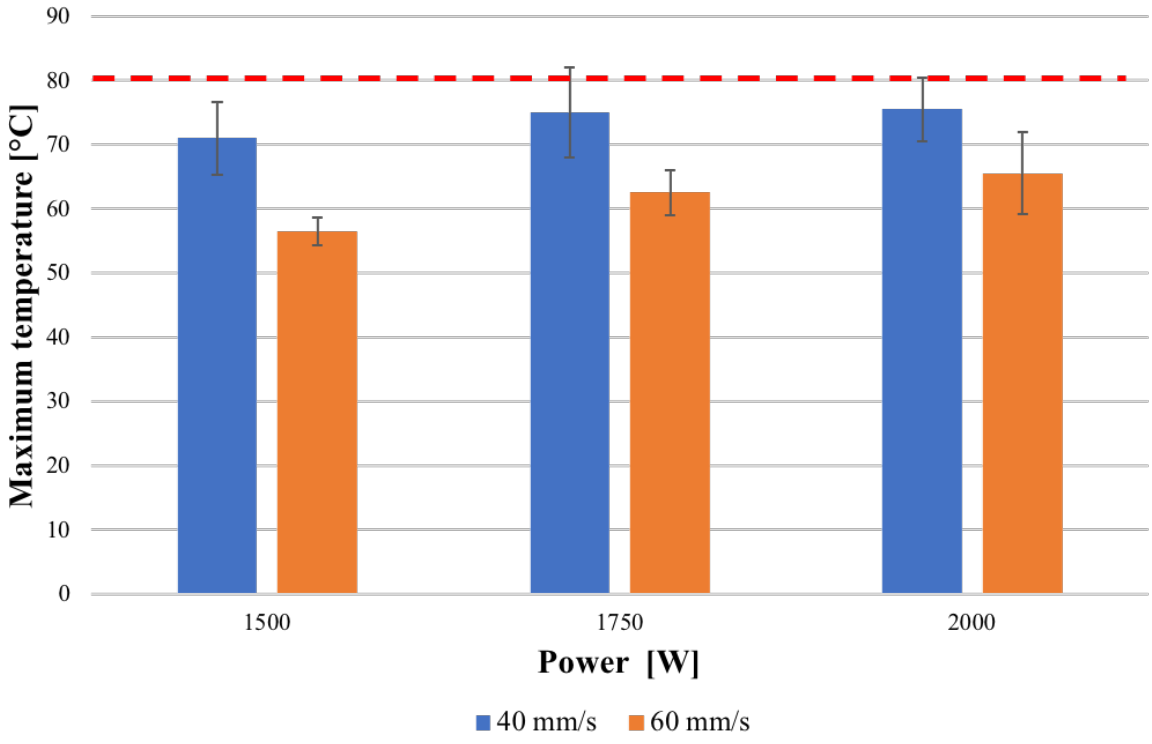

Figure 106: Temperature results for busbar-tab configuration.

5.7. Conclusions

Busbar - tab configuration required in the welding of battery modules based on prismatic cells has been studied by means of continuous wave laser welding with spatial beam oscillation of the beam and the results have been characterized through metallographic analysis, mechanical characterization tests with the aim of respecting the main process constraint imposed by the application. The conclusions of the activities can be summarized as follows:

- With the process parameters investigated, weld beads characterized by good morphology were obtained; as the laser power increases, with a fixed welding speed, both the width of the seam interface and the depth of penetration increase as the heat input is greater. The presence of porosity and above all the dimensions of the latter decrease as the speed increases for all the powers investigated.
- Mechanical resistance, in terms of maximum breaking load, is linked to the process parameters. Values of about 2-3 kN were obtained at 40 mm/s with the laser power investigated; an increase in welding speed to 60 mm/s results leads to a reduction of the maximum breaking load of about 20%.
- The micro hardness profiles showed a decrease in hardness near the fused zone of a value equal to about 10 HV compared to the base material due to the enlargement of the grain due to the thermal cycle undergone by the material.
- The temperatures reached near the bottom of the last layer, which simulates the cell tab, have never been higher than 80 °C. From this point of view, a clear benefit is given by working with high process speeds thanks to the reduced laser beam-material interaction times.

6. Welding of pure copper hairpins

In the third and last experimental chapter the results concerning the welding of pure copper hairpins have been reported. During the assembly of a winding stator of an electric motor the joining of copper conductors, in a small work zone, with a rectangular shaper are required. For this reason, the welding of the copper pins in edge joint configuration was investigated and the entire process was characterized.

6.1. Materials and methods

Rectangular sticks, 1.5 mm wide and 4.5 mm long, in pure enamelled copper (Cu-ETP) were used for welding test. The samples were cut into 100 mm long chunks before welding, and the insulation was physically removed over a length of around 10 mm. A clamping mechanism was designed and positioned under the scanning lenses to ensure the right position of the samples and, preferably, a zero gap on top of the hairpins. High-pressure air cross-jet was used to protect the lens from spatters and no shielding gas was used during the trials. A sketch of the laser system setup is reported in Figure 107(a). Thanks to the high acceleration and dynamics the galvo scanner a suitable welding path was implemented, consisting of a rectangle filled in with solid lines, as shown in Figure 107(b). The main idea was to supply a pre-heating of the scanned zone by means of the external rectangular perimeter and then generating the molten pool by means of the internal hatching. The rectangle, with an area of 0.8x3.8 mm^2, was centred to the hairpin face and it was smaller than its cross section; the correct position of the scanned trace was guarantee by a coaxial camera to the laser beam.

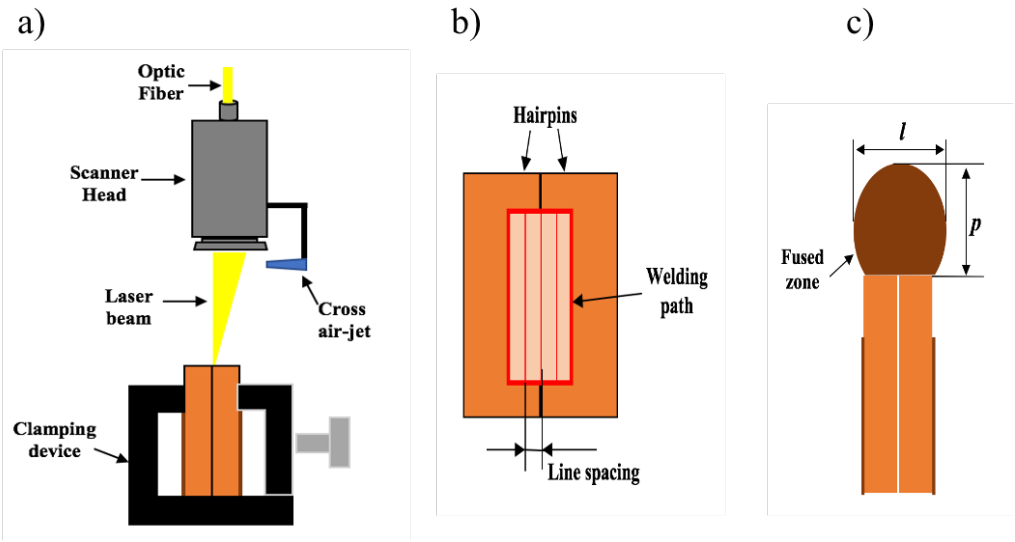

Figure 107: Welding setup (a), scanning strategy (b) and weld bead characteristics (c)[72].

The laser welding system was the same used for the other experimental campaigns whose characteristics are shown in Table 27. The trials were carried out by varying the laser power and welding speed while keeping the rectangular geometry and 0.3 mm line spacing constant. The laser power ranged from 1500 W to 2500 W while welding speed ranging from 50 mm /s to 200 mm /s. The power and welding speed combinations used in the experimental campaign were chosen to maintain a specified range of energy density, identified by means of a preliminary activity not discussed in this work. In fact, it was defined a lower [8 MJ/cm^2] and upper [18 MJ/cm^2] limit for this parameter: too low of an energy density determines insufficient laser-material interaction and lack of fusion in the weld bead, while too high of the same parameter determines over-melting, large porosities and high spatters. The energy density in this study was calculated by multiplying the power density [W/cm^2] by the whole welding time. With that definition, all of the major process factors, such as laser power, spot size, welding speed, and path length, may be considered. The entire experimental campaign is summarized in Table 30. Each combination of parameters has been repeated three times and mean values of weld bead characteristics have been calculated.

Sample	Power [W]	Welding Speed [mm/s]	Power Density [MW/cm^2]	Energy Density [MJ/cm^2]
1	1500	50	41.3	17.8
2	1500	75	41.3	12.2
3	1500	100	41.3	9.4
4	2000	75	55.1	16.3
5	2000	100	55.1	12.5
6	2000	150	55.1	8.8
7	2500	100	68.8	15.6
8	2500	150	68.8	11
9	2500	200	68.8	8.3

Table 30: Process parameter for hairpins welding trials.

Each specimen was cross-sectioned parallel to the hairpin axis, resin-mounted, polished with alumina (grain dimension 0.05 μm), and ultrasonically cleaned to remove sandpaper alumina and copper powder residues from the pores. Chemical etching with a 1:1 solution of nitric acid and distilled water allowed the fused zone of the welding to be demonstrated. All of the specimens had their penetration

depth p and bead width l measured according to the scheme in Figure 107(c), while average porosity inside the weld bead was determined by means of image analysis using ImageJ software. Peeling tests **[86]** were performed at room temperature with an Instron 8500 machine and a crosshead speed of 0.025 mm/s to determine mechanical parameters. Figure 108shows how the samples were bent following welding.

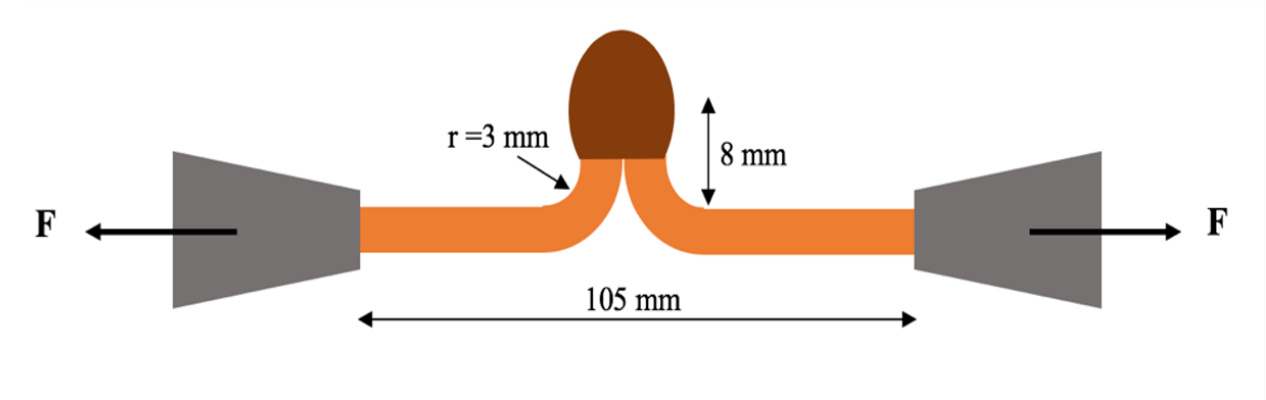

Figure 108: Peeling test scheme.

The change in hardness values were evaluated with Vickers tests with a load of 100 g and a dwell time of 20 seconds: seven indentations with a spacing of 300 µm were carried out to analyze the hardness profile from the base material to the fused zone, as shown in Figure 109(a). Electrical resistance was evaluated by means of the four-points method by means of a Chauvin Arnaux CA 6255 micro-ohmmeter: the resistance of the unwelded base material R_c was compared to the resistance of the welded hairpin Rw. SEM-EDS analysis was also carried out in order to understand the composition of the material in different positions with respect to weld bead and to understand the different microstructures occurring after welding.

a) b)

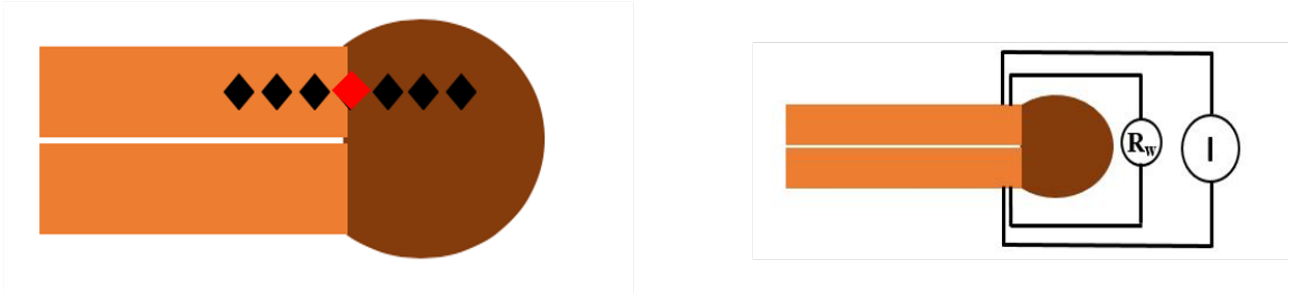

Figure 109: Vickers micro hardness (a) and electrical contact resistance measurements(b) schemes.

6.2. Metallographic analysis

A procedure feasibility window was defined using optical microscope pictures of the welded specimens, as illustrated in Figure 110. The morphology and eventual defects of the fused zone were linked to the judgment of "poor," "good," and "excessive" welding. In the case of column a of Figure 110, "poor welding" refers to a circumstance in which the fused zone has a very limited length and the electrical connection area is quite small. A well-balanced fused zone with a regular ball-shaped morphology (slightly larger than the cross section of the hairpin) and reasonably small pores indicates a "good welding" condition as indicated in column b of Figure 110. “Over welding” condition is distinguished by a large fused zone, characterized by big pores and a generally irregular shape of the weld bead with a high probability to have the dropping of liquid phase during the welding. In Figure 111 the feasibility process window in terms of laser power and welding speed is reported. The graph shows that when welding speed is low the over welding condition is easily reached both for low and high laser powers. As the welding speed increases, the role of the laser power tends to be more evident, since considering the position of the blue triangles and a line joining them, this is steeper than the x axis. In terms of energy density, the values that lead to over-weld conditions are around 16-18 MJ / cm^2, while a poor weld is obtained for around 8-9 MJ /cm^2. Energy density values between 11 and 13 MJ / cm^2 correspond to the green area in Figure 111 and guarantee a good weld with low porosity and an adequate melt zone shape. Each welding condition has been reported in the distribution map, so it can be concluded that it is reliable as a process feasibility map has been defined and areas where the process is not feasible as there is over-welding or poor welding**[72]**. It can be concluded by saying that the process is very sensitive to variations especially in terms of speed and power and that a correct setting of the latter allows to obtain a joint that covers both hairpins avoiding any dripping of material.

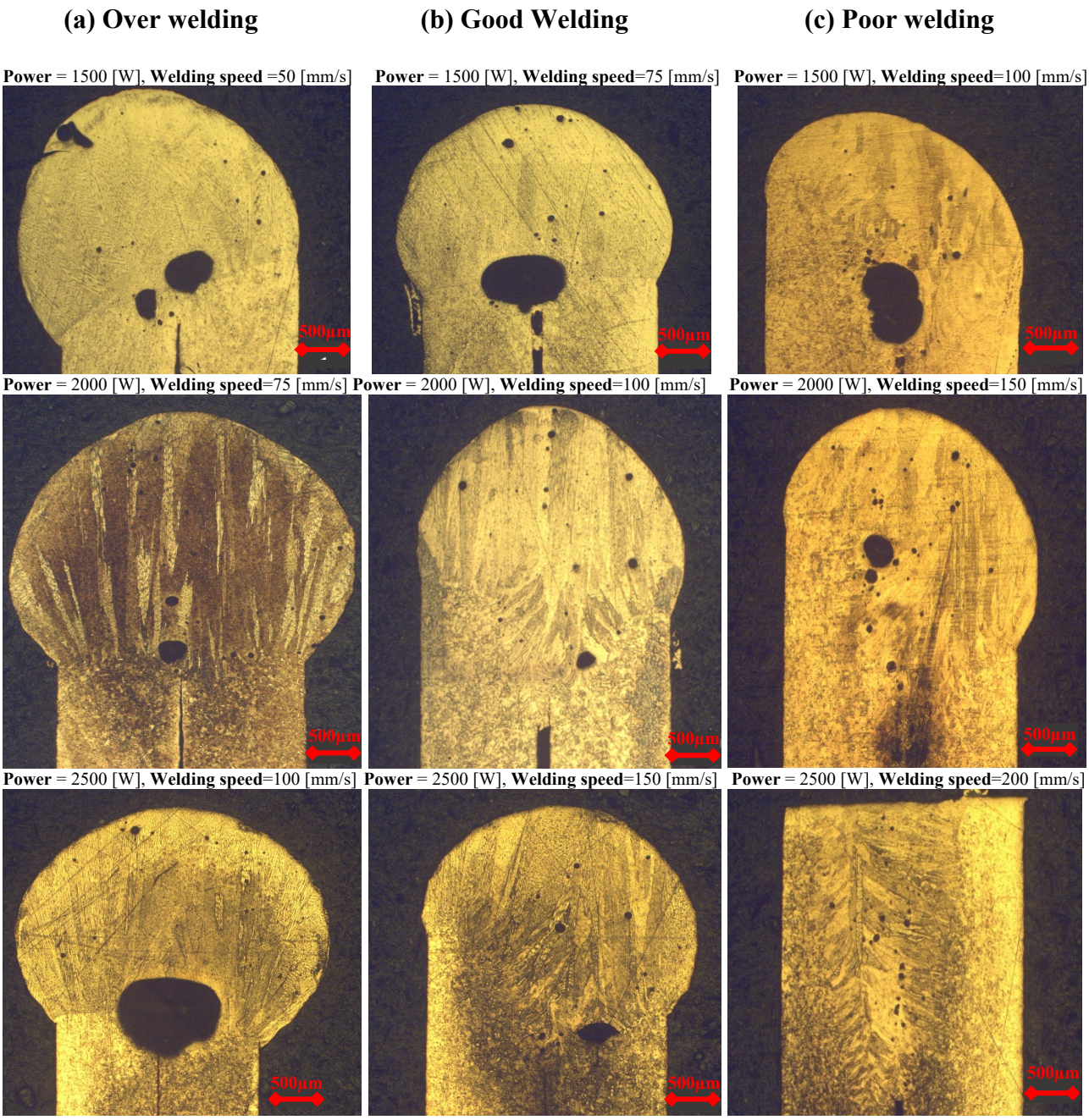

Figure 110: Cross section of pure copper hairpins obtained and type of weld seam: column (a) Over welding condition, column (b) Good welding condition and column (c) Poor welding condition[72].

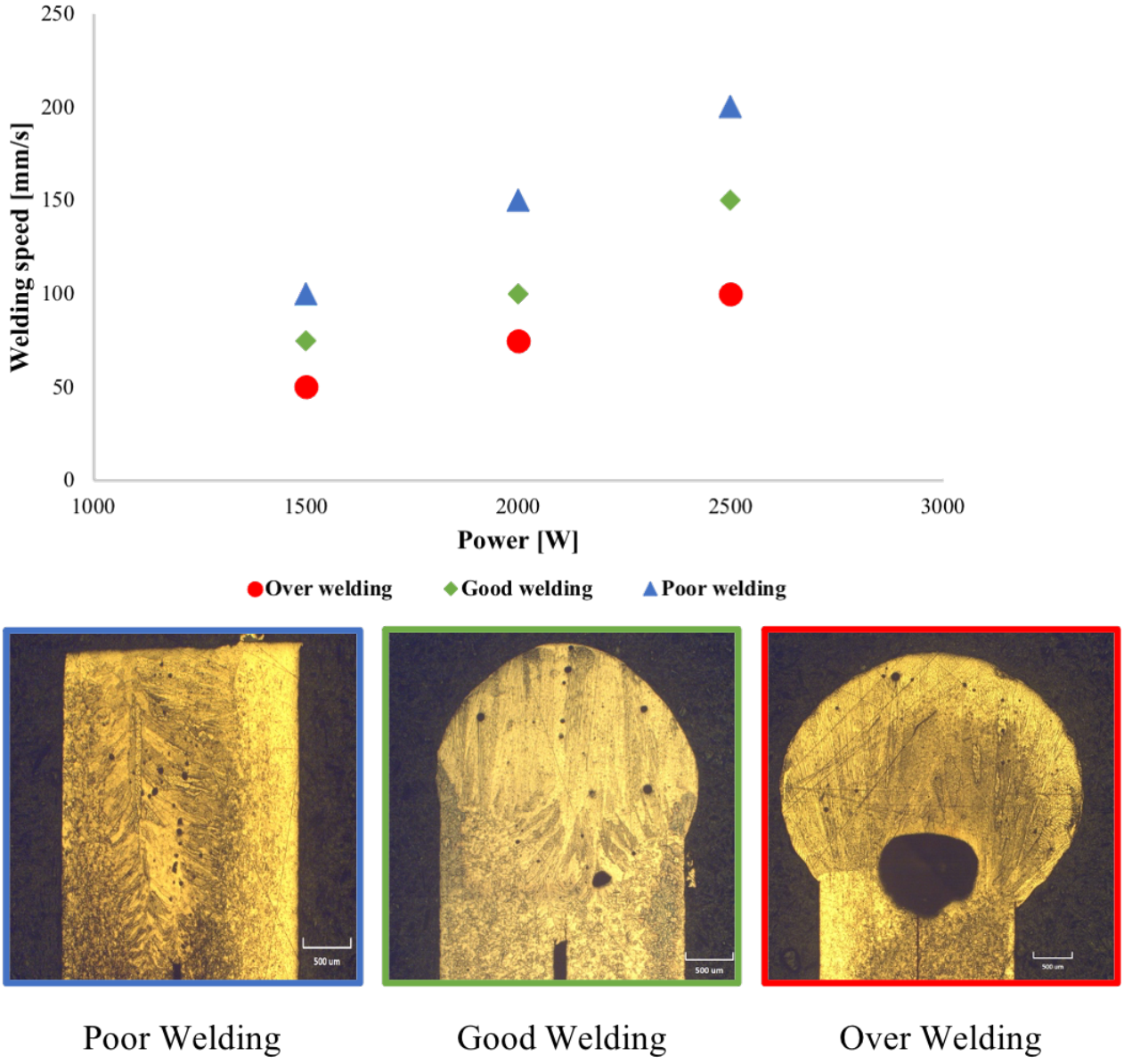

Figure 111:Feasibility process window for hairpins welding.

The bead width dimension as a function of feed rate and power is reported in Figure 112. Bead width is closely linked to the feed rate: it decreases almost linearly as the feed rate increases, regardless of the power level adopted. The graph also shows that bead width strictly depends on energy density: given three different sets of parameters that give very similar widths, their characteristic energy density is very similar one another and remains within a very small range. Considering the repeatability characterizing bead width, it can be noted that a major part of the error bars is very small. Only the specimens achieved with the maximum absolute energy density (laser power 1500 W and welding speed 50 mm/s) show a large variability: this is probably due to the high heat input that promotes low viscosity of the melt pool and low cooling rates.

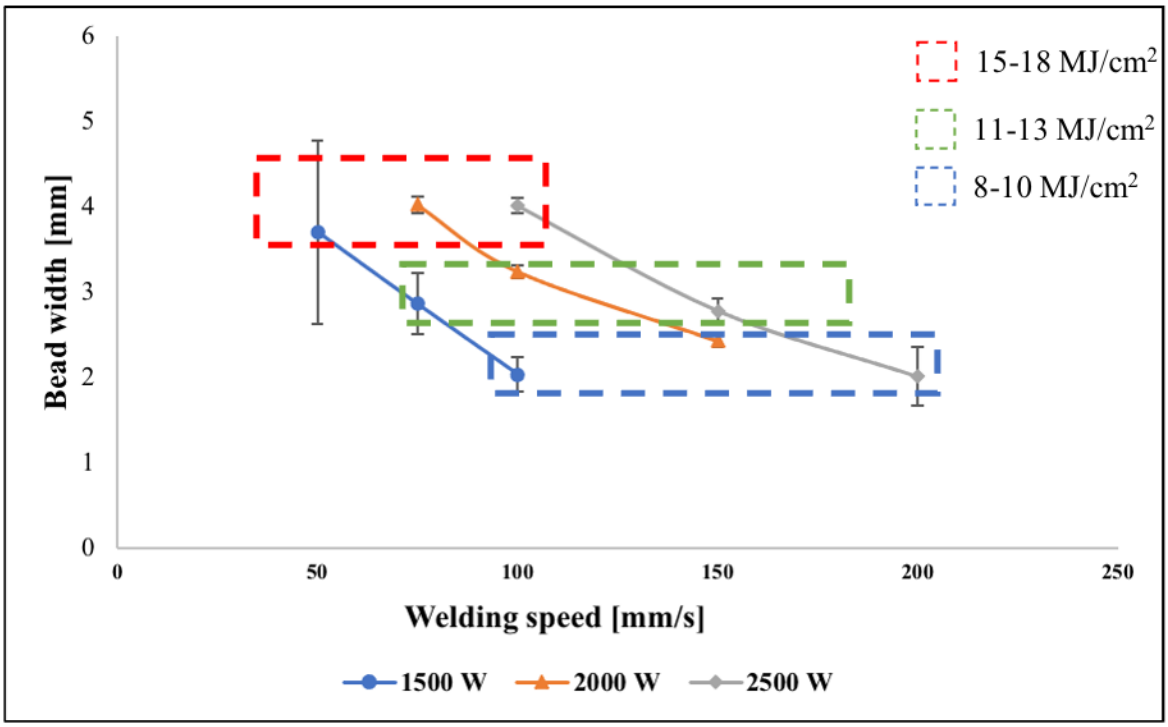

Figure 112: Weld bead width as a function of laser power and welding speed.

Considering penetration depth (see Figure 113) the relationship between this parameter and energy density is different: given three different sets of parameters that give very similar penetration depths, their characteristic energy density can be rather different one another. The repeatability of penetration depth remains good and it tends to decrease exploiting a low laser power: this is probably due to the fact that copper is highly reflective, and a low power density may fail to produce a stable keyhole during the process.

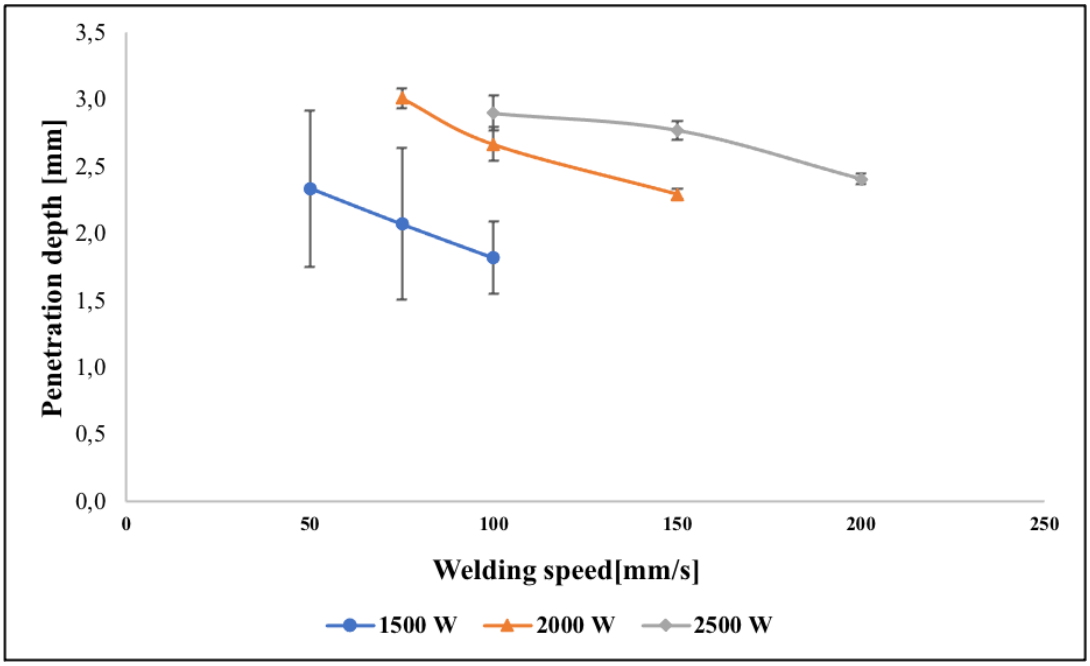

Figure 113: Penetration depth as a function of laser power and welding speed.

When it refers to the application of this type of welding in electro mobility, the main goal is to create joints with minimal electrical resistance. The area of the molten pool, which is directly connected to the area of the section through which the electric current flows, and the presence of defects and pores, which generate discontinuities in the electrical connection, were the first criteria taken into account in order to achieve this. The evaporation recoil pressure, which counterbalances the effects of surface tension and gravity force, forms and maintains a keyhole in deep-penetration laser welding. The effective power intensity is unequal due to several reflections at the bottom of the keyhole, leading in over-expansion of the lower half of the keyhole and instabilities of the keyhole and molten pool. The creation of a metal vapour bubble at the bottom of the keyhole, which ejects molten material if the pressure of the bubble exceeds the load of the melt pool, is responsible for the most common defects during laser welding of copper, such as porosity and spattering. **[87]**. In order to quantify the above-mentioned characteristics image analysis of the cross sections of the specimens was performed and the results are shown in Figure 114. When laser power is equal to 1500 W (samples 1-3) an increase in feed rate leads to a reduction of the molten pool area and to an increase in porosity. The large error bars show that the process in unstable, both in terms of molten area (solid line) and in terms of porosity formation (dashed line): this is due to the fact that the low energy density, together with the high reflectivity of the copper tend to promote the formation of an unstable keyhole during the process. When laser power is equal to 2000 W (samples 4-6) an increase in feed rate leads to a reduction of both the molten pool area and of the porosity. The error bars in this case are much smaller than in the previous case, confirming that an increase in energy density tends to promote a more stable process. When laser power is equal to 2500 W the trend is very similar to the previous case, but an important difference concerns the larger pore dimension especially at lower speeds. In this case pores tend to form near the transition zone between the fused zone and base material (see Figure 110(column a)) due to the turbulent flow of the molten material that prevents a quick release of the gases. Among all the experimental trials the best results in terms of porosity, molten pool area and repeatability of the results are the ones characterized by an energy density between 10 and 12 MJ/cm^2. The large error bars (in particular samples 2,3 and 7) show that the process in unstable in terms of porosity formation; with optimized parameters error bars are reduced but still the presence of pores is variable**[72]**.

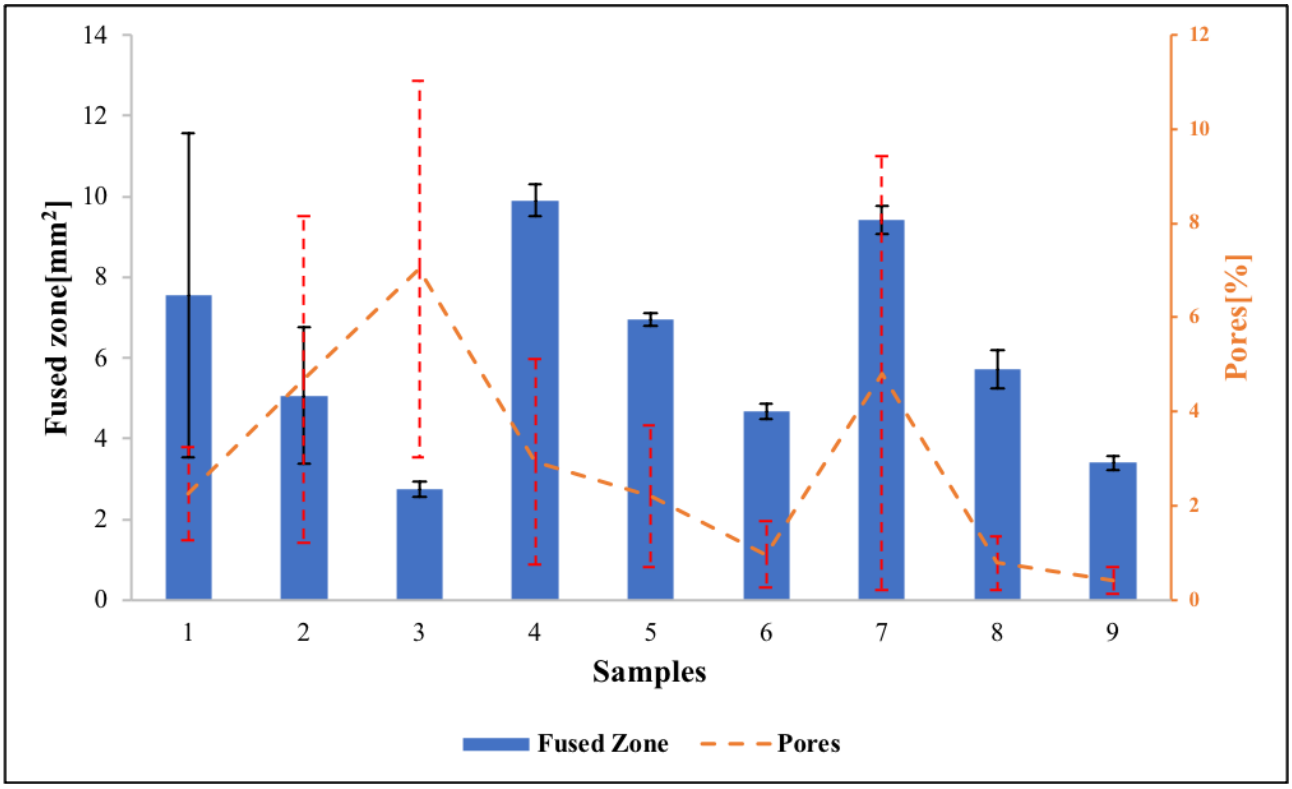

Figure 114: Porosity results obtained through image analysis.

6.3. Peeling test results

Peeling tests were conducted with the aim of obtaining information on mechanical strength of the weld bead and assessing the role of process parameters on the properties of the connection. The test was carried out primarily on the samples with the best morphological characteristics compared to that obtained with the process parameters that result in a reduced connection area or material's dripping. to understand, however, what also happens with the energy densities defined as non-optimal, a sample was also tested for each interval of the latter. Table 31 sums up the process parameters and the weld bead characteristics of the samples used for peeling test.

Sample	Power [W]	Welding speed [mm/s]	Energy density [MJ/cm^2]	Bead width [mm]	Penetration depth [mm]
2	1500	75	12.2	2.85	2.07
4	2000	75	16.3	4	3
5	2000	100	12.5	3.2	2.7
6	2000	150	8.8	2.4	2.3
8	2500	150	11	2.8	2.7
9	2500	200	8.3	2	2.4

Table 31: Process parameters for peeling test.

The results in terms of maximum breaking load as a function of energy density are reported in Figure 115. There is a definite maximum in the region of 11 to 13 MJ/cm^2, which supports the findings in the preceding paragraphs. The decrease in maximum tensile load in relation to low energy densities is owing to the fact that the quantity of molten material is limited in certain conditions, resulting in a tiny resistance section of the joint. When the energy density is high, however, despite the molten pool being quite large and consequently greater resistant section, the presence of pores tends to increase, reducing the total mechanical strength of the joint. The error bars show that when energy density is large, the process tends to be less repeatable. This is due to the fact that, in this case, the molten pool is large and with low viscosity and tends to form randomly asymmetrical weld beads. Of particular interest is the position of the failure; in fact, it has always been detected near the interface area between the base material and the molten area where a change in the microstructural properties of the material could occur but also the area where there is the greatest presence of porosity, as seen by optical microscope images, that weaken the joint.

a) b)

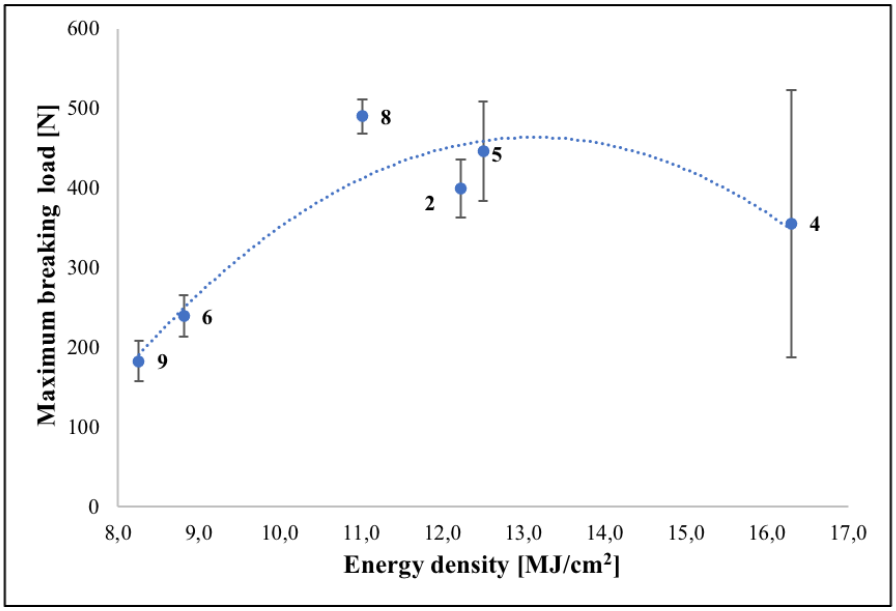

Figure 115: Peeling test results (a) and example of failure mode related to the position of the softening zone (b).

6.4. Micro Hardness results

The distribution of microhardness on the welded cross-section is shown in Figure 116: the indentations were carried out according to the scheme reported in Figure 109(a), where the red one corresponds to 0. Starting from the base materials, which has a hardness of 64 $HV_{0.1}$, the results show that a reduction in hardness values occurs both in the heat affected and in the fused zone reaching a minimum value of about 54 $HV_{0.1}$ near the transition zone between the base material and the fused zone. Since the profiles obtained are similar to each other, i.e. no important variation has been observed, it can be said that there is not an evident influence of the energy density on this phenomenon; it can be seen instead that for high energy density values, the area that has undergone microstructural changes is more extensive. As with any process that confers high heat input to the material, also in this case the softening may be caused by the decrease in dislocation density by the coarsening of grain in the weld seam consequent to the welding thermal cycle **[88].**

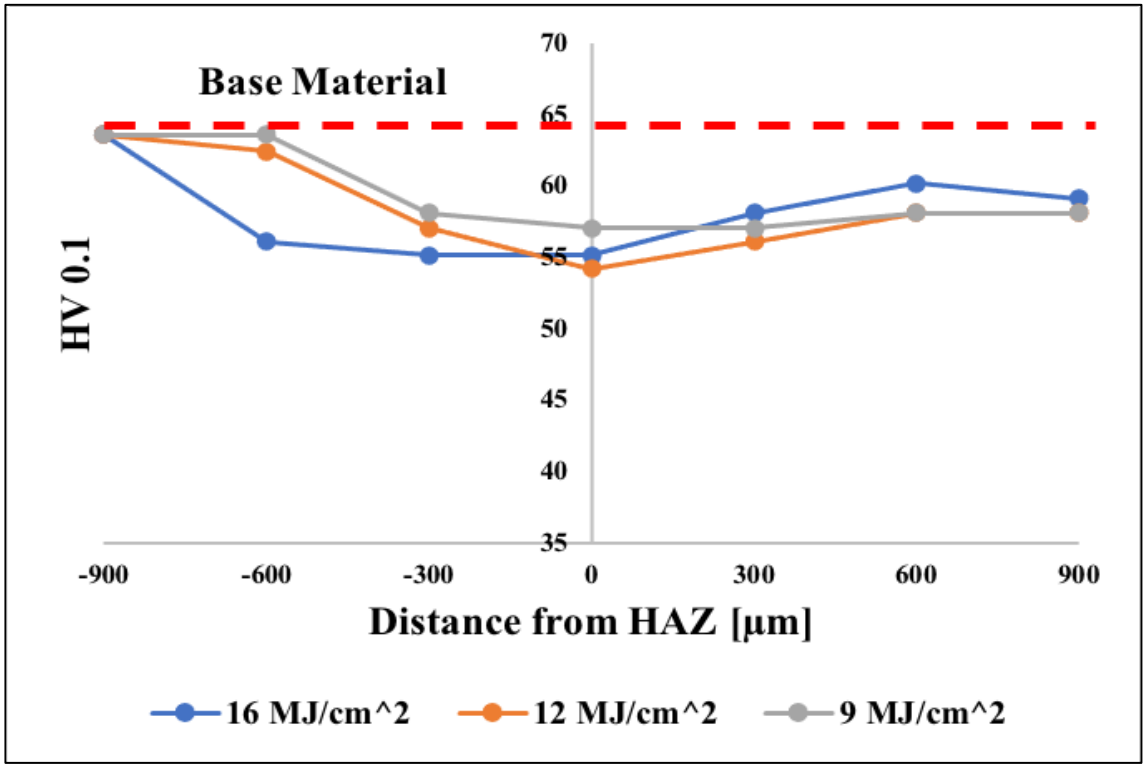

Figure 116: Micro-hardness profiles for the welded joints for the hairpins configuration.

6.5. Electrical contact resistance results

Given the application of hairpins welding in the e-mobility field, it is very important to quantify the resistance of the electrical connection produced. Figure 117 shows the electrical resistance depending on fused zone in area. The resistance of the unwelded conductor was 114 μΩ, with a measurement distance of 40 mm. The lowest resistances measured were in the range of 95 ÷ 100 μΩ, that correspond to a connecting area of 6-9 mm^2. When the connection area is lower, the electrical resistance increases accordingly. When the connection area is larger the electrical resistance increases again: this effect can be explained considering that large molten pool is a consequence of the application of high energy densities and are always accompanied by the formation of large pores that impair the quality of the connection[72].

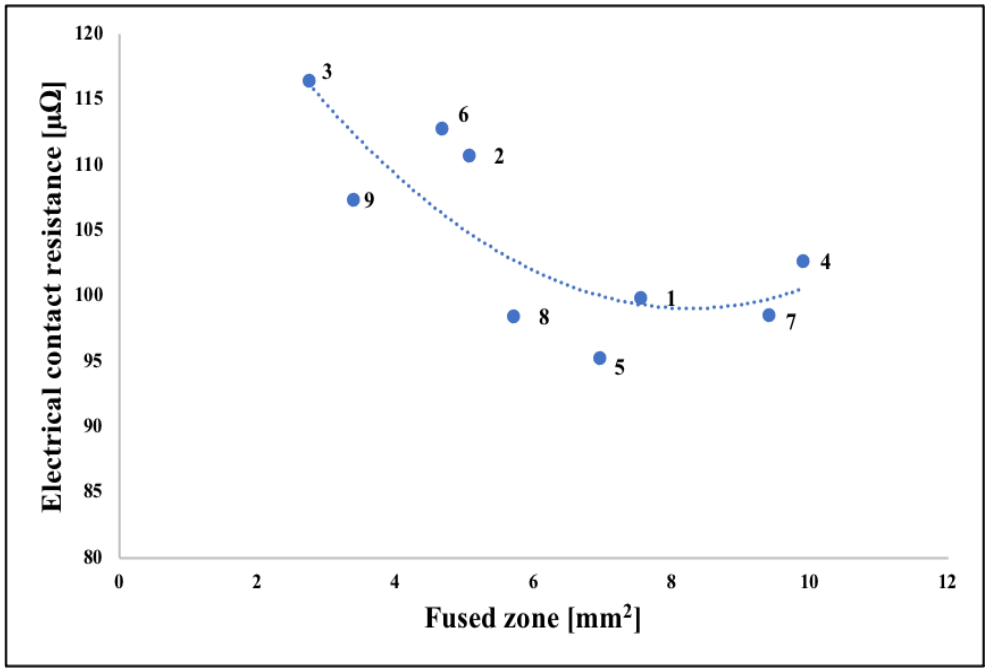

Figure 117: Influence of contacting area on electrical contact resistance [72].

A linear correlation between maximum tensile load and electrical resistance can be observed in in Figure 118, where the numbers on the graph represents the progressive numbering of the samples as reported in Table 31. It can be observed that a linear correlation exists between the mechanical and electrical properties of the connection; in fact, the higher the mechanical strength the lower the contact resistance of the joints which improve the performance of the winding stator composed by a several numbers of connections.

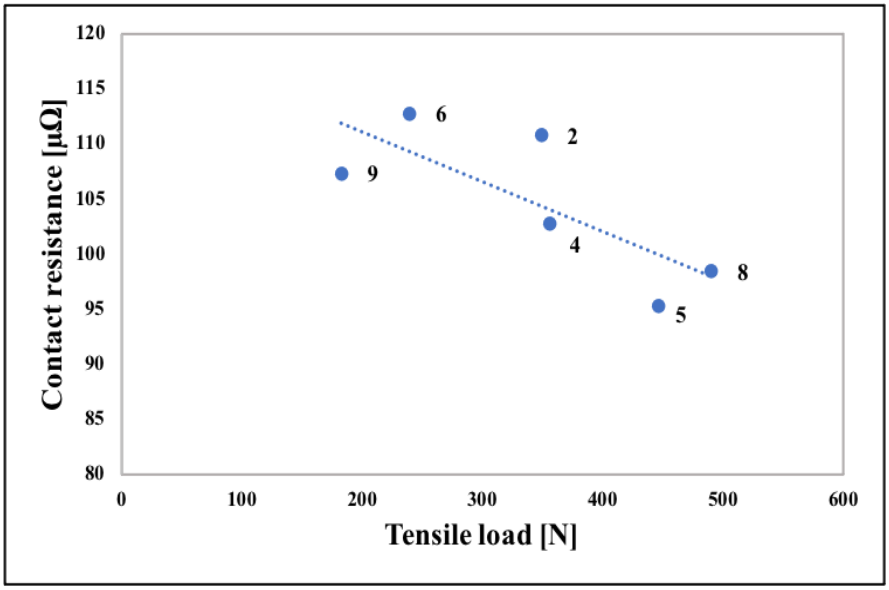

Figure 118: Correlation between tensile load and electrical contact resistance [72].

6.6. SEM-EDS analysis

SEM-EDS analysis pointed out different microstructures in the welded joint. Figure 119 shows the three zones corresponding to the red rectangles underlined: in the fused zone large dendritic grains with different orientations can be observed, while the base material is characterized by smaller equiaxed grains. These differences in the microstructure throughout the welding zones confirm the change in hardness underlined and discussed in paragraph 7.4 and the differences in electrical conductivities reported in 7.5. Concerning the drop of the hardness values in the fused zone, in fact, it was observed that the latter, which is characterized by large grains, shows a lower hardness than the base material that is characterized by smaller grains. Regarding electrical conductivity, on the other hand, it was observed that the welded hairpins show a lower electrical resistance than the unwelded ones: this is due to the fact that the melting process occurred in the joint promoted the formation of larger grains, eliminated the strain hardening of the base material and reduced dislocation density. All these effects are recognized as beneficial in the reduction of electrical resistance as reported in **[89].**

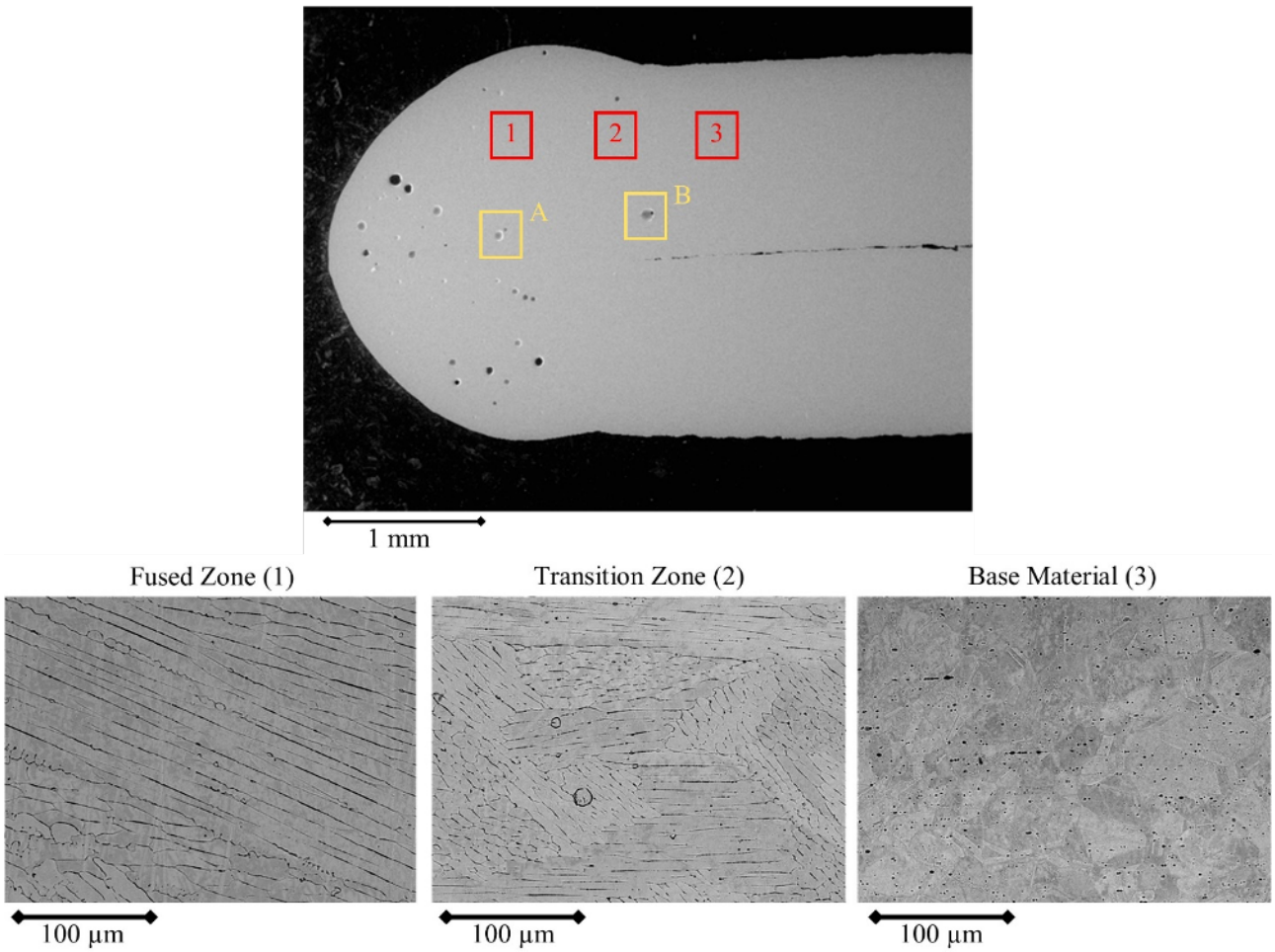

Figure 119: Cross section SEM images of the hairpins welded sample.

Chemical analysis were also carried out in order to obtain information about the chemical composition of different zone; for this purpose, several spectra where measured in the fused zone, both in the solid material and near some pores, as shown in Figure 120.

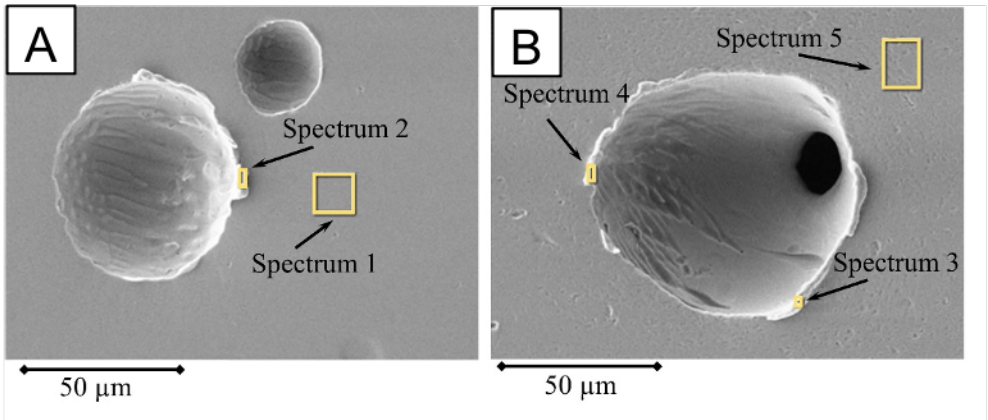

Figure 120: High SEM magnification images of denoted zones in figure 119.

The chemical composition of the marked points in Figure 120 is reported in Table 32; it is clear that the contamination of the molten material is very low, since the maximum quantity of oxygen is about 0.5% and no traces of insulating lacquer are detected.

Zone	O (Wt %)	Cu (Wt%)
Spectrum 1	0.37	99.63
Spectrum 2	0.52	99.48
Spectrum 3	0.36	99.64
Spectrum 4	0.49	99.51
Spectrum 4	0.41	99.59

Table 32: Chemical composition measurements.

6.7. Conclusions

The laser welding of pure copper hairpins was investigated in this chapter. Metallographic evaluations, tensile tests, electrical resistance tests, and micro-hardness tests were used to examine the specimens. The following considerations were made up as a result of these activities:

- With a total energy density of 11-12 MJ /cm^2, a process feasibility window has been developed in terms of welding power and speed; good results were obtained in terms of bead shape and porosity. With this input of energy, a sphere-shaped welding is obtained that covers the hairpins with lower presence of porosity and reduced dimensions of the latter. As the energy supply increases, both the dimensions of the molten area and those of the porosities present inside it increase; while with values lower than the optimal one, there is lack of fusion.

- By setting a high laser power and a high welding speed, the minimum porosity and maximum repeatability of the process were obtained with the same ideal energy density values.

- Maximum tensile load equal to 490 N was achieved and the fracture occurred near the heat affected zone (HAZ) with the optimized parameters.

- Micro hardness profile showed a softening in the HAZ and in the fused zone with a minimum of 54 HV compared to 64 HV of the base material.

- As far as the electrical properties of the connection are concerned, an optimal value in terms of molten area has been found; to this corresponds an electrical contact resistance of 95 μΩ was achieved, while the unwelded material resistance was 114 μΩ.

- SEM-EDS analysis shows that, despite the absence of a shielding gas, the presence of oxygen is very low and no traces of contamination due to insulating lacquer vaporization are detected.

Conclusions and final remarks

The thesis presents the research activity conducted in collaboration with Ferrari Auto S.p.A. for the development and characterization of the laser welding process in the manufacture of components for hybrid and electric vehicles. With this research project, the objective was to exploit the advantages of LBW technology for electrical applications in the automotive sector from a manufacturing point of view. Particular attention was paid to the possibility of creating high-performance battery modules and stator windings entirely in-house produced. In the transport sector, in particular e-mobility, the possibility of designing and manufacturing strategic components, starting from the main elements such as the single lithium-ion cell for batteries and copper conductors for electric motors, would have a significant impact on performance of the cars compared to competitors on the market. To date, most end users require the production of these components to external suppliers who provide the customer with the components without the possibility of performing research and development on the latter; this is equivalent to saying that the performance obtained from certain components, hence the characteristics of the car, are closely linked to the know-how of the supplier.

On the basis of these assumptions, the work was developed in close collaboration with Ferrari's Technical Office - Hybrid Components which deals with the development of components for future hybrid cars. The expertise already acquired by the research and development group and the possibility of studying the applicability of laser technology on this topic, led to the evolution of the project.

In particular, knowledge of the LBW process is still immature for many companies looking to bring the process in-house to build their know-how on the theme. For this reason, the achievement of the described objective required a purely experimental broad-spectrum study to evaluate its feasibility and optimize the technology based on this application and the different components to be produced.

To date, most battery modules are based on pouch cells, the electrodes of which are thin sheets of copper and aluminum, and on prismatic cells where there is a need to join sheets of pure aluminum with different thicknesses. The pouch cells are those that present the best compromise between weight, dimensions and performance in terms of energy; for this reason, the research activity has focused more on this type of cells also due to the greater challenges to be faced.

The study of joining process of battery modules based on pouch cells involves several challenges due to the different welding configurations possible within the same module and to the inevitable formation of hard and brittle intermetallic phases which compromise the performance of the connection. The study aimed to define the best solution in terms of hardware and material positioning solutions in order to achieve the maximum performance.

The configuration with fiber laser source and small spot diameter, less than 100 μm, is the solution that allows to join thin sheets of high-reflective materials with a reduced laser power, thus reducing the interaction time and the total heat input during the process. The process window is wider and better control of the depth of penetration and mixing between the materials can be obtained. Characteristics, that translate into better mechanical properties, with ductile behaviour during shear tensile test, and electrical properties of the joint; a linear correlation was obtained between mechanical and electrical properties of the connections which are fundamental for the performance of the entire battery module. SEM-EDS analysis have shown that with this latest hardware configuration, the formation of copper-rich phases, with a copper composition of about 50-60 at. % which are detrimental to the properties of the joint, can be avoided or minimized. Welding with wobbling scan strategy, obtained through the rotation and translation motion of the laser beam, allows to increase both the resistant section of the joint which increases both the mechanical and electrical characteristics since the area to which current passes is greater. The results have shown that it is not advisable to increase the amplitude of oscillation beyond a certain threshold, since the greater the path of the laser beam, the higher the heat to guarantee a complete melting of the materials with a consequent increase in the dilution between the materials and formations of hard and brittle intermetallic phases. The configuration with copper, a contact with the laser beam, is the most suitable when joining process that includes several layers is required; the physical and chemical characteristics of copper, in particular higher density and lower thermal expansion coefficient than aluminum, allow to obtain morphological characteristics with good morphological characteristics, i.e. homogeneous bead and without surface defects (for example transverse micro cracks) and high mechanical and electrical properties. The thermal aging tests, in which the effect of current transmission was studied, confirmed what was previously found; in particular, for the current profiles investigated, no differences were found in terms of maximum breaking load and morphology of the seam. From the point of view of assembling a battery pack, and therefore of possible errors in the production line, it has been found that the configuration with copper as the superior material is the one that presents the most challenges and requires a correct setup especially in terms of distance of work (lens-workpiece) that must be respected; a rework, in linear mode, without the need to change positioning, can be used in case of errors.

The results obtained, for the previous cell's type, were used for an experimental campaign on prismatic cells, whose tabs are pure aluminum to be welded with a busbar; main challenge is represented by the temperature constraint, not to be overcome during the assembly of the module, which could trigger thermal runway of the cell. The tests have shown that a correct setting of the process parameters, in particular the laser power necessary to melt the material and high process

speeds, allow to reduce the porosities inside the joint and respect the temperature constraints, obtaining good mechanical and electrical properties.

Lastly, the joining process of rectangular pure copper conductors with the same setup defined as optimal was studied. In particular, a particular scanning strategy has been implemented by programming the galvanometric scanner head. Also, in this case a process feasibility window has been identified; with the same optimal energy supplied, high power and speed made it possible to reduce the presence of porosity inside the joint, even if characterized by high variability. Good mechanical and electrical properties were obtained with the optimized parameters, resulting in a linear relationship between the two.

With the results obtained it was finally possible to produce prototypes of battery modules and electric motors, necessary for the validation of the electric and thermal models, entirely designed and produced internally following the results obtained with the experimental activities. Furthermore, both an internal regulation for the qualitative validation of the junctions for the different case studies and the characterization methods, necessary for the end-of-line tests, to evaluate the properties of the different configurations and components (battery and electric motors) have been defined.

The research activity, finally, made it possible to identify which is the laser system, in terms of laser source and welding head, which guarantees correct execution of the processing. In particular, considering the laser sources, those in fiber, with a very small diameter of the latter, which emit in the near infrared range are the most suitable for the analyzed processes. In the next few years, it will also be necessary to consider the availability at industrial level on a large scale of laser sources that emit with shorter wavelengths and particular attention will be paid to blue and green lasers which are better absorbed by high-reflective materials, in particular by the copper. The beam movement system, by means of a galvanometric scanner head, represents the ideal solution for this kind of applications; in fact, the need to work in small spaces, many times with sensitive components nearby and the need to carry out welding seams on very small areas with high processing speeds, make the fixed head unsuitable for use in the manufacturing of components for e-mobility especially if it is considered that the welding head is fixed on the end effector of large robots and the movement of the latter could be limited due to problems of weights and dimensions. Finally, a vision system that scans the work area and guarantees a correct execution of the welding seam must be always added to the system since, particularly in the case of the production of batteries, the error on a single weld it can generate a waste of the entire battery module with a consequent increase in costs for the company.

References

[1] M. Kirchhoff, “Laser Applications in Battery Production - From Cutting Foils to Welding the e Case,” *3rd Int. Electr. Drives Prod. Conf.*, pp. 1–3.

[2] A. Perner and J. Vetter, “Lithium-ion batteries for hybrid electric vehicles and battery electric vehicles,” *Adv. Batter. Technol. Electr. Veh.*, pp. 173–190, Jan. 2015.

[3] A. Das, D. Li, D. Williams, and D. Greenwood, “Joining technologies for automotive battery systems manufacturing,” *World Electr. Veh. J.*, vol. 9, no. 2, 2018.

[4] S. S. Lee, T. H. Kim, S. J. Hu, W. W. Cai, and J. A. Abell, “Joining technologies for automotive lithium-ion battery manufacturing - A review,” *ASME 2010 Int. Manuf. Sci. Eng. Conf. MSEC 2010*, vol. 1, no. May, pp. 541–549, 2010.

[5] E. A. Grunditz and T. Thiringer, “Performance analysis of current BEVs based on a comprehensive review of specifications,” *IEEE Trans. Transp. Electrif.*, vol. 2, no. 3, pp. 270–289, 2016.

[6] T. Glaessel, J. Seefried, and J. Franke, “Challenges in the manufacturing of hairpin windings and application opportunities of infrared lasers for the contacting process,” *2017 7th Int. Electr. Drives Prod. Conf. EDPC 2017 - Proc.*, vol. 2017-Decem, no. 978, pp. 1–7, 2018.

[7] E. Capello, “Le lavorazioni industriali mediante laser di potenza.” pp. 1–68, 2003.

[8] A. Fortunato and A. Ascari, “Tecnologie di Giunzione mediante saldatura, volume 2, lavorazioni con fasci ad alta potenza. Esculapio.” .

[9] W. M. Steen and M. J., *Laser Material Processing*. 2014.

[10] R. P. Verma and M. Kumar Lila, “A short review on aluminium alloys and welding in structural applications,” *Mater. Today Proc.*, no. xxxx, pp. 1–5, 2021.

[11] T. A. Barnes and I. R. Pashby, “Joining techniques for aluminum spaceframes used in automobiles. Part I - solid and liquid phase welding,” *J. Mater. Process. Technol.*, vol. 99, no. 1, pp. 62–71, 2000.

[12] P. Maji, S. K. Ghosh, R. K. Nath, and R. Karmakar, “Microstructural, mechanical and wear characteristics of aluminum matrix composites fabricated by friction stir processing,” *J. Brazilian Soc. Mech. Sci. Eng.*, vol. 42, no. 4, pp. 1–24, 2020.

[13] N. E. Udoye, O. S. I. Fayomi, and A. O. Inegbenebor, “Assessment of wear resistance of aluminium alloy in manufacturing industry-a review,” *Procedia Manuf.*, vol. 35, pp. 1383–1386, 2019.

[14] W. S. Miller *et al.*, “Recent development in aluminium alloys for the automotive industry,” *Mater. Sci. Eng. A*, vol. 280, no. 1, pp. 37–49, 2000.

[15] J. Xin *et al.*, “The microstructures and mechanical properties of dissimilar laser welding of copper and 316L stainless steel with Ni interlayer,” *Cryogenics (Guildf).*, vol. 118, p. 103344, Sep. 2021.

[16] L. J. Zhang, J. Ning, X. J. Zhang, G. F. Zhang, and J. X. Zhang, “Single pass hybrid laser-MIG welding of 4-mm thick copper without preheating,” *Mater. Des.*, vol. 74, pp. 1–18, 2015.

[17] E. Biro, D. C. Weckman, and Y. Zhou, “Pulsed Nd:YAG laser welding of copper using oxygenated assist gases,” *Metall. Mater. Trans. A Phys. Metall. Mater. Sci.*, vol. 33, no. 7, pp. 2019–2030, 2002.

[18] U. F. Shaikh, A. Das, A. Barai, and I. Masters, “Electro-Thermo-Mechanical Behaviours of Laser Joints for Electric Vehicle Battery Interconnects,” *2019 Electr. Veh. Int. Conf. EV 2019*, pp. 7–12, 2019.

[19] P. A. Schmidt, M. Schweier, and M. F. Zaeh, “Joining of lithium-ion batteries using laser beam welding: Electrical losses of welded aluminum and copper joints,” *ICALEO 2012 - 31st Int. Congr. Appl. Lasers Electro-Optics*, vol. 915, no. 2012, pp. 915–923, 2012.

[20] S. Dhara and A. Das, “Impact of ultrasonic welding on multi-layered Al–Cu joint for electric vehicle battery applications: A layer-wise microstructural analysis,” *Mater. Sci. Eng. A*, vol. 791, no. June, p. 139795, 2020.

[21] P. Kah, C. Vimalraj, J. Martikainen, and R. Suoranta, “Factors influencing Al-Cu weld properties by intermetallic compound formation,” *Int. J. Mech. Mater. Eng.*, vol. 10, no. 1, 2015.

[22] M. Weigl, F. Albert, and M. Schmidt, “Enhancing the Ductility of Laser-Welded Copper-Aluminum Connections by using Adapted Filler Materials,” *Phys. Procedia*, vol. 12, no. PART 2, pp. 332–338, Jan. 2011.

[23] S. J. Lee, H. Nakamura, Y. Kawahito, and S. Katayama, “Effect of welding speed on microstructural and mechanical properties of laser lap weld joints in dissimilar Al and Cu sheets,” *Sci. Technol. Weld. Join.*, vol. 19, no. 2, pp. 111–118, 2014.

[24] P. Schmalen, K. Mathivanan, and P. Plapper, “Metallographic Studies of Dissimilar Al-Cu Laser-Welded Joints Using Various Etchants,” *Metallogr. Microstruct. Anal.*, vol. 8, no. 1, pp. 3–11, 2019.

[25] D. Zuo, S. Hu, J. Shen, and Z. Xue, “Intermediate layer characterization and fracture behavior of laser-welded copper/aluminum metal joints,” *Mater. Des.*, vol. 58, pp. 357–362, 2014.

[26] M. H. M. Kouters, G. H. M. Gubbels, and O. Dos Santos Ferreira, “Characterization of

intermetallic compounds in Cu-Al ball bonds: Mechanical properties, interface delamination and thermal conductivity," *Microelectron. Reliab.*, vol. 53, no. 8, pp. 1068–1075, 2013.

[27] A. García-Romero, A. Delgado, A. Urresti, K. Martín, and J. M. Sala, "Corrosion behaviour of several aluminium alloys in contact with a thermal storage phase change material based on Glauber's salt," *Corros. Sci.*, vol. 51, no. 6, pp. 1263–1272, Jun. 2009.

[28] E. A. El-Danaf, M. S. Soliman, A. A. Almajid, and M. M. El-Rayes, "Enhancement of mechanical properties and grain size refinement of commercial purity aluminum 1050 processed by ECAP," *Mater. Sci. Eng. A*, vol. 458, no. 1–2, pp. 226–234, Jun. 2007.

[29] Y. Yang *et al.*, "Microstructure Evolution of 1050 Commercial Purity Aluminum Processed by High-Strain-Rate Deformation," *J. Mater. Eng. Perform.*, vol. 24, no. 11, pp. 4307–4312, 2015.

[30] N. A. Alsaleh, "Micro-crack Characteristics of Aluminum 1050 Sheets in Bending at Elevated Temperatures Micro-crack Characteristics of Aluminum 1050 Sheets in Bending at Elevated Temperatures," vol. 7, no. September, pp. 18–27, 2017.

[31] T. Sun, P. Franciosa, and D. Ceglarek, "Effect of focal position offset on joint integrity of AA1050 battery busbar assembly during remote laser welding," *J. Mater. Res. Technol.*, vol. 14, pp. 2715–2726, 2021.

[32] N. Lewchalermwong, M. Masomtob, V. Lailuck, and C. Charoenphonphanich, "Material selection and assembly method of battery pack for compact electric vehicle," *IOP Conf. Ser. Mater. Sci. Eng.*, vol. 297, no. 1, 2018.

[33] T. Y. Kuo and H. C. Lin, "Effects of pulse level of Nd-YAG laser on tensile properties and formability of laser weldments in automotive aluminum alloys," *Mater. Sci. Eng. A*, vol. 416, no. 1–2, pp. 281–289, Jan. 2006.

[34] J. M. Sánchez-Amaya, T. Delgado, J. J. De Damborenea, V. Lopez, and F. J. Botana, "Laser welding of AA 5083 samples by high power diode laser," *Sci. Technol. Weld. Join.*, vol. 14, no. 1, pp. 78–86, 2009.

[35] M. Zavala-Arredondo *et al.*, "Laser diode area melting for high speed additive manufacturing of metallic components," *Mater. Des.*, vol. 117, pp. 305–315, Mar. 2017.

[36] A. Das, T. Dale, I. Masters, and D. Widanage, "Feasibility of fillet edge weld using laser wobble technique," *Procedia CIRP*, vol. 95, pp. 846–851, 2020.

[37] R. Lin, H. ping Wang, F. Lu, J. Solomon, and B. E. Carlson, "Numerical study of keyhole dynamics and keyhole-induced porosity formation in remote laser welding of Al alloys," *Int. J. Heat Mass Transf.*, vol. 108, pp. 244–256, May 2017.

[38] F. Fetzer, C. Hagenlocher, R. Weber, and T. Graf, "Geometry and stability of the capillary

during deep-penetration laser welding of AlMgSi at high feed rates," *Opt. Laser Technol.*, vol. 133, p. 106562, Jan. 2021.

[39] F. Fetzer, M. Sommer, R. Weber, J. P. Weberpals, and T. Graf, "Reduction of pores by means of laser beam oscillation during remote welding of AlMgSi," *Opt. Lasers Eng.*, vol. 108, pp. 68–77, Sep. 2018.

[40] J. Ning, L. J. Zhang, A. Wang, Q. L. Bai, J. N. Yang, and J. X. Zhang, "Effects of double-pass welding and extrusion on properties of fiber laser welded 1.5-mm thick T2 copper joints," *J. Mater. Process. Technol.*, vol. 237, pp. 75–87, 2016.

[41] L. J. Zhang, J. Ning, X. J. Zhang, G. F. Zhang, and J. X. Zhang, "Single pass hybrid laser–MIG welding of 4-mm thick copper without preheating," *Mater. Des.*, vol. 74, pp. 1–18, Jun. 2015.

[42] S. T. Auwal, S. Ramesh, F. Yusof, and S. M. Manladan, "A review on laser beam welding of titanium alloys," *Int. J. Adv. Manuf. Technol.*, vol. 97, no. 1–4, pp. 1071–1098, 2018.

[43] S. Liebl, R. Wiedenmann, A. Ganser, P. Schmitz, and M. F. Zaeh, "Laser Welding of Copper Using Multi Mode Fiber Lasers at Near Infrared Wavelength," *Phys. Procedia*, vol. 56, no. C, pp. 591–600, Jan. 2014.

[44] E. Biro, D. C. Weckman, and Y. Zhou, "Pulsed Nd : YAG Laser Welding of Copper Using Oxygenated Assist Gases," vol. 33, no. July 2002, pp. 2019–2030, 2019.

[45] A. Hess, R. Schuster, A. Heider, R. Weber, and T. Graf, "Continuous Wave Laser Welding of Copper with Combined Beams at Wavelengths of 1030 nm and of 515 nm," *Phys. Procedia*, vol. 12, no. PART 1, pp. 88–94, Jan. 2011.

[46] D. Petring and V. N. Goneghany, "Parameter dependencies of copper welding with multi-kW lasers at 1 micron wavelength," *Phys. Procedia*, vol. 12, no. PART 1, pp. 95–104, 2011.

[47] A. Heider, P. Stritt, A. Hess, R. Weber, and T. Graf, "Process Stabilization at welding Copper by Laser Power Modulation," *Phys. Procedia*, vol. 12, no. PART 1, pp. 81–87, Jan. 2011.

[48] H. C. Chen, G. Bi, M. L. S. Nai, and J. Wei, "Enhanced welding efficiency in laser welding of highly reflective pure copper," *J. Mater. Process. Technol.*, vol. 216, pp. 287–293, Feb. 2015.

[49] L. J. Zhang, G. F. Zhang, J. Ning, X. J. Zhang, and J. X. Zhang, "Microstructure and properties of the laser butt welded 1.5-mm thick T2 copper joint achieved at high welding speed," *Mater. Des.*, vol. 88, pp. 720–736, Dec. 2015.

[50] M. Weigl and M. Schmidt, "Modulated laser spot welding of dissimilar copper-aluminium connections," *Int. Conf. Multi-Material Micro Manuf. 4M/International Conf. Micro Manuf.*

ICOMM, pp. 211–214, 2009.

[51] T. Solchenbach and P. Plapper, "Mechanical characteristics of laser braze-welded aluminium-copper connections," *Opt. Laser Technol.*, vol. 54, pp. 249–256, 2013.

[52] P. Schmalen, P. Plapper, I. Peral, I. Titov, O. Vallcorba, and J. Rius, "Composition and phases in laser welded Al-Cu joints by synchrotron x-ray microdiffraction," *Procedia CIRP*, vol. 74, pp. 27–32, 2018.

[53] M. Braunovic, "Reliability of power connections," *J. Zhejiang Univ. Sci. A*, vol. 8, no. 3, pp. 343–356, 2007.

[54] V. Dimatteo, A. Ascari, and A. Fortunato, "Continuous laser welding with spatial beam oscillation of dissimilar thin sheet materials (Al-Cu and Cu-Al): Process optimization and characterization," *J. Manuf. Process.*, vol. 44, 2019.

[55] M. Jarwitz, F. Fetzer, R. Weber, and T. Graf, "Weld seam geometry and electrical resistance of laser-welded, aluminum-copper dissimilar joints produced with spatial beam oscillation," *Metals (Basel).*, vol. 8, no. 7, 2018.

[56] M. J. Brand, P. A. Schmidt, M. F. Zaeh, and A. Jossen, "Welding techniques for battery cells and resulting electrical contact resistances," *J. Energy Storage*, vol. 1, no. 1, pp. 7–14, 2015.

[57] M. Kraetzsch, J. Standfuss, A. Klotzbach, J. Kaspar, B. Brenner, and E. Beyer, "Laser Beam Welding with High-Frequency Beam Oscillation: Welding of Dissimilar Materials with Brilliant Fiber Lasers," *Phys. Procedia*, vol. 12, no. PART 1, pp. 142–149, Jan. 2011.

[58] F. Fetzer, M. Jarwitz, P. Stritt, R. Weber, and T. Graf, "Fine-tuned remote laser welding of aluminum to copper with local beam oscillation," *Phys. Procedia*, vol. 83, pp. 455–462, 2016.

[59] A. Ascari, A. Fortunato, and V. Dimatteo, "Short pulse laser welding of aluminum and copper alloys in dissimilar configuration," *J. Laser Appl.*, vol. 32, no. 2, p. 022025, 2020.

[60] A. Ascari, A. Fortunato, E. Liverani, and A. Lutey, "Application of different pulsed laser sources to dissimilar welding of Cu and Al alloys," *Proc. Lasers Manuf. Conf.*, pp. 1–10, 2019.

[61] F. Lerra, A. Ascari, and A. Fortunato, "The influence of laser pulse shape and separation distance on dissimilar welding of Al and Cu fi lms," vol. 45, no. July, pp. 331–339, 2019.

[62] M. Nava, "The road ahead for electric vehicles," *EC M Electr. Constr. Maint.*, vol. 118, no. 3, pp. C20–C22, 2019.

[63] T. F. Fuller, M. Doyle, and J. Newman, "Simulation and Optimization of the Dual Lithium Ion Insertion Cell," *J. Electrochem. Soc.*, vol. 141, no. 1, pp. 1–10, 1994.

[64] A. Das, D. Li, D. Williams, and D. Greenwood, "Weldability and shear strength feasibility

study for automotive electric vehicle battery tab interconnects," *J. Brazilian Soc. Mech. Sci. Eng.*, vol. 41, no. 1, pp. 1–14, 2019.

[65] H. Saariluoma, A. Piiroinen, A. Unt, J. Hakanen, T. Rautava, and A. Salminen, "Overview of optical digital measuring challenges and technologies in laser welded components in ev battery module design and manufacturing," *Batteries*, vol. 6, no. 3, pp. 1–15, 2020.

[66] A. N. Jansen, K. Amine, A. E. Newman, D. R. Vissers, and G. L. Henriksen, "Low-cost, flexible battery packaging materials," *Jom*, vol. 54, no. 3, 2002.

[67] P. Berg, J. Soellner, M. Herrmann, and A. Jossen, "Structural dynamics of lithium-ion cells—part II: Investigation of large-format prismatic cells and method evaluation," *J. Energy Storage*, vol. 28, no. January, p. 101246, 2020.

[68] L. Shui, F. Chen, A. Garg, X. Peng, N. Bao, and J. Zhang, "Design optimization of battery pack enclosure for electric vehicle," *2018 6th Int. Conf. Mech. Automot. Mater. Eng. C. 2018*, pp. 79–84, 2018.

[69] Q. Wang, P. Ping, X. Zhao, G. Chu, J. Sun, and C. Chen, "Thermal runaway caused fire and explosion of lithium ion battery," *J. Power Sources*, vol. 208, pp. 210–224, Jun. 2012.

[70] N. Yang, X. Zhang, B. Shang, and G. Li, "Unbalanced discharging and aging due to temperature differences among the cells in a lithium-ion battery pack with parallel combination," *J. Power Sources*, vol. 306, pp. 733–741, Feb. 2016.

[71] M. F. R. Zwicker, M. Moghadam, W. Zhang, and C. V. Nielsen, "Automotive battery pack manufacturing – a review of battery to tab joining," *J. Adv. Join. Process.*, vol. 1, no. November 2019, p. 100017, 2020.

[72] V. Dimatteo, A. Ascari, P. Faverzani, L. Poggio, and A. Fortunato, "The effect of process parameters on the morphology, mechanical strength and electrical resistance of CW laser-welded pure copper hairpins," *J. Manuf. Process.*, vol. 62, no. November 2020, pp. 450–457, 2021.

[73] A. Mahr, A. Mayr, T. Jung, and J. Francek, "Robot-assisted concept for assembling form coils in laminated stator cores of large electric motors.pdf." .

[74] T. Glaessel *et al.*, "Process Reliable Laser Welding of Hairpin Windings for Automotive Traction Drives," *2019 Int. Conf. Eng. Sci. Ind. Appl. ICESI 2019*, pp. 1–6, 2019.

[75] T. Ishigami, Y. Tanaka, and H. Homma, "Development of motor stator with rectangular-wire lap winding and an automatic process for its production," *Electr. Eng. Japan (English Transl. Denki Gakkai Ronbunshi)*, vol. 187, no. 4, pp. 51–59, 2014.

[76] T. Glaessel, F. Baat, Schwinghammer, Danie, J. Seefried, A. Kuehl, and J. Francek, "Infrared laser based contacting of bar-wound windings in the field of electric drives production." pp.

17–22, 2018.

[77] P. Mock, “January 2019 Co2 Emission Standards for Passenger Cars and Light-Commercial Vehicles in the European Union,” no. January 2019, 2021.

[78] V. Dimatteo, A. Ascari, E. Liverani, and A. Fortunato, “Experimental investigation on the effect of spot diameter on continuous-wave laser welding of copper and aluminum thin sheets for battery manufacturing,” *Opt. Laser Technol.*, vol. 145, no. July 2021, p. 107495, 2022.

[79] H. G. Jiang, J. Y. Dai, H. Y. Tong, B. Z. Ding, Q. H. Song, and Z. Q. Hu, “Interfacial reactions on annealing Cu/Al multilayer thin films,” *J. Appl. Phys.*, vol. 74, no. 10, pp. 6165–6169, Nov. 1993.

[80] V. Dimatteo, A. Ascari, and A. Fortunato, “DISSIMILAR LASER WELDING PROCESSES OF COPPER AND ALUMINUM ALLOYS IN MULTILAYER CONFIGURATION FOR BATTERY APPLICATIONS,” *J. Laser Appl.*, vol. 33, no. 4, 2021.

[81] S. Yan and Y. Shi, “Influence of laser power on microstructure and mechanical property of laser-welded Al/Cu dissimilar lap joints,” *J. Manuf. Process.*, vol. 45, no. 7089, pp. 312–321, 2019.

[82] J. M. Sánchez-Amaya, T. Delgado, L. González-Rovira, and F. J. Botana, “Laser welding of aluminium alloys 5083 and 6082 under conduction regime,” *Appl. Surf. Sci.*, vol. 255, no. 23, pp. 9512–9521, Sep. 2009.

[83] F. Fetzer, M. Sommer, R. Weber, J. P. Weberpals, and T. Graf, “Reduction of pores by means of laser beam oscillation during remote welding of AlMgSi,” *Opt. Lasers Eng.*, vol. 108, no. May, pp. 68–77, 2018.

[84] K. Li, F. G. Lu, S. T. Guo, H. C. Cui, and X. H. Tang, “Porosity sensitivity of A356 Al alloy during fiber laser welding,” *Trans. Nonferrous Met. Soc. China*, vol. 25, no. 8, pp. 2516–2523, Aug. 2015.

[85] J. T. Norris, C. V. Robino, D. A. Hirschfeld, and M. J. Perricone, “Effects of laser parameters on porosity formation: Investigating millimeter scale continuous wave Nd:YAG laser welds,” *Weld. J.*, vol. 90, no. 10, 2011.

[86] “ISO 14270:2016-11. Resistance welding - destructive testing of welds - specimen dimensions and procedure for mechanized peel testing resistance spot, seam and embossed projection welds”. 2016.

[87] L. J. Zhang, G. F. Zhang, J. Ning, X. J. Zhang, and J. X. Zhang, “Microstructure and properties of the laser butt welded 1.5-mm thick T2 copper joint achieved at high welding speed.pdf.” Materials and design, 2015.

[88] P. Xue, B. L. Xiao, Q. Zhang, and Z. Y. Ma, “Achieving friction stir welded pure copper joints with nearly equal strength to the parent metal via additional rapid cooling,” *Scr. Mater.*, vol. 64, no. 11, pp. 1051–1054, Jun. 2011.

[89] L. Lu, Y. Shen, X. Chen, L. Qian, and K. Lu, “Ultrahigh Strength and High Electrical Conductivity in Copper,” *Science (80-.).*, vol. 304, no. 5669, pp. 422–426, 2004.